

**Massachusetts Institute of Technology  
Woods Hole Oceanographic Institution**



**Joint Program  
in Oceanography/  
Applied Ocean Science  
and Engineering**



---

**DOCTORAL DISSERTATION**

Inversion for Subbottom Sound Velocity Profiles in the  
Deep and Shallow Ocean

by

Luiz L. Souza

February 2005

**DISTRIBUTION STATEMENT A**  
Approved for Public Release  
Distribution Unlimited

# Inversion for Subbottom Sound Velocity Profiles in the Deep and Shallow Ocean

by

Luiz Alberto Lopes de Souza

Engenheiro Eletricista, Faculdades Reunidas Nuno Lisboa, Brazil (1976)

M.Sc. E.E. and Eng. Acoustics, Naval Postgraduate School (1989)

Submitted to the Departments of Ocean Engineering, MIT, and

Applied Ocean Physics and Engineering, WHOI,

in partial fulfillment of the requirements for the degree of

Doctor of Philosophy in Applied Ocean Sciences

at the

MASSACHUSETTS INSTITUTE OF TECHNOLOGY

and the

WOODS HOLE OCEANOGRAPHIC INSTITUTION

February 2005

© Luiz Alberto Lopes de Souza, MMV. All rights reserved.

The author hereby grants to MIT and WHOI permission to reproduce  
and distribute publicly paper and electronic copies of this thesis  
document in whole or in part.

Author.....

.....  
Luiz Alberto Lopes de Souza  
Departments of Ocean Engineering, MIT, and  
Applied Ocean Physics and Engineering, WHOI,

January 18th, 2005

Certified by.....

George V. Frisk.....  
George V. Frisk  
Scientist Emeritus, WHOI

Thesis Supervisor

Accepted by.....

Mark A. Grosenbaugh.....  
Mark A. Grosenbaugh

Chair, Joint Committee in Applied Ocean Science and Engineering,  
MIT/WHOI

# Inversion for Subbottom Sound Velocity Profiles in the Deep and Shallow Ocean

by

Luiz Alberto Lopes de Souza

Submitted to the Departments of Ocean Engineering, MIT, and  
Applied Ocean Physics and Engineering, WHOI,  
on January 18th, 2005, in partial fulfillment of the  
requirements for the degree of  
Doctor of Philosophy in Applied Ocean Sciences

## Abstract

This thesis investigates the application of acoustic measurements in the deep and shallow ocean to infer the sound velocity profile (svp) in the seabed. For the deep water ocean, an exact method based on the Gelfand-Levitan integral equation is evaluated. The input data is the complex plane-wave reflection coefficient estimated from measurements of acoustic pressure in water. We apply the method to experimental data and estimate both the reflection coefficient and the seabed svp. A rigorous inversion scheme is hence applied in a realistic problem.

For the shallow ocean, an inverse eigenvalue technique is developed. The input data are the eigenvalues associated with propagating modes, measured as a function of source-receiver range. We investigate the estimation of eigenvalues from acoustic fields measured in laterally varying environments. We also investigate the errors associated with estimating varying modal eigenvalues, analogous to the estimation of time-varying frequencies in multicomponent signals, using time-varying autoregressive (TVAR) methods. We propose and analyze two AR sequential estimators, one for model coefficients, another for the zeros of the AR characteristic polynomial. The decimation of the pressure field defined in a discrete range grid is analyzed as a tool to improve AR estimation.

The nonlinear eigenvalue inverse problem of estimating the svp from a sequence of eigenvalues is solved by iterating linearized approximations. The solution to the inverse problem is proposed in the form of a Kalman filter. The resolution and variance of the eigenvalue inverse problem are analyzed in terms of the Cramer–Rao lower bound and the Backus–Gilbert (BG) resolution theory. BG theory is applied to the design of shallow-water experiments. A method is developed to compensate for the Doppler deviation observed in experiments with moving sources.

Thesis Supervisor: George V. Frisk  
Title: Scientist Emeritus, WHOI

## Acknowledgments

I would like to thank the people who have contributed to this work. First, to my advisor, Dr. George Frisk, to whom I am deeply grateful. His advice, support, and encouragement were invaluable. I would like also to thank Dr. James Preisig for his advice and insight. My thanks to the other members of my thesis committee, Dr. Ralph Stephen and Prof. Henrik Schmidt for providing guidance during the development of my thesis. I am grateful to Dr. John Colosi, who served as chairman of the thesis defense.

James Doutt and Cynthia Sellers provided me with professional help and friendship. I will miss our group meetings. Prof. Allan Pierce, who took part in many of the meetings, always provided new insights, and I am thankful for them. I would like to thank all my colleagues at MIT and WHOI, in particular Kyle Becker, Travis Poole, Sunwoong Lee, Purnima Ratilal, and my friend Karl Burr, for the fruitful exchange of ideas. A special thank you to Julia Westwater, Marsha Gomes, and Stacey Drange. I counted on them too many times. They made my life a lot simpler.

I want to express my love for Leila, my wife. I could not have done my work without her constant support. I am also deeply indebted to my sons, Daniel and Pedro. I can only hope to compensate them for the part-time father they have had for a while. Finally, I wish to express my love for my parents Darcy (in memoriam) and Judith Souza. My family made the endeavor worthwhile. I dedicate this work to them.

I am grateful for the support of my work provided by the WHOI Academic Programs Office and the Office of Naval Research.

# Contents

<b>1</b>	<b>Introduction</b>	<b>8</b>
1.1	Background . . . . .	8
1.2	Thesis Overview . . . . .	10
<b>2</b>	<b>Inversion for Subbottom Sound Velocity Profiles in the Deep Ocean: Application of an Exact Inverse Method</b>	<b>13</b>
2.1	Introduction . . . . .	13
2.1.1	Inversion from Reflection Coefficient Data . . . . .	14
2.1.2	Measurement of the Reflection Coefficient . . . . .	19
2.2	The Icelandic Basin Experiment . . . . .	24
2.3	Icelandic Basin Data Analysis - Computing the Reflection Coefficient . .	29
2.3.1	Simulated Field Analysis . . . . .	29
2.3.2	From Simulated Fields to Reflection Coefficient . . . . .	34
2.3.3	Analysis of the Measured Acoustic Field . . . . .	41
2.3.4	Reflection Coefficient from Experimental Data . . . . .	49
2.4	Inversion from Reflection Coefficient Data . . . . .	59
2.4.1	Practical Issues Related to the Application of Merab's Method . .	59
2.4.2	Simulation Results . . . . .	65
2.4.3	Inversion from the Icelandic Basin Data . . . . .	71
2.5	Summary and Conclusions . . . . .	75
2.5.1	Reflection Coefficient . . . . .	75

2.5.2 Sound Velocity Profile Inversion . . . . .	77
<b>3 Range-Dependent Modal Eigenvalue Sequential Estimation</b>	<b>79</b>
3.1 Introduction . . . . .	79
3.1.1 The Shallow Water Acoustic Channel . . . . .	81
3.1.2 Eigenvalue Estimation . . . . .	84
3.1.3 The Modal Mapping Experiment (MOMAX) . . . . .	90
3.2 Difference Equation Representation of a Sum of Adiabatic Modes . . . . .	92
3.2.1 Range-Independent Case . . . . .	97
3.2.2 Range-Dependent Case: Single Mode . . . . .	100
3.2.3 Sum of Two Modes . . . . .	102
3.2.4 Sum of an Arbitrary Number of Modes . . . . .	109
3.2.5 A Realistic Example: Inverse Techniques Workshop . . . . .	111
3.3 Sequential Autoregressive Estimate . . . . .	118
3.3.1 Range-Varying Autoregressive Model . . . . .	118
3.3.2 Kalman Filter Implementation . . . . .	120
3.3.3 The VFF Adaptive Zero Estimator . . . . .	124
3.3.4 Competitive Smoother . . . . .	127
3.3.5 Pressure Field Decimation and Eigenvalue and Range Resolution	131
3.4 Numerical and Experimental Results . . . . .	140
3.4.1 A Note on Model Order Selection . . . . .	140
3.4.2 Abrupt Change of Eigenvalues: Synthetic Data . . . . .	141
3.4.3 Single-Mode Eigenvalue Estimation: Experimental Data . . . . .	143
3.4.4 Multiple Mode Estimation: Experimental Data - 50 Hz . . . . .	148
3.4.5 Multiple Mode Estimation: Experimental Data - 125 Hz . . . . .	150
3.4.6 Sloping Bottom: Synthetic Data . . . . .	154
3.5 Summary and Conclusions . . . . .	159

<b>4 Inversion for Subbottom Sound Velocity Profiles in the Shallow Ocean: Eigenvalue Inversion</b>	<b>166</b>
4.1 Introduction . . . . .	166
4.1.1 Eigenvalue Inverse Problem . . . . .	167
4.1.2 The Inverse Perturbative Technique . . . . .	168
4.1.3 The Stochastic Inverse . . . . .	172
4.1.4 The Backus-Gilbert (BG) Resolution Theory . . . . .	175
4.2 The Inverse Eigenvalue Problem . . . . .	179
4.2.1 The Measurement Equation . . . . .	180
4.2.2 The Derivative of the Modal Eigenvalues . . . . .	181
4.2.3 The Range-Varying Eigenvalue Inverse . . . . .	186
4.3 Variance and Resolution of the Inverse Eigenvalue Problem . . . . .	188
4.3.1 Cramer-Rao Bound for the Eigenvalue Inversion . . . . .	188
4.3.2 Sound Velocity Variance and Resolution . . . . .	191
4.3.3 Analysis of a Prototype Problem . . . . .	192
4.4 Source Speed Compensation . . . . .	201
4.4.1 Eigenvalue Bias due to Doppler Deviation . . . . .	201
4.4.2 Perturbative Formulation . . . . .	202
4.5 Data Analysis . . . . .	204
4.5.1 Prototype Problem with Source Speed Compensation . . . . .	204
4.5.2 Synthetic Data: Abrupt Modal Change . . . . .	220
4.6 Summary and Conclusions . . . . .	227
<b>5 Summary</b>	<b>231</b>
5.1 Contributions . . . . .	231
5.1.1 Chapter 2 . . . . .	231
5.1.2 Chapter 3 . . . . .	232
5.1.3 Chapter 4 . . . . .	233

5.2 Suggestions for Future Work . . . . .	235
<b>A MOMAX Raw Data Signal Processing</b>	<b>238</b>
A.1 Introduction . . . . .	238
A.2 The Short-Term Fourier Transform of the Raw Data . . . . .	243
A.3 DFT Implementation of the Short-Term Fourier Transform . . . . .	248
A.3.1 Selection of the Transform Size and Window Function . . . . .	249
A.3.2 Four Discrete Windows . . . . .	252
<b>B Difference Equation (DE) for a Sum of Varying Complex Exponentials</b>	<b>256</b>
B.1 DE for a Sum of $M$ Complex Exponentials[35] . . . . .	257
B.2 From DE Coefficients to First-Order Poles . . . . .	259
B.3 Error Between DE Characteristic Polynomial Roots and First-Order Poles	260
B.3.1 Error for Sums of Two Complex Exponentials . . . . .	262
B.3.2 Taylor Expansion of the Roots - General Case . . . . .	266
B.3.3 Error for Sums of Three Complex Exponentials . . . . .	269
<b>C The VFF Adaptive Zero Estimator Design</b>	<b>271</b>
C.1 Basic Design . . . . .	271
C.2 Error Gradient . . . . .	273
C.3 The Variable Forgetting Factor (VFF) . . . . .	275
<b>D The Second Order Kalman Filter</b>	<b>278</b>
<b>E Trapezoidal Rule and the Basis Function Representation</b>	<b>282</b>
<b>F Analysis of Sound Velocity and Frequency Perturbations</b>	<b>285</b>
F.1 Eigenvalues . . . . .	286
F.2 Group Speeds . . . . .	288
F.3 Perturbative Integral with Source Speed Compensation . . . . .	290

# Chapter 1

## Introduction

### 1.1 Background

This thesis deals with the problem of measuring geoacoustic properties of the ocean subbottom, the region of the seabed close to the water interface, from acoustic measurements in the water column. One important problem in Ocean Acoustics, as well as other branches of Acoustics, is the prediction of the sound field produced by a source in a given environment, the so called *forward problem*. The environment is characterized by its geometry and the physical properties of the water and surrounding media. In the ocean the geometry is determined by the bathymetry, the varying sea surface position, and the location of source and receiver.

For sound propagation prediction purposes and at sufficiently low frequencies, the sea surface is reasonably and simply modeled as a plane, pressure release surface where the acoustic pressure is zero. The water column and the seabed require a more complex description. In the water, the most important parameters are the sound velocity and absorption coefficient. Sediments may, in many cases, be also characterized as a fluid, but shear speed and absorption become important depending on the frequency and how close the source and receiver are to the bottom. More elaborate sediment models may require 13 or more parameters[72]. The sensitivity of the acoustic field with respect to

these *geoacoustic* properties suggests the idea of using sound measurements to infer their values, the geoacoustic *inverse problem*.

The idea is far from new. For decades marine geophysicists have used sound produced in the water to infer properties of the sea floor, and low frequency echo sounders or subbottom profilers have been used to obtain pictures of the bottom structure[10]. For the purpose of underwater propagation prediction, however, the subbottom must be characterized down to tens of meters below the water interface, not the kilometers geophysicists usually focus on. In the eighties, for example, a set of experiments were conducted in the Icelandic Basin, ultimately to characterize the seabed for application to propagation modeling [21]. When the US Navy started focusing on littoral warfare, the Office of Naval Research sponsored efforts to measure the properties of sediments in shallow waters down to a few hundred meters[71]. The geoacoustic inverse problem is an active area in Ocean Acoustics. The inversion for the sound velocity profile in the subbottom, modeled as a fluid, from acoustic data in water is the focus of the thesis.

Inverse methods can be broadly classified in three groups. One group includes techniques that solve iteratively the forward problem. Starting from a background environmental model, the forward solution is compared to a set of noisy measurements and the environmental parameters are adjusted in order to minimize a measure of the fitting error. These parameter search/optimization methods may involve hundreds of thousands of forward solutions, and are computationally intensive. They are the most used today by the Ocean Acoustics community, as can be inferred from the large number of books, articles, and conference presentations on the subject[9, 26, 74, 13].

On the other extreme are the methods based on a rigorous or exact formulation of the inverse problem[70, 45]. These theories relate some quantity inferred from the measured field (e.g., reflection coefficient, normal mode characteristic wavenumbers) to the desired property (sound velocity profile). Conditions for existence and uniqueness of solutions are usually established. The exact methods are developed for idealized conditions and require data whose measurement may not be feasible. Measurement error (noise) is not

usually considered.

Perturbative inverse techniques[43, 67, 61] provide a compromise between exact methods and those based on parameter search/optimization. The perturbative approach relies on the fact that the typical range of sound velocities and densities in the ocean and seabed are small compared to their mean value. Contrary to the parameter search/optimization methods, perturbative techniques are easily implemented and computationally inexpensive (the solution of the wave equation is computed a small number of times). One advantage over the exact methods is that measurement errors can be easily dealt with.

## 1.2 Thesis Overview

Exact formulations may lead to effective sound velocity profile measurement techniques that do not depend on initial guesses of the solution or its properties, and for which the conditions for uniqueness of the solution, if not attainable, are at least known. The mathematical framework make them suitable candidates for reference inverse methods.

Chapter 2 discusses the application of an exact inverse theory to actual experimental data. The exact theory was developed by Merab[45] and is based on the work of Gelfand and Levitan[25] developed in the context of potential inversion from scattering data in Quantum Mechanics. The input data required by Merab's method is the complex plane-wave reflection coefficient of the bottom.

The measurement of the magnitude and phase of the bottom reflection coefficient is an important issue in ocean acoustics by itself. In Chapter 2, a technique developed by Frisk and co-workers[22, 46] is applied to the measurement of the reflection coefficient using monochromatic acoustic data from the deep water experiment at the Icelandic Basin described by Frisk, Doutt, and Hays[21].

Apparently, there is a view in the Ocean Acoustics community

"that there is a difficulty in applying rigorous inversion schemes in realistic

problem, as the latter require much more information than is available in the experiments[74, p. v.].”

As shown in Chapter 2, this is not necessarily true. The reflection coefficient is estimated from actual experimental pressure data, which is then used as input to Merab’s method. The sound velocity profile in the seabed is recovered, and the errors explained.

In order to construct analytically tractable inverse problems, simplifying assumptions such as, for example, depth-only dependence of the geoacoustic parameters and lack of shear rigidity, are made. The results of rigorous methods may be, despite the simplifying assumptions, satisfactory for applications in acoustic propagation prediction. In addition, the inverted sound velocity profile may be used as the initial solution in a non rigorous iterative inversion technique using a more realistic description of the environment.

Normal modes are a dominant feature of the acoustic field in shallow water. In terms of the wavenumber spectrum, most of the power is concentrated in certain characteristic wavenumbers. Estimating the reflection coefficient required by Merab’s method in such conditions, for example, is still an open problem. In shallow-water it seems reasonable to use the modal characteristic wavenumbers, which depend on the environmental properties, as the input data of an inverse method. Perturbative techniques that explore this modal information have been developed by Rajan and co-workers[61]. Chapters 3 and 4 discuss the extension of Rajan’s method to environments whose properties are range-dependent.

Chapter 3 deals with the high-resolution, sequential eigenvalue estimation required for the characterization of range-dependent environments. It shows that the modal sum in a range-dependent environment can be exactly represented by a recursive difference equation, which justifies the application of autoregressive (AR) techniques as proposed by Becker[6]. Chapter 3 also shows, however, that the AR eigenvalue estimation is biased in range dependent environments. Synthetic data from a workshop on inverse techniques [9] is analyzed. The sequential estimators, associated with a competitive

smoother[51], successfully estimate jumps in eigenvalues caused by abrupt environmental changes, a problem that motivated Chapter 3. Data from the Modal Mapping Experiments (MOMAX)[18] are analyzed. The data consist of monochromatic acoustic fields measured as a function of position in a shallow-water environment, where horizontal synthetic aperture arrays are formed by drifting buoys or by a moving source.

Chapter 4 discusses the eigenvalue inversion problem. Backus-Gilbert theory[4] is applied to the analysis of the trade-off between resolution and variance in the eigenvalue inverse problem. The framework of estimation theory is also applied to the analysis of the problem. Measurements of acoustic fields produced by moving sources result in eigenvalue estimation bias due to the Doppler effect. A method is developed to account for these eigenvalue estimation errors directly in the perturbative formulation. Finally, a state-space formulation of the inverse eigenvalue problem leads to a Kalman filter solution suitable for range-dependent environments. Sequences of eigenvalues estimated as a function of range with the techniques of Chapter 3 are then inverted for sound velocity profiles in the seabed.

## Chapter 2

# Inversion for Subbottom Sound Velocity Profiles in the Deep Ocean: Application of an Exact Inverse Method

### 2.1 Introduction

This chapter discusses the application of an exact inverse theory to actual experimental data. The exact theory was developed by Merab[45] and is based on the work of Gelfand and Levitan[25] on potential inversion from scattering data in Quantum Mechanics. The input data required by Merab's method is the complex plane-wave reflection coefficient at a fixed frequency.

The measurement of the magnitude and phase of the reflection coefficient of the ocean bottom is an important issue in Ocean Acoustics by itself. In this chapter, we apply a technique developed by Frisk and co-workers[22, 46] to the measurement of the reflection coefficient using monochromatic acoustic data from the deep water experiment

at the Icelandic Basin described by Frisk, Doutt, and Hays[21].

Section 2.1 reviews Merab's method and Frisk's technique. Section 2.2 describes the Icelandic Basin experiment. Section 2.3 analyzes the experimental data up to the measurement of the reflection coefficient. We use simulated pressure fields to discuss the data analysis procedure and to evaluate the effects of experimental factors not accounted for in the underlying acoustic model, such as source depth variations with range. We introduce the concept of residual pressure, an extension of Mook's[46] residual phase, and apply it to the analysis of the measured and simulated fields. The residual pressure analysis allowed us to identify measurement errors and recover the pressure data phase. We estimate the complex, plane-wave reflection coefficient at the experimental site.

Section 2.4 applies Merab's method to the reflection coefficient measured in Section 2.3. Various issues associated with the use of this method in realistic ocean environments are discussed and illustrated by examples. We introduce a density discontinuity compensation procedure that allows the use of Merab's method in more realistic settings, and correct an expression for the cutoff frequency for trapped modes in the subbottom. Finally, we estimate the sound velocity profile at the Icelandic Basin experiment site.

### 2.1.1 Inversion from Reflection Coefficient Data

A plane wave<sup>1</sup>,  $p_{inc}(z) = e^{ik_z z}$ , incident from a homogeneous half-space onto a boundary at  $z = 0$  (Figure 2-1) at an angle  $\theta$  is partially reflected and transmitted into the lower half-space. The wavenumber vector  $\mathbf{k}_0 = (k_r, k_z)$  has a vertical component  $k_z = k_0 \cos \theta$  and horizontal component  $k_r = k_0 \sin \theta$ , where  $k_0 = \omega/c_0$  is the magnitude of  $\mathbf{k}_0$ . The ratio of reflected and incident waves is the plane-wave reflection coefficient  $R_b$ , a function of the frequency  $\omega$ , the incidence angle  $\theta$ , and the geoacoustic properties of both half-spaces, in particular of the sound velocity profile  $c(z)$  of the lower half-space.

Merab[45] developed a method for inverting reflection coefficient data for the seabed sound velocity profile in a horizontally stratified media. The method is based on a work

---

<sup>1</sup>The time dependence  $e^{-i\omega t}$  is assumed.

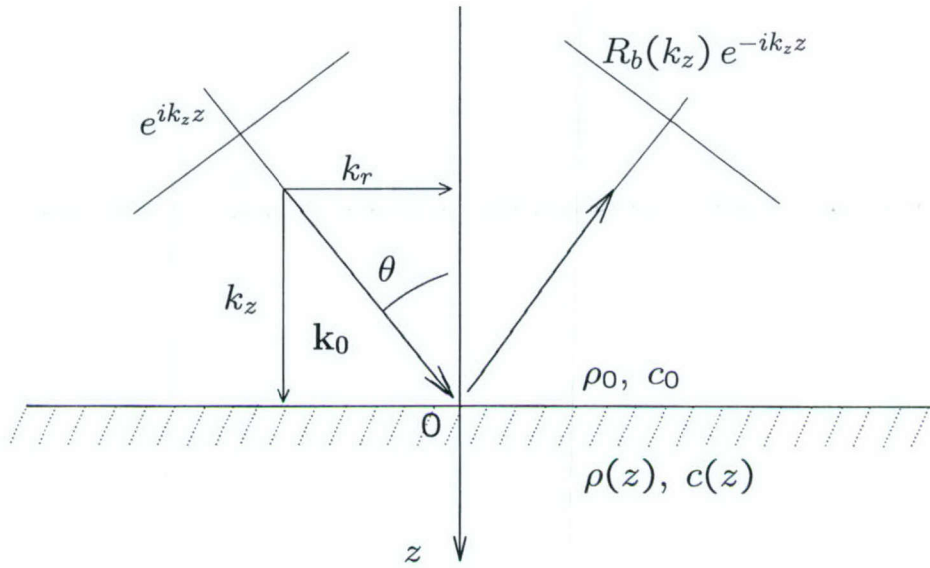


Figure 2-1: Reflection coefficient

by Gelfand and Levitan[25] related to the potential inversion in Quantum Mechanics. The input data is the complex plane-wave reflection coefficient as a function of the vertical wavenumber  $k_z$  measured in the water at the water-seabed interface at a single frequency,  $R_b(k_z)$ .

The Fourier transform of the reflection coefficient, seen as a function of the vertical wavenumber  $k_z$ ,

$$r_b(z) = \frac{1}{2\pi} \int_{-\infty}^{\infty} R_b(k_z) e^{-ik_z z} dk_z, \quad (2.1)$$

is related to the index of refraction  $n(z) = c_0/c(z)$  through the Gelfand-Levitan integral equation

$$K(z, y) + r_b(z + y) + \int_{-y}^z r_b(t + y) K(z, t) dt = 0, \quad y \leq z, \quad (2.2)$$

and the potential

$$V(z) = 2 \frac{dK(z, z)}{dz} = k_0^2 [1 - n^2(z)], \quad z \geq 0, \quad (2.3)$$

Note that the reference potential is  $V(z) = 0$ ,  $z \leq 0$ , corresponding to the sound velocity in water,  $c(z) = c_0$ ,  $n(z) = 1$ ,  $z \leq 0$ . The computation of the Fourier transform, eq.(2.1),

is reduced to the interval  $0 \leq k_z < \infty$  by using the conjugate-symmetry property  $R_b(-k_z) = R_b^*(k_z)$ , and simplifies to

$$r_b(z) = \frac{1}{\pi} \Re \left\{ \int_0^\infty R_b(k_z) e^{-ik_z z} dk_z \right\}, \quad (2.4)$$

where  $\Re\{\cdot\}$  denotes the real part.

Equations (2.1) and (2.4) are valid strictly only in absence of trapped modes in the seabed, which may be excited due to sound velocity profile minima smaller than the water sound velocity. These trapped modes are analogous to the bound states of Quantum Mechanics that may occur in regions of negative potential  $V$ . When trapped modes are excited in the seabed, an additional term in eq.(2.1) is required in order to satisfy  $r_b(z) = 0$ ,  $z < 0$ . The term is related to the poles of the reflection coefficient in the upper  $k_z$  complex plane. The poles and their residues should, therefore, be also measured.

As pointed out in [45], however, such trapped modes can be avoided by measuring the reflection coefficient at sufficiently low frequencies given by the condition

$$\omega < g\sqrt{3} \left( 1 - \frac{c_{min}}{c_0} \right)^{-3/2}, \quad (2.5)$$

where  $g = dc/dz$  ( $\text{sec}^{-1}$ ) is the constant, positive sound velocity gradient and  $c_{min} < c_0$  is the minimum sound velocity in the seabed. Equation (2.5) is valid for linear sound velocity profiles in the seabed.

In Subsection 2.4.1 we show that eq.(2.5) is valid, in fact, when the sound velocity minimum occur away from the boundary  $z = 0$ , for a bilinear velocity profile (where  $g$  is the magnitude of the gradient above and below the minimum). We derive an expression to account for the case when the minimum sound velocity occurs at the boundary.

One limitation of the Merab method is that the starting point is the standard wave equation<sup>2</sup> over all domain  $-\infty < z < \infty$ , where density is assumed constant. Consider-

---

<sup>2</sup>We refer to the standard form of the time-independent, depth-dependent pressure wave equation

ering that density discontinuities may be present in the water-seabed interface, this is a major restriction of the method. In the presence of smooth density variations, the acoustic wave equation can be reduced to the standard form with a modified index of refraction[45]

$$(n')^2 = n^2 + k_0^{-2} \left[ \frac{1}{2\rho} \frac{d^2\rho}{dz^2} - \frac{3}{4} \left( \frac{1}{\rho} \frac{d\rho}{dz} \right)^2 \right] \quad (2.6)$$

and Merab's method can be used to recover  $n'(z)$ .

Density discontinuities, on the other hand, can not be directly dealt with. First, as  $|k_z| \rightarrow \infty$ ,  $R_b(k_z) \rightarrow O(k_z^{-2})$ [45] when the density is constant, but tends to a constant in the presence of density discontinuities, and the Fourier transform in eq.(2.1) would require a representation in terms of impulses. In fact, the time-independent, depth-dependent pressure wave equation, which includes derivatives of density, is not valid at points of density discontinuity. This is circumvented by introducing interfaces at these points and imposing continuity of pressure and normal particle velocity. We discuss this issue in Section 2.4.1.

Another important issue on the application of Merab's method is the truncation of  $R_b(k_z)$  to a limited aperture  $a < k_z < b$ . In practice, the reflection coefficient will be usually available on a range corresponding to real angles of incidence  $0 \leq k_z \leq k_o$ , and the Fourier integral must be truncated. In a series of simulations, Merab[45] shows a degradation of the inverted profile as the  $k_z$  range decreases, where the reconstructed profile is a smoothed version of the original. The reconstruction was shown to be reasonably accurate when the range includes the critical incidence region  $0 \leq k_z \leq k_{zcritical} = k_0 \cos \theta_c$ , where  $|R_b| = 1$ .

Merab's method requires solving the integral equation (2.2) at each depth. In the Nystrom method[29], the integral is approximated by a quadrature by setting  $t_n = -y + n\Delta z$  and  $K(z, y)$  is evaluated at the discrete points  $y_m = -z + m\Delta z$ . If the data  $[r_b(z)]$  are available at depths  $z_q = q\Delta z$ ,  $q = 0, 1, \dots$ , the resulting linear system is

---

$u''(z) + k_z^2(z)u(z) = 0$ , as opposed to the more general form  $\rho(z)(u'(z)/\rho(z))' + k_z^2(z)u(z) = 0$ .

given by

$$K(z_q, -z_q + m\Delta z) + r_b(m\Delta z) + \Delta z \sum_{n=0}^m w_{nm} r_b(n\Delta z) K(z_q, z_q - (m-n)\Delta z) = 0, \quad m = 1, \dots, 2q, \quad (2.7)$$

where, from eq.(2.2),  $K(z, -z) = -r_b(0)$ . After solving for  $K(z, y)$ , the derivative in eq.(2.3) is computed numerically. Notice that the system (2.7) has dimensions  $2q \times 2q$ , which increases with depth and requires  $r_b(z)$  in the range  $0 \leq z \leq 2q\Delta z$ .

Another method that incorporates the computation of the derivatives of  $K(z, y)$  into the linear system was introduced by Khanh[39] and is based on the Hermite corrector formula of order two

$$\int_a^b g(x)dx = \sum_{k=1}^M \frac{h}{2} [g(t_{k-1}) + g(t_k)] + \frac{h^2}{12} [g'(a) - g'(b)] + O(h^4). \quad (2.8)$$

By differentiating eq.(2.2) with respect to  $z$  and  $y$ , including the mixed derivative, three other integral equations are obtained. The discretization of the four integral equations using eq.(2.8) leads to four coupled linear systems of dimensions  $(4q + 2) \times (4q + 2)$  where, in addition to  $K(z, y)$ , the derivatives  $\partial_z K(z, y)$  and  $\partial_y K(z, y)$  are obtained. The potential can be computed as [cf. eq.(2.3)]

$$V(z_q) = 2 [\partial_z K(z_q, y) + \partial_y K(z_q, y)]_{y=z_q},$$

which avoids the approximation of derivatives by finite differences. The main issues with Khanh's method are (1) the linear system dimension grows fast with depth, and (2) the use of the first and second derivatives of  $r_b(z)$  imposes more restrictive requirements on the behavior of  $R_b(k_z)$  near infinity.

Other solution methods are described in [45]. One that avoids the solution of linear

systems is based on the series expansion of the integral equation (2.2), leading to

$$V(z) = V^{(0)}(z) + V^{(1)}(z) + V^{(2)}(z) + \dots, \quad (2.9)$$

where

$$V^{(0)}(z) = -2 \frac{dr_b}{dz}(2z) \quad (2.10)$$

corresponds to the Born approximation, and the other two lowest order terms are

$$V^{(1)}(z) = 4r_b(2z) \quad (2.11)$$

and

$$V^{(2)}(z) = 4r_b(2z) \int_0^{2z} r_b^2(t) dt + 2 \int_{-z}^z \int_{-t}^z r_b(z+t) r_b(t+\eta) \frac{\partial r_b}{\partial z}(z+t) d\eta dt. \quad (2.12)$$

### 2.1.2 Measurement of the Reflection Coefficient

#### From Acoustic Pressure to Reflection Coefficient

The technique described here was developed by Frisk and co-workers[22, 46]. Figure 2-2 is a model for the reflection coefficient measurement setup in deep water, as described by Frisk, Doutt, and Hays[21]. A monochromatic sound source drifts away from a receiver close to the bottom, in a homogeneous water half-space overlying a horizontally stratified seabed. The signal recorded at the receiver is given by the Hankel transform

$$p(r; z, z_0) = \int_0^\infty g(k_r, z, z_0) J_0(k_r r) k_r dk_r, \quad (2.13)$$

where  $g(k_r, z, z_0)$  is the depth dependent Green's function and  $k_r$  is the horizontal component of the water wavenumber  $k_0 = \omega/c_0$ , which is related to the vertical wavenumber  $k_z$  by  $k_0^2 = k_r^2 + k_z^2$  (see Figure 2-1).

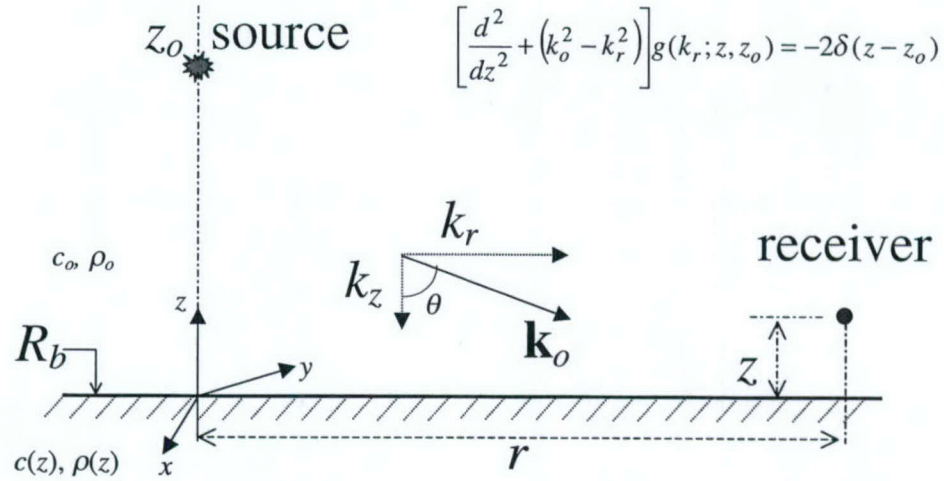


Figure 2-2: Reflection coefficient measurement model: a homogeneous water half-space overlaying a horizontally stratified seabed.

For the environment of Figure 2-2 the depth dependent Green's function is given by

$$g(k_r; z, z_0) = \frac{i}{k_z} [e^{ik_z|z_0-z|} + R_b(k_r) e^{ik_z(z_0+z)}]. \quad (2.14)$$

Notice that the reflection coefficient  $R_b$  is described as a function of  $k_r$ , not  $k_z$  as in Merab's method.

Given the pressure as a function of range at constant source and receiver depth, the Green's function can be computed as the inverse transform

$$g(k_r; z, z_0) = \int_0^\infty p(r; z, z_0) J_0(k_r r) r dr. \quad (2.15)$$

The Hankel transform is performed numerically using the Fourier-Bessel series [76, 47]

$$\tilde{f}(x) = \int_0^\infty f(y) J_0(xy) y dy = \frac{2}{X^2} \sum_{n=1}^N w(y_n) \frac{f(y_n) J_0(xy_n)}{J_1^2(\lambda_n)}, \quad 0 \leq x \leq X, \quad (2.16)$$

where the function  $f$  to be transformed is given on the grid  $y_n = \lambda_n/X$ ,  $\lambda_n$  is the  $n$ -th

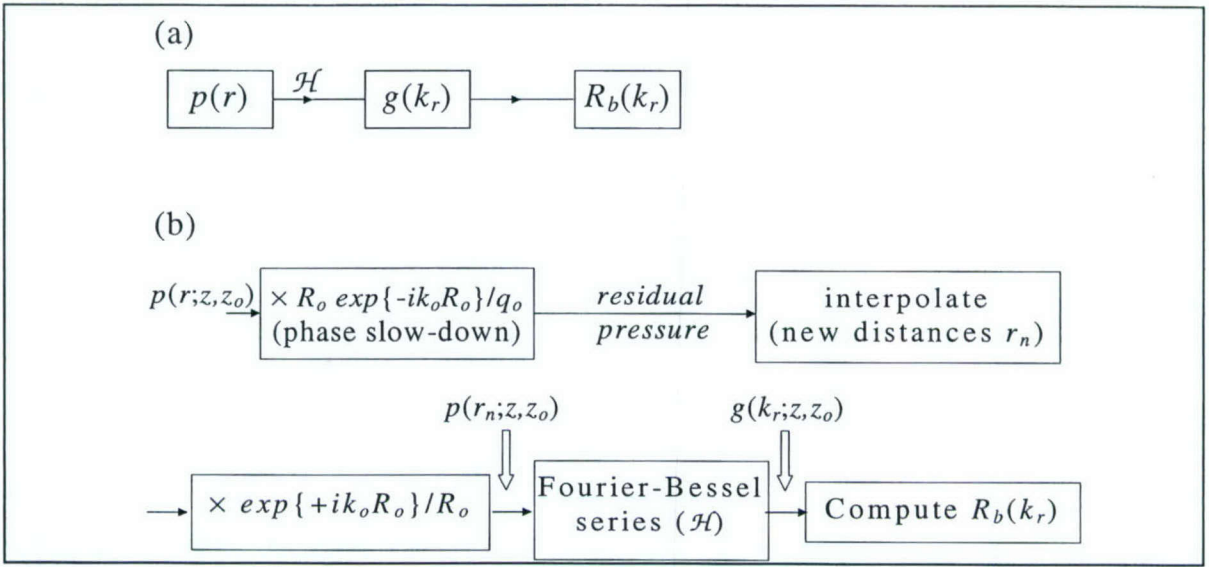


Figure 2-3: Reflection Coefficient Measurement Technique. (a) The basic method: from a measured pressure field as a function of range  $r$  to the reflection coefficient. The Hankel transform ( $\mathcal{H}$ ) of the pressure is the depth dependent Green's function, from which the plane-wave reflection coefficient is calculated. (b) A more detailed description, including the pressure normalization (computation of residual pressure to slow down the rate of change of the phase with range), the interpolation for the ranges  $r_n$  required by the Fourier-Bessel series, and the recovery of the pressure data from the residual pressure.

zero of  $J_0(z)$ ,  $X$  is the bandwidth of  $\tilde{f}$ , i.e.  $\tilde{f}(x) = 0$  for  $x > X$ , and  $w(y_n)$  is a windowing sequence.

Given the Green's function, the reflection coefficient is obtained as a function of the horizontal wavenumber  $k_r$  using eq.(2.14). In principle, the reflection coefficient can be computed not only for real angles of incidence, where  $0 \leq k_r \leq k_0$ , but also for evanescent waves with  $k_r > k_0$ .

The steps of the reflection coefficient measurement technique are shown in Figure 2-3. In order to compute the Hankel transform of the pressure field using eq.(2.16), the field must be interpolated in a range grid determined by the zeros  $\lambda_n$  of  $J_0(x)$ ,  $r_n = \lambda_n/K$ , where  $K$  is the bandwidth of the Green's function  $g(k_r)$ .

Although the magnitude of the pressure changes slowly with distance (as seen, for

example, in Figure 2-5), the phase is dominated by a geometric phase factor  $\exp\{ik_oR_0\}$ , corresponding to a  $2\pi$  radian variation in phase per wavelength change in the distance, a reasonably fast change. In order to assist the interpolation process, the phase rate of the pressure field is reduced by normalizing the pressure signal (the phase slow-down block of Figure 2-3), resulting in the *residual pressure*. After interpolation, the signal is denormalized and transformed to obtain the Green's function.

### Analysis of The Pressure Field - Residual Pressure

As described above, the rate of phase of the acoustic pressure signal is reduced for interpolation. This is accomplished by removing the contribution  $\exp\{ik_oR_0\}$  from the field. This phase factor corresponds to the direct field that would be observed in the absence of the seabed. By removing it, we obtain a signal, the residual pressure, whose phase variations reflect the seabed contribution to the total field. We analyze properties of the residual signal, which is useful in the interpretation of experimental data.

The pressure field given by eqs.(2.13) and (2.14) can be decomposed into direct and bottom interacting (or reflected) components as [23]

$$p(r; z, z_o) = \underbrace{\frac{e^{ik_oR_o}}{R_o}}_{\text{direct field}} + i \overbrace{\int_0^\infty \frac{1}{k_z} R_b(k_r) e^{ik_z(z_o+z)} J_o(k_r r) k_r dk_r}^{\text{bottom interacting}} \quad (2.17)$$

$$= \frac{e^{ik_oR_o}}{R_o} + B(r; z, z_o) e^{i\gamma(r; z, z_o)}, \quad (2.18)$$

where  $R_o = \sqrt{r^2 + (z - z_o)^2}$  is the slant distance source-receiver. Mook [46] introduced the concept of *residual phase*, which is the phase of the pressure when the geometrical phase component  $k_oR_o$  is removed. When this dominant phase component is removed, the remaining phase variations, due to bottom interaction, change slowly with range. This slowly varying pressure can be easily interpolated into the range grid required by the Fourier-Bessel series, eq.(2.16). The residual phase is the phase of the *residual*

pressure obtained by normalizing the total pressure by the direct field. From eq.(2.17), the residual pressure is given by

$$p_r(r; z, z_0) = R_o e^{-i k_o R_o} p(r; z, z_0) = 1 + B(r; z, z_0) R_0 e^{i[\gamma(r; z, z_0) - k_o R_0]}, \quad (2.19)$$

with magnitude

$$|p_r(r; z, z_0)| = \sqrt{1 + 2B(r; z, z_0)R_0 \cos[\gamma(r; z, z_0) - k_o R_0] + B^2(r; z, z_0)R_0^2} \quad (2.20)$$

and (residual) phase

$$\phi_r(r; z, z_0) = \tan^{-1} \frac{B(r; z, z_0)R_0 \sin[\gamma(r; z, z_0) - k_o R_0]}{1 + B(r; z, z_0)R_0 \cos[\gamma(r; z, z_0) - k_o R_0]}. \quad (2.21)$$

The behavior of the residual magnitude and phase as a function of range can be qualitatively assessed by looking at two extreme conditions[23]. If the reflected field is small compared to the direct field, then  $B$  is small and  $BR_0 \ll 1$ . To the first order in  $BR_0$ , the residual magnitude and pressure are given by

$$|p_r(r; z, z_0)| \simeq 1 + B(r; z, z_0)R_0 \cos[\gamma(r; z, z_0) - k_o R_0] \quad (2.22)$$

and

$$\phi_r(r; z, z_0) \simeq B(r; z, z_0)R_0 \sin[\gamma(r; z, z_0) - k_o R_0], \quad (2.23)$$

which indicates that variations of magnitude and residual phase with range are similar and small in those conditions.

When the pressure magnitude goes through a minimum, eqs.(2.20) and (2.22) indicate that  $\cos[\gamma - k_o R_0] \simeq -1$  and, therefore,  $\gamma - k_o R_0 \simeq (2n+1)\pi$ . Near the magnitude minima, the argument  $(\gamma - k_o R_0)$  changes from some value  $[(2n+1)\pi - \varepsilon]$  to  $[(2n+1)\pi + \varepsilon]$ , where  $\varepsilon$  is some small value. The change in residual phase around a minimum is, as a

consequence,

$$|\Delta\phi_r| \simeq \left| 2 \tan^{-1} \frac{B(r; z, z_0) R_0 \sin \varepsilon}{1 - B(r; z, z_0) R_0 \cos \varepsilon} \right|. \quad (2.24)$$

When, in addition,  $BR_0$  is small,

$$|\Delta\phi_r| \simeq 2B(r; z, z_0)R_0 \sin \varepsilon, \quad (2.25)$$

a small change of phase for a small change in magnitude near a minimum. If, on the other hand,  $BR_0$  is close to one, the minimum will be nearly a magnitude null and the change in residual phase  $\Delta\phi$  approaches  $\pi$ .

## 2.2 The Icelandic Basin Experiment

The acoustic pressure data were obtained in 1981 in the Icelandic Basin. A detailed description can be found in reference [21] (the data are from a region referred to as *site B4*). As shown in Figure 2-4, an acoustic source was towed away from two low-frequency receivers located at 1.2 m and 54.6 m from the bottom. The whole system, including the receivers, an 11 kHz pinger, and the 220 Hz source, was lowered on a single cable. When the mooring system anchor reached 35 m from the bottom, the receivers were released with the anchors. The ship drifted away at about 0.5 knots. The average source height during the experiment was 124.9 meters.

Every 12 seconds, the source emitted a 220-Hz, 4-s long CW pulse. Simultaneously, the pinger transmitted a CW pulse of 11 kHz used to signal the receivers to start the 220-Hz pulse acquisition. The 11-kHz signal was also used for measuring the pinger-receivers propagating times, and, in conjunction with the towing ship's depth recorder, the source depth. The 11 kHz receivers were located near the low-frequency units, at 2.54 m and 54.37 m from the bottom.

The receivers sampled the complex envelope of the 220 Hz signal at a 5 Hz sampling rate and stored 30 pulse samples and the times of emission and reception of each pulse.

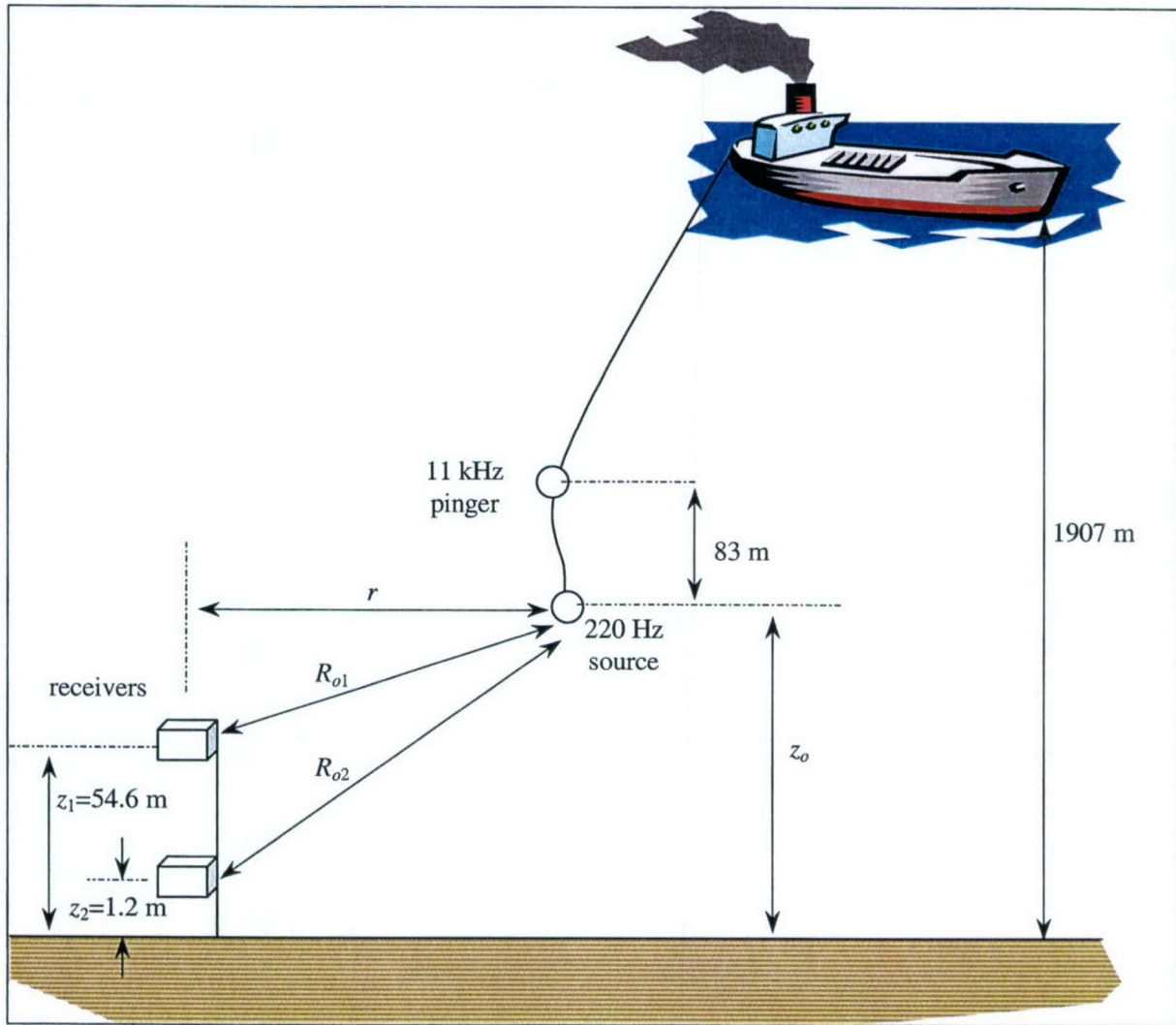


Figure 2-4: The experimental setup in the Icelandic basin. The sound velocity near the bottom was 1495 m/s and the gradient,  $0.009 \text{ s}^{-1}$ . The average source height was 124.9 m. The source drifted away from the fixed receivers at 0.5 knots. Every 12 s, a pulse was simultaneously emitted from the source and the pinger. The distance between emissions was, therefore, about 3.1 m, close to half-wavelength at 220 Hz[21, 23].

From this raw data, the posterior analysis used only one sample of each received pulse. The fourth sample was selected for the receiver at 1.2 m (that is, 4/5 s after the 11 kHz pulse reception) and the fifth sample (1 s after the 11 kHz pulse), for the 54.6 m receiver. The surface reflected pulse arrived at the receivers after these chosen sample times (for distances up to about 3700 meters). Therefore, these samples are representative of the sum of the direct and bottom interacting field components.

In Figure 2-5 the magnitude of the samples are shown as a function of distance, along with simulated fields. These simulated fields are based on a seabed model shown in Figure 2-6, previously inferred from the magnitudes of the measured fields[21]. Measurements taken with a 3.5 kHz echo sounder suggests that the environment is range-independent in the region of interest. The use of the water half-space model of eq.(2.14) is justified by the small sound velocity gradient near the bottom and by the use of signal samples free of the surface reflected signal.

The good fit between measured and computed fields in Figure 2-5 suggests that the range-independent, fluid subbottom model of Figure 2-6 captures the essential environmental characteristics that influence the acoustic field at 220 Hz, for the given experimental geometry.

One important deviation from the basic acoustic model of Section 2.1.2 during the experiment is the source depth variation as a function of range. Measured source height variations are shown in Figure 2-7. The source height changed by about 30 meters during the experiment, a large change when compared to the wavelength of 6.8 meters.

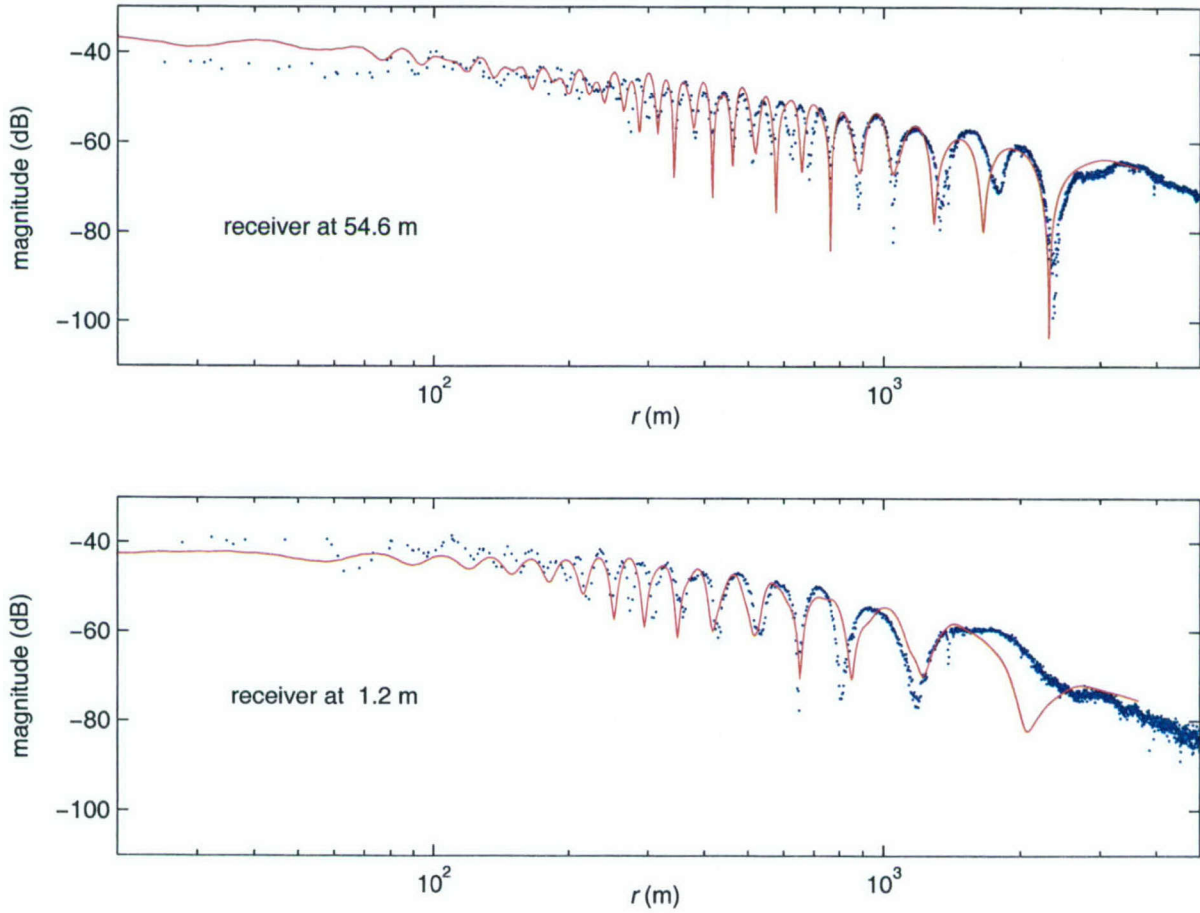


Figure 2-5: Magnitude of the Icelandic Basin receiver outputs, one sample per pulse (dots). The solid lines correspond to fields computed for a geoacoustic model of Figure (2-6), obtained by matching the pattern of the measured magnitude[21]. The units are dB relative 1 Volt. The computed field magnitudes are adjusted by the receiver calibration factor (see Table 2.1 on page 45).

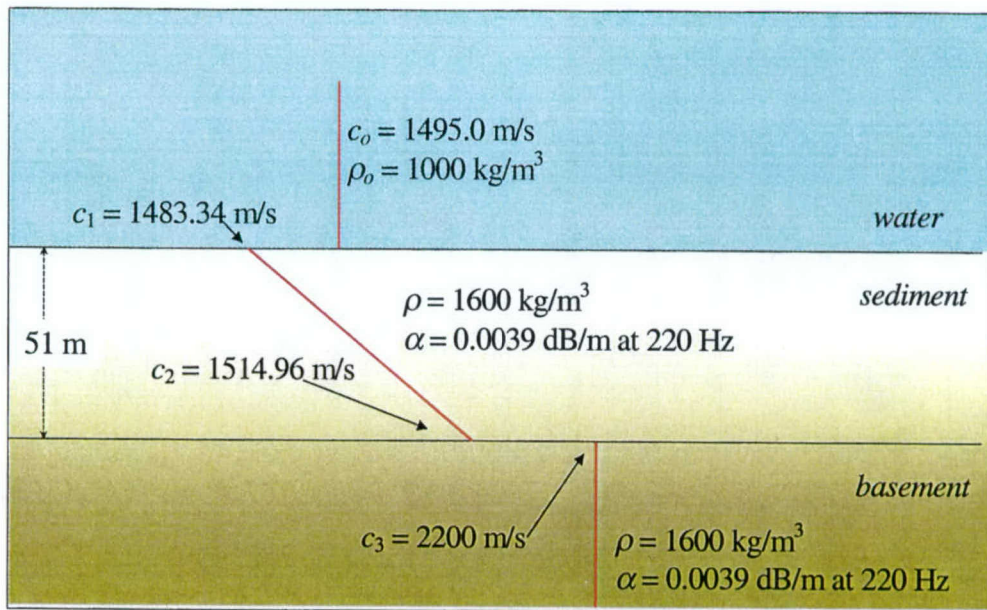


Figure 2-6: Geoacoustic model of the Icelandic Basin (site B4) based on direct measurements of water sound velocity and seabed density, 3.5 kHz echo soundings, and the magnitude of the acoustic pressure measured at 220 Hz as a function of range[21].

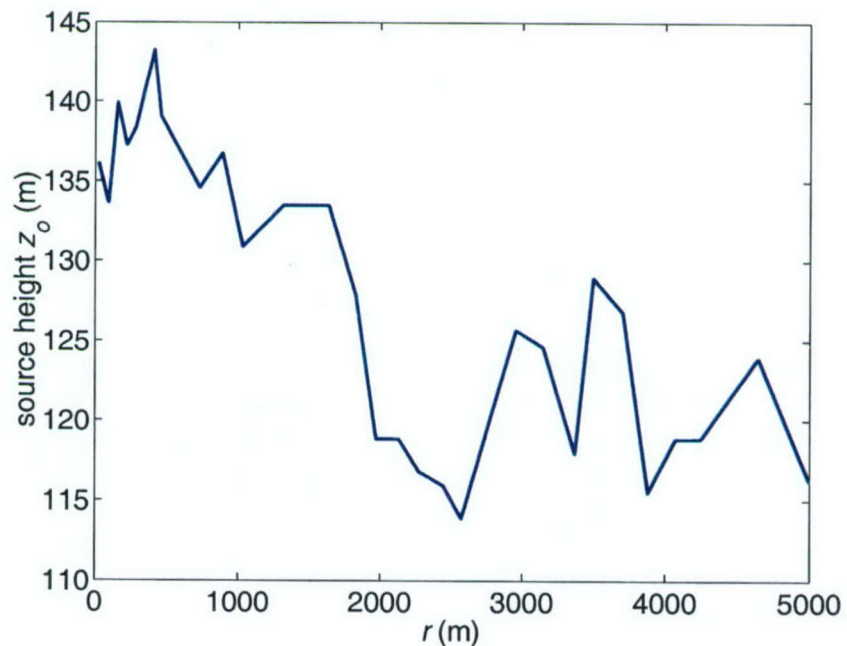


Figure 2-7: Source height variations observed during the Icelandic Basin experiment.

## 2.3 Icelandic Basin Data Analysis - Computing the Reflection Coefficient

### 2.3.1 Simulated Field Analysis

#### The *Ideal* and *Synthetic* Simulated Fields

Simulated fields were generated for the Icelandic model shown in Figure 2-6, in order to evaluate the measurement technique and compare with the experimental results. The computed reflection coefficient and the Green's function for a source height of 124.9 m and receiver heights of 1.2 m and 54.6 m are shown in Figure 2-8. Notice the pole in the reflection coefficient at a horizontal wavenumber nearly 0.08% above the water wavenumber due to a trapped mode in the sediment near the water interface.

The pressure fields were computed using the Fourier-Bessel series, eq.(2.16), with an uniform window  $w(k_{rn}) \equiv 1$  and  $X = r_{max} = 2 \times 10^4$  m, above which the field is assumed zero. The output of the Fourier-Bessel series was smoothed to remove oscillations (due to aliasing) introduced by the assumption of null field for  $r > r_{max}$ .

Two simulated (residual) pressure fields are in shown in Figure 2-9 as a function of distance. The first, here called *ideal*, was computed for a constant source height of 124.9 m and on the range grid required by the inverse Hankel transform, in order to avoid the interpolation process shown in Figure 2-3 when inverting for the reflection coefficient.

The second field, called *synthetic*, was computed with the source height variations shown in Figure 2-7 and on the range grid of the experimental field, resulting in a more realistic simulation of the experimental conditions. The magnitude of both fields have the same general behavior—the difference is the location of the magnitude and phase extrema. This indicates that source height variations causes changes in the phase difference between direct and reflected fields, as expected.

Corresponding fields with similar characteristics were computed for the 54.6 m receiver. Another set of fields were generated by interpolating the ideal field into the

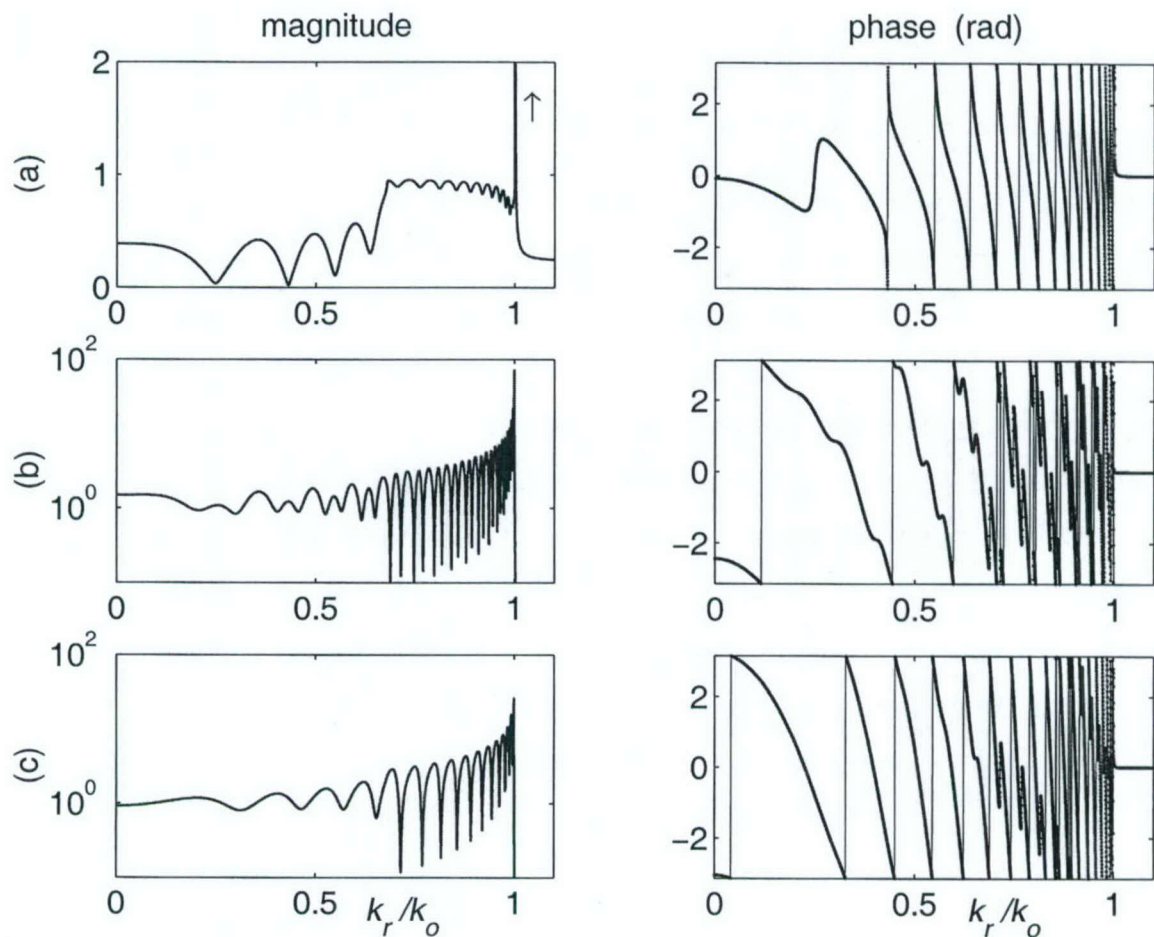


Figure 2-8: (a) Icelandic model (Figure 2-6) reflection coefficient at 220 Hz; (b) Green's function magnitude and phase for a source at  $z_0 = 124.9$  m and a receiver at  $z = 54.6$  m; (c) Green's function magnitude and phase for a source at  $z_0 = 124.9$  m and a receiver at  $z = 1.2$  m. All plots are versus the ratio  $k_r/k_0$  (sine of the angle of incidence for  $k_r/k_0 \leq 1$ ). Total reflection starts at  $k_r/k_0 = c_0/c_3 = 0.6795$ , corresponding to a critical angle of incidence of  $42.8^\circ$ . The minimum in sound velocity in the seabed results in the pole of the reflection coefficient, observed at  $k_r/k_0 \sim 1.0008$ .

experiment range grid, which allowed to verify the effect of the interpolation stage of Figure 2-3.

The phase shown in Figure 2-9 excludes the geometric phase factor  $\exp\{ik_0 R_0\}$  and is the phase of the residual pressure at the output of the first block of Figure 2-3b. In order to assess qualitatively the effect of an error in the source position measurement, the residual phase of the field with source height variations is computed in two ways:

- Ignore the source height variations: an average source height was used to compute the slant distances  $R_o$  in the phase slow-down step (first block of Figure 2-3b). The result, shown in the lower plot of Figure 2-9, is a large change in the residual phase in the first 1000 meters.
- Use the correct, variable source heights to compute the slant distances. As shown in the lower plot of Figure 2-9, the resulting residual phase has the same general behavior of the constant height source. The large phase trend observed previously is eliminated.

The effect of the source height variations (when correctly accounted for) on the residual phase is observed mainly as a (non constant) shift in range of the phase and magnitude extrema, as compared to the constant height case (compare the solid and dashed lines in Figure 2-9).

When the wrong source height is used to slow down the phase, though, the residual phase presents a large change as the distances increases from zero (about 12 radians in the first 1000 meters), but the phase error tends to a constant at larger ranges, suggesting that the depth variations have stronger effects at smaller ranges.

### Migration - Compensating for Source Height Variations

The ideal and synthetic fields are used as input for the reflection coefficient measurement technique described in Section 2.1.2 and shown schematically in Figure 2-3. As shown in eq.(2.15), the Green's function is the Hankel transform of the measured pressure field,

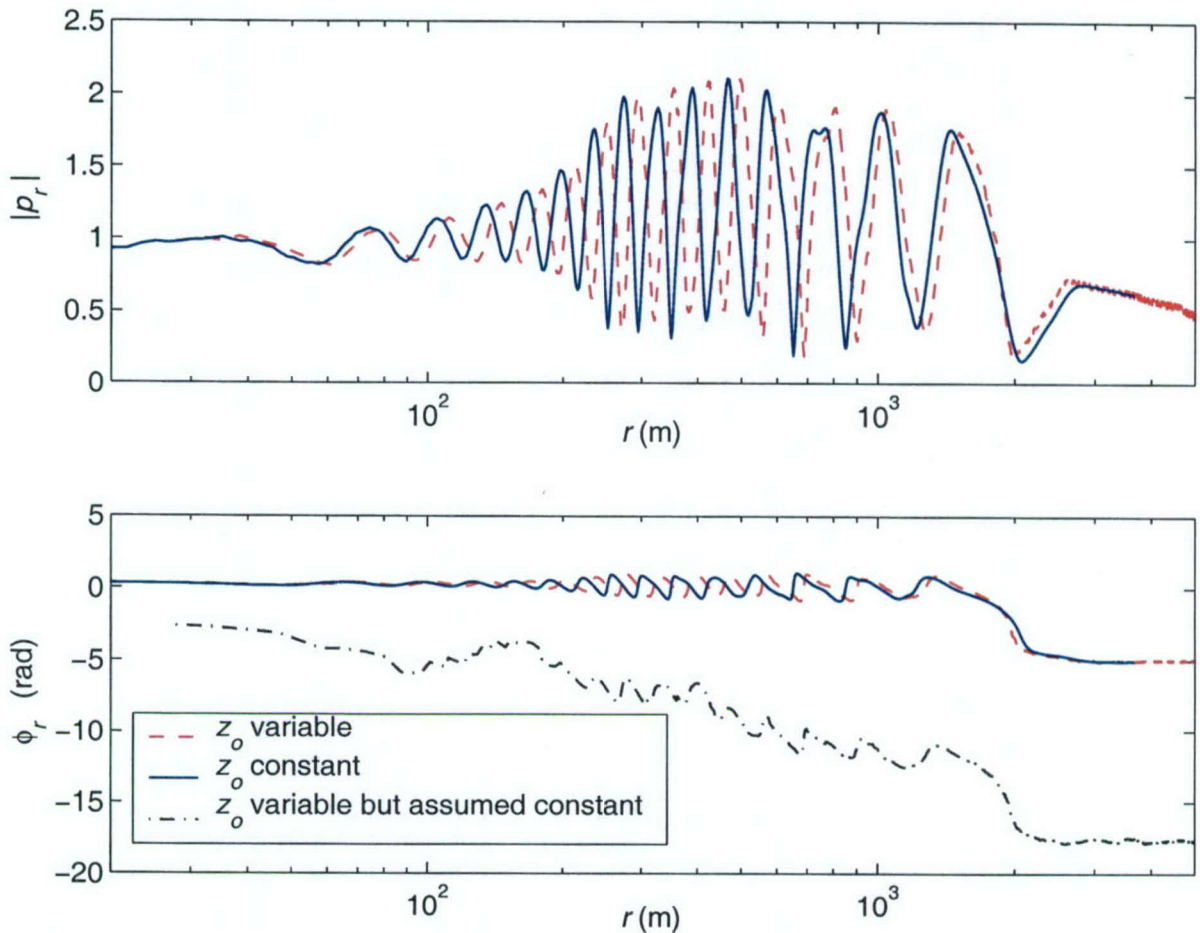


Figure 2-9: Synthetic residual pressure at  $z = 1.2\text{m}$ . The upper plot shows the residual magnitudes for an ideal, constant source depth (124.9 m, solid line), and for the source depth variations shown in Figure 2-7 (dashed line). The lower plot shows the corresponding residual phases. When source height variations are ignored in the computation of the residual phase and an average value is used instead, an error is introduced, as shown by the dash-dot line.

assuming both the source and receiver heights are independent of range. In order to apply eq. (2.15) to the pressure field, a *migration* process was implemented to compensate, at least partially, the synthetic fields for the source height variations.

As described above, the effect of the height variations is to shift the residual magnitude and phase extrema. It is reasonable to assume, therefore, that the residual field can be approximately described as the field of a source at a certain constant height. The migration process consists of using an average source height to compute the slant distances  $R_o$  when restoring the pressure after interpolation (third block of Figure 2-3b), instead of the actual varying height.

As can be seen from Eq. (2.17), the direct field can be modified to any source height by simply computing  $R_o$  corresponding to that source height. This migration process is, therefore, exact for the direct field. On the other hand, there is no simple relation between the phase of the reflected field and the slant distance  $R_o$ , and the migration will not compensate exactly the source height variation effect on the bottom reflected field.

If migration actually compensated for the height variations, the plots labeled " $z_o$  variable" and " $z_o$  constant" in Figure 2-9 would superimpose (the constant source height in the later case and the average source height in the former are the same). This migration method is a simplification of the compensation technique described in [23], a report of an initial analysis of the Icelandic Basin data where the compensation for the source height variations consisted in adjusting, separately, the phase of the direct and bottom-interacted fields according to a geometrical acoustics approximation model. Results using either technique are qualitatively indistinguishable.

The measured source heights at closer ranges, where the influence of the height variations is greater, averages 136 m, and this value is used for migration of the synthetic and experimental fields.

## Extrapolation of the Fields at Short Ranges

The experimental range grid started at nearly  $r = 26$  m, which is larger than the initial distance required by the Fourier-Bessel series, eq.(2.16). In order to extrapolate the measurements for these few points while minimizing numerical artifacts, computed values for the direct field alone (setting  $p_r = 1$ ) were used.

As an alternative, we used values based on the geometric acoustics approximation associated with a simple half-space model. At these small ranges, the geometrical incidence angle is below  $20^\circ$  for both receivers, and we approximate the reflection coefficient by that of normal incidence.

At normal incidence, the reflection coefficient for a plane wave incident from the water (sound velocity  $c_o$ , density  $\rho_o$ ) onto the boundary to a half-space of sound velocity  $c_1$  and density  $\rho_1$  is given by

$$R_b = \frac{\rho_1/\rho_0 - c_0/c_1}{\rho_1/\rho_0 + c_0/c_1}. \quad (2.26)$$

For a density ratio of 1.6 (as in the Icelandic Basin sites), and assuming  $c_o/c_1 \approx 1$  (a reasonable assumption for a sediment layer), the reflection coefficient at normal incidence is  $R_b \approx 0.6/2.6 = 0.23$ . Therefore, the residual pressure field at those ranges is approximately given, from eq.(2.19), by

$$p_r(r; z, z_0) = p(r; z, z_0) R_0 e^{-ik_0 R_o} = 1 + 0.23 \frac{R_0}{R_1} e^{ik_0 (R_1 - R_o)}, \quad (2.27)$$

where  $R_1$  is the distance from the source to the image of the receiver at the bottom,  $R_1 = [r^2 + (z + z_o)^2]^{1/2}$ .

### 2.3.2 From Simulated Fields to Reflection Coefficient

#### Green's Function

The Green's function is computed from the simulated fields using eq.(2.16), assuming a bandwidth  $K = X = 1.8492 = 2k_0$ . For the values of  $z_0$  ( $\approx 125$  m) and  $z$  ( $\geq 1.2$  m)

used in the Icelandic Basin experiment, the magnitude of the Green's function  $g$  decays fast to zero for  $k_r > k_0$ , as can be inferred from Eq. (2.14) and shown in Figure 2-8. A window based on the Hamming window of spectral analysis was employed to reduce oscillations caused by the truncation of the pressure field, and is given by

$$w(r_n) = 0.5 + 0.5 \cos(\pi r_n / R_{max}) = 0.5 + 0.5 \cos(\pi \lambda_n / \lambda_N), \quad n = 1, \dots, N, \quad (2.28)$$

where  $r_n = \lambda_n / K$ ,  $R_{max} = \lambda_N / K$ , and  $N$  was chosen to use all available data up to 3700 m, where the water half-space model is assumed valid, as discussed in Section 2.2.

Figure 2-10 shows the Green's functions estimated from the simulated fields at  $z = 1.2$  m. The reference Green's function (used to compute the ideal, constant source height field and also shown in Figure 2-8) is shown in the upper plots. There is no significant difference between the ideal field result and the reference Green's function, indicating that the implementation of the basic method (without interpolation, smoothing, or migration) is correct.

The general characteristics of the Green's function estimated from the synthetic (varying source height) fields are similar to the ideal case, although, because of the different source heights, an exact agreement between the two (i.e., ideal versus synthetic) is not to be expected. Figure 2-11 shows analogous results for the  $z = 54.6$  m simulated fields. The quality of the results for the lower receiver (as compared to the ideal case) is better than the one at 54.6 m.

When analyzing these results, it should be taken into account that the synthetic field was extrapolated for small distances ( $r < 26$  m). From a geometrical acoustics perspective, the data that supports results for low  $k_r$  (less than  $0.2k_o$  for the 1.2 m receiver; less than  $0.14k_0$  for the 54.6 m receiver) comes from that region.

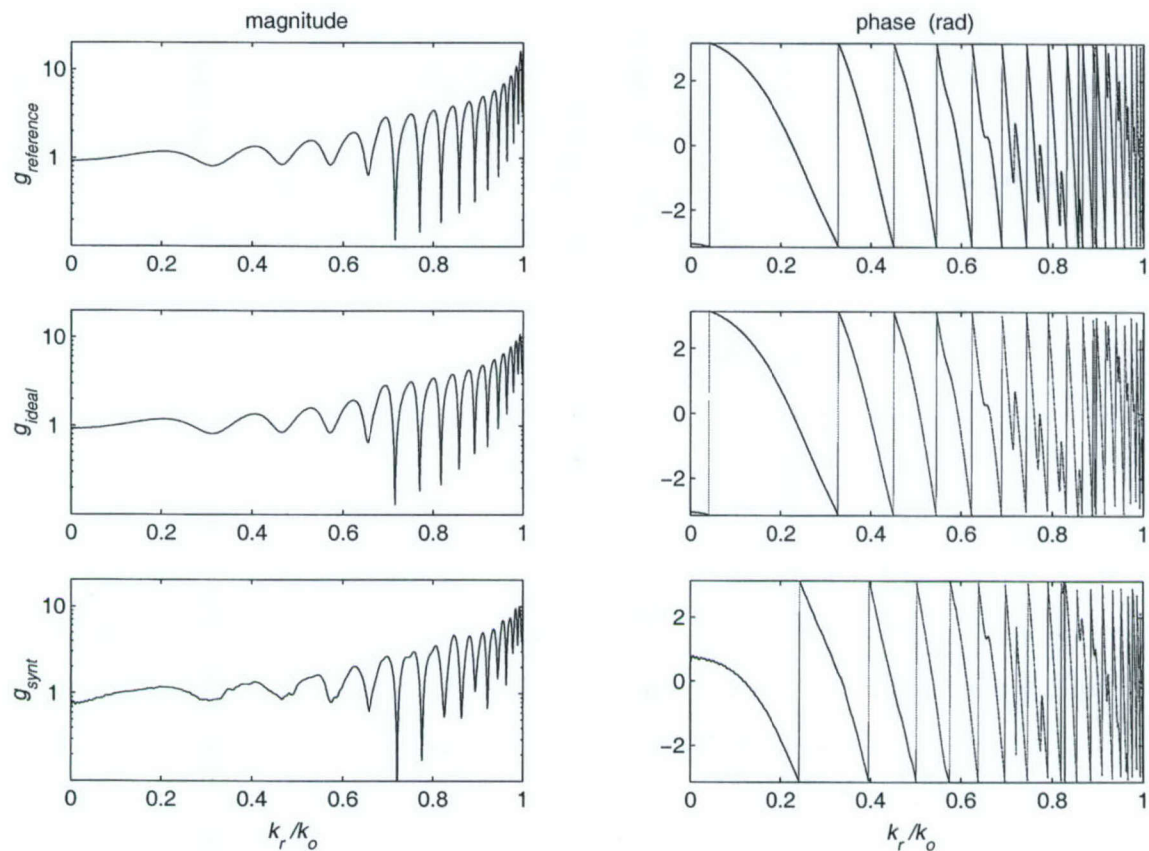


Figure 2-10: Green's functions (in Newton) obtained from computed fields at  $z = 1.2$  m.  $g_{\text{ref}}$  is the reference Green's function used to compute the ideal field (same as in Figure 2-8).  $g_{\text{ideal}}$  was computed from the ideal (constant source depth) field.  $g_{\text{synt}}$  was computed from the synthetic field and include effects of the interpolation and migration of the pressure field.

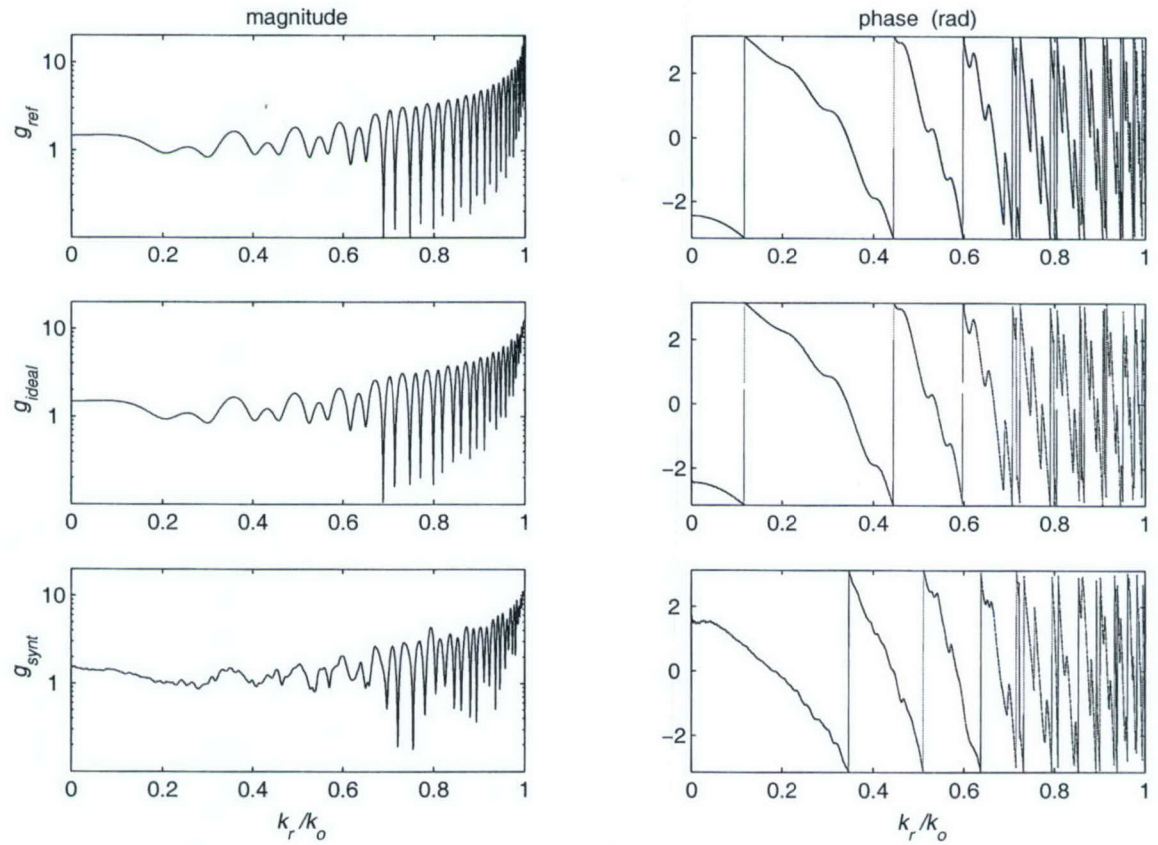


Figure 2-11: Green's functions (in Newton) obtained from computed fields at  $z = 54.6\text{m}$ .  $g_{ref}$  is the reference Green's function used to compute the ideal field (same as in Figure 2-8).  $g_{ideal}$  was computed from the ideal (constant source depth) field.  $g_{synt}$  was computed from the synthetic field and include effects of the interpolation and migration of the pressure field.

## Reflection Coefficient Computation

Figures 2-12 ( $z = 1.2\text{m}$ ) and 2-13 ( $z = 54.6\text{m}$ ) show the reflection coefficients estimated from the simulated fields using eq.(2.14). For the ideal field, the result differs only slightly from the reference reflection coefficient, which is an indication of the small errors introduced by the approximation of the Hankel transform by the Fourier-Bessel series of eq. (2.16).

A noticeable error in the ideal field result is the reduction in the magnitude of the reflection coefficient in the neighborhood of  $k_r = k_o$ . The dip in the magnitude is caused by the windowing of the pressure field [ $w(r_n)$  in eq. (2.28)], which reduces the pressure at the longer ranges that dominates the Green's function for high (near  $k_o$ )  $k_r$ . This effect is negligible when using a uniform window [ $w(r_n) \equiv 1$ ] (not shown), at the cost of a poorer reflection coefficient estimate for low  $k_r$ .

The reflection coefficients obtained from the synthetic field can be regarded as a reasonable estimate of the model reflection coefficient. Given that reliable results for small  $k_r$  could not be expected, as discussed in the last paragraph of Section 2.3.2 on the Green's functions results, the synthetic reflection coefficient estimates are reasonably good in that region.

Critical incidence on both results is near the true value of  $k_r = 0.68k_o$ . For larger  $k_r$ , the estimated reflection coefficient has a behavior similar to the reference, both in magnitude and phase. The main error is the large oscillation of the reflection coefficient magnitude in the supercritical region, where, at some points, it is larger than one.

Results from a synthetic field computed with a constant source height (but at distances  $r$  that required the interpolation step) do not show these large oscillations, which suggests that they are caused by the wrong application of the Hankel transform to fields that do not satisfy the assumption of a constant source height and also shows that the migration process is an approximated compensation for the source height variations.

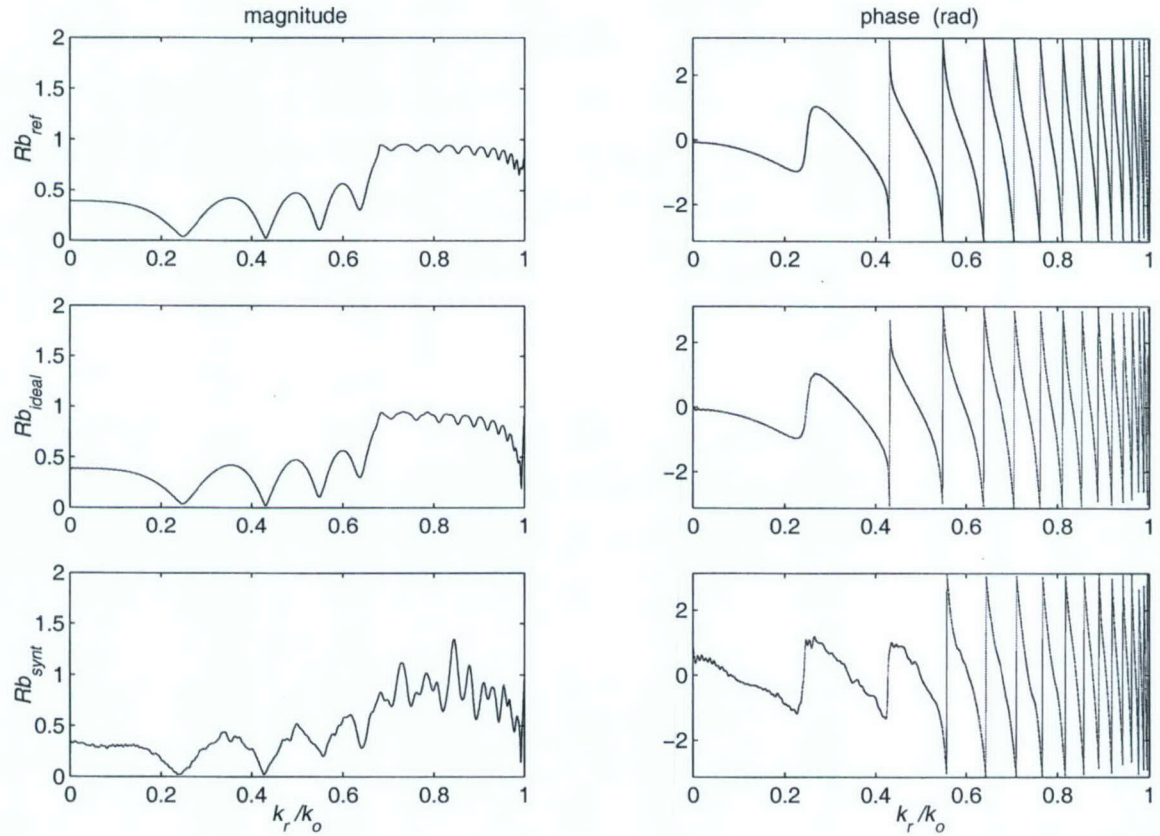


Figure 2-12: Reflection coefficient inferred from the simulated fields. The upper plots are the magnitude and phase of the reference reflection coefficient used to compute the fields and shown in Figure 2-8. The middle plot is the reflection coefficient estimated from the ideal, constant source height field. The lower plots are from the synthetic, varying source height field and illustrate the effect of the partial compensation due to the migration process.

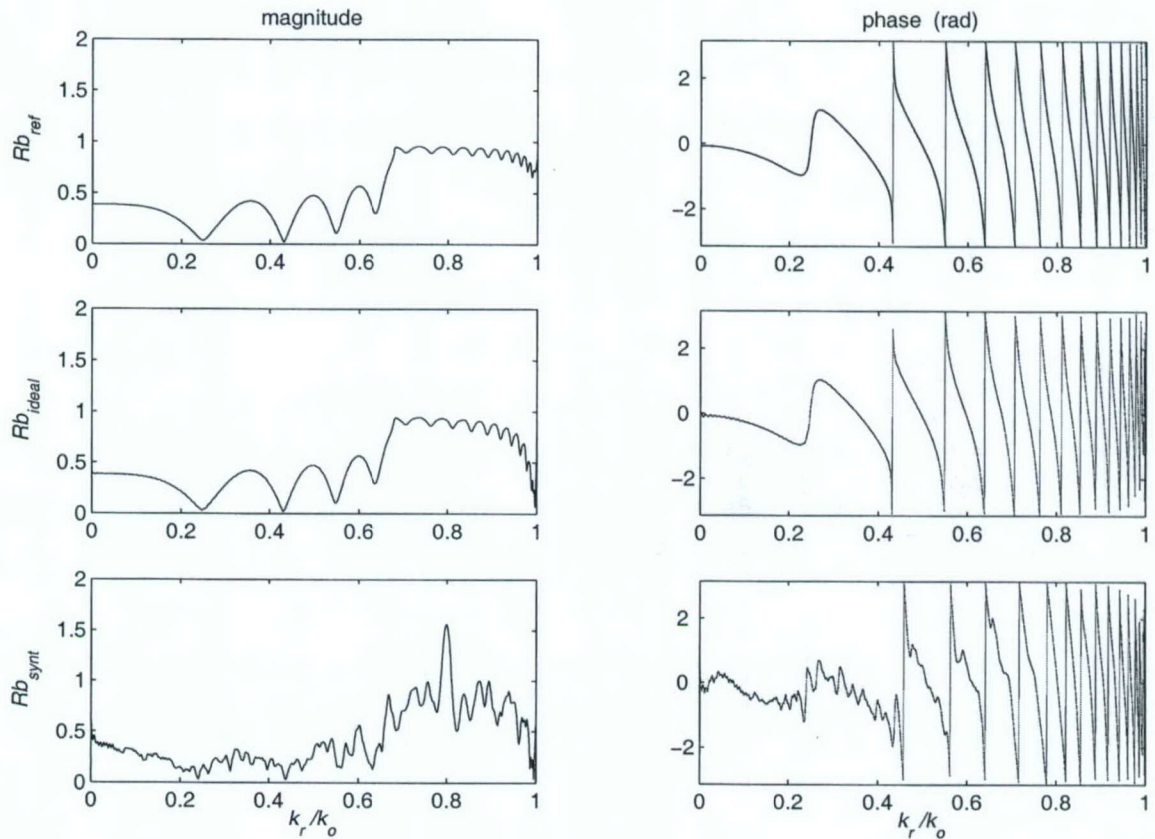


Figure 2-13: Reflection coefficient inferred from the simulated fields at  $z = 54.6\text{m}$ . The upper plots are the magnitude and phase of the reference reflection coefficient used to compute the fields and shown in Figure 2-8. The middle plot is the reflection coefficient estimated from the ideal, constant source height field. The lower plots are from the synthetic, varying source height field and illustrate the effect of the partial compensation due to the migration process.

### 2.3.3 Analysis of the Measured Acoustic Field

#### Identifying Phase Measurement Errors

The residual pressure for the synthetic and experimental pressure fields at  $z = 1.2\text{m}$  are plotted in Figure 2-14. The variations of magnitude and phase of the synthetic field are in agreement with the qualitative analysis of residual magnitude and phase in Section 2.1.2. For short ranges, the variations in magnitude and phase are small and nearly equal. At these distances, waves near normal incidence dominate, the value of the reflection coefficient is small and the field at the receiver is mainly the direct field, that is,  $BR_o$  is small and eqs. (2.22), (2.23), and (2.25) apply.

As the range increases, the variations of the magnitude and phase become larger, again in agreement with the analysis of Section 2.1.2. For large distances, waves reflected at critical and above critical incidence dominate the reflected field (large  $BR_o$ ).

The measured field residual magnitude and phase variations are not compatible. The magnitude variations are similar to those of the synthetic field, except in a region of distances between approximately 50 m and 100 m, where the magnitude presents a dip. The changes in magnitude of the experimental field are consistent with the picture delineated above involving the reflected fields, magnitude of reflection coefficient and distances. The residual phase, however, presents large variations (up to distances of approximately 500 m) that are not compatible with the changes in magnitude, neither in terms of value nor in terms of length scale<sup>3</sup>.

Notice that the measured source height variations were taken into account in computing the experimental residual pressure, which was sufficient to eliminate the same kind of phase variations observed in the synthetic field when source height variations were initially neglected, as shown in Figure 2-9.

---

<sup>3</sup>The term *length scale* refers to the range-varying distance between peaks of the residual magnitude and phase plots.

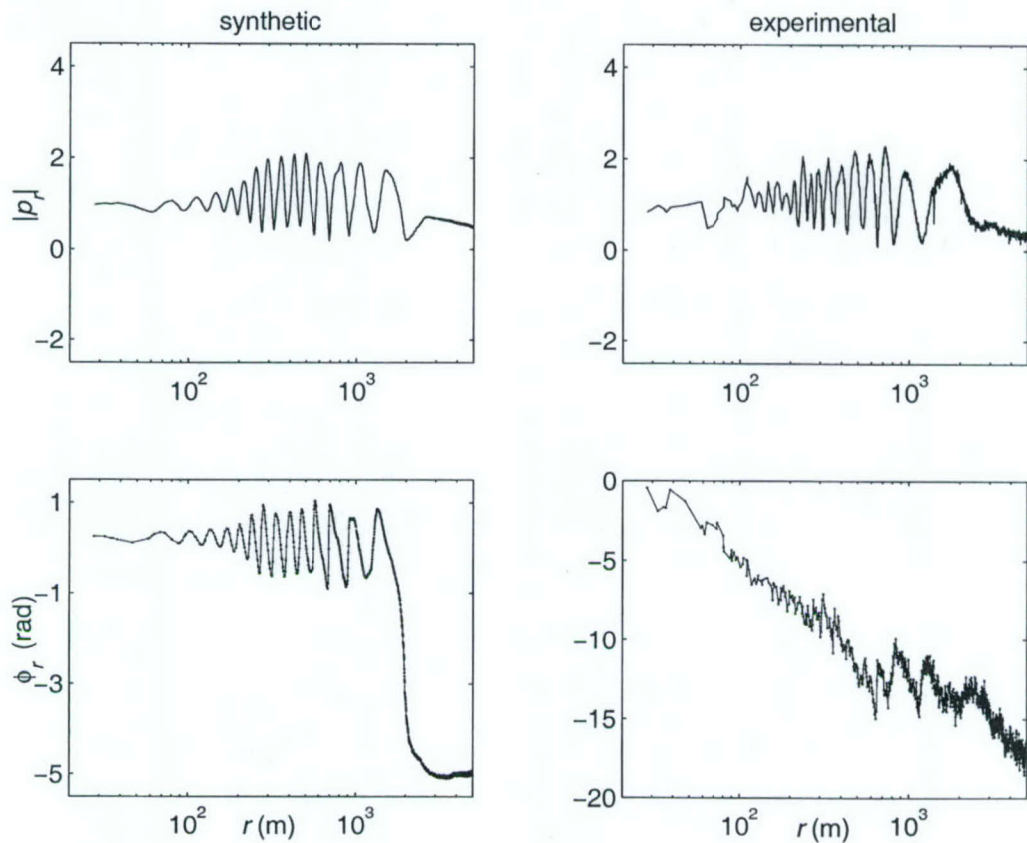


Figure 2-14: Residual pressure and unwrapped phase. (a) Synthetic, variable source height field. (b) Experimental field, receiver at 1.2 m. In both cases the pressure normalization took the source height variations into account. The vertical scales on these plots, with exception of the experimental phase, are the same.

## Phase Error Compensation

As discussed above, the large and slow changes in residual phase with range are not compatible with the residual pressure magnitude and, therefore, not consistent with the physical model underlying the measurement process. These changes can be regarded as resulting from measurement errors.

In the analysis of the plots in Figure 2-9, it was observed that errors in the source height (that is, assuming the height is constant when computing the residual pressure) lead to errors in the residual phase similar to those observed in Figure 2-14. Consequently, errors in the measurement of the source position or, equivalently, receiver synchronization could explain the observed residual phase.

The error in the residual phase is responsible for the poor results in the previous analysis[23], even after the field was migrated using the measured source height variations. Errors in the measured data preclude the estimation of the reflection coefficient.

However, these errors can be partially compensated for. Those phase variations not compatible with the residual pressure magnitude can be regarded as trends due to measurement errors. In Figure 2-15, the residual phase (from the measured pressure at the 1.2 m receiver) is plotted along with a trend corresponding to those large slow phase changes mentioned above. The phase after the removal of the trend is also shown. The resulting de-trended field can be regarded as an estimation of the actual field.

The phase trend was obtained by fitting a 10-th degree polynomial to the phase in the region  $r < 500$  m, which models the large, slow change in the unwrapped phase. For distances above 500 m, the trend was assumed a constant value equal to the polynomial value at 500 m, which is a multiple of  $2\pi$ . Therefore, no further phase adjustment was necessary.

Not all phase errors can be compensated for and the process is not unique. First, as discussed above, only errors that cause phase variations incompatible with the model can be identified. For example, the model predicts small residual phase variations at small distances. In the present analysis, only the large, slow changes of phase at small

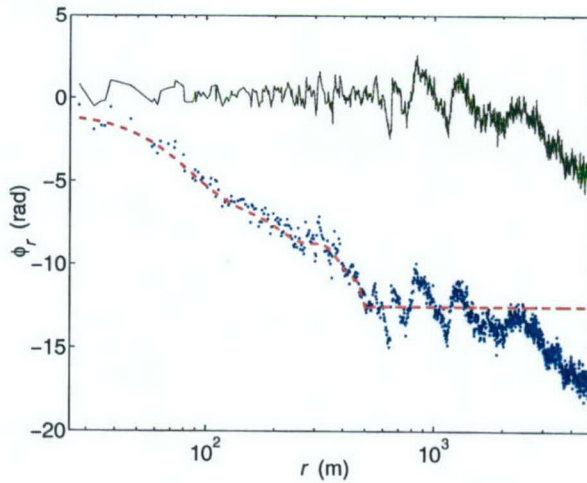


Figure 2-15: Residual phase of the measured field and trend removal for the receiver at 1.2 m (cf. Figure 2-14). The dots are the residual phase; the dashed line is a polynomial fit by parts of the slow, large phase variations observed up to  $r = 500$  m, interpreted as a measurement error; the solid line is the residual phase after the trend removal.

distances were discarded, as shown by the polynomial fit in Figure 2-15.

Second, the de-trend process is not unique because the exact form of the trend error is not known *a priori*. Depending on the chosen form of the polynomial fit to the phase, different trend estimations may result.

### The Field at the 54.6 m Receiver

During the experiment, the receiving calibration factors (conversion from measured signal voltage to pressure) were measured while the system was being lowered from the research vessel, when the source and receivers were on the same vertical and reasonably far from both the surface and bottom. The magnitude of the measured and synthetic fields in the lower (1.2 m) receiver show good agreement, after compensation for the calibration factor, as shown in Figure 2-14. The removal of the phase trend left, essentially, a  $2\pi$  rad difference in phase at long ranges, also suggesting that the phase of the calibration factor was correct.

For the higher (54.6 m) receiver, the calibration factor magnitude had to be adjusted

Table 2.1: The calibration factor  $q_0$ (Pa/V) is used to convert the voltage measured at the receiver output to acoustic pressure.  $p(r)/q_0$  reduces the values recorded at the receiver output  $p(r)$  (Volts) to the receiver input pressure (Pa) relative to a source level of 0 dB ref. 1 Pa@1 m, [that is, equivalent to a source term  $-4\pi\delta(\mathbf{r}-\mathbf{r}_0)$  in the wave equation].  $q_0$  was measured using data acquired while the mooring system was being lowered and the source and receivers were connected to the same cable from the research vessel (column *measured*). The values shown in the *inferred* column were estimated during the present analysis of phase and magnitude errors.

receiver (m)	$ q_0 $		$\angle q_0$ (deg)	
	measured	inferred	measured	inferred
1.2	5277	—	127.9	128.5
54.6	2424	4286	-7.4	-134.7

by about 5dB through comparison with the synthetic field. The phase was adjusted by  $-127.3^\circ$  using the difference in phase remaining at long ranges after the phase trend removal. Both measured and inferred calibration factors are shown in Table 2.1.

A qualitative analysis of the residual pressure at the 54.6 m receiver, based on the characteristics of the residual phase, as discussed in Section 2.1.2 and shown in Figure 2-16, reveals that:

- For  $r > 1000$  m, phase and magnitude are of reasonable quality; below 1000 m, the phase presents a slow, large change with distance, as observed (below 500 m) for the 1.2 m receiver;
- Under 170 m, the measured phase seem degraded, and the rate of change of phase is larger than above 170 m;
- Below 100 m, the behavior of the phase changes again, presenting even larger fluctuations.

The de-trend process was implemented on the 54.6 m receiver data through four polynomial fits, roughly according to the above regions:

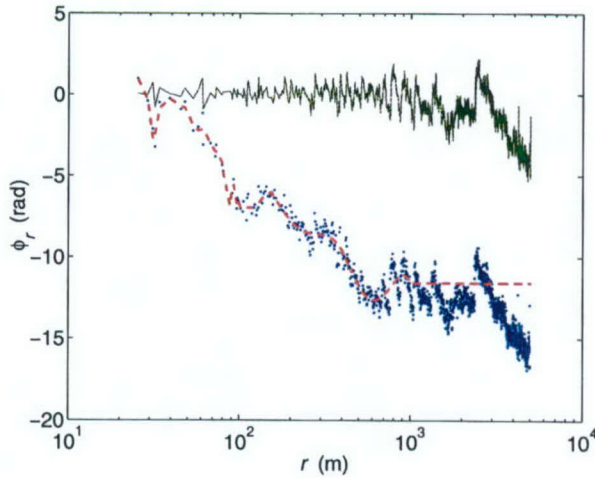


Figure 2-16: Residual phase of the measured field and trend removal for the receiver at 54.6 m (cf. Figure 2-15). The dots are the residual phase; the dashed line is a polynomial fit by parts of the slow, large phase variations observed up to  $r = 1000$  m, interpreted as a measurement error; the solid line is the residual phase after the trend removal.

- A polynomial of degree 15 for  $r < 100$  m;
- Two polynomials of degree 5 for  $100 \leq r < 170$  m, and  $150 \leq r < 500$  m;
- A polynomial of degree 3 for  $450 \leq r < 1000$  m.

The polynomial fits were applied in the order given above. The overlap between regions allowed for reduced discontinuities in the transition points. Figure 2-16 illustrates the process. The trend line above 1000 m is a constant, as in the other receiver. The constant, in the present case, was not an integer multiple of  $2\pi$ , which required a further phase correction in the complex calibration factor  $q_o$ , as shown in Table 2.1. The final residual pressure, including the synthetic field for comparison, is shown in Figure 2-17.

Notice that below 100 m the residual magnitude is noticeably smaller than one, which is not to be expected in a region where the direct field dominates (cf. Figure 2-14 for  $z = 1.2$  m). This may suggest an additional experimental error mechanism for the first 20 data samples.

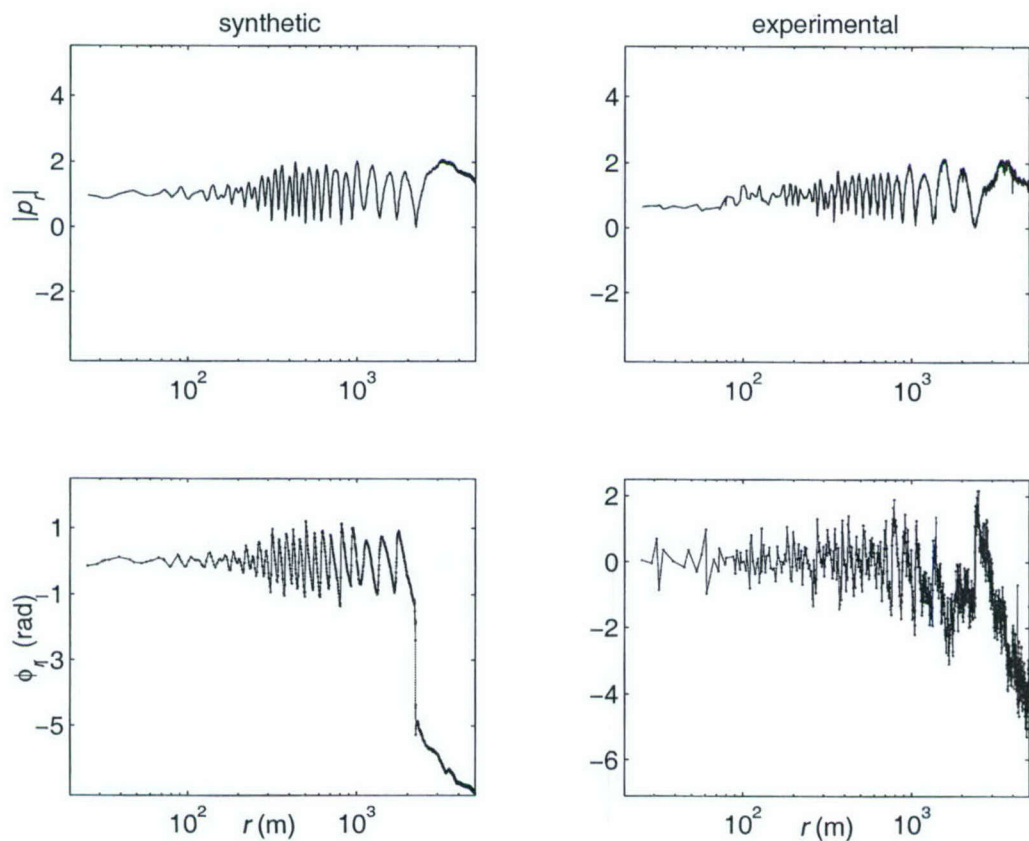


Figure 2-17: Residual pressure and unwrapped phase of the synthetic, variable source height field and of the experimental field (after phase de-trend), receiver at 54.6 m. The vertical scales on these plots are the same.

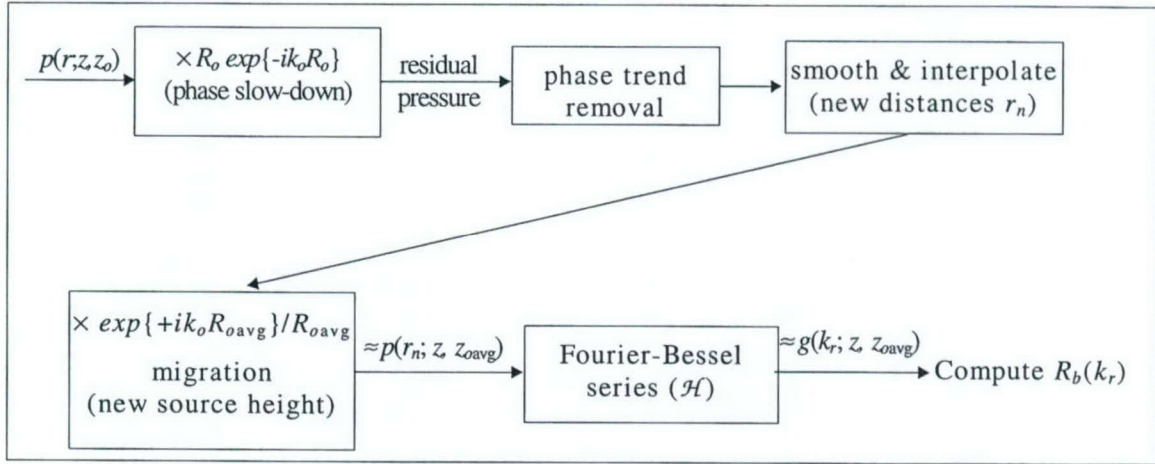


Figure 2-18: The complete reflection coefficient estimation includes compensation for source height variations (migration) and phase measurement errors (phase de-trend), in addition to the basic steps of Figure 2-3.

### The Complete Reflection Coefficient Measurement Process

The process of estimation of the reflection coefficient that includes migration and phase de-trend is shown in Figure 2-18 (cf. Figure 2-3). After the phase slow-down stage, the estimated residual phase trend is removed and the residual pressure is interpolated.

After the interpolation, the phase factor removed during the first stage is restored using a new geometric phase factor based on a constant, average source height  $z_{0avg}$ :

$$\exp\{ik_0R_{0avg}\} = \exp\{ik_0\sqrt{r^2 + (z - z_{0avg})^2}\}$$

This is the migration process discussed in Section 2.3.1. The interpolated and migrated pressure data is the input for the computation of the Green's function and the reflection coefficient.

### 2.3.4 Reflection Coefficient from Experimental Data

#### Experimental Green's Function

The residual pressure was interpolated into the range grid required by the Fourier-Bessel series, eq.(2.16), associated to the zeros of  $J_0(\cdot)$ . A smoothing cubic spline was used for the interpolation as implemented in Matlab<sup>®</sup><sup>4</sup> by the functions *csaps.m* and *spaps.m*[12].

Results are shown for two degrees of pressure field smoothing, in order to verify its effect on the final result, which is to obtain estimates with different degrees of smoothness. When applied to the synthetic fields, the same degrees of smoothing do not affect the result appreciably.

The smoothed/interpolated fields at the two receivers are shown in Figures 2-19 and 2-20. For small ranges, the fields were extrapolated using the geometrical acoustic model of eq.(2.27), as explained in Section 2.3.1.

The general characteristics of the estimated Green's functions, shown in Figure 2-21, are reasonably close to the synthetic case (cf. Figures 2-10 and 2-11). As  $k_r$  increases, the magnitude goes from slowly to quickly changing with pronounced nulls. The behavior of the phase is also similar. The effect of the extra residual pressure smoothing is to produce a smoother estimate of the Green's function, which indicates that the additional smoothed signal still captures some essential characteristics of the measured fields.

#### Inferred Reflection Coefficient

The inferred reflection coefficients are shown in Figure 2-22 (cf. Figures 2-12 and 2-13). Smoothing of the residual pressure has the effect of also smoothing the estimated reflection coefficient and reducing its peaks. The phase of the reflection coefficient computed from the 1.2 m receiver has, for  $k_r > 0.55k_0$ , a negative slope, as observed in the model reflection coefficient and the synthetic field results for large  $k_r$ . This is only observed for

---

<sup>4</sup>Matlab is a registered trademark of The MathWorks, Inc.

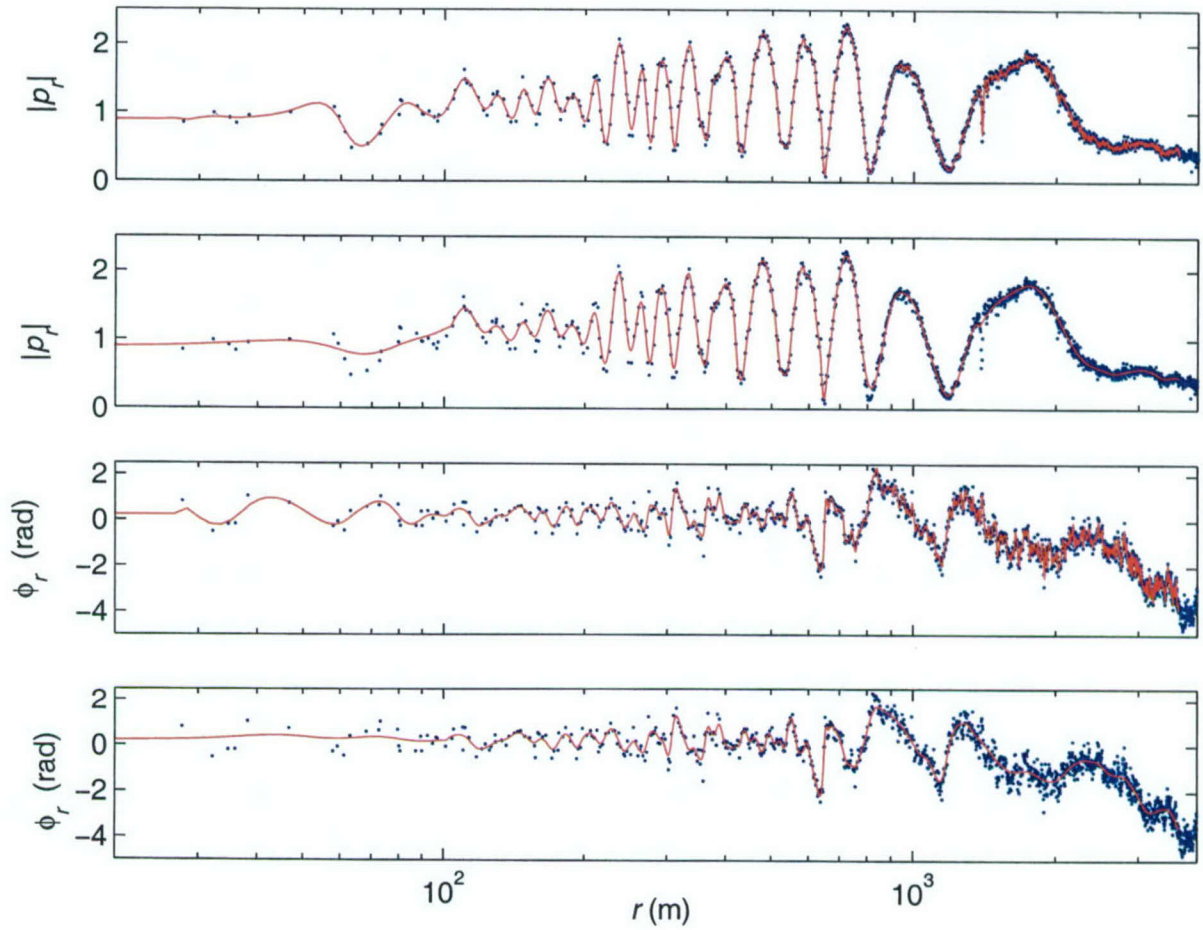


Figure 2-19: Experimental residual fields,  $z = 1.2\text{m}$ , original (dots) and smoothed and interpolated (solid lines); two degrees of smoothing are shown. The final results preserve the main features of the measured experimental field. In order to preserve these features, the total range was divided in up to 5 regions with different smoothing parameters.

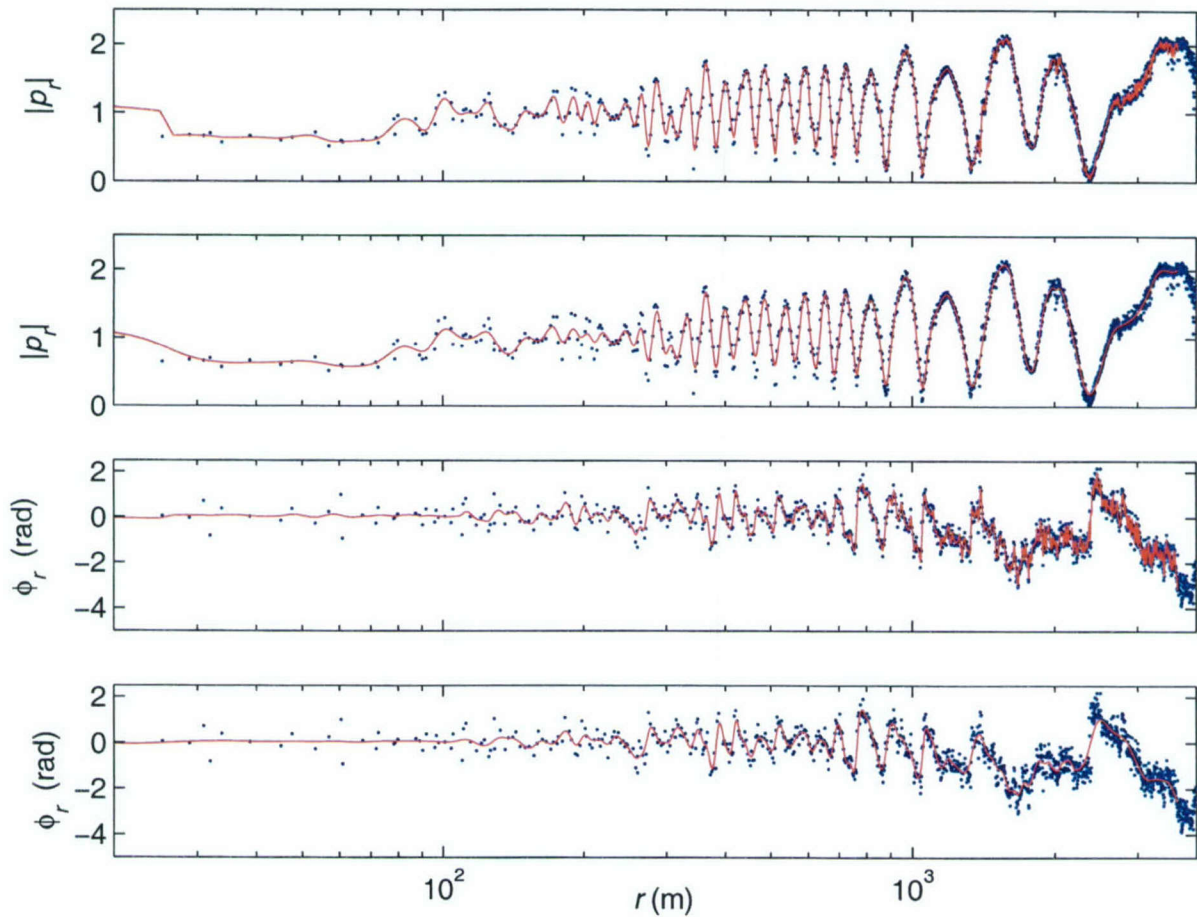


Figure 2-20: Experimental residual fields,  $z = 54.6\text{m}$ , original (dots) and smoothed and interpolated (solid lines); two degrees of smoothing are shown. The final results preserve the main features of the measured experimental field. In order to preserve these features, the total range was divided in up to 4 regions with different smoothing parameters.

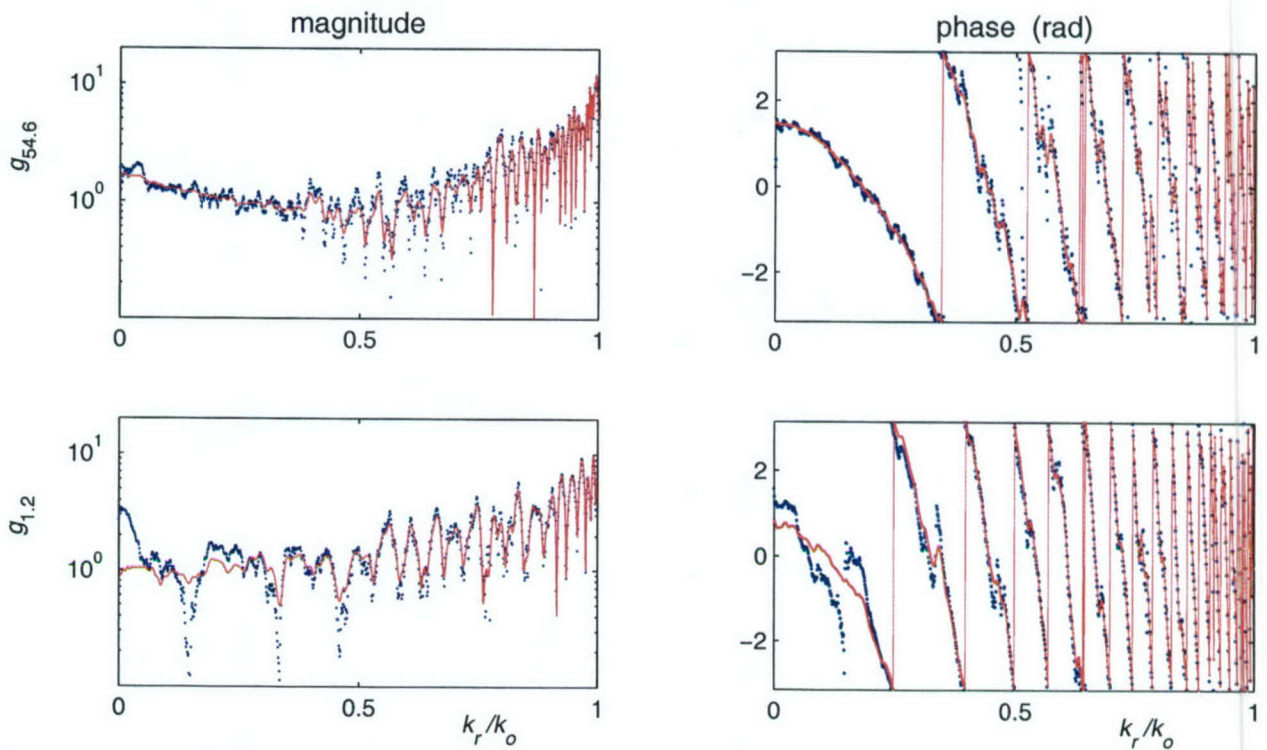


Figure 2-21: Green's function (in Newton, relative to source level of 0 dB ref. 1Pa @ 1 m) estimated from the measured fields for  $z = 54.6\text{m}$  (upper plot) and  $z = 1.2\text{m}$ . The solid lines are results from the smoother signals shown in Figures 2-19 and 2-20.

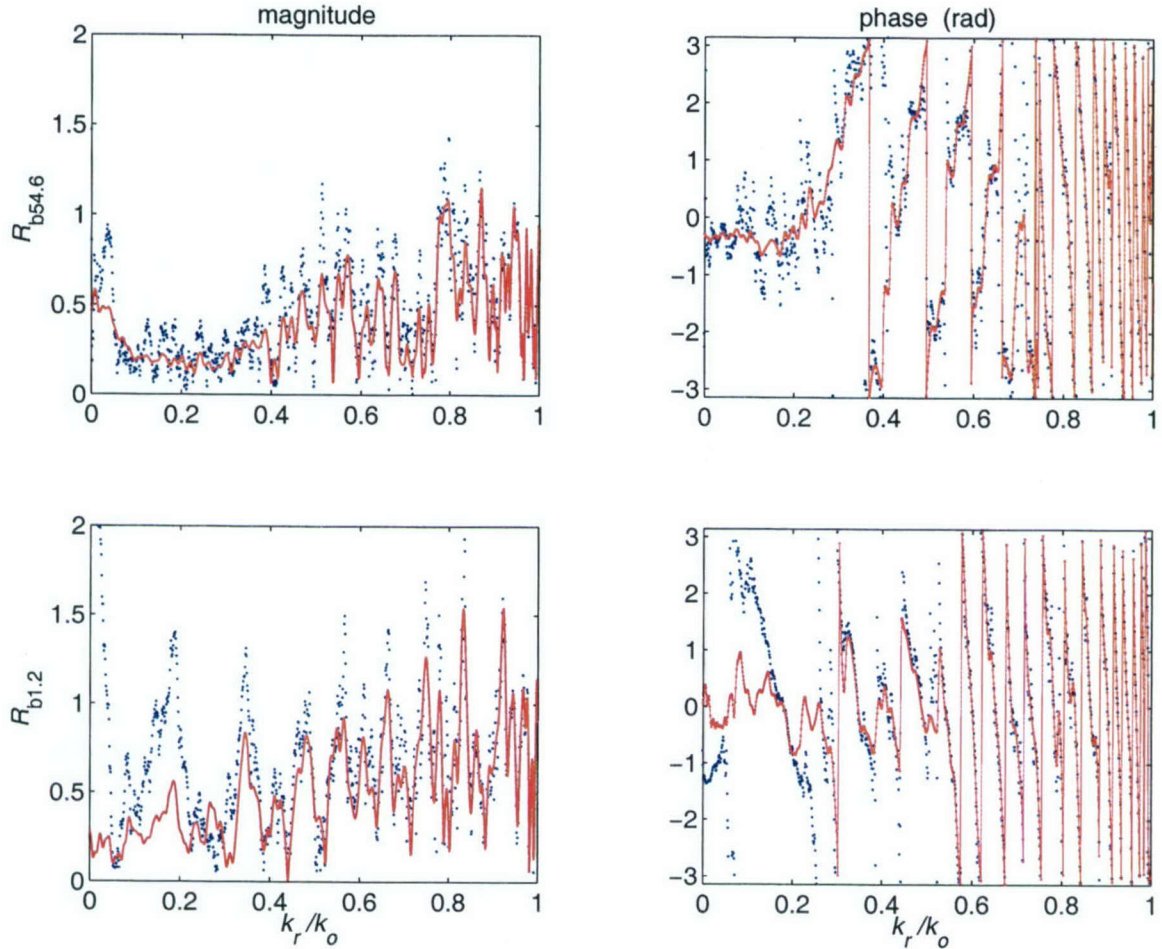


Figure 2-22: Reflection coefficient inferred from the experimental fields at  $z = 54.6$  m (upper plot) and 1.2 m. The solid lines corresponds to the smoother fields shown in Figures 2-19 and 2-20.

$k_r > 0.75k_o$  on the 54.6 m receiver, which indicates a better quality of the 1.2 m receiver estimate. The large magnitude oscillations in the supercritical region  $k_r > 0.78k_o$  is similar to those observed in the synthetic results, suggesting a similar cause (degradation of the Hankel transform due to source height variations).

The magnitude of the reflection coefficient estimated from the 54.6 m receiver data has a pronounced change at  $k_r/k_o \approx 0.78$  typical of critical incidence, suggesting a basement sound velocity of 1917 m/s, instead of 2200 m/s as previously obtained by matching the field magnitude[21]. The 1.2 m receiver results present similar changes

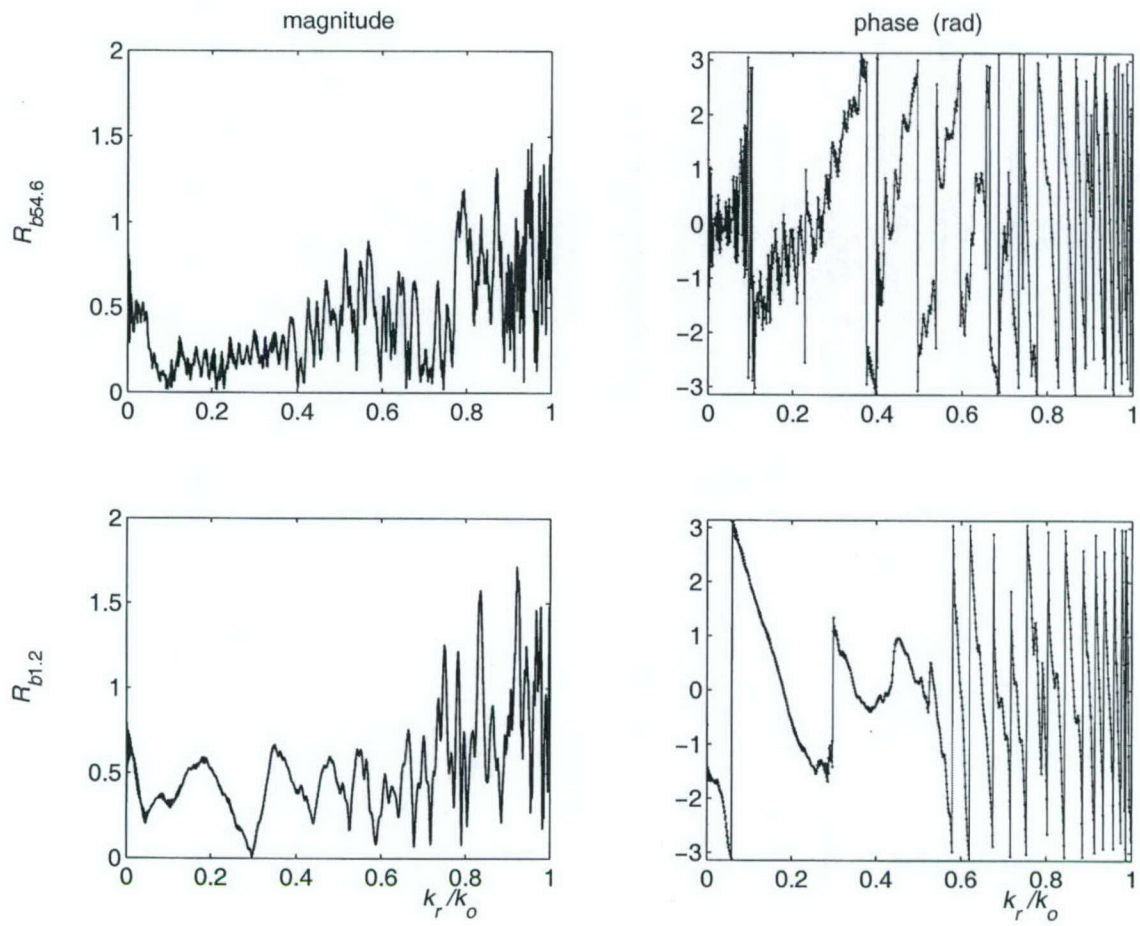


Figure 2-23: Reflection coefficient inferred from the experimental fields at  $z = 54.6$  m (upper plot) and 1.2 m, using an alternate smoothing scheme, extrapolation of fields using only direct field, and Fourier-Bessel series with uniform window.

in magnitude at  $k_r/k_o \approx 0.75$ , although not so well defined, resulting in a basement velocity estimate of 1993 m/s.

Figure 2-23 shows the resulting reflection coefficients when using still another smoothing scheme on the experimental fields, where the field was extrapolated for small ranges using only the direct field, and a uniform window  $[w(r_n) \equiv 1]$  was used when computing the Green's function.

The results using this simpler scheme are qualitatively similar to those shown previously (Figure 2-22), indicating a certain degree of insensitivity of the estimate to details

in the data processing. The more obvious features are:

- The magnitude is closer to one near  $k_r = k_o$ ; (caused by the use of the uniform window);
- The critical region is better defined in the 1.2 m receiver result, although not as well as in the other receiver's.

### Fields Computed from Inferred Reflection Coefficients

An assessment of the quality of the estimate can be achieved by comparing the measured field with a synthetic field generated from the inferred reflection coefficients. The estimated reflection coefficients were first extended to high  $k_r$  values ( $k_o < k_r < 2k_o$ ) by assuming a constant value of -1 in that region.

In order to observe the effect of such extension, fields were computed using the model reflection coefficient truncated to  $k_r = k_o$  and then extended to  $k_r = 2k_o$  as described above. The result is shown in the upper plot of Figure 2-24. A noticeable, but not significant error in the magnitude of the field is observed only at large distances.

The remaining plots show computed fields at 54.6 m using the reflection coefficient of Figures 2-12 and 2-13, inferred from the synthetic fields. The deterioration observed on these other plots is also more pronounced at large distances, suggesting that the estimate of the reflection coefficient is worse near  $k_r = k_o$ . In addition, these plots suggest that the reflection coefficient estimate is better from the  $z = 1.2$ m data.

The analogous results for the experimental reflection coefficients are shown in Figures 2-25 and 2-26. The mismatch at large distances is qualitatively similar to that observed with the synthetic fields, suggesting a comparable quality of the reflection coefficient estimate for large  $k_r$ . At smaller distances, the fields differ more than in the synthetic case, which can be explained by the phase errors at these distances.

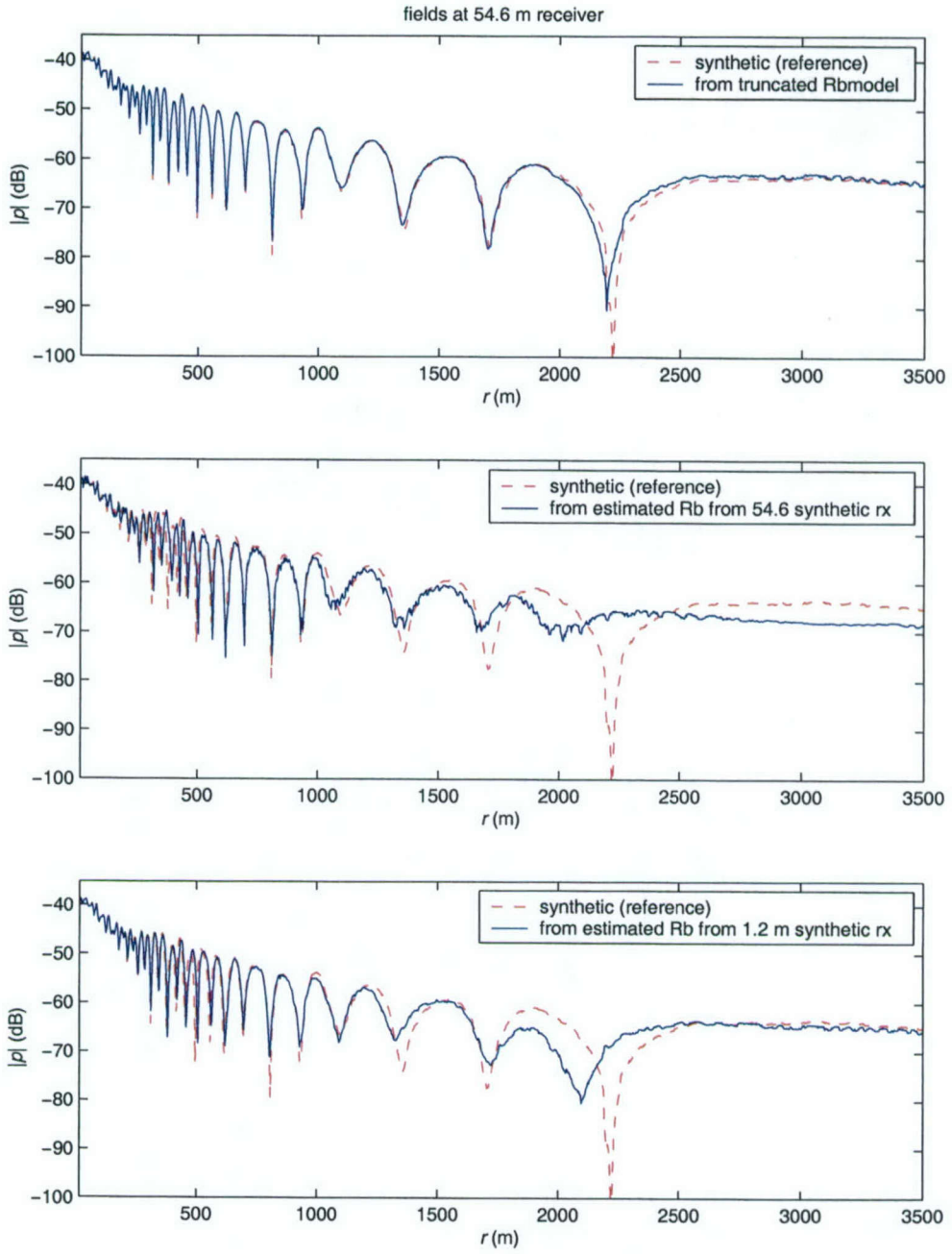


Figure 2-24: Magnitude (dB re 1V at the receiver output) of the original synthetic field at  $z = 54.6$  m from the model reflection coefficient (dashed lines) compared with a new set of synthetic fields computed from reflection coefficients inferred the original synthetic fields(solid lines) shown in Figures 2-12 and 2-13. The reflection coefficients were extended to the region  $k_o \leq k_r \leq 2k_0$  by assuming  $R_b = -1$  in that region. (a) model  $R_b$  truncated to  $k_0$ , for reference; (b)  $R_b$  inferred from the synthetic field at  $z = 54.6$  m; (c)  $R_b$  inferred from the synthetic field at  $z = 1.2$  m.

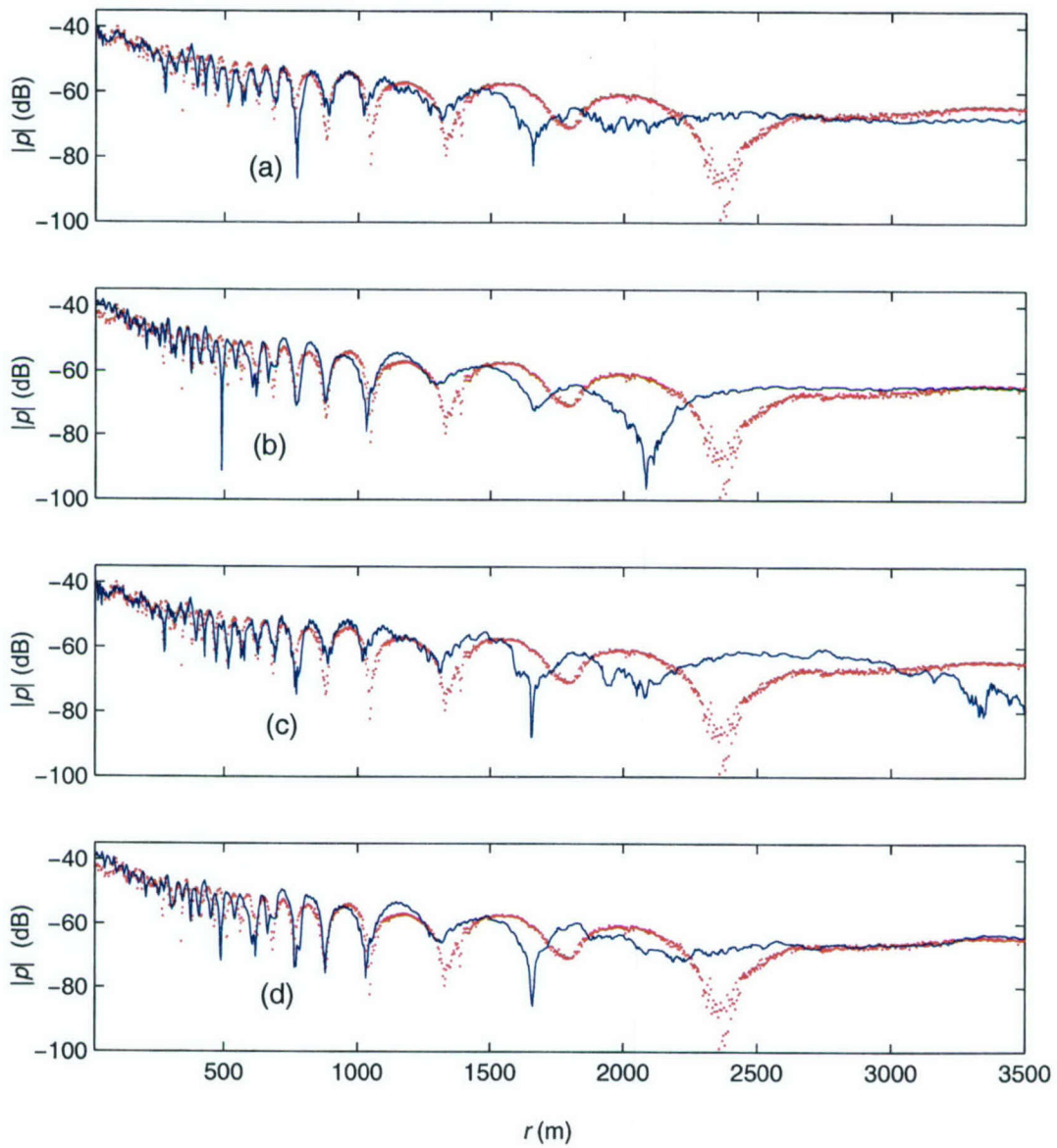


Figure 2-25: Magnitude (dB re 1V at the receiver output) of measured (dots) and synthetic (solid lines) fields generated from reflection coefficients estimated from experimental data: (a) smooth Rb estimate from receiver at 54.6 m (Figure 2-22, upper plot); (b) smooth Rb estimate from receiver at 1.2 m (Figure 2-22 lower plot); (c) alternate smooth scheme, Rb from receiver at 54.6 m (upper plot of Figure 2-23); (d) alternate smooth scheme, Rb from receiver at 1.2 m (lower plot of Figure 2-23).

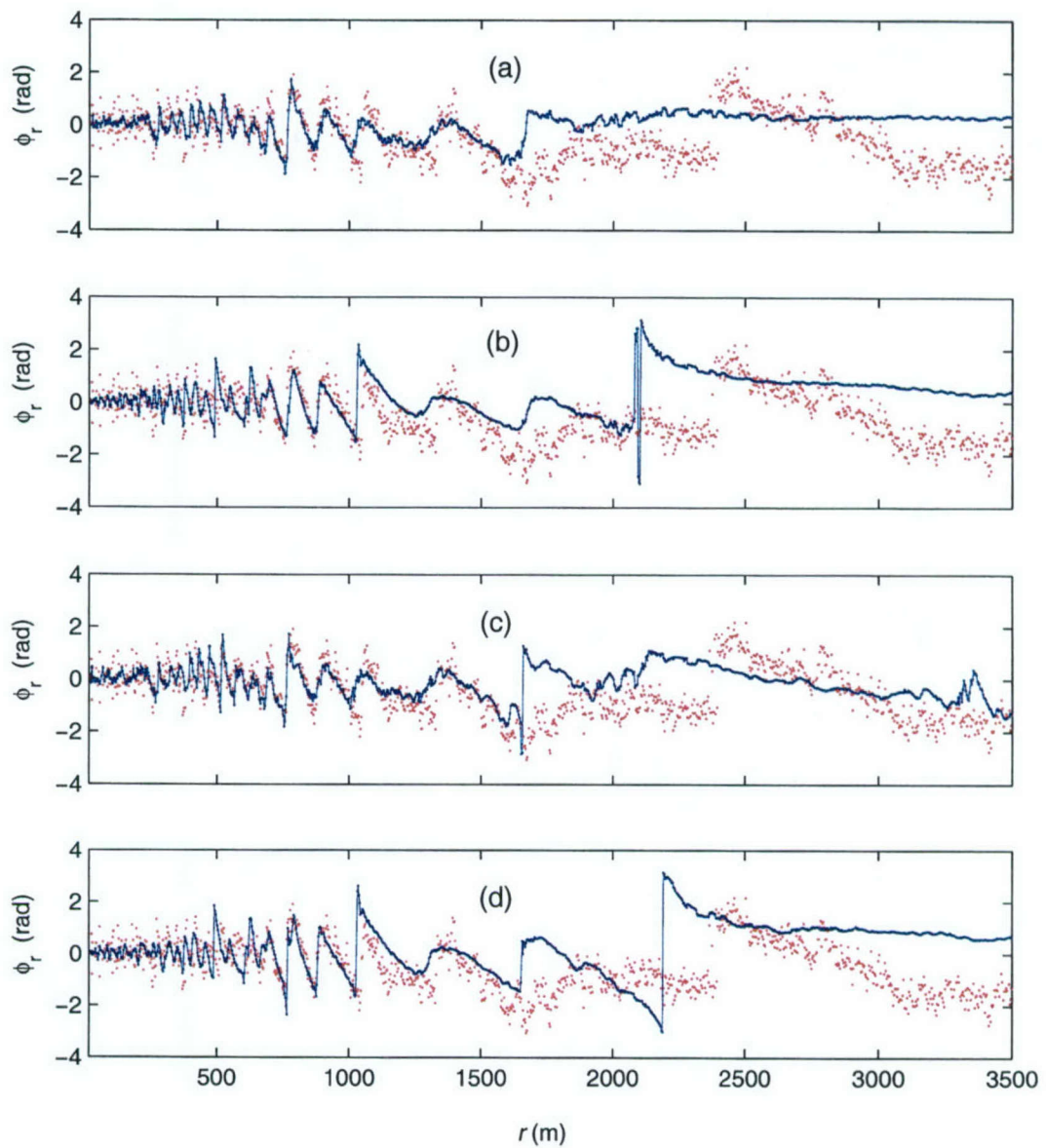


Figure 2-26: Residual phase of measured (dots) and synthetic (solid lines) fields generated from reflection coefficients estimated from experimental data, corresponding to Figure 2-25: (a) smooth Rb estimate from receiver at 54.6 m (Figure 2-22, upper plot); (b) smooth Rb estimate from receiver at 1.2 m (Figure 2-22 lower plot); (c) alternate smooth scheme, Rb from receiver at 54.6 m (upper plot of Figure 2-23); (d) alternate smooth scheme, Rb from receiver at 1.2 m (lower plot of Figure 2-23).

## 2.4 Inversion from Reflection Coefficient Data

### 2.4.1 Practical Issues Related to the Application of Merab's Method

Merab's method is based on the exact inverse theory of estimating the potential from scattering data in Quantum Mechanics. It requires knowledge of the reflection coefficient in the domain  $0 < k_z < \infty$  and, when trapped modes are present, the location and residues of its poles in the upper half-plane. In actual measurements, the reflection coefficient is estimated only in a finite region of the real line, usually in the range  $0 < k_z < k_0$  corresponding to real angles of incidence, and no method to measure the required information about its poles has yet been devised. Another issue is its validity only in regions free of density discontinuities. This Section discusses these issues.

#### Compensating for Density Discontinuity

As pointed out in Section 2.1.1, Merab's method is not valid in the presence of density discontinuities, which is a major restriction of its application to the measurement of sound velocity in the seabed.

A density discontinuity at the water-seabed interface can, however, be compensated for by modifying the reflection coefficient[66]. The continuity of the vertical impedance imposes a relation between the values of the reflection coefficient measured on each side of the interface [75] (see Figure 2-27)

$$\frac{\rho_0}{k_{z0}} \frac{1 + R_{b0}(k_{z0})}{1 - R_{b0}(k_{z0})} = \frac{\rho_1}{k_{z1}} \frac{1 + R_{b1}(k_{z1})}{1 - R_{b1}(k_{z1})}, \quad (2.29)$$

where the subscript '0' refers to the water side, and '1' to the seabed side, and  $k_{z1} = k_z(z = 0^+) = \sqrt{(\omega/c_1)^2 - (\omega/c_0)^2 + k_{z0}^2}$ . If the density of the water were "increased" to  $\rho_1$ , the new measured reflection coefficient at  $z = 0^-$ ,  $\tilde{R}_{b0}(k_{z0})$ , would satisfy, from

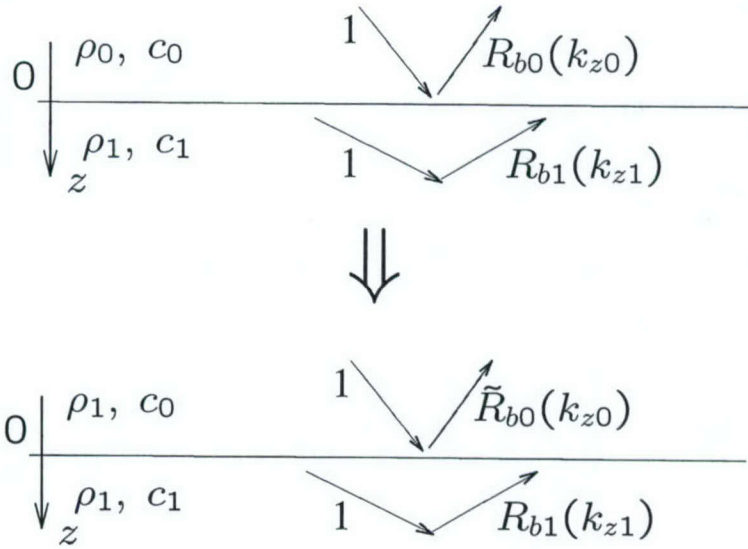


Figure 2-27: Density discontinuity compensation of the seabed reflection coefficient. If  $\rho_0$  is changed to  $\rho_1$ , the density discontinuity is eliminated, resulting in a different reflection coefficient  $\tilde{R}_{b0}$ .

eq.(2.29),

$$\frac{\rho_1}{k_{z0}} \frac{1 + \tilde{R}_{b0}(k_{z0})}{1 - \tilde{R}_{b0}(k_{z0})} = \frac{\rho_1}{k_{z1}} \frac{1 + R_{b1}(k_{z1})}{1 - R_{b1}(k_{z1})}. \quad (2.30)$$

Comparing eqs.(2.29) and (2.30), one obtains

$$\tilde{R}_{b0}(k_{z0}) = \frac{1 - \frac{\rho_1}{\rho_0} + \left(1 + \frac{\rho_1}{\rho_0}\right) R_{b0}(k_{z0})}{1 + \frac{\rho_1}{\rho_0} + \left(1 - \frac{\rho_1}{\rho_0}\right) R_{b0}(k_{z0})}. \quad (2.31)$$

Equation (2.31) can be used to compensate the measured reflection coefficient, given the seabed density at the interface.

### Avoiding Excitation of Trapped Modes

For the Icelandic model of Figure 2-6, the water sound velocity is  $c_0 = 1495$  m/s, the minimum sound velocity in the seabed is  $c_{min} = 1483.34$  m/s, and the sound velocity gradient is  $g = 0.62$  s<sup>-1</sup>. For these parameters, eq.(2.5) predicts that frequencies below

248 Hz do not excite trapped modes, but the pole at the reflection coefficient in Figure 2-8 shows otherwise.

In [45], the starting point to establish the criterion for non excitation of trapped modes, eq.(2.5), is an expression derived for bound states in a central field of force. A more realistic criterion is obtained by using the WKB approximation for modes, in which traveling waves have phase factors of the form

$$\exp \left\{ \pm i \int_{z_0}^z k_z(z') dz' \right\}, \quad (2.32)$$

where  $k_z = \sqrt{[\omega/c(z)]^2 - k_r^2}$  is real.

For the Icelandic model, where trapped modes reflect at the surface and refract back from below, a mode is defined by setting to  $2\pi n$ ,  $n$  integer, the total phase change of a wave traveling from a reference depth to the lower turning point  $z_T$ , to the water interface at  $z = 0$  where it is reflected, and back to the reference depth[75]:

$$2 \int_0^{z_T} k_z(z) dz + \frac{\pi}{2} + \phi_{R_{10}} = 2\pi n, \quad n = 1, 2, \dots, \quad (2.33)$$

where the first term corresponds to the WKB approximation of phase change due to the propagation,  $\pi/2$  accounts for the total reflection at the lower turning point (when contributions from other layers below  $z_T$  are neglected), and  $\phi_{R_{10}}$  is the phase of the reflection coefficient at the water interface, given by

$$\phi_{R_{10}} = -2 \tan^{-1} \left[ \frac{\rho_1}{\rho_0} \frac{\sqrt{k_r^2 - k_0^2}}{k_z} \right]. \quad (2.34)$$

Equation (2.33) is solved for the modal eigenvalues  $k_{rn}$ . Substituting eq.(2.34) into eq.(2.33) and taking the tangent on both sides, one obtains the eigenvalue characteristic equation

$$\tan \left( \int_0^{z_T} k_z(z) dz - \frac{\pi}{4} \right) = \frac{\rho_1}{\rho_0} \frac{\sqrt{k_r^2 - k_0^2}}{k_z}. \quad (2.35)$$

A closed form expression for the integral can be obtained for the constant gradient profile with a minimum at the water interface,  $c(z) = c_{min} + gz$ , which, upon the substitution  $u = k_z(z)/k(z)$ , for which  $u(z_T) = 0$ , becomes

$$\int_0^{z_T} k_z(z) dz = \frac{\omega}{g} \left( 0.5 \ln \frac{1+y}{1-y} - y \right),$$

where  $y = u(0) = k_z(0)/k(0)$  is the cosine of the angle of incidence at the water interface.

Using the variable  $y$ , the characteristic equation (2.35) becomes, for a linear sound velocity profile,

$$\tan \left[ \frac{\omega}{g} \left( 0.5 \ln \frac{1+y}{1-y} - y \right) - \frac{\pi}{4} \right] = \frac{\rho_1}{\rho_0} \frac{\sqrt{a^2 - y^2}}{y}, \quad (2.36)$$

where  $a = \sqrt{1 - (c_{min}/c_0)^2}$ . Trapped modes are the roots of eq.(2.36) in the interval  $0 < y < a$  corresponding to evanescent waves in the water ( $k_r > k_0$ ).

In order to avoid trapped modes, eq.(2.36) can not have solutions. As shown in Figure 2-28, the right-hand side of eq.(2.36) is a positive function in  $0 < y < a$  that decreases monotonically to zero at  $y = a$ . The left-hand side is  $(-1)$  at  $y = 0$  and increases monotonically to zero at the point  $y_0$  where the argument of the tangent function becomes zero. Therefore, solutions in the interval  $(0, a)$  will not exist if  $a < y_0$ , or, equivalently, if the left-hand side of eq.(2.36) is negative at  $y = a$ , i.e.,

$$\frac{\omega}{g} \left( 0.5 \ln \frac{1+a}{1-a} - a \right) < \frac{\pi}{4},$$

from which the criterion for no trapped modes is

$$\omega < \frac{\pi}{4} g \frac{1}{\left( 0.5 \ln \frac{1+a}{1-a} - a \right)}. \quad (2.37)$$

For typical environments,  $c_{min}/c_0 \sim 1$ ,  $a = \sqrt{1 - (c_{min}/c_0)^2} \simeq \sqrt{2} \sqrt{1 - c_{min}/c_0}$ , and

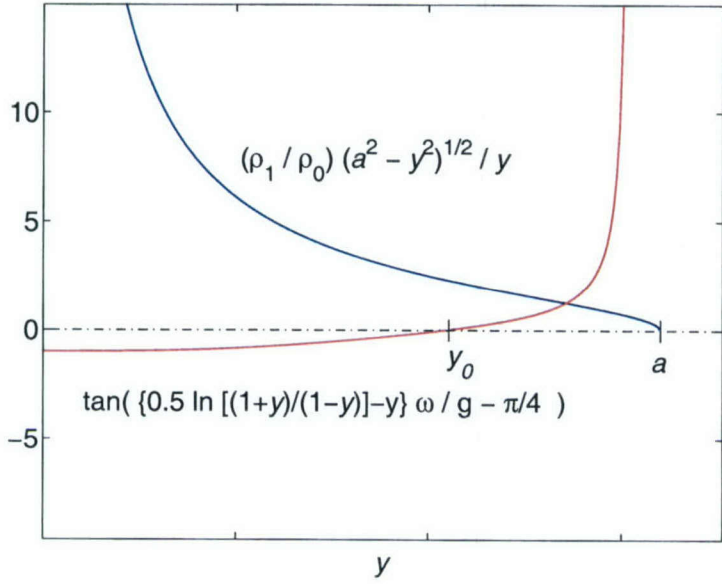


Figure 2-28: Terms of the trapped mode equation (2.36), illustration of a single solution (mode). Axis scales are arbitrary. No solution exists when  $a < y_0$ .

eq.(2.37) simplifies to<sup>5</sup>

$$\omega < \frac{3\pi}{8\sqrt{2}}g \left(1 - \frac{c_{min}}{c_0}\right)^{-3/2}, \quad (2.38)$$

which is nearly 52% below eq.(2.5). Back to the Icelandic Basin model of Figure 2-6, eq.(2.38) predicts that no mode is excited below 119 Hz, not the 248 Hz predicted by eq.(2.5). Using the KRAKEN[57] normal mode code, trapped modes were found down to 112 Hz for that model, 6% below eq.(2.38). Equation (2.38) is the criterion that must be applied when the sound velocity minimum is close to the water interface.

If the sound velocity minimum is away from the water interface and the modal solutions have two turning points (instead of being reflected by the water interface), eq.(2.33) is modified by taking  $\phi_{R_{10}} = \pi/2$  (neglecting the effect of the water interface).

---

<sup>5</sup>The Taylor series expansion of the denominator in eq.(2.37) is

$$0.5 \ln \frac{1+a}{1-a} - a = \frac{a^3}{3} + \frac{a^5}{5} + \dots, \quad 0 \leq a < 1.$$

Following an analogous analysis, but now for a symmetric, bi-linear profile of gradient  $\pm g$  near the minimum, modes with characteristic wavenumbers below that of the water are avoided if

$$\omega < \frac{3\pi}{4\sqrt{2}}|g| \left(1 - \frac{c_{min}}{c_0}\right)^{-3/2}, \quad (2.39)$$

which is just 4% below Merab's criterion, eq.(2.5). The present result suggests that his "starting point" of a central field of force mentioned above is related to the two turning point case.

As shown in eq.(2.38), trapped modes can be avoided by using a sufficiently low frequency that depends on the ratio  $c_{min}/c_0$  between the minimum sound velocity in the sediment and the velocity in water. If trapped modes are excited, but the information about the bound state (that is, the poles of the reflection coefficient) is not included in the inversion, as in eq.(2.4), the inferred sound velocity profile would not include the corresponding minima.

For the Icelandic Basin model of Figure 2-6 trapped modes are excited at 220 Hz, the frequency of the experiment. In order to avoid trapped modes at a given frequency, the sound velocity in water should satisfy, from eq.(2.38),

$$c_0 < \frac{c_{min}}{1 - [3\pi g/(8\omega\sqrt{2})]^{2/3}} = \frac{8c_{min}}{8 - (3g/f)^{2/3}}, \quad (2.40)$$

where  $\omega = 2\pi f$ . In order to avoid trapped modes in the Icelandic model seabed ( $c_{min} = 1483.34$  m/s,  $g = 0.62$  s $^{-1}$ ) at  $f = 220$  Hz, the water sound velocity should be, from eq.(2.40), smaller than 1491.07 m/s, which is not satisfied by the model.

If a measured reflection coefficient is modified to account for a smaller water sound velocity, say  $c'_o = c_0 - \epsilon$ , then the inverted profile may change to include sound velocities down to this new water sound velocity, indicating a possible trapped mode in the original environment<sup>6</sup>. Using the continuity condition of eq.(2.29) with the lower sound velocity

---

<sup>6</sup>Joyce R. McLaughlin, Dept. of Mathematical Sciences, Rensselaer Polytechnic Institute, Troy, NY.

$c'_0$ , and the new vertical wavenumber

$$k'_{zo} = \sqrt{(\omega/c'_0)^2 - k_r^2} = \sqrt{(\omega/c'_0)^2 - (\omega/c_0)^2 + k_{z0}^2}, \quad (2.41)$$

one obtains

$$\frac{\rho_0}{k'_{z0}} \frac{1 + R_{b0}(k'_{z0})}{1 - R_{b0}(k'_{z0})} = \frac{\rho_1}{k_{z1}} \frac{1 + R_{b1}(k_{z1})}{1 - R_{b1}(k_{z1})},$$

which, when compared with eq.(2.29), results in

$$R_{b0}(k'_{z0}) = \frac{k'_{zo} - k_{zo} + (k'_{zo} + k_{zo})R_{b0}(k_{zo})}{k'_{zo} + k_{zo} + (k'_{zo} - k_{zo})R_{b0}(k_{zo})}. \quad (2.42)$$

The original reflection coefficient is available for vertical wavenumbers  $k_{z0} \geq 0$ . The modified coefficient can, therefore, be computed, from eq.(2.41), for  $k'_{z0} \geq \sqrt{(\omega/c'_0)^2 - (\omega/c_0)^2} \sim \omega/c_0 \sqrt{2\epsilon/c_0}$ . In the region  $0 \leq k'_{z0} < \omega\sqrt{2\epsilon/c_0}/c_0$ , which corresponds to information not available in the original measurement, the reflection coefficient must be extrapolated. This suggests that  $\epsilon/c_0$  must be small.

## 2.4.2 Simulation Results

### Inversion from a Numerical Reflection Coefficient

As a first example, the reflection coefficient for the Icelandic model shown in Figure 2-8 is used as input data to Merab's method. The reflection coefficient as a function of the vertical wavenumber is shown in Figure 2-29 after the density discontinuity compensation of eq.(2.31). The coefficient was computed at the Icelandic Basin Experiment frequency, 220 Hz, and at 50 Hz, for comparison of the recovered profiles. Only the region  $0 \leq k_z \leq k_0$  is shown and is used for the inversion in order to illustrate the smoothing effect of the truncation to real angles of incidence.

The inverted profiles are shown in Figure 2-30. The 220 Hz result tracks the gradient better than the 50 Hz. The numerical solution of the Gelfand-Levitan integral equation

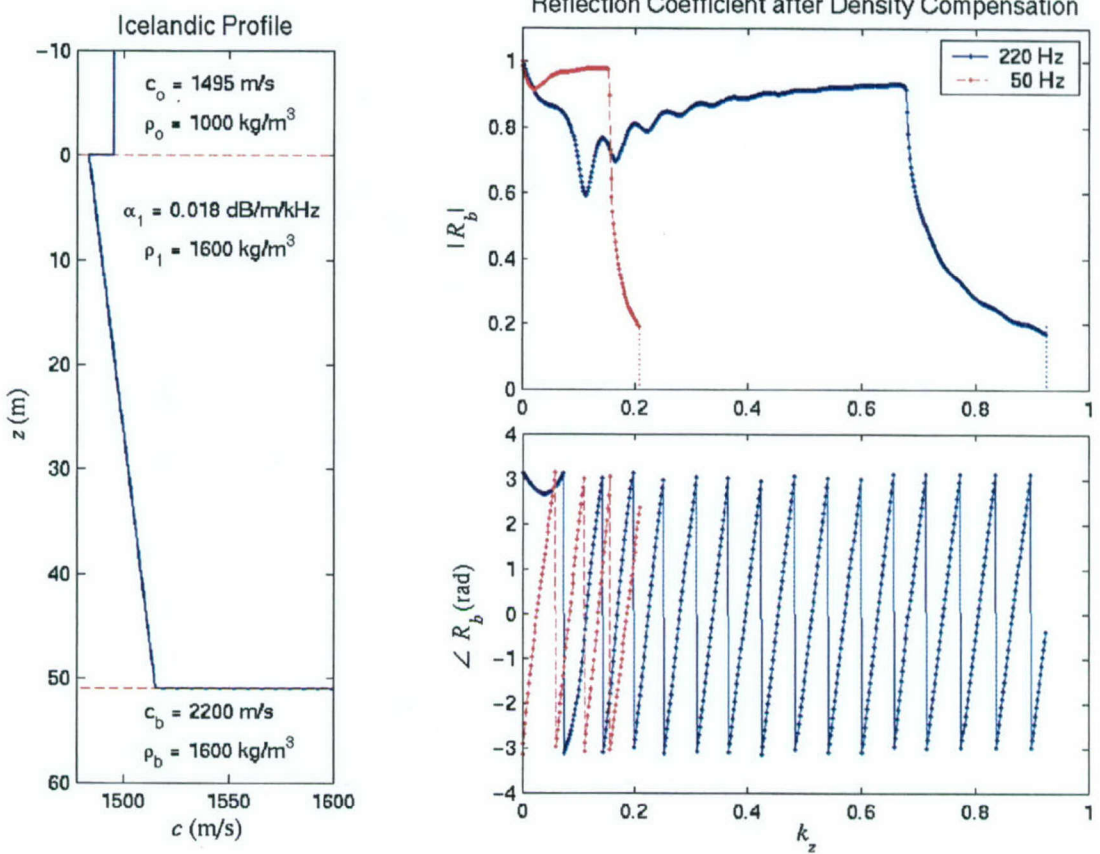


Figure 2-29: Icelandic model (from Figure 2-6) and reflection coefficient at two frequencies, after compensation for the density discontinuity at the seabed interface. The vertical wavenumber  $k_z$  is shown in rad/m.

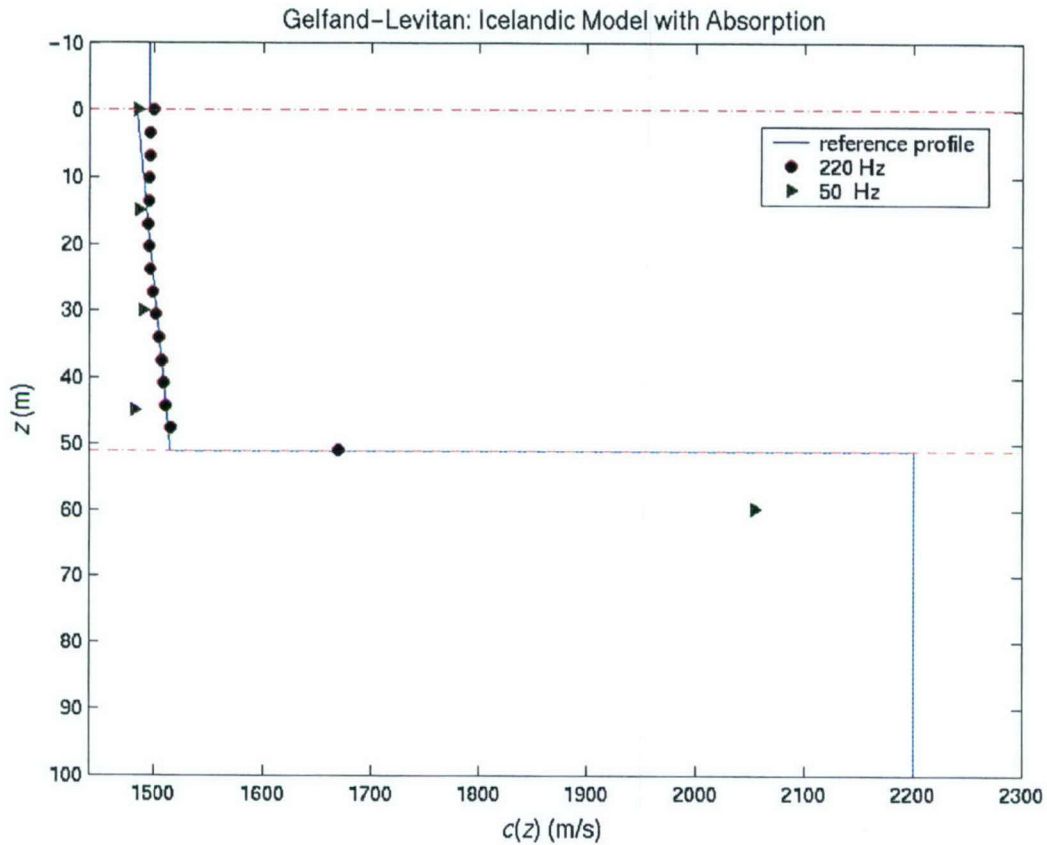


Figure 2-30: Profiles inverted from the Icelandic model numerical reflection coefficients.

becomes unstable below a certain depth, about 50 m for 220 Hz and 75 m for 50 Hz, but both profiles show an abrupt increase of the sound velocity near  $z = 51$  m.

A closer view of the sediment region  $0 \leq z \leq 51$  m is shown in Figure 2-30. The effect of the trapped mode neglected in the 220 Hz inversion is a degradation of the recovered profile near the minimum at the interface. The smoothing effect of the truncation in  $k_z$  is clearly shown. At 50 Hz no trapped mode is excited (cutoff is 112 Hz for this environment) and the inverted sound velocity at  $z = 0$  is below that of the water, close to the actual value. This result suggests that, in the absence of trapped modes, the velocity minimum is recovered.

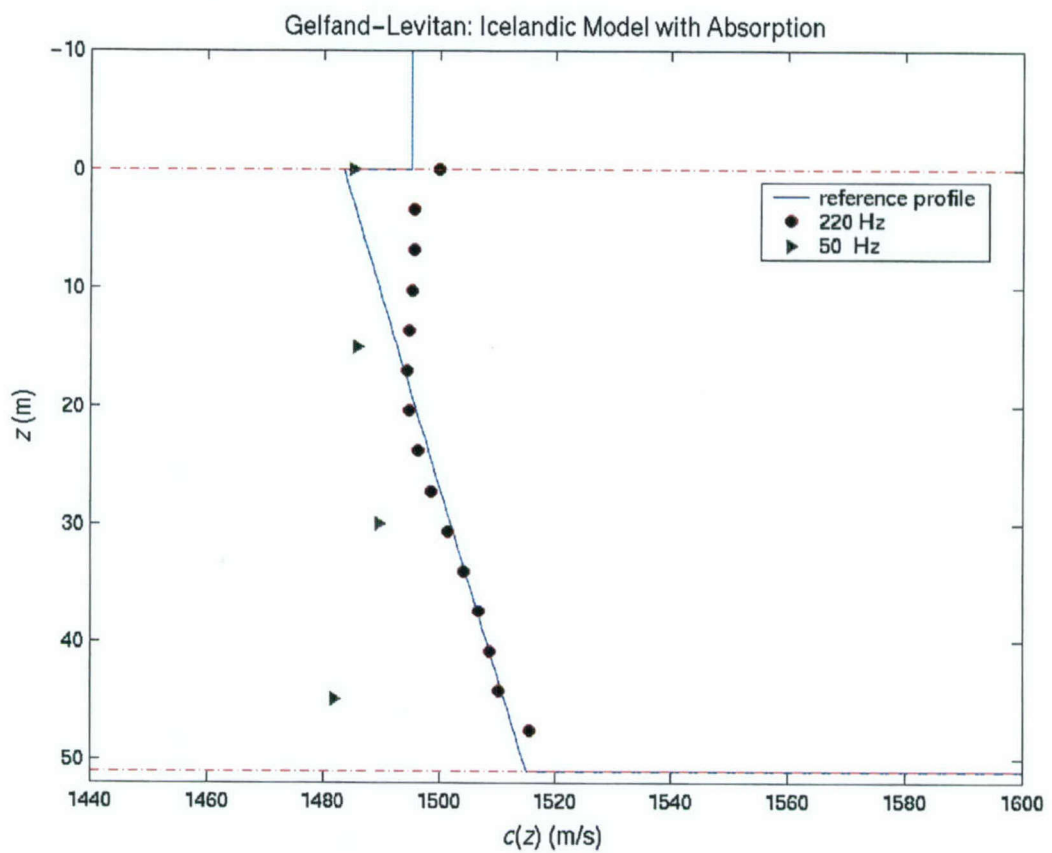


Figure 2-31: Profiles inverted from the Icelandic model numerical reflection coefficients. Zoom in the sediment.

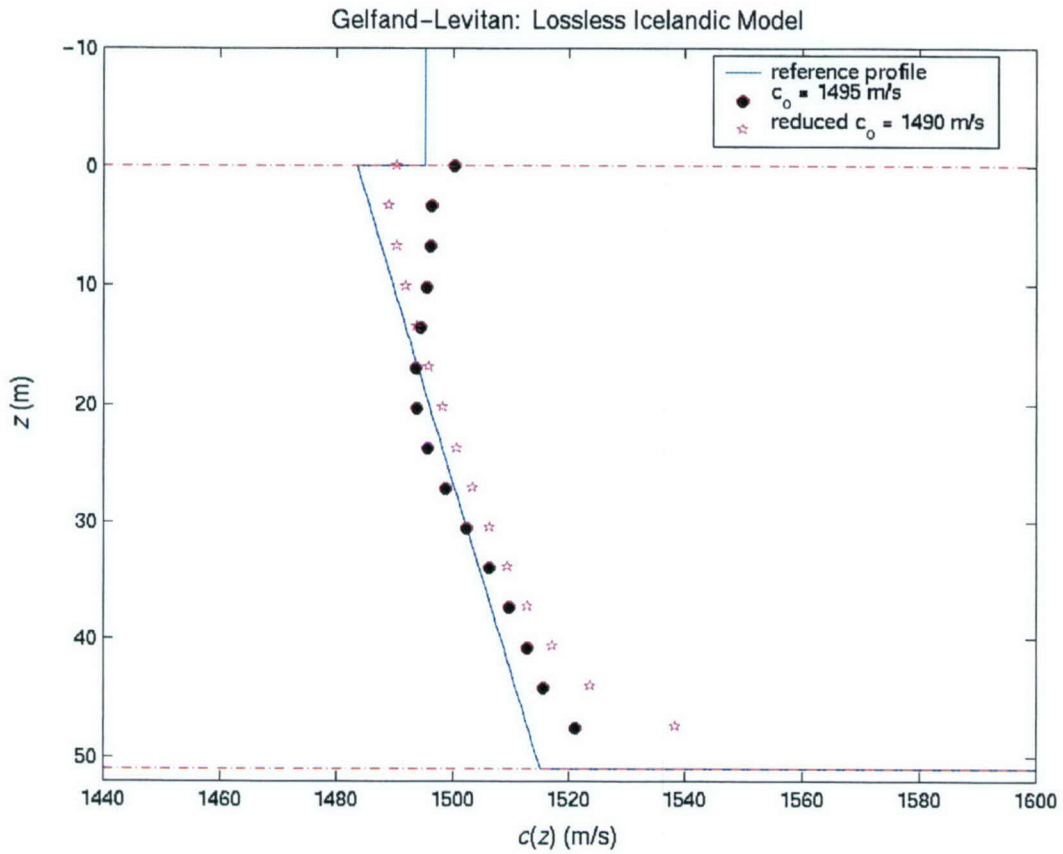


Figure 2-32: Profiles inverted from the Icelandic model numerical reflection coefficient at 220 Hz. By reducing the water sound velocity to 1490 m/s, the modified reflection coefficient inversion gives an indication of a sound velocity minimum near the interface[68, 24].

As discussed in connection with eq.(2.40), trapped modes are not excited if the water sound velocity is, for the Icelandic model of Figure 2-29, below 1483.34 m/s. In order to verify the effect of a small reduction in the water sound speed, we used eqs.(2.41) and (2.42) with  $c'_o = 1490 \text{ m/s}$  to modify the “measured” reflection coefficient at 220 Hz.

The new inverted sound velocity is shown in Figure 2-32 together with the original inversion result. The inverted velocity at the water interface was reduced, which indicates the presence of trapped modes in the original data.

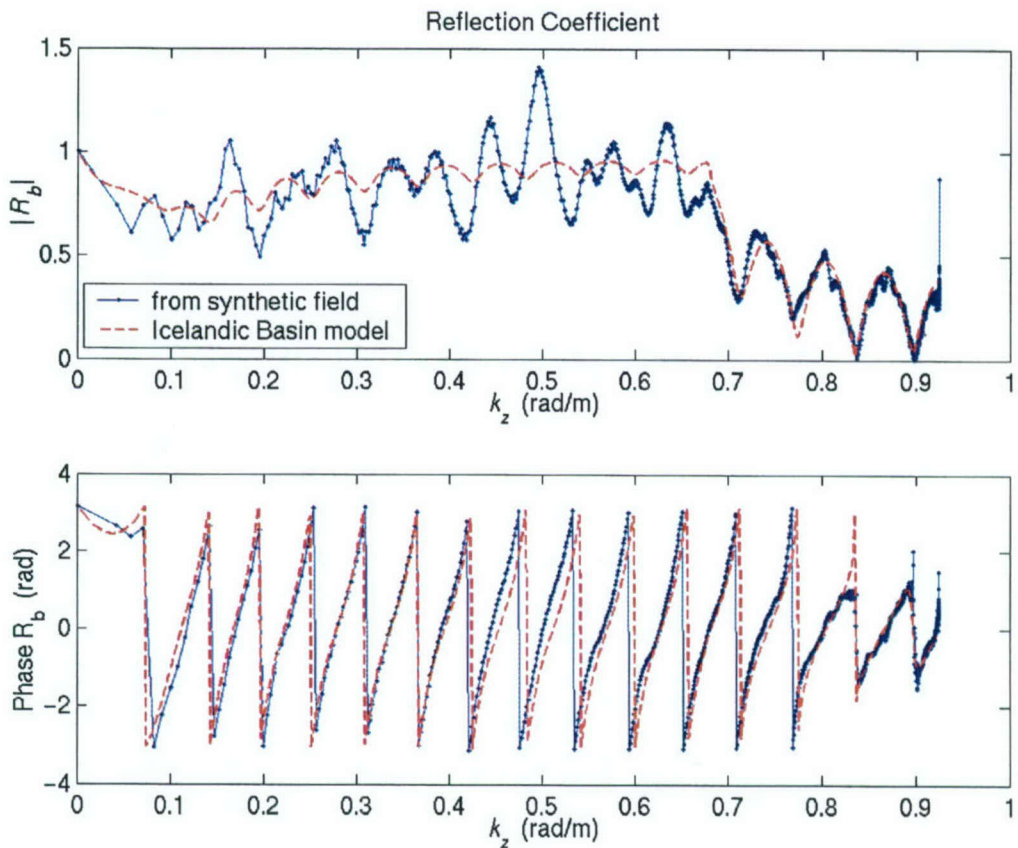


Figure 2-33: Reflection coefficient from the synthetic field from Figure 2-12 as a function of the vertical wavenumber  $k_z$ , before density discontinuity compensation (solid line). The dashed line shows the reference (numerical) reflection coefficient.

### Inversion from a Synthetic Pressure Field Data

As a second and more realistic example, the inversion is performed using the reflection coefficient, shown in the lower plot of Figure 2-12, "estimated" from the synthetic field that includes the effect of source height variations. In Figure 2-33,  $R_b$  is plotted as a function of the vertical wavenumber together with the numerical reflection coefficient used in Section 2.4.2.

As discussed in Section 2.3.2, source height variations manifest as high values ( $>1$ ) of the magnitude of the reflection coefficient in the critical incidence region. In addition

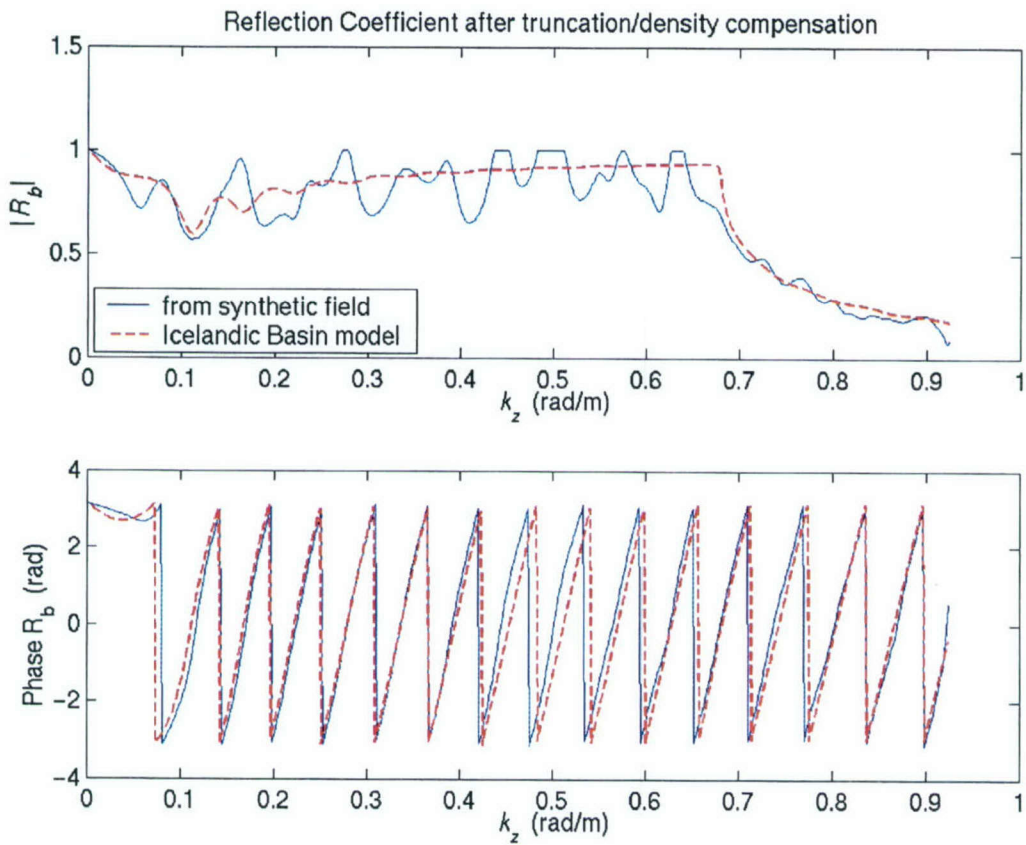


Figure 2-34: Reflection Coefficients of Figure 2-33 after density discontinuity compensation and magnitude truncation.

to the density discontinuity compensation, the magnitude of the reflection coefficient is hard-clipped to one prior to its use for inversion, as shown in Figure 2-34.

The inverted profile is shown in Figure 2-35. Compared to Figure 2-31, the errors introduced by the source height variations manifest as oscillations in the profile.

### 2.4.3 Inversion from the Icelandic Basin Data

The reflection coefficient estimated from the Icelandic Basin experiment data, shown in the lower plot of Figure 2-23, is used to recover the sound velocity profile. The resulting  $R_b$ , after density discontinuity compensation and magnitude hard-clipping to

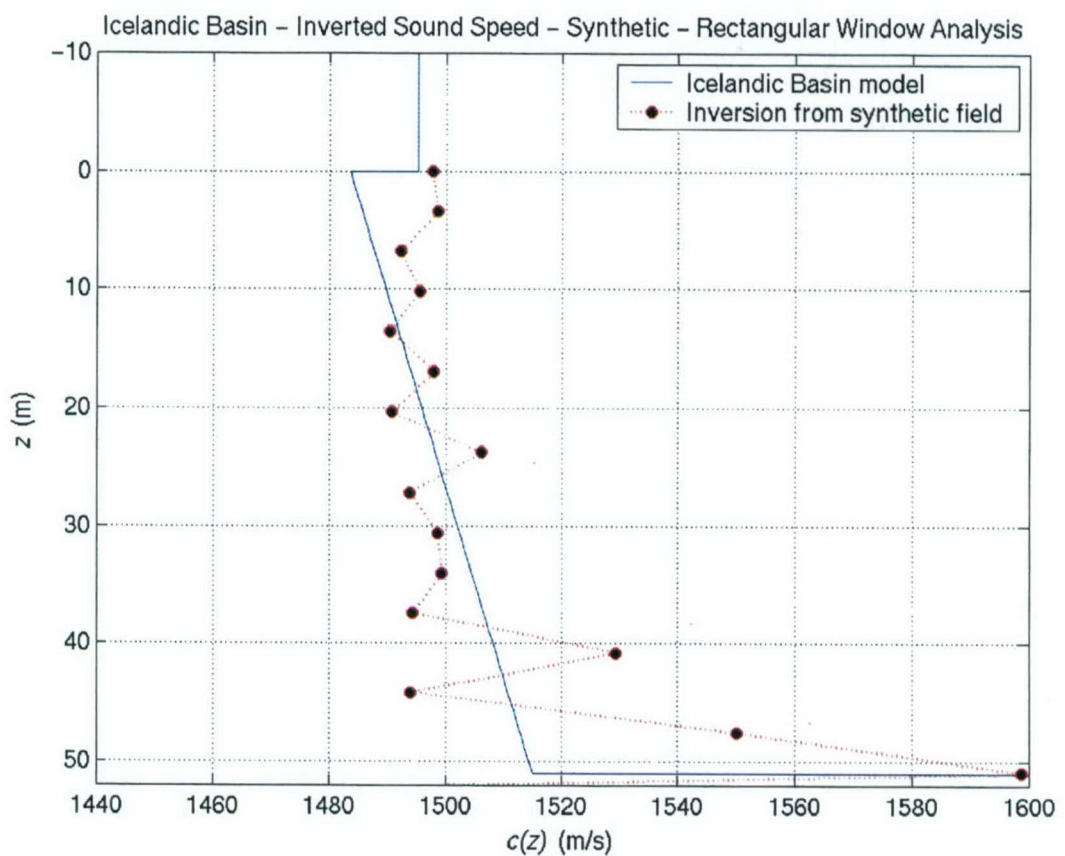


Figure 2-35: Inversion from the reflection coefficient from Figure 2-34, inferred from the synthetic field at 1.2m, which includes source height variations.

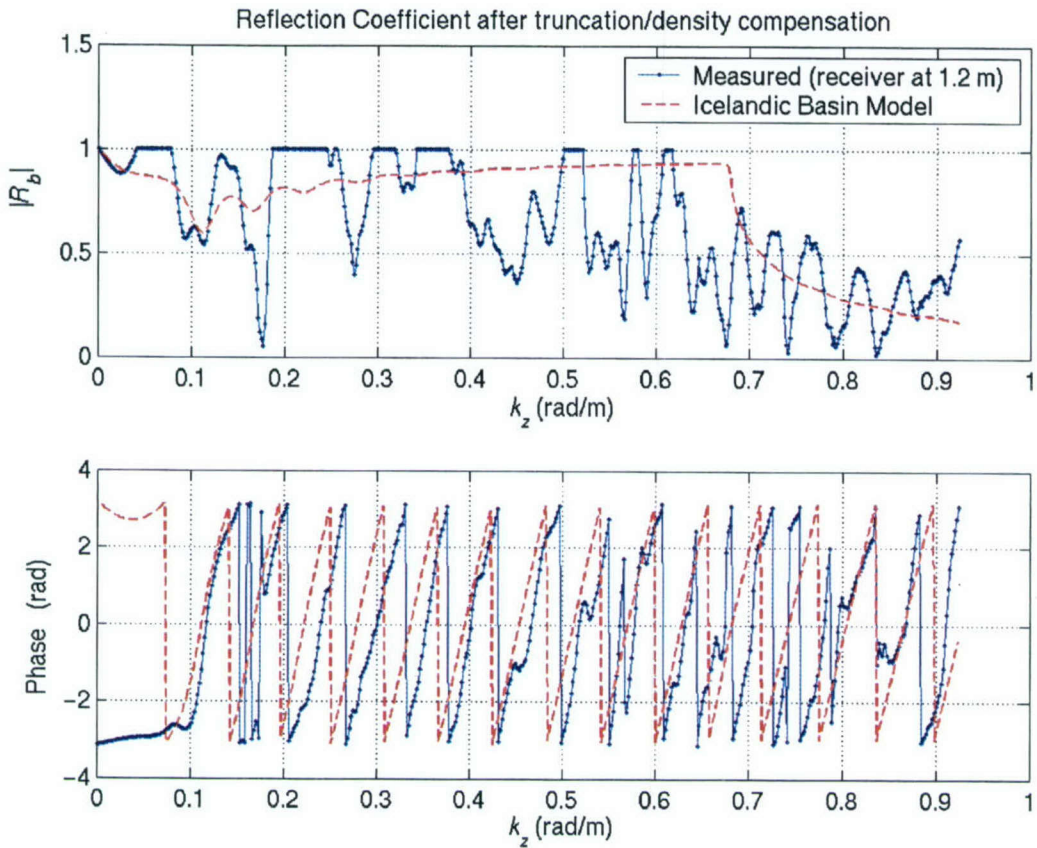


Figure 2-36: Experimental reflection coefficient (solid line) after compensation for density discontinuity and magnitude clipping. The Icelandic model reflection coefficient (dashed line) is shown for reference.

one is shown in Figure 2-36.

Contrasted to the synthetic case above, the effect of density compensation on the magnitude is small, suggesting that other environmental factors, such as additional density variations (discontinuous or not), could be at play.

The recovered profile is shown in Figure 2-37. The general behavior is similar to the synthetic case of Figure 2-35, suggesting similar error mechanisms: truncation of the reflection coefficient to real angles of incidence and source height variations, and a degradation of the integral equation solver result as depth increases.

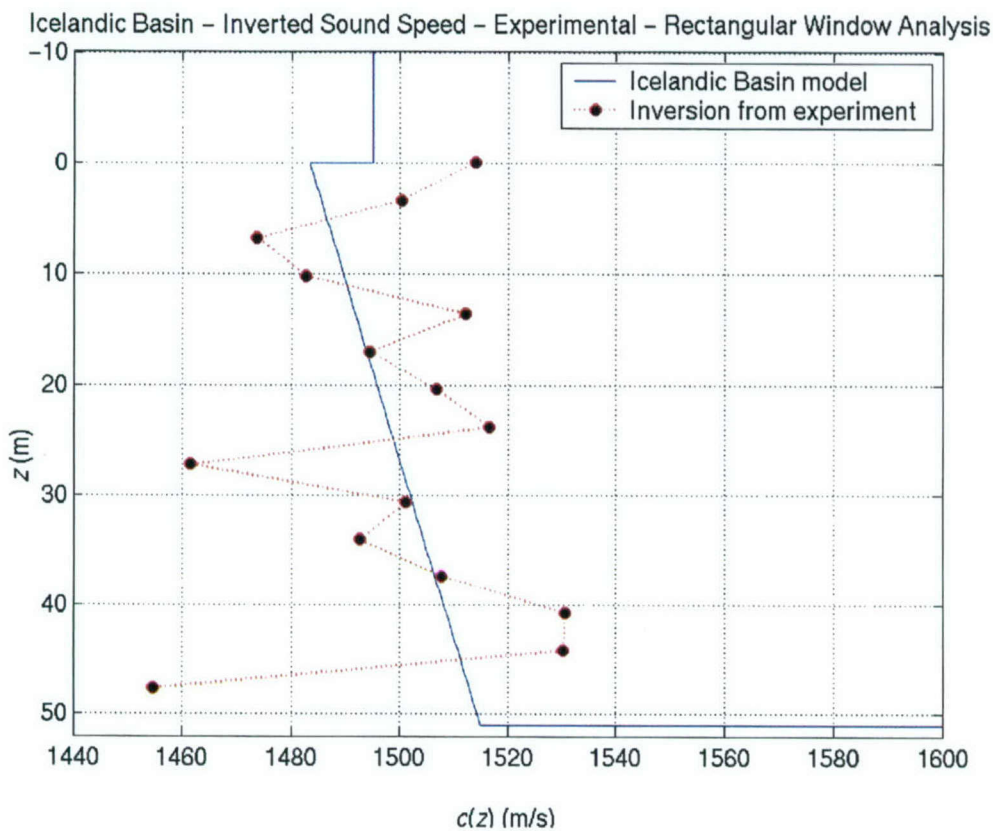


Figure 2-37: Profile recovered from the reflection coefficient of Figure 2-36, inferred from the Icelandic Basin experiment data at 1.2 m. The Icelandic model (dashed line) is included as a reference only and must not be interpreted as the "right answer".

There are additional sources of error in the experimental data analysis, such as the phase de-trend discussed in Section 2.3.3, and an apparently inaccurate density compensation or, equivalently, lack of a more detailed information about the density structure. The similarity with the synthetic, or even the fact that "reasonable" sound velocity values were estimated, is somehow surprising. In fact, as discussed in relation to eq.(2.6), the recovered profile is possibly contaminated by the density profile, and could only be expected to be recovered by a measurement in a second frequency.

## 2.5 Summary and Conclusions

### 2.5.1 Reflection Coefficient

Section 2.3 analyzes the Icelandic Basin pressure data. We investigated the application of the technique developed by Frisk and co-workers [22, 46] for the measurement of the reflection coefficient to experimental data. We generated simulated fields in order to assess the influence of the experimentally observed source height variations on the technique and lack of data at close range.

We showed that the residual pressure, essentially a normalization of the pressure field by the direct field component, had characteristics that could be explored for the analysis of experimental data. We used the residual pressure to identify and compensate for errors in the experimental data.

We observed that the simulated field had residual phase and magnitude variations similar to the one observed in the experimental data, which were compensated by migrating the synthetic field to a constant depth by changing the direct field. The effect of source height variations was observed mainly as fluctuations on the magnitude of the inferred reflection coefficient in the total reflection region.

The synthetic results indicate that the adopted migration process does not entirely compensate for the source height variations. Even without the phase error observed in

the actual data, the reflection coefficient obtained from the synthetic field (as opposed to the ideal field) has magnitude larger than 1 for some angles of incidence. The wrong (non-physical) relation between the direct and bottom reflected fields (caused by the migration) reflects itself as this non-physical value of the coefficient. Nevertheless, the general characteristics of the model reflection coefficient used to compute the synthetic fields, such as critical angle of incidence and behavior of the phase with  $k_r$ , are recovered in the inferred reflection coefficients.

We showed that even after migration, the experimental field residual phase still had variations not compatible with the physical model, as indicated by comparing residual phase and magnitude fluctuations. By estimating the phase trend and removing it through a polynomial fit, we obtained a signal with compatible magnitude and phase variations. In this process, we also identified apparent errors in one receiver calibration factor. We proposed a modification of the basic methodology to take into account source height variations and phase de-trend.

Errors in the experimental reflection coefficients are qualitatively similar to the errors observed (and explained) for the synthetic case. This suggests a similar error mechanism, the source height variations with range. It also suggests that the de-trend procedure, based on the analysis of the residual pressure, is a valid technique.

Phase error compensation (de-trend) and smoothing schemes are not unique and influence, to some degree, the results. The large fluctuations of the experimental reflection coefficient magnitudes and the behavior of its phase (as compared to the synthetic results) may result from imperfect phase de-trend associated with the simple range-independent, fluid bottom model.

We tested the sensitivity of the method to slight different analysis approaches. We inferred the reflection coefficient using two smoothing and extrapolation schemes. The results were mixed. The estimate from the receiver close to the bottom improved, as observed by a better defined critical angle. The change in the estimate using the upper receiver data was marginal.

## 2.5.2 Sound Velocity Profile Inversion

We extended Merab's method to deal with a density discontinuity at the water-seabed interface, becoming more suitable to ocean environments. The criterion for trapped modes was corrected for the case of reflection at the water interface, and a method for checking for velocity minima after the inversion was tested.

We corrected the expression for the modal cutoff frequency when the seabed sound velocity minima occurs at the water interface and verified that Merab's expression is valid for modes that do not interact with the water interface.

We inverted for the sound velocity profile in the seabed using a reflection coefficient inferred from experimental data (Figure 2-37), a result not previously available.

We showed, by simulation, that the effect of source height variations on the estimation of the reflection coefficient is to introduce oscillations in the inverted profile, as long as the magnitude of the reflection coefficient is clipped at one.

When inverting for experimental data, the density discontinuity compensation had little effect on the reflection data, suggesting that the density of the seabed is not constant. Measurements at more than one frequency, as suggested in [45], could be used to test this hypothesis, if the density profile in the seabed is sufficiently smooth.

The recovered sound velocity profile has characteristics similar to the synthetic case, suggesting similar error mechanisms, in addition to the possible density variations in the experiment site.

Merab's method reveals some of the advantages and restrictions of methods based in exact theories. The requirements for uniqueness are well established, in the present case, the reflection coefficient must be given on the half-line  $0 \leq k_z \leq \infty$ , and the poles in the upper  $k_z$  complex plane must be known (position and residue). Such requirement on the input data is not realistic, in the sense that input data is measured only in a limited finite region, and no information regarding the poles could be extracted from the available data. The effects of truncating the domain to  $0 \leq k_z \leq k_0$  and of neglecting the trapped modes are, nevertheless, well understood. Another issue is the effect of

measurement noise, not usually included in such theories.

This is a one dimensional theory, which requires that the environment be well approximated by a range-independent model. The plane-wave reflection coefficient measurement technique of Section 2.3 requires measurement in a reasonably large aperture where the properties of the environment are assumed constant, and therefore, is restricted to reasonably range independent environments.

Application to coastal, shallow-water environments presents two major difficulties. First, the assumption of range independence over large apertures is usually not valid. Spatial variations in the seabed structure and bathymetry, and temporal variations in the water column induced by currents and internal waves, in particular tides and tide-induced solitary waves, are the norm in such environments.

Second, the low-frequency acoustic field is usually dominated by normal modes, and the continuous wavenumber spectrum, such as the one represented by the Green's functions of Section 2.3, is small compared to the discrete, modal spectral lines.

In practice, even if the range independence assumption is valid, estimating the reflection coefficient at wavenumbers different from the modes in such conditions is, to put it mildly, challenging.

Exact methods in shallow-water based on measurements of the continuous spectrum of the field may be feasible if, first, no modes are excited (requiring a sufficiently low frequency in typical coastal environments), and second, the data can be acquired in small regions in order to be considered representative of *local* properties. In fact, by requiring that no mode be excited, the field may fall-off fast enough with range to be considered representative of the local environment. Stickler[70] has proposed a method for shallow-water whose requirement is that no mode be excited.

# Chapter 3

## Range-Dependent Modal Eigenvalue Sequential Estimation

### 3.1 Introduction

This chapter investigates the high-resolution estimation of range-dependent modal eigenvalues. It extends the technique described by Becker and Frisk[7] and Becker, Rajan, and Frisk[5], which uses a sliding-window, autoregressive (AR) spectral estimator. The use of AR techniques is an improvement over the short-time Fourier transform proposed by Ohta and Frisk[54], which requires large range apertures to resolve low order modes, resulting in poor tracking of modal evolution in range.

When the environment changes rapidly with range, for example due to a sudden change in the seabed type, the assumption, implicit in these techniques, of constant modal content over a range analysis window is not valid, and the spectra degrade significantly.

We propose the use of sequential AR estimation, where the properties are allowed to change on a sample-by-sample basis, associated with competitive smoothing, which combines estimates generated by different estimators and results in improved spatial tracking characteristics. Synthetic and experimental data results are presented.

Section 3.1 reviews the normal mode representation of acoustic fields in shallow water and the estimation of modal eigenvalues. Section 3.1.3 describes the modal mapping experiments (MOMAX), which provide the data to be analyzed. Appendix A discusses the issue of acoustic data analysis in MOMAX.

In Section 3.2 we raise the issue of the validity of modeling a sum of modes as an AR process and investigate the errors associated with the use of the AR techniques in estimating range-varying eigenvalues. The theory of the exact representation of a sum of time-varying real sinusoids introduced by Kayhan [38] is reviewed, and we derive the analogous model for complex exponentials. A detailed derivation is given in Appendix B.

Section 3.3 presents two sequential estimator implementations, based on the Kalman filter[2, 51] and an adaptive filter[48]. One of our motivations for this work was the need to improve the estimation of eigenvalues when the environment changes abruptly. For this purpose, we apply a technique developed by Niedźwiecki, the competitive smoother[49], which improves the tracking characteristics of the estimators. In Appendices C and D we discuss the design of the adaptive filter of Section 3.3 and a second order Kalman filter.

In Section 3.3 we investigate, in addition, the application of signal decimation prior to the eigenvalue estimation. Decimation allows for a reduction on the size of the AR model, while maintaining or improving the tracking characteristics of AR estimators. Smaller model size also results in reduced computational load. Ultimately, the discussion is about the selection of a suitable range sampling interval ( $\Delta r$ ) for the pressure signal.

In Section 3.4 we present and discuss estimation results from numerical and experimental data. In particular, we show the improvement in the measurement of eigenvalues that change abruptly.

### 3.1.1 The Shallow Water Acoustic Channel

Consider the propagation of a time-harmonic wave of frequency  $\omega$  in the waveguide shown in Figure 3-1. As a first approximation the medium is considered horizontally stratified, i.e., the acoustic parameters of interest<sup>1</sup>, namely, the sound speed  $c$  and density  $\rho$ , can be considered a function of depth only. The sea surface is modeled as a plane pressure-release boundary, and the basement (last layer in the seabed) as a plane boundary characterized by the normal acoustic impedance  $\xi$  or, equivalently, the reflection coefficient  $R_b$ , functions of the sound speed and density of the seabed.

Under these assumptions, the pressure field at a depth  $z$  and range  $r$  from a point source localized at a depth  $z_o$  is given by the Hankel transform[19]<sup>2</sup>

$$\begin{aligned} p(r, z; z_o) &= \int_0^\infty g(k_r, z; z_o) J_o(k_r r) k_r dk_r, \\ &= \frac{1}{2} \int_{-\infty}^\infty g(k_r, z; z_o) H_o^{(1)}(k_r r) k_r dk_r, \end{aligned} \quad (3.1)$$

where the depth-dependent Green's function  $g$  is the solution of the boundary value problem (BVP),

$$\left[ \rho \frac{\partial}{\partial z} \frac{1}{\rho} \frac{\partial}{\partial z} + (k^2 - k_r^2) \right] g(k_r, z; z_o) = -2\delta(z - z_o) \quad (3.2)$$

$$g = 0 \text{ at } z = 0, \quad (3.3)$$

$$g - \xi \frac{1}{i\omega\rho} \frac{\partial g}{\partial z} = 0 \text{ at } z = h, \quad (3.4)$$

where  $\rho = \rho(z)$  is assumed to be a smooth function of depth,  $k(z) = \omega/c(z)$ ,  $\xi = \xi(k_r)$ , and  $h$  is the depth of the basement.

If the basement is included in the problem domain, the radiation condition is applied at  $z = \infty$ , which imposes, for the waveguide in Figure 3-1, a decaying exponential

---

<sup>1</sup>The absorption coefficient  $\alpha$  will be ignored in this discussion.

<sup>2</sup>A time dependence  $e^{-i\omega t}$  is assumed for the pressure field.

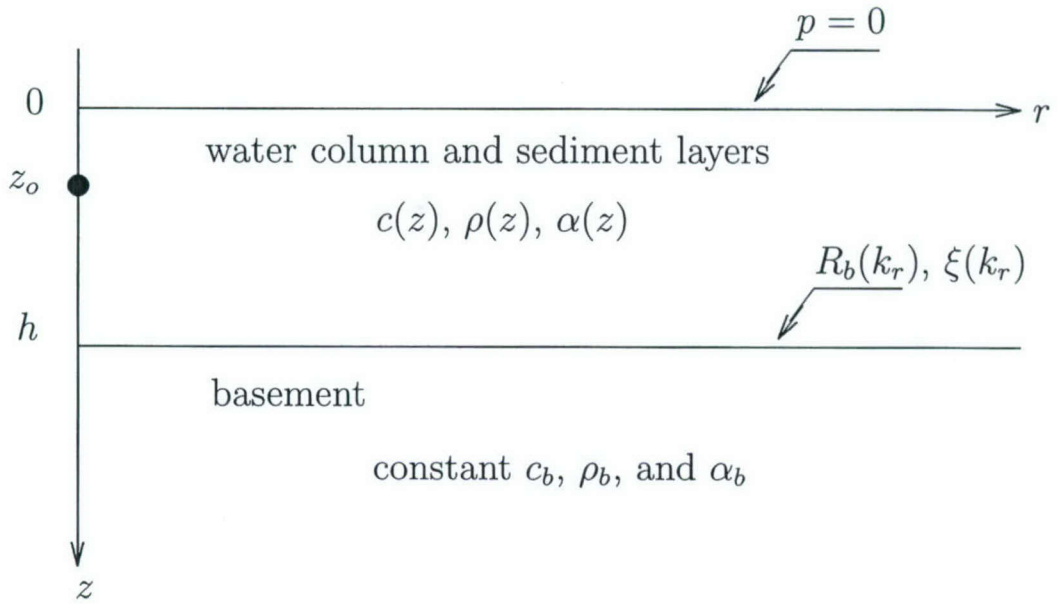


Figure 3-1: The shallow water acoustic channel.

solution in the basement,  $g \sim \exp\{-\gamma_\infty z\}$ ,  $z > h$ , where  $\gamma_\infty = \sqrt{k_r^2 - (\omega/c_\infty)^2} > 0$ . Such condition can also be described as total reflection at the basement interface, i.e., by the reflection coefficient  $R_b(k_r) = \exp\{i\phi\}$ , where

$$\phi(k_r) = -2 \tan^{-1} \left[ \frac{\rho(h^-)}{\rho_\infty} \frac{\gamma_\infty}{\sqrt{[\omega/c(h^-)]^2 - k_r^2}} \right],$$

or yet, by the normal impedance  $\xi(k_r) = -i\omega\rho_\infty/\gamma_\infty$ . Equation (3.1) and the BVP (3.2) to (3.4) are valid in the presence of density discontinuities, as long as boundary conditions of continuity of  $g$  and  $(1/\rho)dg/dz$  are imposed at the depth of the discontinuities.

Under typical conditions of interest in shallow-water acoustics, the pressure field can be modeled by the normal mode sum arising from the contributions of the poles of the Green's function in the integral in eq.(3.1), which at long ranges assumes the form

$$p(r, z; z_o) = \frac{e^{i\pi/4}}{\rho(z_o)} \sqrt{\frac{2\pi}{r}} \sum_{n=1}^N u_n^*(z_0) u_n(z) \frac{e^{ik_{rn}r}}{\sqrt{k_{rn}}}. \quad (3.5)$$

In eq.(3.5),  $u_n$  is the  $n$ -th eigenfunction corresponding to the characteristic wavenumber  $k_{rn}$  of the problem described by eqs.(3.2) to (3.4), and  $N$  is the number of real characteristic wavenumbers (or propagating modes). Contributions from branch line integrals (that is, from the continuous spectrum of the BVP system), which decay rapidly with distance, are neglected in eq.(3.5).

The mode functions  $u_n(z)$  and the associated eigenvalues<sup>3</sup>  $k_{rn}$  can also be obtained as solutions of the Sturm-Liouville problem

$$\left[ -\rho(z) \frac{d}{dz} \frac{1}{\rho(z)} \frac{d}{dz} - k^2(z) \right] u_n(z) = -k_{rn}^2 u_n(z), \quad (3.6)$$

$$u_n = 0 \text{ at } z = 0, \quad (3.7)$$

$$u_n - \xi(k_{rn}) \frac{1}{i\omega\rho} \frac{\partial u_n}{\partial z} = 0 \text{ at } z = h, \quad (3.8)$$

and both  $u_n$  and  $u'_n/\rho$  are continuous across the domain.

If the environmental parameters (depth, sound speed, density) change with range, eq.(3.5) can be still be considered, with slight modifications, a good approximation to the field. The adiabatic approximation, valid for a slowly range-dependent environment, is obtained by replacing the phase term by the integral  $\int k_n(r) dr$  and including range as a parameter of the eigenfunctions:

$$p(r, z; z_o) = \frac{e^{i\pi/4}}{\rho(0, z_o)} \sqrt{\frac{2\pi}{r}} \sum_{n=1}^N u_n^*(0, z_0) u_n(r, z) \frac{e^{i \int^r k_{rn}(r') dr'}}{\sqrt{k_{rn}}}. \quad (3.9)$$

Under the adiabatic approximation, the eigenvalues and eigenfunctions at each range  $r$  are still obtained from the BVP in eqs.(3.2) to (3.4), where, now,  $r$  is considered a parameter of the Green's function  $g$ , and  $c = c(r, z)$ ,  $\rho = \rho(r, z)$ ,  $h = h(r)$ , and  $\xi = \xi(k_{rn}, r)$ .

---

<sup>3</sup>The modal characteristic wavenumbers  $k_{rn}$  will be referred to as the eigenvalues, although, strictly, the eigenvalues associated with eq.(3.6) are  $\lambda_n = -k_{rn}^2$ .

### 3.1.2 Eigenvalue Estimation

In the adiabatic approximation, eq.(3.6) is solved at each range step, and its solution depends on the local characteristics of the water and seabed. The eigenfunctions and eigenvalues adapt to the local properties of the environment. For slow range variations, the change in pressure is dominated by the modal phases  $\exp\{i \int^r k_{rn}(r') dr'\}$ . Under these circumstances, the estimation of the local eigenvalues is analogous to the estimation of the instantaneous frequency of a multicomponent signal in time series analysis.

In range independent environments, the Green's function  $g$  is obtained from the pressure by the inverse operation of eq.(3.1). For large distances, the inverse transform reduces to

$$g(k_r, z; z_o) = \frac{e^{i\pi/4}}{\sqrt{2\pi k_r}} \int_{-\infty}^{\infty} p(r, z; z_o) \sqrt{r} e^{-ik_r r} dr, \quad (3.10)$$

which shows the Fourier transform  $\mathcal{F}$  relation between the pressure and the Green's function,

$$g\sqrt{k_r} \xleftrightarrow{\mathcal{F}} e^{i\pi/4} p\sqrt{r}. \quad (3.11)$$

Along the real  $k_r$  line, the magnitude of  $g(k_r)$  has peaks (spectral lines) corresponding to the eigenvalues associated with the propagating modes. Therefore, an estimate of the propagating mode eigenvalues is given by the position of the peaks in the magnitude of the Fourier transformed pressure field (multiplied by  $\sqrt{r}$ ).

In actual experiments, the pressure is measured over finite apertures, say  $r \in [R_1, R_2]$ . An estimate of the Green's function is obtained by performing the integral of eq.(3.10) over the available interval. Using the normal mode representation of eq.(3.5), the estimate of  $g$  is

$$\begin{aligned} \hat{g}(k_r, z; z_o) &= \frac{i}{\rho(z_o) \sqrt{k_r}} \sum_{n=1}^N \frac{u_n^*(z_0) u_n(z)}{\sqrt{k_{rn}}} \int_{R_1}^{R_2} e^{-i(k_r - k_{rn})r} dr, \\ &\approx \frac{i\Delta R}{\rho(z_o) \sqrt{k_r}} \sum_{n=1}^N \frac{u_n^*(z_0) u_n(z)}{\sqrt{k_{rn}}} e^{-i0.5(k_r - k_{rn})(R_1 + R_2)} \text{Sa}[0.5(k_r - k_{rn})\Delta R], \end{aligned} \quad (3.12)$$

where  $\Delta R = R_2 - R_1$  is the range aperture and  $\text{Sa}(x) = \sin x/x$  is the sampling function. For sufficiently separate eigenvalues, the sampling function main lobes do not overlap and  $|\hat{g}|$  exhibits peaks at the eigenvalue positions,  $k_r = k_{rn}$ . The peak positions are estimates of the eigenvalues.

The issues associated with these estimates are the same found in spectral estimation. For example, windows can be used to reduce the sidelobe level[30] at the cost of poorer resolution. Figure 3-2 shows estimates of  $|\hat{g}|$  for actual experimental data using the rectangular window [as in eq.(3.12)] and the Hann (or hanning) window, given by

$$w(n) = 0.5(1 - \cos \frac{2\pi n}{N}), \quad n = 0, \dots, N - 1,$$

where, for an aperture  $R_1 \leq r \leq R_2$ , the signal is given on the discrete range points  $r_n = R_1 + n\Delta r$ , and  $\Delta R = N\Delta r$ .

For a range-dependent environment, the eigenvalues must be associated with distance. Ohta and Frisk[54] used the short-time Fourier transform (STFT), where the transform in eq.(3.10) is taken over a finite distance aperture  $(r, r + \Delta R)$ . By sliding the aperture (that is, by changing  $r$ ), a range-dependent wavenumber spectrum (spectrogram) is obtained and, again, the positions of the peaks are an estimate of the varying mode eigenvalues. The aperture  $\Delta R$  has to be short enough to localize variations of the eigenvalues, but long enough to allow close eigenvalues to be resolved, a classical trade-off issue in time-frequency analysis[11]. As in the range-independent case, windows are applied to improve the estimate. In order to resolve close eigenvalues using smaller apertures, [54] processes the signal prior to the transformation through mode filtering, in which modes are separated by using data from a vertical array installed in a known environment.

Figure 3-3 depicts the spectrogram for an experimental data set. This figure should be compared to Figure 3-2, where a single spectrum is computed for the full available range aperture. Notice that about 6 spectral lines can be observed in the spectrogram at

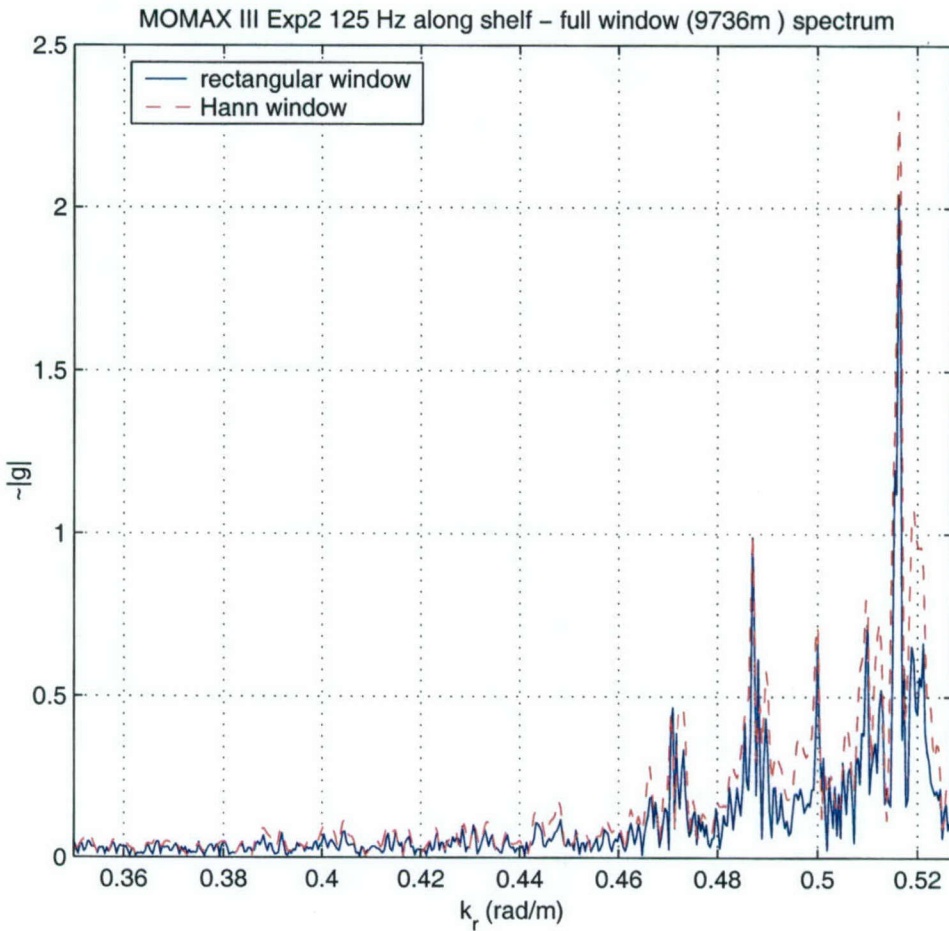


Figure 3-2: The wavenumber spectrum corresponding to the experimental data labeled *along shelf* in Figure 3-8. The vertical scale is arbitrary, only the position of the spectral lines are of interest. The spectra were computed using the full range aperture available (9736 m) using rectangular (solid line) and Hann (dashed line) windows of spectral analysis. The three peaks in the region  $0.46 < k_r < 0.5$  (the water wavenumber is roughly 0.53) are associated with the highest modes propagating to the receiver location. The highest peak is probably the first mode, and the others close to it are possibly changes in the mode due to variability of the environment near the moving source. By using a full aperture Fourier transform, the variability of the eigenvalues with range translates into a broadening of the peaks or the appearance of multiple peaks in the spectrum.

all ranges. Figure 3-2 has a larger number of spectral peaks, which may be an indication that some of the lines in Figure 3-2 are caused by variations of the modes with range, suggesting that the range-independent assumption is not valid.

For low-frequency, shallow-water propagation, the eigenvalues tend to concentrate near the wavenumber  $k_0 = \omega/c_0$ , where  $c_0$  is a representative sound speed in water. In order to resolve the closely spaced spectral lines, one must resort to large range apertures  $\Delta R$ . The rate at which the environment changes its properties imposes a maximum range aperture. These opposing requirements impose a limitation on the use of the STFT technique.

An improvement of the resolution and spatial tracking characteristics is obtained by using a high resolution method instead of the Fourier transform in the computation of the spectrogram. Becker[6] (see also Becker and Frisk[7]) proposed the use of autoregressive (AR) spectrum estimators. Figure 3-4 compares the two spectrograms (STFT with Hann window—cf. Figure 3-3—and AR) for the same experimental data of the previous figures<sup>4</sup>. Despite the improvement of the AR method, the sliding window approach still assumes that the eigenvalues do not change inside each analysis window. Systematic changes and abrupt variations degrade the performance of the estimator as represented by bias or a smearing of the spectra lines to the point where they disappear. The next logical development, suggested in [6], is to incorporate the variability of the eigenvalues into the spectral estimator. Candidate techniques are the available time-frequency analysis tools [11], including time-varying AR estimators [64].

In Section 3.2 we discuss the issue of validity of the AR model for the representation of range-varying modal sums and estimate the errors introduced by associating the zeros of the AR characteristic polynomial with the varying eigenvalues.

---

<sup>4</sup>Prior to the AR processing, the signal was filtered and decimated to an effective sampling range of 60 m. The effect of decimation is to spread the AR model poles, whose positions are related to the spectral peaks, around the unit circle in the complex plane. This way, it would be easier for the AR algorithm to resolve the peaks. For the case of a stationary process (constant spectrum), the improvement in resolution (or reduction in the required AR model order) by decimation is justified in Quirk[59].

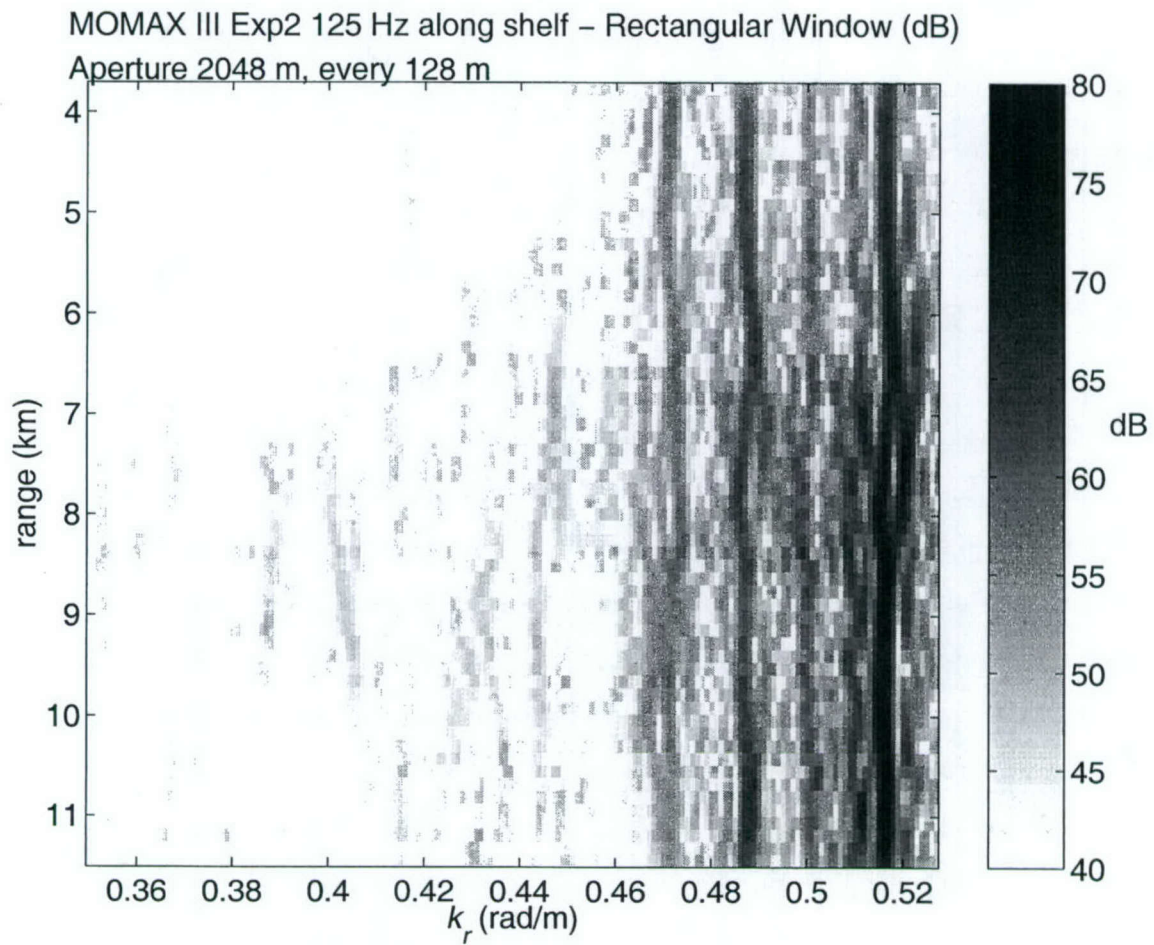


Figure 3-3: The wavenumber spectrum computed by sliding a 2048 m rectangular window along the 9736 m of available data. The gray scale in dB (arbitrary units) is shown in the bar on the right. Compare to Figure 3-2. The three peaks in the region  $0.46 < k_r < 0.5$  are still identifiable. However, in this analysis it is possible to observe the variability of the peaks with range. In the region near the first mode, it is possible to identify a strong peak just below  $k_r = 0.52$ , as before, and a weaker, but consistent peak below the strong one. The spatial resolution is not sufficient to observe in detail the behavior of these two lower modes with distance.

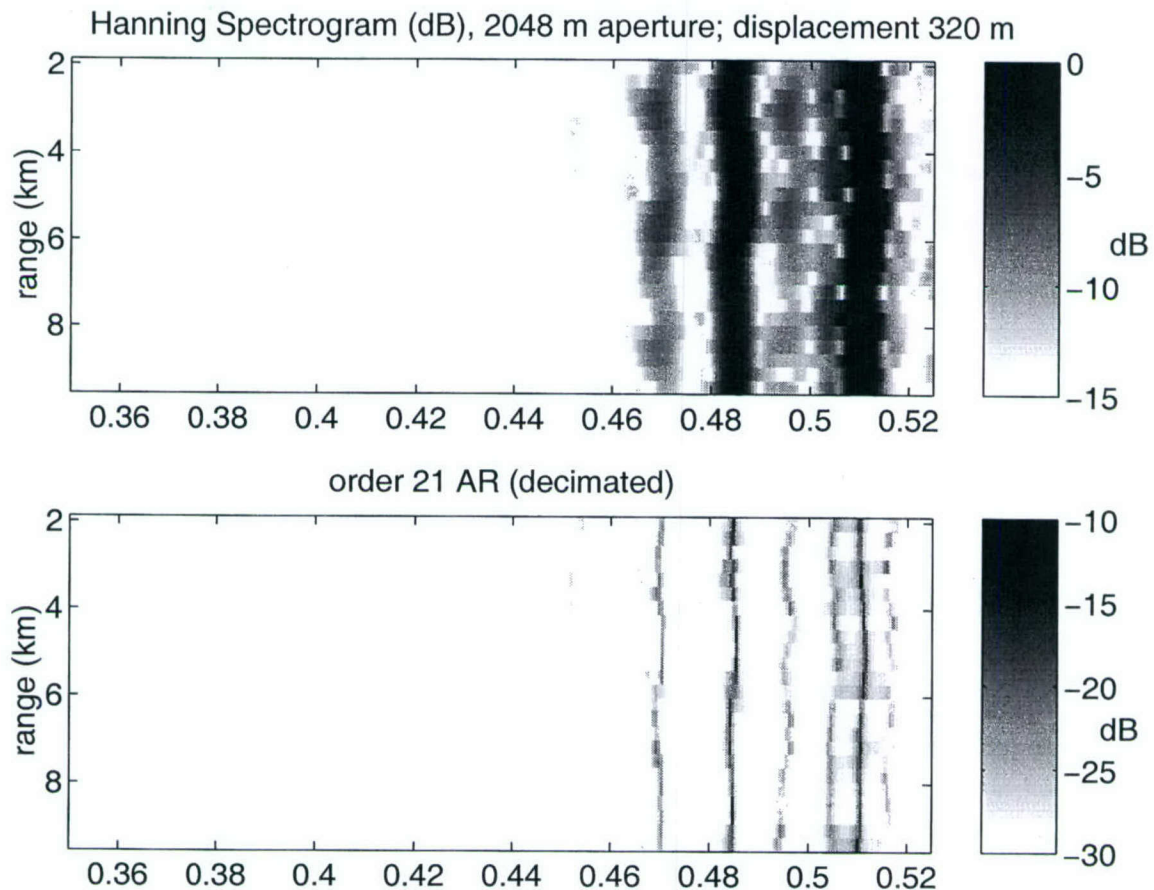


Figure 3-4: Wavenumber spectrogram. The upper plot is a spectrogram computed using Hann window periodograms. The horizontal axis is the wavenumber, the vertical axis is the source-receiver range along a track. The lower spectrogram was computed with the modified covariance AR method. Both were computed using a 2048 m aperture every 320 m over the available pressure data. The data, at 125 Hz, is from the MOMAX III / SWAT 2000 experiment. In order to reduce the order of the AR model, the acoustic data were filtered and decimated down to a range sample interval of 60 meters (see Section 3.3.5).

In Section 3.3 we extend the concept of the sliding window–AR approach to sequential estimation, where the AR parameters are updated at each range sample. The sliding window approach treats each set of samples independently. Sequential estimators take into account the effect of previous data when computing the AR parameters at a given range, which may lead to better resolution or better spatial tracking.

Another extension is the use of competition between the estimates obtained running a signal twice through an estimator forward and backward in range, as described by Niedźwiecki[51]. Competition improves spatial tracking and allows the localization of abrupt changes in eigenvalues. Competition among different pairs of forward–backward estimators tuned to different signal statistics allows the estimator to adapt to changing signal statistics. The design of individual estimators can, therefore, focus on the resolution aspect of the resolution/spatial tracking trade-off.

### 3.1.3 The Modal Mapping Experiment (MOMAX)

The acoustic data analyzed in this chapter were obtained during the Modal Mapping Experiments (MOMAX), in which a source emits a small number of pure tones in a shallow water environment[18, 14]. The typical experimental configuration is shown in Figure 3-5. A set of buoys equipped with a hydrophone, a GPS receiver and two radio-frequency links (for the acoustic signal and the GPS data) drift and, in doing so, form synthetic arrays that sample the acoustic field. The data collected consist of time series of GPS and acoustic signal from each buoy, all synchronized through the GPS clock.

During analysis, the GPS data are converted into  $(x, y)$  position and range  $r = \sqrt{x^2 + y^2}$  with respect to the source. The acoustic time series are demodulated generating a separate time series for each frequency corresponding to a modal sum. Appendix A describes in detail the MOMAX raw acoustic data processing. The position and acoustic time series are then merged, forming a signal that can be modeled as an adiabatic modal sum, eq.(3.9).

Three such experiments have been conducted, two in the East Coast STRATAFORM

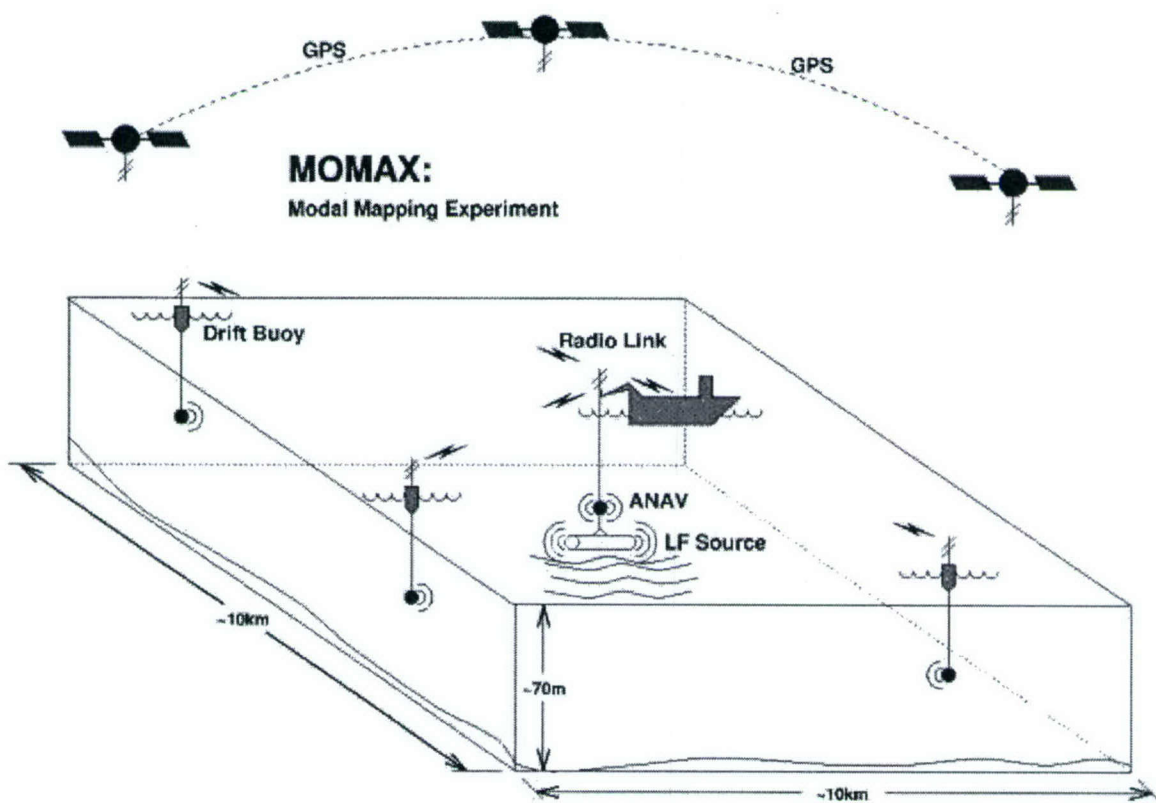


Figure 3-5: The typical MOMAX configuration. From reference [20].

site, and one in the Gulf of Mexico. Tracks from experiment 2 in MOMAX III are shown in Figure 3-6. The source was towed at 2m/s, while a single buoy drifted at speeds between 0.25 m/s and zero. In the SE track and in the NE direction of the NE track the source transmitted a 125 Hz tone (between the points labeled (05:00 and 08:00). During this period, the receiving buoy drifted in the general NW direction (shown SW of the point S10).

Between 11:30 and 12:30, the source frequency was 50 Hz (NE track, in the SW direction) and the receiving buoy was nearly stationary at the position indicated by a triangle between the earlier buoy track and S10. The position of two temperature sensor strings (T strings) are also shown. The 125 Hz acoustic time series corresponding to the tracks in Figure 3-6 is shown in Figure 3-7. The corresponding pressure versus range signal is shown in Figure 3-8.

### 3.2 Difference Equation Representation of a Sum of Adiabatic Modes

The autoregressive methods assume that the signal is modeled by a recursive difference equation. Although the motivation for their use in eigenvalue estimation is their characteristic high resolution, there is a basic question of how accurately can a sum of range-varying modes (or, more generally, of complex exponentials with varying amplitudes and frequencies) be represented by such a model.

Kayhan[38] analyzed the related problem of representation of a sum of real chirp signals (sinusoids with varying frequencies and amplitudes) by a time-varying difference equation, after the works by Kamen, Khargonekar, and Poola[36], and Kamen[35, 34]. One of the main results of [38] is an exact formulation (in terms of an initial value problem) for the computation of instantaneous frequencies and amplitudes, given the time series of coefficients of the difference equation.

A similar formulation is developed in this section for the case of complex exponentials.

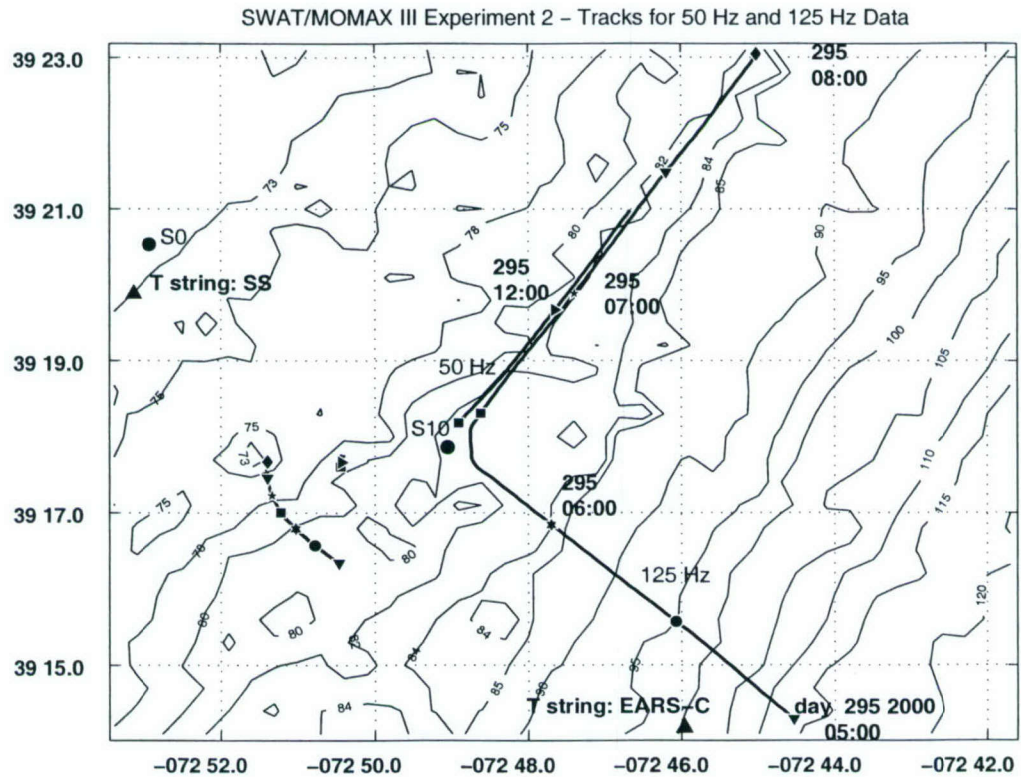


Figure 3-6: MOMAX III experiment 2, off the New Jersey Coast. Source and receiving buoy tracks. Latitude and longitude shown in degree-minutes (DD MM.M) notation and depth in meters. Along the source track (long SE and NE lines), some points are labeled with the UTC time of the year 2000 Julian day 295. Marks on the tracks are shown every 30 minutes. The buoy track is shown SW of the point labeled S10.

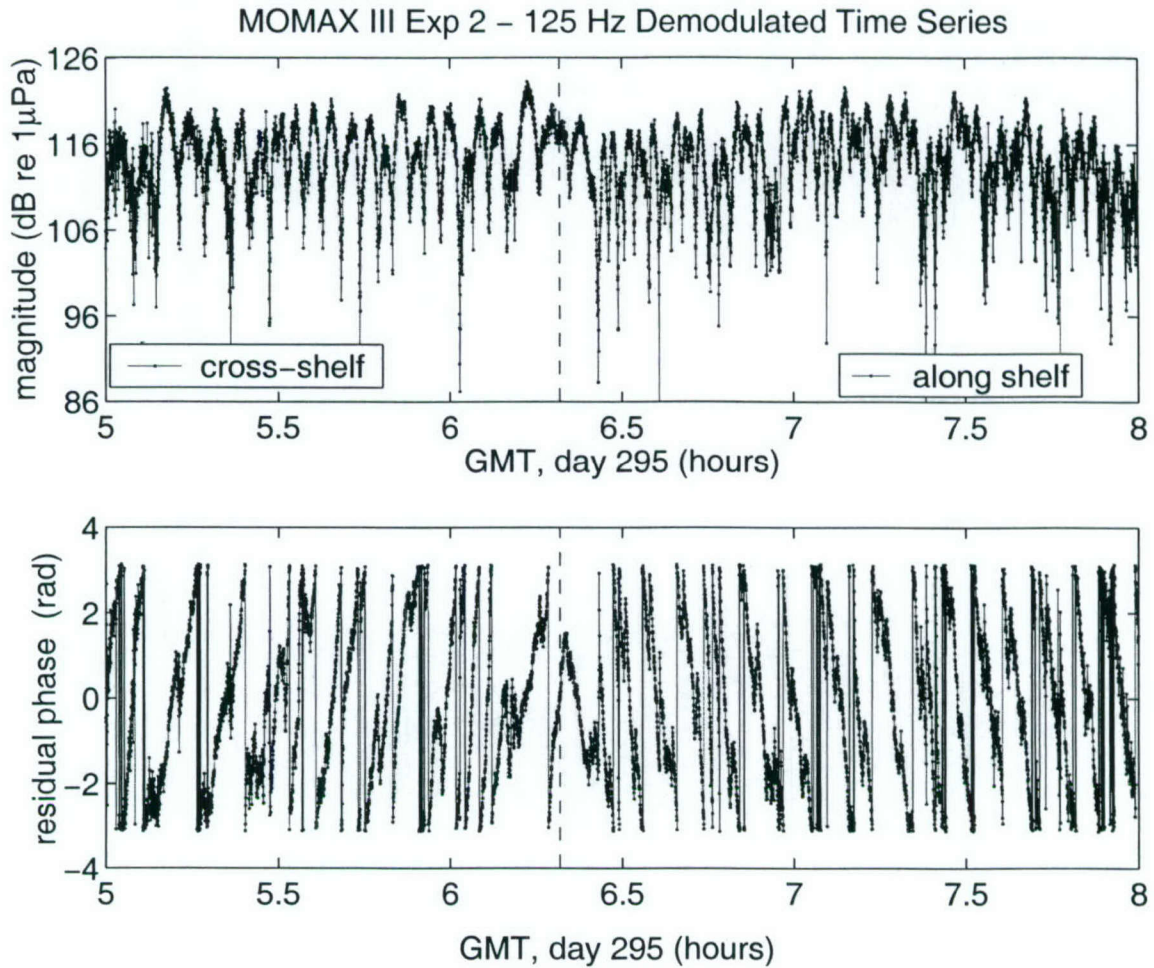


Figure 3-7: Magnitude and residual phase of the acoustic pressure time series corresponding to the tracks shown in Figure 3-6 at 125 Hz. The closest point of approach source-receiver is indicated by the vertical dashed line on both plots. *Cross-shelf* refers to the SE source track, while *along-shelf* refers to the NE track. The magnitude exhibits the interference pattern characteristic of multiple propagating modes, which are better depicted when the magnitude is plotted versus distance. The residual phase is obtained by multiplying the signal by a complex exponential  $\exp\{-ik_{refr}\}$ , where  $k_{refr}$  is a wavenumber close to the minimum characteristic modal wavenumber, in order to slow down phase variations, allowing for a better visualization.

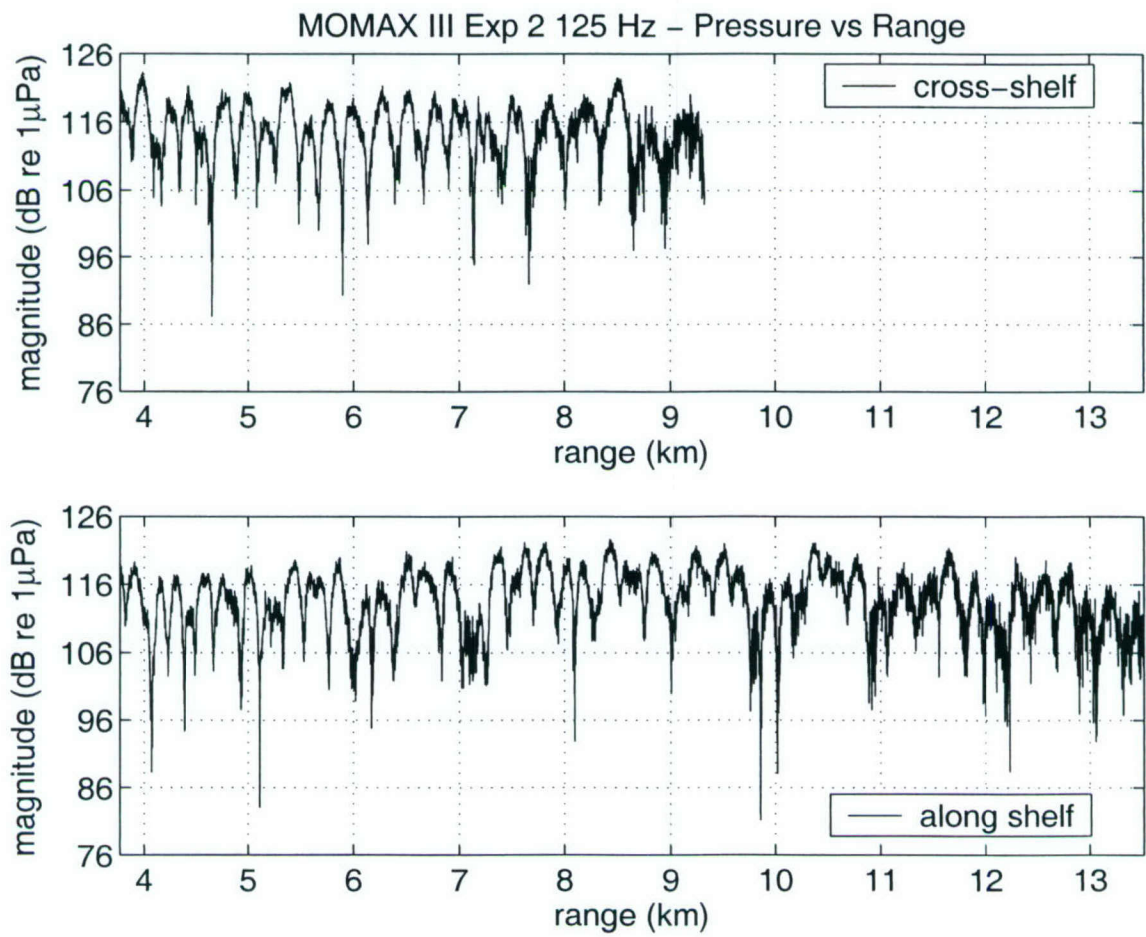


Figure 3-8: Magnitude of the pressure as a function of range, corresponding to the time series shown in Figure 3-7.

In the traditional time-varying AR method, the instantaneous frequencies are estimated from the roots of a characteristic polynomial formed with the coefficients of the difference equation. The error introduced by this approach, as compared to the exact formulation, is investigated.

Subsection 3.2.5 illustrates the issues related to exact DE representation of modal sums, and errors in eigenvalue estimation. The example is based on a realistic, range-dependent, shallow-water waveguide.

The normal mode equation (3.9) describes the pressure field as a sum of exponentials with range-varying amplitude and eigenvalues. Including the effects of absorption [replacing  $ik_{rm}$  by  $(-\alpha_m + ik_{rm})$ , where  $\alpha_m$  is the modal absorption coefficient in  $\text{m}^{-1}$ ] in eq.(3.9), one can write,

$$y(r, z; z_0) \equiv p(r, z; z_0)\sqrt{r} = \sum_{m=1}^M C_{m0} U_m(r, z, z_0) \exp\{-A_m(r)\} \exp\{iK_m(r)\}, \quad (3.13)$$

where  $C_{m0}$  are complex constants,

$$C_{m0} = \frac{e^{i\pi/4}}{\rho(0, z_0)} \sqrt{2\pi} e^{i \int_{r_0}^{r_0} k_{rm}(r') dr'} e^{- \int_{r_0}^{r_0} \alpha_m(r') dr'} \quad (3.14)$$

$U_m(r, z, z_0)$  are real modal amplitudes,

$$U_m(r, z, z_0) = \frac{u_m(0, z_0) u_m(r, z)}{\sqrt{k_{rm}(r)}}, \quad (3.15)$$

$$A_m(r) = \int_{r_0}^r \alpha_m(r') dr', \quad (3.16)$$

$$K_m(r) = \int_{r_0}^r k_{rm}(r') dr', \quad (3.17)$$

and  $r_0$  is some initial range.

The discretization of eq.(3.13) with  $r_n = r_0 + n\Delta r$ , leads, allowing for a slight abuse

of notation where  $f(n) \equiv f(r_n)$ , and omitting the explicit dependence on depth, to

$$y(n) = \sum_{m=1}^M C_{m0} U_m(n) \exp \{-A_m(n)\} \exp \{iK_m(n)\}, \quad n \geq 0. \quad (3.18)$$

This section addresses the question of representing this signal by a recursive difference equation such as the one that is the basis of the autoregressive (AR) spectral estimation, and the error incurred in using the roots of the AR characteristic equation to estimate range-varying eigenvalues.

### 3.2.1 Range-Independent Case

In the range-independent case, eq.(3.18) can be written as

$$y(n) = \sum_{m=1}^M C_{m0} U_m \exp \{(-\alpha_m + ik_m) n \Delta r\}, \quad n \geq 0. \quad (3.19)$$

The results of this subsection are:

- The signal  $y(n)$  is the solution to a linear, time-invariant difference equation (DE)

$$y(n) = \sum_{j=1}^M a_j y(n-j), \quad n \geq 0, \quad (3.20)$$

with suitable initial conditions  $y(-1), \dots, y(-M)$ .

- The roots of the characteristic polynomial  $(1 - a_1 z^{-1} - \dots - a_M z^{-M})$  are given by  $\exp\{(-\alpha_m + ik_m) \Delta r\}$ . Their phases are the eigenvalues (times  $\Delta r$ ) and their magnitudes are the absorption factors  $\exp\{-\alpha_m \Delta r\}$ .

In this sense, the DE (3.20) is a representation of the range-independent modal sum. If the coefficients of the DE ( $a_j$ ) are given, the eigenvalues and absorption coefficients can be computed. The AR model is basically eq.(3.20) with a source term. Fitting

a sum of complex exponentials to the AR model, and computing the zeros of the AR characteristic equation is hence a valid way for the estimation of constant eigenvalues.

The tool to be used in this analysis is the unilateral  $z$ -transform<sup>5</sup> of a sequence  $y(n)$  defined as[55]

$$Y(z) = \mathcal{Z}[y(n)] = \sum_{n=0}^{\infty} y(n)z^{-n}, \quad (3.21)$$

or, symbolically,  $y(n) \xrightarrow{\mathcal{Z}} Y(z)$ .  $z$  is a complex variable and the transform is defined in a region of convergence  $|z| > R$  in the complex plane where the above sum converges. The two properties needed here are

- *linearity*: if  $y_1(n) \xrightarrow{\mathcal{Z}} Y_1(z)$  and  $y_2(n) \xrightarrow{\mathcal{Z}} Y_2(z)$ , then

$$a_1y_1(n) + a_2y_2(n) \xrightarrow{\mathcal{Z}} a_1Y_1(z) + a_2Y_2(z);$$

- *delay*: if  $y(n) \xrightarrow{\mathcal{Z}} Y(z)$ , then

$$y(n-k) \xrightarrow{\mathcal{Z}} z^{-k}Y(z) + z^{-k+1}y(-1) + \cdots + z^{-1}y(-k+1) + y(-k).$$

For a single mode  $y_m(n)$ , eq.(3.19) indicates that  $y_m(n) = c_m y_m(n-1)$ , where

$$c_m = y_m(n)/y_m(n-1) = \exp\{(-\alpha_m + ik_m) \Delta r\}.$$

Applying the unilateral  $z$ -transform to this first-order DE and using the above properties, one obtains  $Y_m(z) = c_m[Y_m(z)z^{-1} + y_m(-1)]$ , and

$$Y_m(z) = c_m y_m(-1)/(1 - c_m z^{-1}).$$

---

<sup>5</sup>The independent variable range  $r$  is always positive, and the unilateral (as opposed to the bilateral, defined for  $-\infty < n < \infty$ )  $z$ -transform is suitable for representing sequences associated with a discrete range grid, as in the present case.

The characteristic polynomial  $(1 - c_m z^{-1})$  has the single zero  $c_m$ . Hence,  $c_m$  is the pole of  $Y(z)$  from which the eigenvalue  $k_m$  and the absorption coefficient  $\alpha_m$  are recovered. Also, given  $c_m$  and an initial value  $y_m(n_o)$ , the whole signal can be recovered by direct substitution into the first-order DE.

For two modes,  $y(n) = y_1(n) + y_2(n) = c_1 y_1(n-1) + c_2 y_2(n-1)$  can be represented by the DE

$$y(n) = a_1 y(n-1) + a_2 y(n-2) = a_1 y_1(n-1) + a_1 y_2(n-1) + a_2 y_1(n-2) + a_2 y_2(n-2).$$

Substitute the  $y_1$  and  $y_2$  first-order DE's into this expression to obtain

$$y(n) = (a_1 + c_1^{-1} a_2) y_1(n-1) + (a_1 + c_2^{-1} a_2) y_2(n-1).$$

Comparing these two last expressions, one obtains the system

$$\begin{bmatrix} 1 & c_1^{-1} \\ 1 & c_2^{-1} \end{bmatrix} \begin{bmatrix} a_1 \\ a_2 \end{bmatrix} = \begin{bmatrix} c_1 \\ c_2 \end{bmatrix}, \quad (3.22)$$

from which the coefficients can be computed:  $a_1 = c_1 + c_2$  and  $a_2 = -c_1 c_2$ . Note that  $c_1$  and  $c_2$  are the zeros of the polynomial  $1 - a_1 z^{-1} - a_2 z^{-2}$ . The  $z$ -transform of the second order DE is

$$Y(z) = a_1 z^{-1} Y(z) + a_1 y(-1) + a_2 z^{-2} Y(z) + a_2 z^{-1} y(-1) + a_2 y(-2),$$

from which

$$Y(z) = \frac{a_1 y(-1) + a_2 y(-2) + a_2 z^{-1} y(-1)}{1 - a_1 z^{-1} - a_2 z^{-2}}.$$

The poles of  $Y(z)$ , are, as noted above, the first-order poles  $c_1$  and  $c_2$ , i.e.,

$$1 - a_1 z^{-1} - a_2 z^{-2} = (1 - c_1 z^{-1})(1 - c_2 z^{-2}). \quad (3.23)$$

Given the DE coefficients  $a_1$  and  $a_2$ , the first-order poles and the corresponding eigenvalues and absorption factors can be recovered. The signal itself can be also recovered [given initial values  $y(n_0)$ ,  $y(n_0 - 1)$ ].

For the sum of an arbitrary number of distinct complex exponentials, the same procedure above leads to the system

$$\begin{bmatrix} 1 & c_1^{-1} & c_1^{-M+1} \\ & \dots & \\ 1 & c_M^{-1} & c_M^{-M+1} \end{bmatrix} \begin{bmatrix} a_1 \\ \vdots \\ a_M \end{bmatrix} = \begin{bmatrix} c_1 \\ \vdots \\ c_M \end{bmatrix}. \quad (3.24)$$

Any row of this system can be written (after dividing by the corresponding  $c_m$ ) as  $1 - a_1 c_m^{-1} - \dots - a_M c_m^{-M} = 0$ , which indicates that the  $c_m$  are the zeros of the polynomial  $s^M - a_1 s^{M-1} - \dots - a_M$ . A trivial generalization of the expression for  $Y(z)$  above shows that this is the DE characteristic polynomial. The first-order poles, eigenvalues and absorption coefficients, as well as the signal itself [given initial values  $y(n_0), \dots, y(n_0 - M + 1)$ ] can be recovered from the DE coefficients. The sum of complex exponentials is exactly represented by the DE and a set of initial values.

The concept of representation of a sum of complex exponentials by an exact DE and the relation between its coefficients and the first-order poles is now generalized for the range-dependent modal sum.

### 3.2.2 Range-Dependent Case: Single Mode

Kayhan[38] analyzed the representation of a sum of real chirp signals by a range-varying difference equation. Here the interest is in the sum of complex exponentials, a more general model. The main results of this and the following subsections are:

- Range-varying modes, in the adiabatic approximation, can be exactly represented

by a DE with varying coefficients,

$$y(n) = \sum_{j=1}^M a_j(n)y(n-j), \quad n \geq 0. \quad (3.25)$$

Differently from the case of constant coefficients, the zeros of the now varying characteristic equation are not the first-order poles associated with the signal  $y(n)$  (from which the eigenvalues can be estimated). The zeros are, at best, an approximation. The DE is the basis for the time-varying AR (TVAR) model<sup>6</sup>.

- The first-order poles can be computed from a given series of coefficients  $a_j(n)$  by solving an initial value problem (IVP) that, except for the trivial case of a single mode, is nonlinear in the poles. The IVP is sensitive to errors and is not a useful tool for estimating the first-order poles.
- In practice, the zeros of the AR characteristic polynomial are used to estimate the varying eigenvalues. The error between polynomial zeros and first-order poles is analyzed. The error is a function of the sampling distance  $\Delta r$ , of the rate of change of the modal eigenvalues with range, and of the separation between adjacent eigenvalues.

Each modal component in eq.(3.13),

$$y_m(n) = U_m(n) \exp \{-A_m(n)\} \exp \{iK_m(n)\}, \quad m = 1, \dots, M,$$

can be represented by the first-order difference equation

$$y_m(n) = c_m(n)y_m(n-1), \quad (3.26)$$

---

<sup>6</sup>For the present application, the model is, in fact, “range-varying”, but we keep the nomenclature “time-varying AR” (TVAR) commonly found in the (mostly time-series analysis related) literature.

where<sup>7</sup>

$$\begin{aligned} c_m(n) &= y_m(n)/y_m(n-1) = |c_m(n)| \exp \{i\delta K_m(n)\} \\ &= \frac{U_m(n)}{U_m(n-1)} \exp \{-\delta A_m(n)\} \exp \{i\delta K_m(n)\}, \end{aligned} \quad (3.27)$$

$$\delta K_m(n) = K_m(n) - K_m(n-1) = \int_{r_{n-1}}^{r_n} k_m(r) dr, \quad (3.28)$$

and

$$\delta A_m(n) = A_m(n) - A_m(n-1) = \int_{r_{n-1}}^{r_n} \alpha_m(r) dr. \quad (3.29)$$

By analogy with the range-independent case,  $c_m(n)$  is called the first-order pole of the DE (3.26). Its phase is the increment of the signal phase, called *instantaneous frequency*<sup>8</sup> by Kayhan, and its magnitude is the ratio of the magnitudes of adjacent samples. Given a sequence of coefficients  $c_m(n)$ , the local eigenvalues and modal amplitudes (except for a constant) of the original component signal  $y_m(n)$  are recovered.

### 3.2.3 Sum of Two Modes

#### Iteration for the First-Order Poles

The sum of two complex exponentials can be represented by a second order difference equation

$$y(n) = y_1(n) + y_2(n) = a_1(n)y(n-1) + a_2(n)y(n-2). \quad (3.30)$$

The relation between the coefficients  $\{a_1, a_2\}$  and the individual first-order poles  $\{c_1, c_2\}$  is obtained by substituting the first-order difference equation (3.26) into (3.30), leading

---

<sup>7</sup>Under the slow modal variation condition of the adiabatic modal approximation, and for typical values of the absorption coefficients  $\alpha_m$ ,  $|c_m(n)| \sim 1$ . The first-order poles are close to the unit circle.

<sup>8</sup>To the first-order in  $\Delta r$ , the phase of the pole  $c_m$  is  $\delta K_m = k_m(r_n)\Delta r$ , a measure of the local (instantaneous) modal eigenvalue.

to[cf. eq.(3.22)]

$$\begin{bmatrix} 1 & c_1^{-1}(n-1) \\ 1 & c_2^{-1}(n-1) \end{bmatrix} \begin{bmatrix} a_1(n) \\ a_2(n) \end{bmatrix} = \begin{bmatrix} c_1(n) \\ c_2(n) \end{bmatrix}. \quad (3.31)$$

The first-order coefficients are not zeros of the polynomial  $1 - a_1(n)s^{-1} - a_2(n)s^{-2}$ , as in the range-independent case. Each row of eq.(3.30) can be written as  $1 - c_m^{-1}(n)a_1(n) - c_m^{-1}(n)c_m^{-1}(n-1)a_2(n) = 0$ , which does not reduces to the above polynomial equation unless the first-order pole  $c_m$  does not change from sample  $n-1$  to  $n$ .

The problem of interest is to obtain the first-order poles  $c_1(n)$  and  $c_2(n)$  and, therefore, the local eigenvalues and amplitudes, given  $a_1(n)$  and  $a_2(n)$ . Here, the  $z$ -transform is not used because the DE coefficients are not constant. In [35], Kamen defined, instead, an operator  $z$  and a product 'o'

$$[a(n)z^{-j}]f(n) = a(n)f(n-j), \quad (3.32)$$

$$[a(n)z^{-j}] \circ f(n) = a(n)f(n-j)z^{-j}, \quad (3.33)$$

where  $z$  can be seen as a delay operator related to the  $z$ -transform of a sequence  $f(n)$ . Equation (3.30) can, therefore, be written as

$$[1 - a_1(n)z^{-1} - a_2(n)z^{-2}] y(n) = 0. \quad (3.34)$$

Assume there are complex functions  $p_1(n)$ ,  $p_2(n)$  such that

$$[1 - a_1(n)z^{-1} - a_2(n)z^{-2}] y(n) = [1 - p_1(n)z^{-1}] \circ v(n) = 0$$

and

$$v(n) = [1 - p_2(n)z^{-1}] y(n)$$

decompose the second order system in two cascade first-order systems with a *left-pole*

$p_1(n)$  and a *right-pole*  $p_2(n)$ . Substitute the second expression into the first to obtain

$$\begin{aligned}[1 - a_1(n)z^{-1} - a_2(n)z^{-2}]y(n) &= v(n) - p_1(n)z^{-1} \circ v(n), \\ &= y(n) - p_2(n)z^{-1}y(n) - p_1(n)z^{-1}y(n) + p_1(n)z^{-1} \circ p_2(n)z^{-1}y(n), \\ &= [1 - (p_1(n) + p_2(n))z^{-1} + p_1(n)p_2(n-1)z^{-2}]y(n),\end{aligned}$$

from which follows the relations

$$\begin{aligned}a_1(n) &= p_1(n) + p_2(n), \\ a_2(n) &= -p_1(n)p_2(n-1).\end{aligned}\tag{3.35}$$

Equation (3.35) is not a relation between polynomial coefficients and zeros, unless  $p_2(n) = p_2(n-1)$ . If the right and left poles are constant, so are the coefficients, and we recover the range-independent case. Given series of polynomial coefficients  $a_1(n)$  and  $a_2(n)$ , and an initial value for the right-pole  $p_2(n_0-1)$ , eq.(3.35) can be solved iteratively for the left and right-poles for  $n \geq n_0$ .

A single recursion is obtained by multiplying the first eq.(3.35) by  $p_2(n-1)$  and substituting the second equation to obtain

$$p_2(n) = a_1(n) + a_2(n)p_2^{-1}(n-1).\tag{3.36}$$

This is the initial value problem for the right-poles. For a given series of coefficients  $a_j(n)$ ,  $j = 1, 2$ , different initial values  $p_2(n_0-1)$  lead, in general, to different series of right-poles  $p_2(n)$ . Iteration of the left-pole  $p_1(n)$  is irrelevant for the present application.

The importance of iteration (3.36) for the somewhat arbitrary right-pole  $p_2$ , is that when the iteration is initialized with one of the first-order poles  $c_m$  representing the modes, the sequence of first-order poles is recovered. In other words, set  $p_2(n_0-1) = c_m(n_0-1)$  to recover  $c_m(n)$ ,  $n \geq n_0$  and, in consequence, the original signal  $y_m(n)$  [given suitable initial conditions, see eq.(3.26)]. Similarly, a backward iteration recovers

the first-order poles for  $n < n_0$  when  $p_2(n_0)$  is initialized to  $c_m(n_0)$ . This result can be verified by examining either row of eq.(3.31),  $c_m(n) = a_1(n) + a_2(n)c_m^{-1}(n - 1)$ , which shows that both first-order poles satisfy the iteration (3.36) of the right-pole.

### From DE Coefficients to First-Order Poles: Estimation Issues

Kayhan[38] introduced an estimator of instantaneous frequencies (our local eigenvalues) and amplitudes based on the exact DE representation, in particular, iteration (3.36). Given the signal  $y(n)$ , the sum of two range-varying modes<sup>9</sup>, estimate the coefficients of the DE representation,  $a_j(n)$ . Then, for each mode  $m$ , use iteration (3.36) to compute the series of first-order poles  $c_m(n)$ , given an initial value  $c_m(n - 1)$ .

The local eigenvalues (instantaneous frequencies)  $k_m(n)$  are then estimated from the phases of the  $c_m(n)$ , using eqs.(3.27) and (3.28). The local amplitude of each mode (coupled with the absorption factor) can also be recovered using eq.(3.27), except for a multiplying constant. A number of methods are available to estimate the varying  $a_j(n)$  [52, 38] and one is discussed in Section 3.3.

Iteration (3.36) requires an initial value of the first-order coefficient  $c_m$ , which may pose a problem when analyzing an actual signal. If the first-order poles do not change between a pair of adjacent samples,  $c_m(n) = c_m(n - 1) = c_{mO}$ , the second order coefficients simplify to [cf. Subsection 3.2.1]  $a_1^{(O)}(n) = c_{1O} + c_{2O}$  and  $a_2^{(O)}(n) = -c_{1O}c_{2O}$  and, therefore,  $c_{1O}$  and  $c_{2O}$  are the zeros of the characteristic polynomial [cf. eq.(3.34)]  $s^2 - a_1^{(O)}(n)s - a_2^{(O)}(n)$ . In a region where the coefficients are nearly constant, one should expect the roots of the polynomial to be a reasonable approximation to the actual first-order coefficients.

In order to illustrate the effects of a change in one of the complex exponentials on those roots, let  $c_1(n) = c_{1O} + \epsilon_{10}$ . The exact expressions for the new polynomial

---

<sup>9</sup>See eq.(3.48) for the iteration of the right-pole in the case of the sum of an arbitrary number of modes.

coefficients  $a_1(n)$  and  $a_2(n)$  are, from eq.(3.31),

$$\begin{aligned}
a_1(n) &= \{c_1(n-1)c_1(n) - c_2(n-1)c_2(n)\} / [c_1(n-1) - c_2(n-1)], \\
&= (c_{1O}(c_{1O} + \epsilon_{10}) - c_{2O}^2) / (c_{1O} - c_{2O}), \\
&= a_1^{(O)}(n) + c_{1O}\epsilon_{10} / (c_{1O} - c_{2O}), \\
&= a_1^{(O)}(n) + \delta_{a1},
\end{aligned} \tag{3.37}$$

$$\begin{aligned}
a_2(n) &= c_2(n-1)c_1(n-1)[c_2(n) - c_1(n)] / [c_1(n-1) - c_2(n-1)], \\
&= c_{2O}c_{1O}(c_{2O} - c_{1O} - \epsilon_{10}) / (c_{1O} - c_{2O}), \\
&= a_2^{(O)}(n) - c_{2O}c_{1O}\epsilon_{10} / (c_{1O} - c_{2O}), \\
&= a_2^{(O)}(n) + \delta_{a2}.
\end{aligned} \tag{3.38}$$

These equations are an intermediate result for obtaining the perturbed roots. They show that even small changes in the modal eigenvalues or magnitudes (and, therefore in the first-order poles) may lead to large changes in the second order coefficients, depending on the separation (difference) between poles.

Substituting eqs.(3.37) and (3.38) into the equation  $s^2 - a_1(n)s - a_2(n) = 0$  with roots  $s_m(n) = c_{mO} + \delta_{sm}$  and using either standard perturbation methods[65], or solving directly the second degree equation, one obtains

$$\delta_{sm} = \frac{c_{mO}\delta_{a1} + \delta_{a2}}{2c_{mO} - a_1^{(O)}} = \frac{c_{1O}}{c_{1O} - c_{2O}} \frac{c_{mO} - c_{2O}}{2c_{mO} - a_1^{(O)}} \epsilon_{10}$$

for the changes in the roots, leading to the perturbed roots

$$s_1(n) = c_{1O} + \frac{c_{1O}}{c_{1O} - c_{2O}} \epsilon_{10} = c_1(n) + \frac{c_{2O}}{c_{1O} - c_{2O}} \epsilon_{10}, \tag{3.39}$$

and

$$s_2(n) = c_{2O} = c_2(n). \tag{3.40}$$

Only the root corresponding to the changing pole is affected: the second row of eq.(3.31)

guarantees that  $c_{2O}$  is a root of the characteristic polynomial when  $c_2(n-1) = c_2(n) = c_{2O}$ .

The error between the root and the actual coefficient is of the order of the change in the coefficient relative to the difference between the poles. Notice, again, that even small changes in  $c_1$  may lead to large changes in the polynomial roots. Appendix B.3 discusses the case where both  $c_1(n)$  and  $c_2(n)$  are perturbed [see eq.(B.27)].

In the *frozen time approach* of frequency estimation[38], after the polynomial coefficients are estimated, the roots of the polynomials at each sample are taken as estimates of the actual poles  $c_1$  and  $c_2$ . Equations (3.39) and (3.40) give the error in this approach when only  $c_1(n)$  is changing. [38] suggests to increase the sampling rate (decreasing  $\Delta r$ ) in order to reduce the change in the poles between samples,  $\epsilon_{m0}$ , when analyzing a continuous signal.

As an example, let the phase of  $c_1$  change by  $\exp\{i\beta_1(\Delta r)^2\}$  due to a linear increase in the eigenvalue of the first mode with range, i.e.,  $c_1(n) = c_{1O}\exp\{i\beta_1(\Delta r)^2\}$ ,  $\epsilon_{10} = c_1(n) - c_{1O} = -c_{1O}(1 - \exp\{i\beta_1(\Delta r)^2\})$ . Also, let  $c_1(n-1) = c_{1O} = \exp\{ik_1\Delta r\}$  and  $c_2(n) = c_2(n-1) = c_{2O} = \exp\{ik_2\Delta r\}$ . Using eq.(3.39), the error magnitude  $|\Delta c_1| = |s_1 - c_1(n)|$  is

$$\begin{aligned} |\Delta c_1| &= \frac{|c_{2O}c_{1O}|}{|c_{1O} - c_{2O}|} \left| 1 - e^{i\beta_1(\Delta r)^2} \right|, \\ &= \frac{\left| 1 - e^{i\beta_1(\Delta r)^2} \right|}{\left| 1 - e^{i(k_2 - k_1)\Delta r} \right|}, \\ &= \sqrt{\frac{1 - \cos[\beta_1(\Delta r)^2]}{1 - \cos[(k_2 - k_1)\Delta r]}}. \end{aligned} \quad (3.41)$$

As  $\Delta r \rightarrow 0$ ,

$$|\Delta c_1| \rightarrow \beta_1\Delta r/(k_2 - k_1) + O[(\Delta r)^2] \quad (3.42)$$

and indeed the error magnitude decreases with  $\Delta r$ .

The implicit assumption in Kayhan's suggestion [38] is that the estimation of the

coefficients  $a_j(n)$  from the signal  $y(n)$  is not affected as  $\Delta r$  decreases. An indication that decreasing  $\Delta r$  may lead, instead, to larger errors is that the lower bound on the eigenvalue estimation error variance (the Cramer-Rao bound–CRB) [40, for constant eigenvalues] is proportional to  $(\delta k \Delta r)^{-2(M-1)}$ , where  $M$  is the number of modes and  $\delta k$  is the (small) eigenvalue difference between the most widely spaced eigenvalues.

Hence, although the decrease in  $\Delta r$  may reduce  $|\Delta c_1|$ , errors in estimating  $a_j(n)$  may increase, offsetting the effect of a reduced change  $\epsilon_{10}$  and, in fact, deteriorating the estimation of the first-order poles. When the spacing between poles is large  $[(k_2 - k_1)\Delta r = \pi$  is the largest distance in the case of two modes], the multiple eigenvalue CRB approaches the CRB for the single mode[62, 69].

Another issue in using the right-pole iteration (3.36) is related to error evolution, i.e., how the first-order pole estimation error changes with  $n$  in a region, for example, were the DE coefficients become constant. The right-pole may converge to either first-order poles or not converge at all, depending on the ratio of the pole magnitudes.

Following the method used in [35] regarding eq.(3.35), assume that  $a_1(n)$  and  $a_2(n)$  are constant for  $n > n_0 - 1$  or, equivalently,  $c_m(n) = c_{mO}$ . Assume also that the iteration at that point resulted in  $p_2(n_0 - 1) = c_{1O} + \delta_0$ . Using eq.(3.36) with  $a_1 = c_{1O} + c_{2O}$  and  $a_2 = -c_{1O}c_{2O}$ , the evolution of the error  $\delta(n)$  is given by

$$\begin{aligned} p_2(n) &= a_1(n) + a_2(n)p_2^{-1}(n-1) \Rightarrow \\ c_{1O} + \delta(n) &= c_{1O} + c_{2O} - \frac{c_{1O}c_{2O}}{c_{1O} + \delta(n-1)}, \Rightarrow \\ \delta(n)\delta(n-1) + c_{1O}\delta(n) - c_{2O}\delta(n-1) &= 0, \quad n \geq n_0, \end{aligned} \tag{3.43}$$

with initial condition  $\delta(n_0 - 1) = \delta_0$ . This is a homogeneous Riccati recurrence equation linearized by writing it in terms of the inverse error  $1/\delta$ :

$$\frac{c_{2O}}{\delta(n)} = \frac{c_{1O}}{c_{2O}} \frac{c_{2O}}{\delta(n-1)} + 1. \tag{3.44}$$

This first-order, linear, constant coefficient recursive DE has solution

$$\frac{c_{2O}}{\delta(n_0 + l)} = \left( \frac{c_{1O}}{c_{2O}} \right)^{l+1} \frac{c_{2O}}{\delta_0} + \frac{1 - \left( \frac{c_{1O}}{c_{2O}} \right)^{l+1}}{1 - \frac{c_{1O}}{c_{2O}}} = \frac{1}{1 - \frac{c_{1O}}{c_{2O}}} + \left( \frac{c_{2O}}{\delta_0} - \frac{1}{1 - \frac{c_{1O}}{c_{2O}}} \right) \left( \frac{c_{1O}}{c_{2O}} \right)^{l+1}.$$

In the steady state, as  $l \rightarrow \infty$ , if  $|c_{1O}/c_{2O}| > 1$ , then  $c_{2O}/\delta \rightarrow \infty$ , the error  $\delta \rightarrow 0$ , and the right-pole converges to  $c_{1O}$  at a rate that increases with  $|c_{1O}/c_{2O}|$ . If, on the other hand,  $|c_{1O}/c_{2O}| < 1$ ,  $c_{2O}/\delta \rightarrow c_{2O}/(c_{2O} - c_{1O})$ ,  $\delta \rightarrow c_{2O} - c_{1O}$ , and the right-pole tends to  $c_{2O}$  at a rate that increases with  $|c_{2O}/c_{1O}|$ . As a result, the right-pole is “attracted” to the pole with the largest magnitude at a rate that depends on the ratio of the pole magnitudes.

When  $|c_{1O}/c_{2O}| = 1$  (an approximation compatible with the adiabatic mode approximation), we can write  $c_{1O}/c_{2O} = \exp\{i(k_{1O} - k_{2O})\Delta r\}$ . In this case, the solution to the inverse error is

$$\frac{c_{2O}}{\delta(n_0 + l)} = \frac{1}{1 - e^{i(k_{1O} - k_{2O})\Delta r}} + \left( \frac{c_{2O}}{\delta_0} - \frac{1}{1 - e^{i(k_{1O} - k_{2O})\Delta r}} \right) e^{i(l+1)(k_{1O} - k_{2O})\Delta r},$$

$1/\delta$  is oscillatory and the right-pole converges to neither first-order poles.

### 3.2.4 Sum of an Arbitrary Number of Modes

The generalization of the results of the above Section for an arbitrary number of complex exponentials is obtained by substituting the first-order equations (3.26) into

$$\begin{aligned} y(n) &= \sum_{m=1}^M y_m(n), \\ &= \sum_{j=1}^M a_j(n)y(n-j). \end{aligned} \tag{3.45}$$

Following the procedure developed in [35] and described in Appendix B.1, one obtains the expression for the  $M$ -th order coefficients as [see eq.(B.8)]

$$D(n)\mathbf{a}(n) = \mathbf{c}(n), \tag{3.46}$$

where  $\mathbf{a}(n) = [a_1(n), \dots, a_M(n)]^T$ ,  $\mathbf{c}(n) = [c_1(n), \dots, c_M(n)]^T$ , and the elements of the matrix  $D(n)$  are obtained by the recursion [cf. eq.(3.31)]

$$(D(n))_{m,j} = \begin{cases} 1, & j = 1, \\ c_m^{-1}(n - j + 1)d_{m,j-1}, & 2 \leq j \leq M. \end{cases} \quad (3.47)$$

In order to compute  $\mathbf{a}(n)$ , eq.(3.47) requires the series  $\{c_m(n - M + 1), \dots, c_m(n)\}$ ,  $m = 1, \dots, M$ , the present and  $M - 1$  past first-order poles.

A recursion for the right-poles corresponding to a given series of coefficients  $\mathbf{a}(n)$  is obtained following the procedure described in [35] as [cf. eq.(3.36) and Appendix B.2, eq.(B.10)]:

$$\begin{aligned} p_M(n) \prod_{j=1}^{M-2} p_M(n - j) &= \frac{a_M(n)}{p_M(n - M + 1)} \\ &+ a_{M-1}(n) + \sum_{j=1}^{M-2} a_j(n) \prod_{k=j}^{M-2} p_M(n - k). \end{aligned} \quad (3.48)$$

The recursion for  $p_M(n)$  requires initialization using the  $M - 1$  past right-poles. As in the two-mode case, if eq.(3.48) is initialized with  $\{c_m(n_0 - M + 1), \dots, c_m(n_0 - 1)\}$ , then  $c_m(n_0)$  is recovered.

Also as in the second order case, initial first-order poles can be estimated from the roots of the polynomial

$$-\sum_{j=0}^M a_j(n) s^{M-j}, \quad a_0(n) = -1,$$

provided that they are constant, or nearly so, for  $M$  signal samples (present and  $M - 1$  past samples). In order to approximate the  $M - 1$  past poles by roots, therefore, the signal components should have constant poles for  $2M - 2$  samples, a requirement that becomes more restrictive as the number  $M$  of distinct complex exponentials increases.

Appendix B.3 analyzes the error between characteristic polynomial zeros and first-order poles for  $M = 3$  [eqs.(B.43) and (B.44)]. The results are qualitatively similar to the

$M = 2$  case discussed in Subsection 3.2.3. The ratio between change in first-order poles to distance between poles determines the error between roots and first-order coefficients. As the order increases, the poles (limited to be close to the unit circle) tend to be closer, degrading the approximation of the poles by the characteristic polynomial zeros.

In addition, as the order increases, the right-pole iteration involves the multiplication of a larger number of past poles. A DE for the error when using the right-pole in a region of constant coefficients [see eqs.(3.43) and (3.44)] is an  $M$ -th order non-linear recursion, which can not be linearized for  $M \geq 3$ .

Where the adiabatic mode approximation is valid, the modes change slowly with range and the roots of the characteristic equation themselves may be a reasonable approximation to the first-order coefficients.

As shown in the  $M = 2$  case, right-pole iteration may not converge or converge to the wrong first-order pole. In addition, the degree of nonlinearity of the right-pole iteration increases with the number the modes . This combination of factors impose limitations to eigenvalue estimation through right-pole iteration as the number of propagating modes increase.

### 3.2.5 A Realistic Example: Inverse Techniques Workshop

We illustrate the issues of representing modal sums by DE's and estimating eigenvalues. As an example, modal amplitudes and eigenvalues were computed for a realistic range-dependent, shallow-water waveguide, used as a test case for the NRL Inversion Techniques Workshop (ITW) held in Gulfport, Mississippi, from May 15 to 18 of 2001.

Chapman and co-workers [9] give a detailed environmental description of the test cases. The objective of the experiment was to estimate the (possibly range-dependent) seabed geoacoustic properties given the sound velocity profile in the water column, the bathymetry, and a set of pressure fields from a point source in the frequency range 25–500 Hz. Acoustic data were available at two “horizontal arrays” (every 5 m from 5 m to 5 km in range) and a number of “vertical arrays” (depth 20-80 m every meter; range

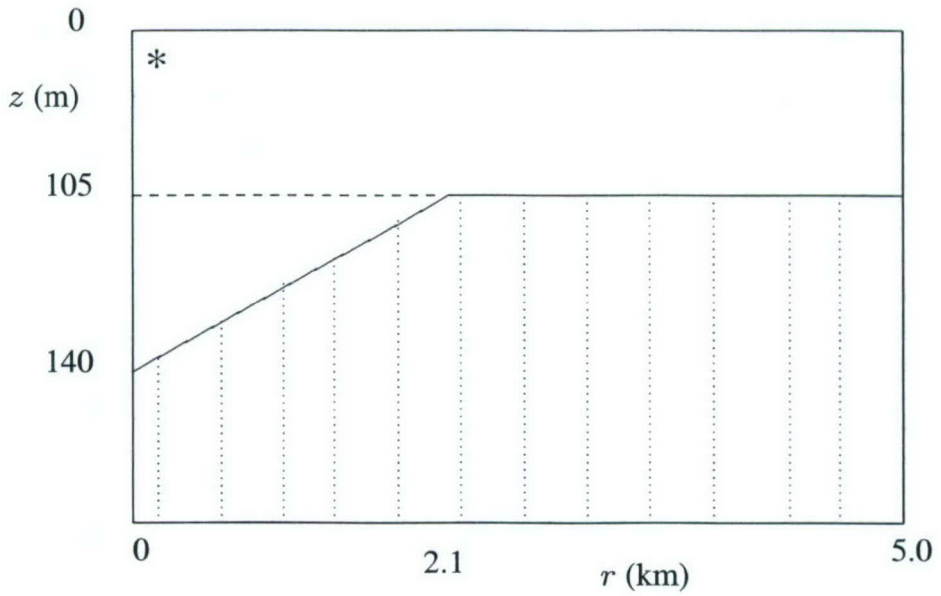


Figure 3-9: Range-Dependent environment, test case 2 of the Inverse Techniques Workshop, Gulfport, MS [9]. The water and seabed properties are range-independent. The bottom slope is constant ( $\sim 0.96^\circ$ ) up to  $r = 2.1$  km, where the local depth becomes constant (105 m).

500m to 5 km, every 500 m). In all cases, the source depth is 20 m (at  $r = 0$ ) and the sound speed in water is known.

The present example is based on test case 2 (TC2) environment, shown in Figure 3-9. The environment consists of a range-varying geometry with a gentle slope followed by a constant depth region. We computed the modal components at 50 Hz, for a source at 20 m and a receiver 25 m deep, using the normal mode code KRAKEN[57].

The amplitudes and eigenvalues of the modal components are shown in Figure 3-10. A sixth mode becomes evanescent near  $r = 1.13$  km and is not included in the example to avoid the discontinuities caused by a modal amplitude decreasing to zero. In the range-independent region, the modal amplitudes decrease due to absorption.

The first-order poles were computed as the ratio between adjacent samples of each mode, as in eq.(3.27). The 5th-order DE coefficients were then computed using eq.(3.46) and are shown in Figure 3-11. Except for the transition to the range-

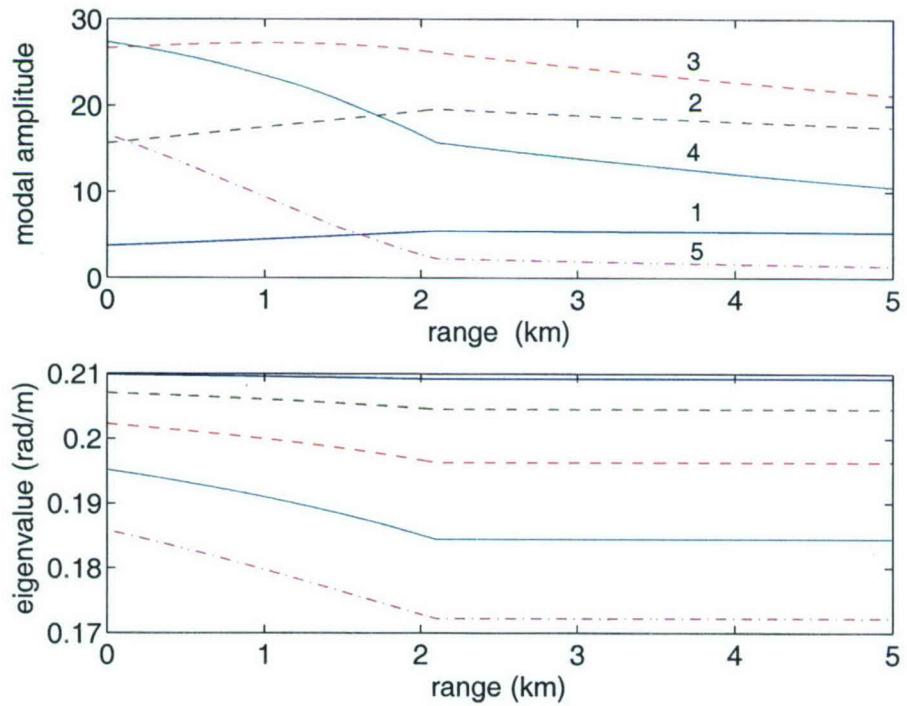


Figure 3-10: Amplitudes and eigenvalues of individual modal components for the TC2 environment at 50 Hz, source at 20 m and receiver at 25 m. The upper plot shows the modal amplitudes  $U_m(n) \exp \{-A_m(n)\}$  from eq.(3.13). The modes are identified by number (lowest mode corresponds to the highest eigenvalue).

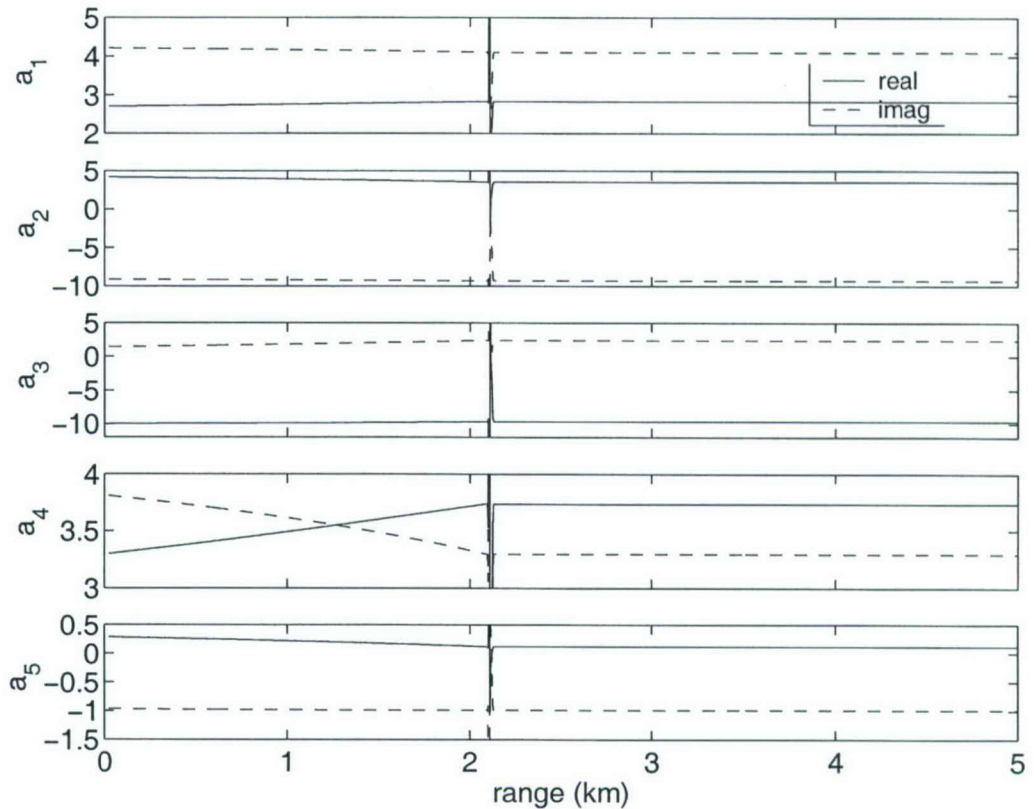


Figure 3-11: Exact DE example,  $\Delta r = 5$  m - real and imaginary parts of the DE coefficients for the sum of complex exponentials of Figure 3-10.

independent region at  $r = 2.1$  km, the variations of the coefficients are smooth. It was observed, however, that small discontinuities on the ratio of the modal component amplitudes (of the order of  $10^{-9}$  in 1) cause large discontinuities in the DE coefficients. In the present example, these discontinuities were caused by small variations between range steps of the algorithm used to compute the modes. The amplitudes in Figure 3-10 were smoothed before computing the first-order pole and DE coefficients, eliminating the problem.

In an actual eigenvalue estimation application, the individual modal components are not available, only the modal sum. The estimation of eigenvalues would comprise three

steps: estimation of the DE coefficients, estimation of the first-order poles, and finally, the computation of eigenvalues from the phases of the poles. For the present example, we start with the DE coefficients, computed to machine precision.

The first-order poles were estimated by two methods. First, we computed the roots of the DE characteristic equation at each range step and considered them as estimates of first-order poles. This is how the TVAR method (frozen-time approach) works. As a second method, we used iteration of right-poles, eq.(3.48), which derives from the theory of exact DE representation of modal sums.

In order to initialize the iteration, we need four values (for a system of order  $M = 5$ ) of each first-order pole. We checked the accuracy of the DE coefficients by initializing the iteration with the exact first-order poles (not available in actual applications). All poles were recovered with negligible errors, within machine accuracy (about  $10^{-12}$  or better).

In actual applications, one could use, for initialization, the roots of the characteristic equation in a region where the environment is nearly range independent. Figure 3-11 shows that the DE coefficients are constant for  $r > 2.1\text{km}$ . We used the roots at  $r = 5\text{ km}$  as initial values. As a third estimate, we used the iteration of right-poles, but initialized by the roots at  $r = 0$  where the DE coefficients are changing, in order to assess the effects of initialization errors.

Figure 3-12 shows the estimated eigenvalues (plots on the left) and the corresponding eigenvalue error (on the right, with logarithmic vertical scale). The first row are “TVar” estimates from the roots of the DE characteristic equation. The second row shows estimates and errors from the iteration (3.48) initialized by the roots at  $r = 5\text{ km}$ . Finally, the third row shows the results when the iteration is initialized by roots at  $r = 0$ . Only the first and fifth eigenvalues are shown for this last case. The actual eigenvalues are also plotted on the left (dashed curves), but are only discernible in the third row of plots.

The eigenvalues estimated from the roots of the exact characteristic polynomial are

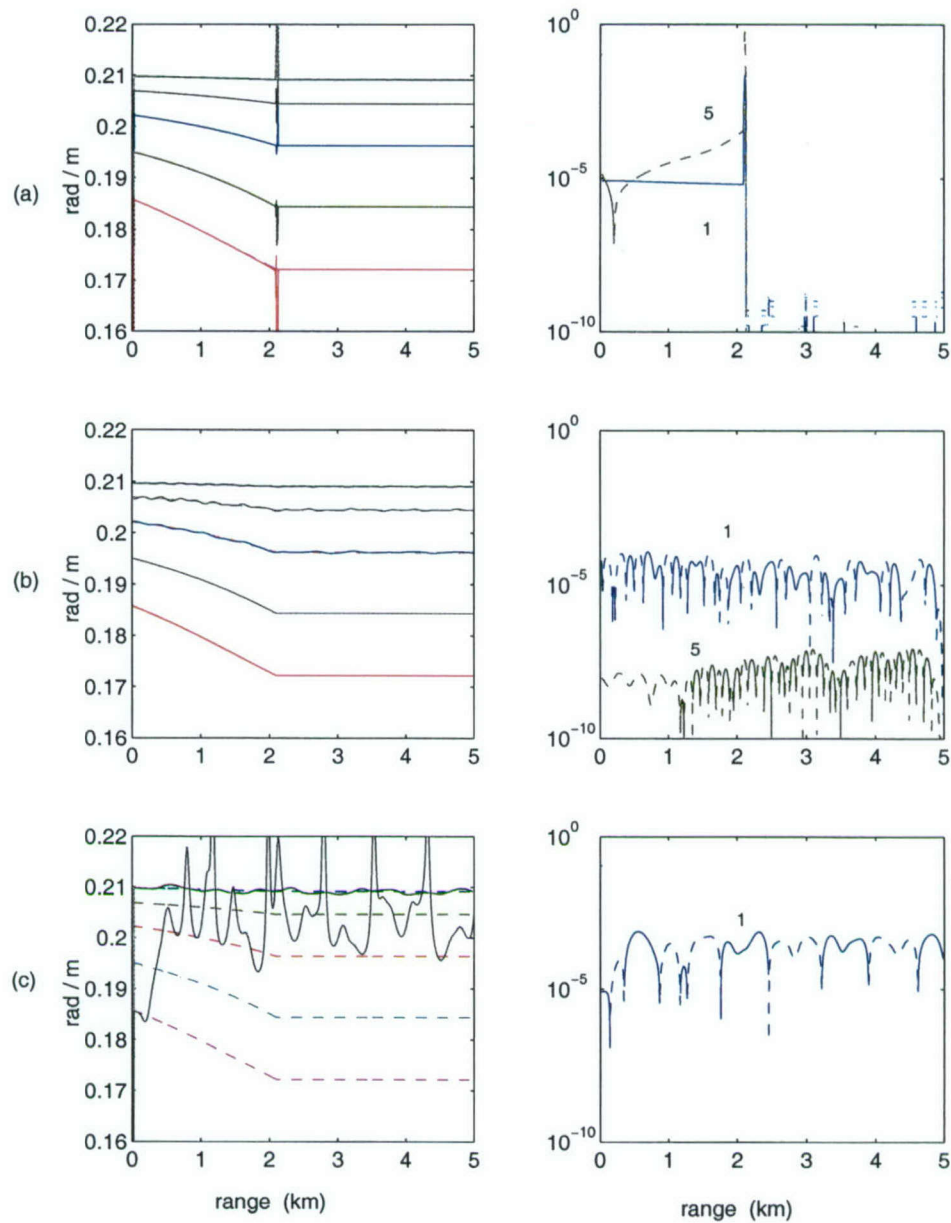


Figure 3-12: Exact DE example,  $\Delta r = 5$  m - estimation of eigenvalues. Plots on the left show actual (dashed line) and estimated (solid line) modal eigenvalues. Semi-log plots on the right show the estimation error for selected modes (indicated by mode number), where positive values of error are represented by the solid portions of the lines, while the dashed portions represent negative error. Eigenvalues derived from first-order poles estimated: (a) as DE characteristic polynomial zeros; (b) and (c) from iteration of right-poles, eq.(3.48) initialized with polynomial zeros at (b)  $r = 5$  km, and, for modes 1 and 5, (c)  $r = 0$ .

in good agreement with the actual eigenvalues, except for some outliers in the transition to the range independent region ( $r = 2.1$  km). The error in the range-independent region ( $r > 2.1$  km) is negligible, as expected.

The outliers at  $r = 2.1$  km are not observed in the middle plots (iteration initialized by roots in the range-independent region). The error in the range-dependent region is smaller for the higher order modes, suggesting that the error in initial values (roots) were smaller for the roots that are farther apart in the complex plane (the separation between adjacent first-order poles is between 1 and 3.5 degrees near the unit circle for a sampling distance of 5 m).

In the lower set of plots, the right-pole iteration was initialized using the roots of the characteristic equation near  $r = 0$ , in the range-dependent region. Only estimated modes 1 and 5 are shown. The degradation in mode 1 estimation is apparent, but there is still a reasonable agreement with the actual eigenvalue.

The fifth mode estimation, on the other hand, deviates significantly from the actual value. This is the mode that changes the fastest with range, and the corresponding error between roots (used for initialization of the right-pole iteration) and first-order poles are the highest. The small error in the initialization of the iteration (3.48) caused the estimation to diverge<sup>10</sup>.

The right-pole initially associated with the fifth mode diverges but its phase remains in the neighborhood of the second and third modal eigenvalues. This suggests a parallel with the behavior of the simpler two-mode example of error evolution from eq.(3.43), where the right-pole is “attracted” to the first-order pole with the largest magnitude.

---

<sup>10</sup>The phases of the roots themselves are in good agreement with the actual first-order poles (as indicated by the first few points near  $r = 0$  in first row of plots of Figure 3-12). This suggests that the right-pole iteration is sensitive to initialization errors.

### 3.3 Sequential Autoregressive Estimate

#### 3.3.1 Range-Varying Autoregressive Model

The range-varying AR model is a simple extension of the conventional, stationary process model, where the AR coefficients are allowed to change at each range step. As before, using the notation  $r_n = r_o + n\Delta r$ ;  $y(n) \equiv p(r_n, z)\sqrt{r_n}$ , where  $r_o$  is some initial range, the range-varying, order- $p$  [not to be confused with the pressure  $p(r_n, z)$ ] AR model is given by

$$\begin{aligned} y(n) &= a_1(n)y(n-1) + \dots + a_p(n)y(n-p) + v(n), \\ &= \mathbf{a}^T(n)\varphi(n) + v(n), \end{aligned} \tag{3.49}$$

where  $v(n)$  is a white noise sequence of variance  $\sigma_v^2$ ,  $\mathbf{a}(n) = [a_1(n) \dots a_p(n)]^T$  is the vector of AR coefficients, and  $\varphi(n) = [y(n-1) \dots y(n-p)]^T$  is the vector of the past  $p$  signal samples. The AR parameters are the set of coefficients  $\mathbf{a}(n)$  and the noise variance. In the limiting case of no input noise ( $\sigma_v^2 = 0$ ), this model reduces to the exact DE representation of a sum of modes when the order  $p$  is equal to the number of modes.

The power spectrum associated with this model can be defined as

$$P_y(k_r; r_n) = \frac{\sigma_v^2}{|1 - a_1(n)s^{-1} - \dots - a_p(n)s^{-p}|_{s=\exp\{i\Delta r k_r\}}^2}. \tag{3.50}$$

This expression is exact for range-independent AR models. Here, it is used as the definition of local spectrum. These same definitions are used in the sliding-window AR method [6], where  $P_y(k_r; r_n)$  is associated with the range of the center of the window, and the AR parameters are computed over a number of samples larger than the order  $p$  (usually,  $3 \times p$  samples). The peaks in the spectra are associated, from eq.(3.50), with the zeros of the characteristic polynomial  $\{[1 - a_1(n)s^{-1} - \dots - a_p(n)s^{-p}]$  or  $[s^p - a_1(n)s^{p-1} - \dots - a_p(n)]\}$  close to the unit circle, which, as discussed in Section 3.2, are approximations to the first-order poles.

The sequential estimator of the DE coefficient vectors  $\mathbf{a}(n)$  is implemented as a Kalman filter. For spectrum peak identification, the position of the peaks of  $P_y(k_r; r_n)$  or the zeros of the characteristic polynomials are computed at each range step<sup>11</sup>. In a second example of sequential estimators, the zeros of the characteristic polynomial are estimated directly by an adaptive filter with variable forgetting factor (VFF).

Both filters use eq.(3.49) to predict, at each “instant”  $n$ , the value of  $y(n)$ , and use the error in the prediction to update the estimate. Suppose an estimate  $\hat{\mathbf{a}}(n_0-)$  based on all  $y(n)$ ,  $n < n_0$  is available. From eq.(3.49), the next value of  $y$  should be  $y(n_0) \sim \hat{\mathbf{a}}^T(n_0-) \varphi(n_0)$ . When  $y(n_0)$  is measured, the prediction error is computed,

$$\epsilon(n_0) = y(n_0) - \hat{\mathbf{a}}^T(n_0-) \varphi(n_0).$$

The prediction error will be small if the  $\hat{\mathbf{a}}(n_0-)$  is indeed a good approximation to the actual coefficients. If it is large, this estimate needs to be updated. The idea is to use the prediction error to drive the change in the estimate, such as in

$$\hat{\mathbf{a}}(n_0+) = \hat{\mathbf{a}}(n_0-) + K\epsilon(n_0),$$

where  $K$  is some gain matrix.

If the noise variance  $\sigma_v^2$  is high, the prediction error could be large, even if the estimate is close to the actual value. The filter gain  $K$  may take into account the variance  $\sigma_v^2$  of the noise. The higher the noise variance, the smaller the gain, so that corrections to the estimate occur over longer periods, taking into account a larger number of  $y(n)$  samples, effectively integrating them in order to reduce the influence of the white noise  $v(n)$ .

Another desired property of  $K$  is that the changes in  $\hat{\mathbf{a}}$  should improve the estimate, decrease estimate errors. In other words, the direction of change must be related to the negative of gradient of the prediction error,  $[-\partial\epsilon/\partial\mathbf{a}]$ . From the prediction error formula

---

<sup>11</sup>In order to avoid that  $P_y = 0$  for deterministic signals ( $\sigma_v^2 = 0$ ), any positive number may be used instead of  $\sigma_v^2$  in eq.(3.50). The qualitative properties of the power spectrum and the use of its peak positions as estimates of eigenvalues are not affected by this change.

above, the gradient is given by  $[-\varphi(n)]$ . In order to decrease the prediction error,  $K$  should contain a factor  $[+\varphi(n)]$ .

The gain  $K$  is selected according to some criteria. One possibility, is to choose  $K$  that minimizes the mean square prediction error  $E[\epsilon^2(n)]$ . This is the principle of the adaptive zero estimator described in Subsection 3.3.3 and, in some detail, in Appendix C.

Another possibility is to choose  $K$  that minimizes the mean square estimation error  $E[\|\mathbf{a}(n) - \hat{\mathbf{a}}(n/n)\|^2]$  between the estimate and the actual vector of coefficients, assumed a random process in itself. This is the principle of the Kalman filter discussed in Subsection 3.3.2 and Appendix D.

### 3.3.2 Kalman Filter Implementation

For the Kalman filter implementation, eq.(3.49) is interpreted as the *measurement equation*, relating the measured quantity, the sequence  $y(n)$ , to the *system state*  $\mathbf{a}$ . In addition, the system state is assumed to evolve in range according to a *state equation*. For the present example, a simple Gaussian random walk model will be assumed:

$$\mathbf{a}(n) = \mathbf{a}(n-1) + \mathbf{w}(n), \quad (3.51)$$

where the *plant-noise*  $\mathbf{w}(n)$  is a white Gaussian noise vector of covariance  $\sum_w = \rho^2 I_p$  and  $I_p$  is the  $p \times p$  identity matrix.

From eqs.(3.49) and (3.51), the Kalman identifier can be written as shown in Algorithm 1 [51, 2], where,

$$\xi = \rho^2 / \sigma_v^2, \quad (3.54)$$

$V^\oplus(n/n \oplus 1)$  and  $V^\oplus(n/n)$  are the normalized error covariance matrices

$$V^\oplus(n/n \oplus 1) = E \left\{ (\mathbf{a}(n) - \hat{\mathbf{a}}^\oplus(n/n \oplus 1)) (\mathbf{a}(n) - \hat{\mathbf{a}}^\oplus(n/n \oplus 1))^H \right\} / \sigma_v^2, \quad (3.55)$$

---

**Algorithm 1** *Forward and Backward Kalman AR identifier* [51]. Initialize the forward filter with values  $\hat{\mathbf{a}}^-(p/p)$  and  $V^-(p/p)$ , and estimate the coefficients for  $n = p+1, \dots, N$ . Initialize the backward filter with  $\hat{\mathbf{a}}^+(N+1/N+1)$  and  $V^-(N+1/N+1)$ , and estimate the coefficients for  $n = N, N-1, \dots, p+1$ . The only parameter in this implementation is  $\xi$ , which controls the speed of convergence. The higher the  $\xi$ , the faster the convergence and the larger the variance of the estimate.

---

1. Prediction

$$\begin{aligned}\varphi(n) &= [ y(n-1), \dots, y(n-p) ], \\ \hat{\mathbf{a}}^\oplus(n/n \oplus 1) &= \hat{\mathbf{a}}^\oplus(n \oplus 1/n \oplus 1), \\ \epsilon^\oplus(n) &= y(n) - \varphi^T(n)\hat{\mathbf{a}}^\oplus(n/n \oplus 1).\end{aligned}\tag{3.52}$$

2. Update

$$\begin{aligned}V^\oplus(n/n \oplus 1) &= V^\oplus(n \oplus 1/n \oplus 1) + \xi I_p, \\ V^\oplus(n/n) &= V^\oplus(n/n \oplus 1) \times [I_p - \varphi^*(n)\varphi^T(n)V^\oplus(n/n \oplus 1)] \\ &\quad / [1 + \varphi^T(n)V^\oplus(n/n \oplus 1)\varphi^*(n)], \\ \hat{\mathbf{a}}^\oplus(n/n) &= \hat{\mathbf{a}}^\oplus(n/n \oplus 1) + V^\oplus(n/n)\varphi^*(n)\epsilon^\oplus(n).\end{aligned}\tag{3.53}$$


---

$$V^\oplus(n/n) = E \left\{ (\mathbf{a}(n) - \hat{\mathbf{a}}^\oplus(n/n)) (\mathbf{a}(n) - \hat{\mathbf{a}}^\oplus(n/n))^H \right\} / \sigma_v^2, \quad (3.56)$$

and  $(\cdot)^H$  denotes complex transpose. We use the notation in [51]: the symbol  $\oplus$  is a binary operator or label that can assume the values  $\{-, +\}$  to designate, respectively, forward and backward Kalman filters<sup>12</sup>, allowing to refer to both simultaneously.

The only free parameter in this implementation is  $\xi$ , the ratio of state and measurement noise variances. According to the description at the end of Subsection 3.3.1, we should expect that the higher the measurement noise variance (small  $\xi$ ), the smaller should be the gain  $K_f^\oplus$  of the filter and the corrections to the estimate  $\hat{\mathbf{a}}$ . The filter should take a long “time” to update estimates. On the other hand, if  $\xi$  is high, indicating that variations in  $y(n)$  are mostly driven by changes in the state vector  $\mathbf{a}$ , the filter should react quickly, through an increase in  $K_f^\oplus$ .

This is accomplished by the Kalman filter through matrix  $V^\oplus(n/n)$ . The update equations in Algorithm 1 indicate that the Kalman gain, the matrix that multiplies the prediction error, is given by<sup>13</sup>

$$K_f^\oplus(n) = V^\oplus(n/n) \varphi^*(n).$$

The update of  $V^\oplus(n/n)$ , eq.(3.53), can be written<sup>14</sup> as

$$[V^\oplus(n/n)]^{-1} = [V^\oplus(n/n \oplus 1)]^{-1} + \varphi^*(n) \varphi^T(n),$$

where  $V^\oplus(n/n \oplus 1) = V^\oplus(n \oplus 1/n \oplus 1) + \xi I_p$ . High  $\xi$  (low measurement noise compared to plant-noise) tends to “increase”  $V^\oplus(n/n \oplus 1)$  and  $V^\oplus(n/n)$ , and, as a consequence, the Kalman gain increases, as we expected.

---

<sup>12</sup>When all measurements  $y(n)$  are available, they can be processed either forward, i.e., starting at  $n = 0$ , or backward, starting at the last sample. In Subsection 3.3.4 we combine estimates obtained both ways, in order to improve the tracking of changes in the AR coefficients  $\mathbf{a}$ .

<sup>13</sup>Note the factor  $\varphi(n)$  in  $K_f$ , as discussed in Subsection 3.3.1.

<sup>14</sup>Use the matrix inverse lemma[32] in the form  $A - ABDA/(\lambda + DAB) = (A^{-1} + BD/\lambda)^{-1}$ , for  $\lambda$  scalar.

The influence of the term  $\varphi^*(n)\varphi^T(n)$  on the  $V^\oplus(n)$  update is better understood if we de-normalize the error covariance matrix  $V^\oplus$  and use the actual error covariance  $P^\oplus(n/n) = \sigma_v^2 V^\oplus(n/n)$ . Then, the update becomes

$$[P^\oplus(n/n)]^{-1} = [P^\oplus(n/n \oplus 1)]^{-1} + \varphi^*(n)\varphi^T(n)/\sigma_v^2.$$

Under high signal-to-noise ratio conditions, the second term ( $\varphi$  is a vector of signal samples) is high. At each update, the inverse of  $P^\oplus(n/n)$  is increased, and  $P^\oplus(n/n)$  decreased, indicating that the high SNR measurement is reducing the estimate error. If the SNR is low, the second term in the above update is low, and the improvement in error covariance due to measurement is small.

The standard Kalman filter is derived for models where  $\varphi(n)$  in the measurement equation is independent of the data. The application of the Kalman filter as the AR identifier, where  $\varphi(n)$  is the vector of past signal samples, results in the following [2]:

- $V^\oplus(n)$  depends on the signal  $y$  through  $\varphi(n)$ , as shown in the update equation (3.53). Under the Gaussian assumption,  $\sigma_v^2 V^\oplus(n)$ , can still be interpreted as an error covariance matrix, but conditioned to the set of measurements. If the measurement noise  $v(n)$  and plant noise  $w(n)$  are not Gaussian,  $\sigma_v^2 V^\oplus(n)$  can not be interpreted as error covariance;
- the correction to the state estimation,  $V^\oplus(n/n)\varphi^*(n)\epsilon(n)$  is a nonlinear function of the measurements  $y$ .

The Kalman filter described in Algorithm 1 was developed based on the underlying state-space model given by eqs.(3.49) and (3.51). From this point on, the filter is seen as an instrument to estimate DE coefficients, one whose response to changes is controlled by the parameter  $\xi$ . In Section 3.3.4, estimates from filters with different parameters are combined in such a way that the filter with the “best fit” to the local (in range) properties of the signal is weighted more. This justifies the concept that eqs.(3.49) and (3.51) do not, in fact, need to model the signal in a “global” sense[51].

### 3.3.3 The VFF Adaptive Zero Estimator

Instead of polynomial coefficients, zeros  $s_j$  of the polynomial can be estimated[48, 56]. As discussed in Section 3.2, the polynomial zeros have a simple physical interpretation: to the first-order in the sampling distance  $\Delta r$ , their phases are directly related to the eigenvalues<sup>15</sup>  $k_{rj}$ :

$$s_j = \rho_j \exp \{i\Omega_j\} = \exp \{(ik_{rj} - \alpha_j)\Delta r\}, \quad (3.57)$$

as long as the order of the AR model is the same as the number of propagating modes. When the order is larger, we either search for zeros close to the unit circle (small  $|\alpha_j|$ ) or for peaks of the spectrum  $P_y(k_r; r_n)$ , as discussed in Subsection 3.3.1.

The relation between the available signal  $y(n)$  and the AR coefficients  $\mathbf{a}(n)$ , eq.(3.49), is linear. Now we are faced with the problem of estimating the roots (in fact, their magnitudes and phases) of the associated characteristic equation (with  $a_0 = -1$ )

$$-\sum_{j=0}^p a_j s^{-j} = \prod_{j=1}^p (1 - s^{-1} s_j) = 0,$$

a nonlinear problem. In fact, estimating first the AR coefficients (linear estimation problem), and then finding the roots of the associated polynomial (a nonlinear, but reasonably well understood problem), is how Subsection 3.3.2 solves this nonlinear problem<sup>16</sup>.

The zero estimator minimizes the mean square prediction error  $\zeta(n; \theta) = E[|\epsilon(n; \theta)|^2]/2$  with respect to the parameters to be estimated, the magnitudes and phases of the roots grouped in the vector

$$\theta(n) = [\rho_1, \dots, \rho_p, \Omega_1, \dots, \Omega_p]^T. \quad (3.58)$$

---

<sup>15</sup>The magnitude of the first-order pole  $c_j$ ,  $\rho_j = [U_j(n)/U_j(n-1)] \exp\{-\alpha_j \Delta r\}$  [cf. eq.(3.27)], includes the ratio of modal amplitudes. For simplicity, we incorporate all magnitude factors in the exponential. The  $\alpha_j$  of eq.(3.57), therefore, has a contribution from the ratio of modal amplitudes.

<sup>16</sup>A concept developed by the eighteen century French engineer Gaspard Riche, Baron de Prony[32].

As discussed in Subsection 3.3.1, the minimization is carried out through the recursion

$$\hat{\theta}(n) = \hat{\theta}(n-1) + K(n)\epsilon(n). \quad (3.59)$$

The desired form of the gain  $K$  can be obtained by examining the Newton-Raphson method. Recursion (3.59) is designed to find the zero of  $[\partial_\theta \zeta(n)] = \epsilon(n)\partial_\theta \epsilon(n)$ . In the one-dimensional problem of finding the zero of  $f(x)$ , the Newton-Raphson iteration computes  $x_n = x_{n-1} + [-f'(x)]^{-1}f(x)$ . By analogy, the correction to  $\hat{\theta}$  in eq.(3.59) should be of the form  $[-\partial_\theta^2 \zeta(n)]^{-1}\partial_\theta \zeta(n)$ . Discarding the expectation operator, this correction reduces to  $P(n)\psi(n)\epsilon(n)$ , where  $\psi(n) = -\partial_\theta \epsilon(n)$ , and  $P(n)$  is an estimate of the second derivative of  $|\epsilon(n)|^2$ . Hence,  $K(n) = P(n)\psi(n)$  is the filter gain. Note the similarity with the Kalman gain in Algorithm 1,  $K_f(n) = V^\oplus(n/n)\varphi^*(n)$ , where  $\varphi(n)$  is  $-\partial_\theta \epsilon(n)$ .

In Appendix C we show that  $P(n)$  is updated at each step by a recursion of the form  $P^{-1}(n) = wP^{-1}(n-1) + \psi(n)\psi^T(n)$ , where  $0 < w \leq 1$  is the *forgetting factor*, which controls the tracking characteristics of the filter. If we set  $w = 1$ ,  $P^{-1}$  grows with  $n$ , the gain decreases, and at some point the filter stops updating the estimate. This makes sense if  $\theta$  is constant and the initial guess  $\theta_0$  is sufficiently closed to the solution of this nonlinear problem. For varying  $\theta$ , we make  $w < 1$ , and past measurements<sup>17</sup> are weighted less, allowing the estimate to adapt to changes in  $\theta$ . As  $w$  increases, the contribution from  $P^{-1}(n-1)$  decreases, and  $P^{-1}(n)$  is more representative of the present data, allowing for quicker adaptation.  $w$  is analogous to the parameter  $\xi$  in the Kalman identifier.

The choice of  $w$  is related to the expected variability of  $\theta$  (just as the choice of  $\xi$  is). We decided to use the *variable forgetting factor* proposed by Fortescue and co-workers.[16], which is data adaptive. The basic principle is that, under low noise conditions, changes in prediction or estimation errors (driven by changes in the measured signal) must be related to changes in  $\theta$ , and the filter should respond quickly by reducing

---

<sup>17</sup> $\psi(n) = \partial_\theta a^T(n)\varphi(n)$  contains information of past measurements through  $\phi(n) = [y(n-1), \dots, y(n-p)]^T$ .

---

**Algorithm 2** *VFF Adaptive Zero Estimator.* Initialize the forward filter with  $\widehat{\theta}^-(p)$  and  $P(p)$ , and estimate the zeros for  $n = p + 1, \dots, N$ . Initialize the backward filter with  $\widehat{\theta}^+(N+1)$  and  $P(N+1)$ , and estimate the zeros for  $n = N, N-1, \dots, p+1$ . The parameter of this implementation is  $J_0$  [see eq.(C.21) and related discussion].

---

$$\varphi(n) = [ y(n-1), \dots, y(n-p) ]$$

$$\begin{aligned} \epsilon^\oplus(n) &= y(n) - \mathbf{a}^T(n \oplus 1) \varphi(n). \\ L &= \left[ P(n \oplus 1) - \frac{1}{2} \frac{P(n \oplus 1) \psi(n) \psi^H(n) P(n \oplus 1)}{w(n) + \frac{1}{2} \psi^H(n) P(n-1) \psi(n)} \right] / w(n), \\ P(n) &= L - \frac{1}{2} \frac{L \psi^*(n) \psi^T(n) L}{1 + \frac{1}{2} \psi^T(n) L \psi^*(n)}, \\ \widehat{\theta}^\oplus(n) &= \widehat{\theta}^\oplus(n \oplus 1) + P(n) \Re[\psi(n) \epsilon^{\oplus*}(n)], \end{aligned} \quad (3.60)$$

Prepare for the next step:

1. Compute  $\mathbf{a}(n)$  using the zeros in vector  $\widehat{\theta}^\oplus(n)$ , and  $\Delta\mathbf{a} = \mathbf{a}(n) - \mathbf{a}(n \oplus 1)$ ;
2. Compute the gradient  $\psi(n \ominus 1)$  at  $\theta = \widehat{\theta}^\oplus(n)$ , eqs.(C.9), (C.12), and (C.14);
3. Compute the forgetting factor

$$w(n \ominus 1) = 1 - |\epsilon^\oplus(n) - \Delta\mathbf{a}^T(n) \varphi(n)|^2 / J_0. \quad (3.61)$$


---

w. Appendix C describes the formulation. The forgetting factor  $w(n)$  is computed at each step and its variations are controlled by a parameter  $J_0$ , chosen according to the measurement noise variance and the expected variability of the eigenvalues with range.

The design of the adaptive filter, based on a general recursive prediction error algorithm described by Ljung[44], is detailed in Appendix C. The estimator is described in Algorithm 2 in the form of forward and backward filters. The symbol  $\ominus$  is the complement of  $\oplus$  (see Algorithm 1 and related text), i.e.,  $\ominus = -\oplus = \{-, +\}$ .

There are differences between Algorithm 2 and the above simplified description of how  $\widehat{\theta}$  and  $P$  are updated. In the simplified description, the variables were assumed real. In fact,  $y$ ,  $\varphi$ ,  $\mathbf{a}$ ,  $\psi$ , and the prediction error are complex. For example, the two-step update

of matrix  $P$  in the algorithm corresponds to  $P^{-1}(n) = w(n)P^{-1}(n-1) + \Re\{\psi(n)\psi^H(n)\}$ .

The parameter  $J_0$  in eq.(3.61) controls the speed of convergence. It is chosen according to the measurement noise variance  $\sigma_v^2$  and the number of samples over which the eigenvalues are expected to be constant,  $N_0$ , as

$$J_0 = \sigma_v^2 N_0. \quad (3.62)$$

$J_0$  keeps  $w(n)$  near unit when the signal is noisy (and needs to be integrated over a large number of samples) or when the eigenvalues are expected to be constant.

### 3.3.4 Competitive Smoother

The algorithms described in the above subsections are controlled by a parameter,  $\xi$  or  $J_0$ , chosen according to the assumed eigenvalue variability and measurement noise level. Estimation errors should be smaller in regions where those parameters best match the local characteristics of the signal. A different estimator (different  $\xi$  or  $J_0$ ) would track better the signal at different regions if, for example, the local rate of change of eigenvalue varies with range.

Niedźwiecki [50] proposed combining a set of estimates according to the behavior of the prediction error. Basically, the best estimate (as indicated by the lowest prediction error) at each range is selected. Later, he applied this concept when developing the theory of competitive smoothers to deal with identification of parameters that change abruptly [51]. One of our main motivations to investigate eigenvalue estimation in range-dependent environments was a shallow-water waveguide where the seabed had a sudden change in properties that reflected in the modal content of a simulated pressure field. This example is discussed in Section 3.4.

The competition involves a forward and a backward filter. Near a parameter jump discontinuity, the estimates degrade in different ways, and so do the corresponding prediction errors. Figure 3-13 describes the concept of competition and the resulting im-

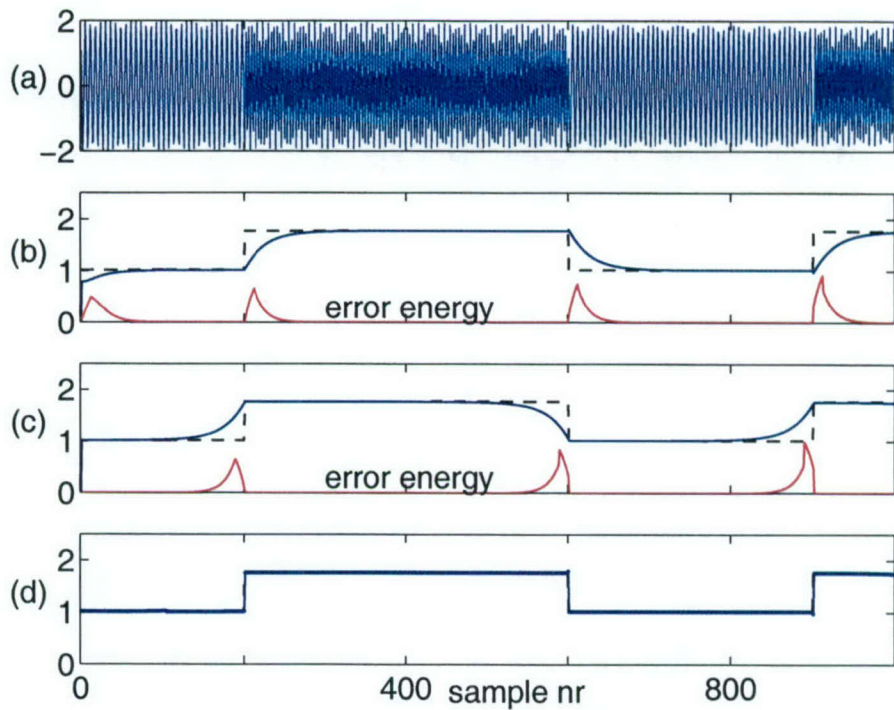


Figure 3-13: Competitive smoother concept. (a) Real part of the test signal; (b) actual (dashed line) and estimated phase rates, and local prediction error energy from a forward Kalman identifier with  $\xi = 0.0004$ ; (c) backward estimate and corresponding local prediction error energy; (d) result of the competition.

provement of the tracking characteristics. The test signal is a complex exponential whose phase rate (eigenvalue) jumps at samples 200, 600, and 900. The estimator is the Kalman identifier, Algorithm 1, with  $\xi = 0.0004$ .

The forward filter estimate (second plot) degrades right after each jump due to the finite “time” response of the filter. The prediction error increases accordingly. The curve labeled *error energy* is the energy,  $E_{M_a}^-(n) = \sum_{j=0}^{M_a-1} |\epsilon^-(n-j)|^2$ , of the prediction error computed over the past 11 and the present sample (over an analysis window of length  $M_a = 12$ ). The change in eigenvalue causes a pulse in the energy waveform after the jump.

The backward estimate and corresponding prediction error energy are shown in the third plot of Figure 3-13. The estimate transient and the error energy pulse are nearly a

mirror image of the forward case with respect to the jump. Here the energy is computed for the future samples (past, from the perspective of the backward filter),  $E_{M_a}^+(n) = \sum_{j=0}^{M_a-1} |\epsilon^+(n+j)|^2$ . The competition, in this example, consisted in choosing, at each sample, the estimate with smaller prediction error energy. The result, shown in the lower plot, is a significant improvement over the two previous estimates.

Niedźwiecki [51] developed the theory of competitive smoother for a moving average process. In the AR model case, the algorithm is not strictly valid, but [51] indicates that computer simulations, as the example in Figure 3-13, yield satisfactory results.

The competitive smoother is defined, in terms of forward and backward Kalman filter estimates, as the weighted average

$$\hat{\mathbf{a}}(n/M_a) = \mu^-(n)\hat{\mathbf{a}}^-(n/n) + \mu^+(n)\hat{\mathbf{a}}^+(n/n), \quad (3.63)$$

where  $M_a$  is the length of the competition analysis window,  $\mu^\oplus$  are *credibility coefficients* given by

$$\mu^\oplus = C \left[ \prod_{j=0}^{M_a-1} |\beta^\oplus(n \oplus j)| \right]^{-1/2} \left[ \sum_{j=0}^{M_a-1} \frac{|\epsilon^\oplus(t \oplus j)|^2}{|\beta^\oplus(n \oplus j)|} \right]^{-M_a/2}, \quad (3.64)$$

$$\beta^\oplus(n \oplus j) = 1 + \varphi^T(n \oplus j)V^\oplus(n \oplus j|n \oplus j \oplus 1)\varphi^*(n \oplus j), \quad (3.65)$$

and  $C$  is a normalization constant such that  $\mu^-(n) + \mu^+(n) = 1$ . When  $\xi \ll 1$  (slowly adapting Kalman filters), the simplified expression

$$\mu^\oplus = C \left[ \sum_{j=0}^{M_a-1} |\epsilon^\oplus(t \oplus j)|^2 \right]^{-M_a/2} \quad (3.66)$$

results.

Equation (3.64) is restricted to Kalman filters. The simplified eq.(3.66), on the other hand, was obtained in [49] for more general prediction-error based identification algorithms. It can be used with a set of forward/backward VFF adaptive zero estimators (Algorithm 2) with different parameters  $J_0$ .

For sufficiently large  $M_a$ , using the credibility given in eq.(3.66) corresponds to switching between estimates according to the prediction error energy [51]:

$$\hat{\mathbf{a}}(n/M) = \begin{cases} \hat{\mathbf{a}}^-(n/n-1), & E_{M_a}^-(n) \leq E_{M_a}^+(n), \\ \hat{\mathbf{a}}^+(n/n+1), & E_{M_a}^+(n) < E_{M_a}^-(n), \end{cases} \quad (3.67)$$

where

$$E_{M_a}^\oplus = \sum_{j=0}^{M_a-1} |\epsilon^\oplus(t \oplus j)|^2. \quad (3.68)$$

This is the rule used in the example of Fig. 3-13, with  $M_a = 12$ .

The competition can be extended to an arbitrary number of estimators. For example, a set of Kalman identifiers with different parameters  $\xi$  could be combined. At each range, the identifier that best models the local behavior of the signal would tend to "win" the competition. In order to reduce the estimate variance in regions where the signal properties do not change, the mean estimate[49]  $[.5\{\hat{\mathbf{a}}^-(n/n) + \hat{\mathbf{a}}^+(n/n)\}]$  or a higher order Kalman filter, can be included in the competition. High order filters are useful in regions where parameters change systematically and the first-order Kalman filter competition tends to introduce 'switching noise', increasing the estimate variance (see Appendix D on page 278).

As a guideline for the selection of control parameter ( $\xi$  or  $J_0$ ) for multiple estimator competition, [49] suggests that the *memory doubling* rule works well in practice. Memory length is the number of signal samples that effectively contributes to the estimate at any given  $n$ . In Subsection 3.3.5 we show that the effective memory length of the Kalman identifier, under conditions of low  $\xi$ , is inversely proportional to the square root of  $\xi$ ,  $N_{eff} \sim \xi^{-1/2}$ . For a bank of Kalman identifiers, therefore, the  $\xi$  must follow a geometric sequence of ratio 4:  $\xi_i = 4\xi_{i-1}$ . For the VFF zero adapter, eq.(3.62) suggests using a geometric sequence of ratio 2,  $J_{0,i} = 2J_{0,i-1}$ .

### 3.3.5 Pressure Field Decimation and Eigenvalue and Range Resolution

In range-dependent eigenvalue estimation, analogous to the time-frequency analysis of time-varying signals, an important issue is the trade-off between eigenvalue resolution, the ability to measure closely spaced eigenvalues, and range resolution, the ability to track eigenvalue changes with range. Eigenvalue resolution improves by increasing the range aperture over which the eigenvalue is estimated, while range tracking requires small apertures. Another associated issue is the estimate variance, which also depends on aperture.

We discuss briefly the issue of variance and eigenvalue resolution. We then propose the decimation of the pressure signal as a way to improve the estimate, reducing the order of the AR model (and the associated computational cost) without sacrificing either eigenvalue or range resolution. The main issue regarding decimation is one of choosing a suitable range spacing  $\Delta r$  for eigenvalue estimation.

Finally, we analyze the effective aperture associated with the sequential estimators of Subsections 3.3.2 and 3.3.3.

#### Eigenvalue Variance and Resolution

The variance of eigenvalue estimation depends on the sampling distance  $\Delta r$ , which, as discussed in Section 3.2, determines the distance between first-order poles in the complex plane. For constant poles (range-independent environments), as the pole distance increases, the Cramer-Rao bound (CRB) for multiple modes decreases and approaches that of a single mode, the lowest possible value it can attain, when the eigenvalue separation exceeds the critical value [62]  $\Delta k_C = 4\pi(N\Delta r)^{-1}$ , where  $N$  is the number of signal samples used in the estimation. This critical value is twice the Fourier resolution for a signal observed over an aperture  $N\Delta r$ , which is typically large for shallow-water, low-frequency acoustic signals.

For the TC2 example shown in Figures 3-9 and 3-10, the closest eigenvalues are the two first modes, with  $\Delta k = k_2 - k_1 \approx 0.003$  rad/m in the range-independent region. In order to attain  $4\pi(N\Delta r)^{-1} \sim 0.003$ , the aperture should be  $N\Delta r \sim 4200$  m, which is more than the available aperture in that region. In the range-dependent region, the eigenvalues are even closer, a problem compounded by their variability. These are the main reasons that high-resolution methods were proposed[6]. AR techniques can resolve eigenvalues using smaller apertures than the Fourier resolution, possibly allowing to track changes with range. The price to be paid by using smaller apertures is increased error variance bound (CRB).

### Pressure Field Decimation

In Subsection 3.2.3, we pointed out that, when the first-order poles are close in the complex plane, so that, for the *most spaced* eigenvalues, the first-order pole angular separation  $\delta k\Delta r$  is small, the CRB is proportional to  $N^{-1}(\delta k\Delta r)^{-2(M-1)}$  [40], where  $M$  is the number of modes. If  $\Delta r$  increases, the CRB improves (faster than increasing  $N$ ). When the spacing between *adjacent* eigenvalues reaches the critical value  $4\pi(N\Delta r)^{-1}$ ,  $\Delta r$  can still be increased, and  $N$  reduced, without affecting the CRB. This is one motivation for decimation. It improves the variance bound for very small  $\Delta k$ , and allow the reduction in the number of processed samples  $N$  when  $\Delta k$  reaches the critical value.

Quirk and Liu[59] analyzed the effects of decimation on AR spectral estimation of sum of of constant frequency sinusoids. The same spectral resolution is obtained with a smaller order when the signal is decimated. Basically, down-sampling by  $D$  (that is, increasing the sampling space to  $D\Delta r$ ) and using an order  $p/D$  has the same effect of using an order  $p$  on the original signal, but at a lower computational cost. The resolution does not change because, for  $N \propto p$ , the aperture  $N\Delta r = (N/D)(\Delta r/D)$  is fixed.

The computational cost of sequential estimators is associated to the size of the parameter vector being estimated. For an AR model of order  $p$ , the parameter vectors is of size  $p$  in the case of Algorithm 1 and  $2p$  for Algorithm 2. For the AR spectrogram, in

[6], the practical rule of setting the AR order to  $p = N/3$ , for a range aperture of  $N\Delta r$ , was adopted. If  $N$  is decreased and  $\Delta r$  increased (decimation), an smaller order can be used without changing the actual aperture.

Decimation is particularly advantageous for the computation of the AR spectrograms. An efficient modified covariance algorithm to compute order  $p$  AR coefficients over  $N$  data points requires  $Np + 6p^2$  operations (add/multiplies) [32]. If the  $N = 3p$  rule is used, the number of operations is  $9p^2$ . For the sliding window spectrogram, this cost is for each window position. If  $K$  total points are available and the AR coefficients are estimated by sliding the window one range step at a time, then the total number of window positions is  $K - N + 1$ , leading to  $9(K - N + 1)p^2 \simeq 9(K - 3p)p^2$  operations to compute all sets of AR parameters. If the signal is decimated by  $D$ , the number of operations per window position drops to  $9p^2/D^2$ , the total number of points to  $K/D$  and the total number of operations to  $9(K - 3p)p^2/D^3$ , a significant reduction.

A question of practical interest is the maximum decimation rate that can be achieved for typical experimental data. As discussed in Appendix A, monofrequency acoustic fields must be sampled at a few samples per wavelength,  $\Delta r = \lambda/n_\lambda = 2\pi/(n_\lambda k_0)$ , where  $k_0 = \omega/c_0$  is some representative water wavenumber. The wavenumber spectrum can represent modes in the range  $|k_r| < \pi/\Delta r = n_\lambda k_0/2$ . On the other hand, modal eigenvalues are restricted to the smaller interval between the water and basement (of sound speed  $c_b$ ) wavenumbers,  $k_b < k_r < k_0$ .

The Nyquist sampling distance for a complex signals of bandwidth  $(k_0 - k_b)$  is  $2\pi/(k_0 - k_b)$ . The original sampling space  $2\pi/(n_\lambda k_0)$  can, therefore, be reduced by the decimation factor  $D = [2\pi/(k_0 - k_b)]/[2\pi/(n_\lambda k_0)] = n_\lambda/(1 - c_0/c_b)$ . As an example, if  $n_\lambda = 3$ ,  $c_0 = 1490$  m/s, and  $c_b = 1800$  m/s, the original sampling space can be increased 17 times. Higher  $n_\lambda$  are common.

The decimation process is shown in Figure 3-14. Initially, the modal spectral lines are concentrated in an interval  $(k_{min}, k_{max})$  around a wavenumber  $k_{avg}$ , and the corresponding poles in an angular sector  $(k_{max} - k_{min})\Delta r$  around the angle  $k_{avg}\Delta r$ . The signal

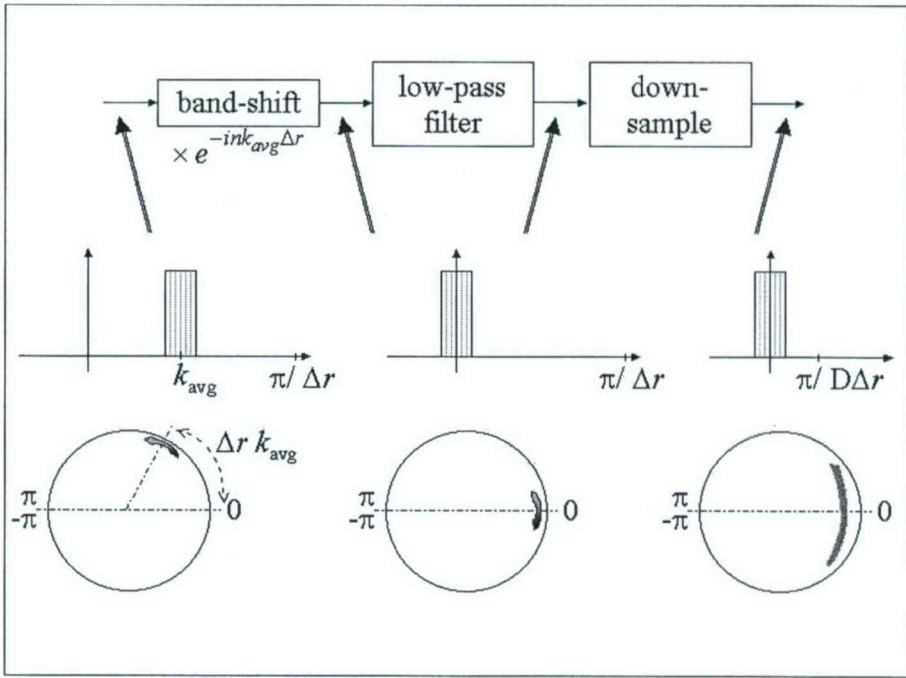


Figure 3-14: Decimation of the complex modal sum. A signal with energy concentrated around the wavenumber  $k_{med}$  is band-shifted to zero, filtered, and down-sampled. The effects of the process on the wavenumber spectrum and on the pole distribution in the unit circle are illustrated.

is multiplied by the complex exponential  $\exp\{-ink_{avg}\Delta r\}$ , resulting in a wavenumber spectrum and pole phases shifted to a region around zero. The low-pass filtering stage removes spectral components outside of the band of interest near  $k_r = 0$ , such as noise, and work as an anti-aliasing filter. In addition, filtering increases the signal-to-noise ratio by decreasing the noise power. In the last stage, one in every  $D$  samples is selected to compose the new signal, increasing the sampling distance to  $D\Delta r$  and spreading the poles in angle. The wavenumber spectrum is now concentrated in an interval  $(k_{min} - k_{avg}, k_{max} - k_{avg})$  around zero, and the poles are spread out in an angular sector  $(k_{max} - k_{min})D\Delta r$ .

The actual bandwidth of the modal sum is larger than the total eigenvalue excursion by an amount related to the eigenvalue rate of change. If the filtering operation remove

spectral energy associated with the rate of change, then the estimated eigenvalue rate of change will be reduced. A long aperture wavenumber spectrum, as the one shown in Figure 3-2, may reveal the total bandwidth and is a helpful tool in selecting  $k_{min}$  and  $k_{max}$ .

The maximum possible decimation factor  $D$  is the one that extends the spread of poles to the whole region  $(-\pi, \pi)$  near the unit circle, i.e.,  $(k_{max} - k_{avg})D\Delta r = 0.5(k_{max} - k_{min})D\Delta r < \pi$  and

$$D < 2\pi/[(k_{max} - k_{min})\Delta r].$$

For  $M$  propagating modes, this maximum decimation rate would roughly correspond to have the first-order poles spread out from  $(k_{avg} - k_M)D\Delta r = -\pi + \pi/M$  to  $(k_1 - k_{avg})D\Delta r = \pi - \pi/M$ .

For range-dependent media, a tighter restriction is imposed by the estimation error when the first-order poles are approximated by the AR characteristic polynomial zeros. To the first-order in variations of the poles with range, the error magnitude is given, for  $M = 2$  modes, by eq.(3.41). For slow eigenvalue variations such that  $\beta_1(D\Delta r)^2 \ll 1$ , eq.(3.41) reduces to

$$|\Delta c_1| \approx \frac{|\beta_1| (D\Delta r)^2}{\sqrt{2 - 2 \cos [(k_2 - k_1)D\Delta r]}},$$

and the error increases with  $\Delta r$  in the region of interest  $[0 < (k_2 - k_1)D\Delta r \leq \pi]$ .

As an example of the effect of decimation, consider the example of Figures 3-9 to 3-12 (2001 ITW test case 2), using the modes computed for the actual experiment. The decimation factor is set to  $D = 4$ , increasing the sampling distance to  $D\Delta r = 20$  m. The decimation process includes only the band-shift and down-sampling of Figure 3-14 and is done directly on the phases and amplitudes of each mode (no filtering necessary). As before, the DE coefficients are computed exactly using eq.(3.46).

Figure 3-15 shows the eigenvalues estimated as the roots of the characteristic equation (upper plots) and by iterating the right-pole [eq.(3.48)] with the roots as initial values (roots from the range independent region for the middle plots, and from the range-

dependent region for the lower plots).

The results in the upper plots are qualitatively similar to those shown in Figure 3-12, with a slight increase of the error of the roots corresponding to the 5th mode (the one with highest rate of change with range) in the range-dependent region.

The middle plots indicate errors smaller for the 1st mode right-pole iteration than with the original  $\Delta r$ , possibly a consequence of the smaller error of the root in the range-independent section.

The comparison of the middle plots of Figures 3-12 and 3-15 reveals an improvement of the estimation when using decimated data, suggesting smaller errors between roots and first-order poles at the initial iteration point  $r = 5$  km. In the range-independent region, where roots and first-order poles coincide, this improvement is an indication of smaller errors in the computation of polynomial roots, a benefit of having them farther apart in the complex plane[58], i.e., another advantage of decimation.

The estimates and the error in the lower plots are similar to those of Figure 3-12. The decimation neither improves or degrades the behavior of the iteration in eq.(3.48) when it is initialized with the polynomial roots at  $r = 0$  (where the error between characteristic polynomial roots and the first-order poles tends to be high because of the eigenvalue rate-of-change).

### Effective Memory Length

For the spectrogram methods discussed in Subsection 3.1.2, the aperture is roughly defined by the length of the range window within which either the periodogram or the AR spectrum is computed at each range. For sequential estimation, the effective sample size  $N$  depends on the particular algorithm.

Gustafsson and co-workers [28] defined a measure of time (range) resolution as an effective number of samples or *effective memory length*  $N_{eff}$ <sup>18</sup>, and obtained expressions for different algorithms, basically variants of the Kalman filter described in Algorithm

---

<sup>18</sup>In [28]  $N_{eff}$  is called *time resolution*.

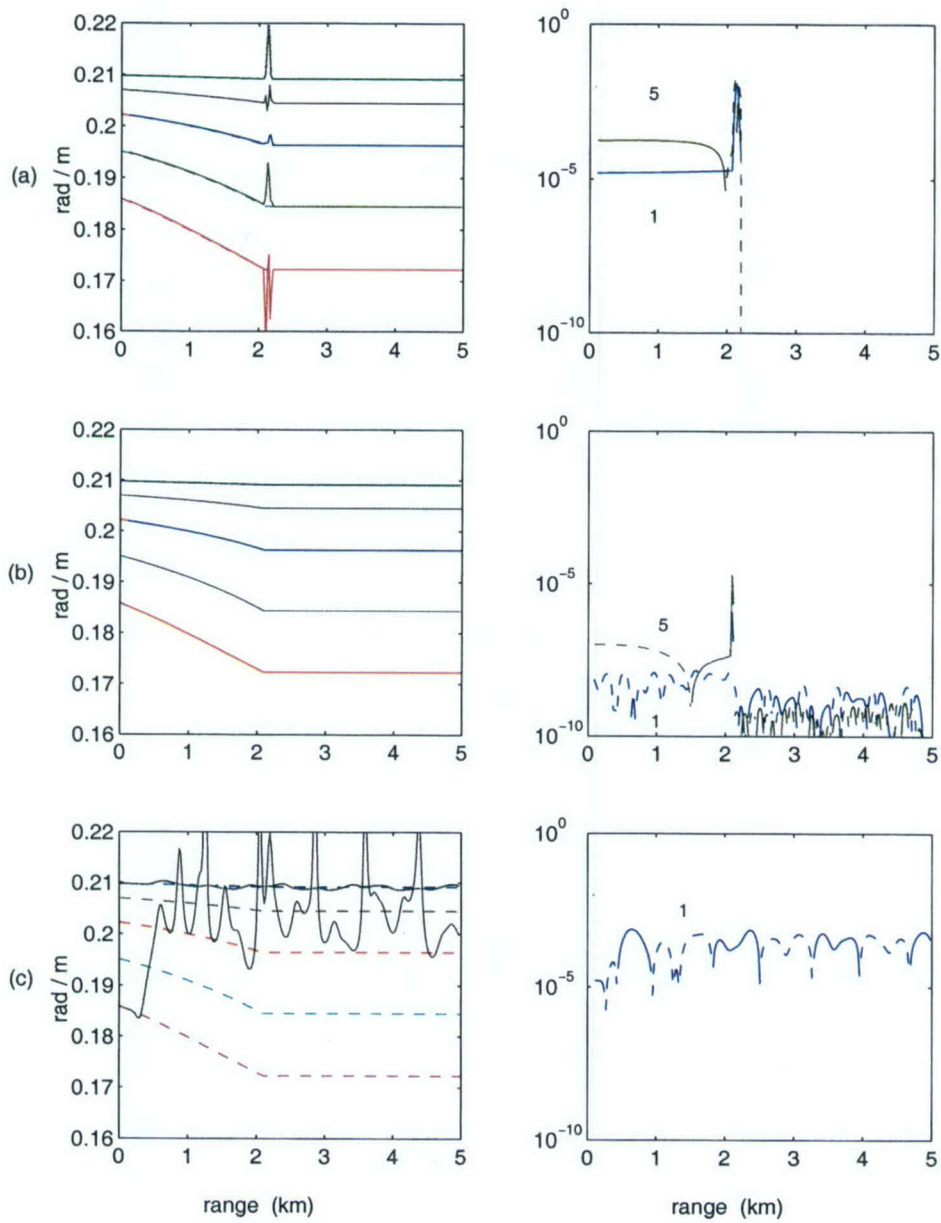


Figure 3-15: Exact DE example, decimated signal,  $D\Delta r = 20$  m - estimation of eigenvalues [cf. Figure 3-12 before decimation,  $\Delta r = 5$  m]. Plots on the left show actual (dashed lines) and estimated (solid lines) modal eigenvalues. Semi-log plots on the right show the estimation error for selected modes (indicated by mode number), where positive values of error are represented by the solid portions of the lines, while the dashed portions represent negative error. Eigenvalues derived from first-order poles estimated: (a) as DE characteristic polynomial zeros; (b) and (c) from iteration of right-poles, eq.(3.48) initialized with polynomial zeros at (b)  $r = 5$  km, and, for modes 1 and 5, (c)  $r = 0$ .

1. For that algorithm, the effective memory length depends on  $k_r$  and is given by

$$N_{eff}(k_r, r_n) \approx \frac{2}{\sqrt{P_y(k_r; r_n)}} \frac{\sqrt{p}\sigma_v}{\sqrt{W^H(k_r) \sum_w W(k_r)}} \quad (3.69)$$

where  $p$  is the order of the AR model,  $W(k_r) = [e^{ik_r \Delta r}, \dots, e^{inp k_r \Delta r}]^T$ , and, as before  $\sum_w = \rho^2 I_p$  is the state noise covariance matrix. This is an asymptotic result valid for  $p \rightarrow \infty$  and  $\|\Sigma_w\| \rightarrow 0$ , i.e., for large model orders and “slow filters”. Using these expressions for  $\sum_w$  and  $W$ , and  $\xi = \rho^2/\sigma_v^2$  [cf. e.(3.54)], eq.(3.69) simplifies to

$$N_{eff}(k_r, r_n) \approx \frac{2}{\sqrt{P_y(k_r; r_n)}} \frac{\sqrt{p}}{\sqrt{\xi W^H(k_r) W(k_r)}} = \frac{2}{\sqrt{\xi P_y(k_r; r_n)}}. \quad (3.70)$$

This result is consistent with the analysis in [49, 51]: the Kalman filter parameter  $\xi$  controls its effective memory length. A set of competing filters corresponds, then, to a set of memory lengths that should fit different range scales of signal variations, as discussed in Subsection 3.3.4.

Equation (3.70) can provide a relation between the parameter  $\xi$  and the signal parameters.  $M$  of the  $p$  zeros of the characteristic equation (those closest to the unit circle) are estimates of the first-order poles  $c_m = |c_m| \exp\{K_m \Delta r\}$ , where typically  $|c_m| \sim 1$ . Using the zeros, eq.(3.50) can be written as

$$P_y(k_r; r_n) = \frac{\sigma_v^2}{\prod_{m=1}^p |1 - s_1(n)s^{-1}|_{s=\exp\{i\Delta r k_r\}}^2}, \quad (3.71)$$

where, without loss of generalization,  $s_m = c_m$  for  $m = 1, \dots, M$ . Let<sup>19</sup>  $|c_m| = 1 - \epsilon_m$  and assume  $k_r$  is close to  $K_1$ , for example. If the other zeros are far enough, the variation of  $P_y$  in the neighborhood of  $K_1$  is dominated by the factor  $|1 - c_1(n)s^{-1}|$  and one can

---

<sup>19</sup>For  $c_m \sim \exp\{-\alpha_m \Delta r\}$ ,  $\epsilon_m \sim \alpha_m \Delta r$ .

assume that the remaining factors are constant, say

$$\begin{aligned}
P_y(k_r; r_n) &\approx \frac{\sigma_v^2}{A^2(K_1) |1 - c_1(n)e^{-ik_r \Delta r}|^2}, \\
&\approx \frac{\sigma_v^2}{A^2(K_1) |1 - (1 - \epsilon_1)e^{i(K_1 - k_r) \Delta r}|^2}, \\
&\approx \frac{\sigma_v^2}{A^2(K_1) [1 + (1 - \epsilon_1)^2 - 2(1 - \epsilon_1) \cos[(K_1 - k_r) \Delta r]]}, \\
&\approx \frac{\sigma_v^2}{A^2(K_1) \{\epsilon_1^2 + [(K_1 - k_r) \Delta r]^2\}},
\end{aligned}$$

where the approximation  $\cos x \approx 1 - x^2/2$  was used for  $k_r$  near  $K_1$ . The term  $A^2(K_1)$  accounts for the product of the other factors,

$$A(k_r) = \prod_{m=2}^p |1 - s_m e^{-ik_r \Delta r}|.$$

Therefore, near  $k_r = K_1$ , the Kalman filter effective memory length is, from eq.(3.70),

$$N_{eff}(k_r, r_n) \approx \frac{2A(K_1)}{\sigma_v} \sqrt{\frac{\epsilon_1^2 + [(K_1 - k_r) \Delta r]^2}{\xi}}, \quad (3.72)$$

which indicates that  $\sqrt{\xi}$  scales with  $\epsilon_1$ , the distance from the pole to the unit circle. In case there is a pole close to  $c_1$ , say  $c_2$ , such that  $\cos[(K_2 - K_1) \Delta r] \approx 1 - [(K_2 - K_1) \Delta r]^2/2$ , eq.(3.72) becomes, near  $k_r = K_1$

$$N_{eff}(K_1, r_n) \approx \frac{2A'(K_1)}{\sigma_v} \sqrt{\frac{\{\epsilon_2^2 + [(K_2 - k_r) \Delta r]^2\} \{\epsilon_1^2 + [(K_1 - k_r) \Delta r]^2\}}{\xi}}, \quad (3.73)$$

where the term  $A'$  is does not contain the contribution of the zero  $s_2 = c_2$ , i.e.,  $A' = \prod_{m=3}^p |1 - s_m e^{-ik_r \Delta r}|$ . The influence of the close pole depends on the angular separation  $|K_2 - K_1| \Delta r$  and its distance to the unit circle,  $\epsilon_2$ .

In [28], the memory length was obtained for a RLS filter, seen as a particular case of the Kalman filter. The RLS effective memory length is then shown to be independent

of  $k_r$  and (asymptotically) given by

$$N_{eff}^{RLS} \approx \frac{2}{1 - w(n)}, \quad (3.74)$$

where  $w(n)$  is the (possibly variable) *forgetting factor*. The VFF filter of Algorithm 2 has an structure similar to the RLS filter. The expression for the VFF estimator memory length from [16, eq.(9)] is consistent with the above expression [cf. eq.(C.20) in Appendix C].

## 3.4 Numerical and Experimental Results

### 3.4.1 A Note on Model Order Selection

Order selection is an important issue in AR estimation discussed by Becker[6] in the context of eigenvalue estimation. When computing AR spectrograms, we follow the rule of one-third of the number of samples in the range window,  $p \sim N/3$ , which must be equal or higher than the number of modes. This rule gives very high orders, especially when the sampling distance  $\Delta r$  is small.

When the  $\Delta r$  is such that the first-order poles are spread over a large angular region of the complex plane, setting the AR order to the number of expected modes, or slightly above, may be feasible even for the spectrogram.

For the sequential algorithms, we set the minimum order as the estimated number of modes from the wavenumber spectrum or AR spectrogram. Improved resolution is typically observed with higher orders. Under the condition of large first-order pole spread, the one-third rule was approximately applied to sequential algorithms by setting the order to three times the expected number of modes  $p \sim 3M$ , which corresponds to using  $3M$  past samples to predict  $y(n)$ .

### 3.4.2 Abrupt Change of Eigenvalues: Synthetic Data

The initial motivation for the present development was the degradation observed with the AR spectrogram of a synthetic acoustic data with an abrupt change in eigenvalues.

The 50 Hz signal used in the present analysis is from the ITW test case 3 (TC-3) [cf. Subsection 3.2.5]. A detailed description of all test cases is given in [9]. Briefly, the TC-3 environment consists of “an intrusion of (high sound velocity) basement in the (lower sound velocity) sediment to simulate an uplifted fault structure”. Figure 3-16 contains a succinct description of the environment. There are three range-independent regions (sediment–intrusion–sediment) in the ranges, respectively, 0–1.1 km, 1.1–2.9 km, and 2.9–5.0 km. The receiver depth is 25 m and the source depth is 20 m.

Figure 3-16 shows the pressure signal and a wavenumber spectrum. Pressure magnitude multiplied by  $\sqrt{r}$  is shown in the upper plot as a function of range; the solid line is the original signal at a range sampling of 5 m. The crosses represent pressure decimated by 25. Residual phase is shown in the middle. The residual pressure is obtained by multiplying the pressure by the complex exponential  $\exp\{-ik_{ref}r\}$ , where  $k_{ref} = \omega/c_{ref}$ , and  $c_{ref}$  is indicated in the figure.

The lower plot shows the order 100 AR wavenumber spectrum using all the original data (5000 m aperture). Four spectral lines corresponding to propagating modes are observed at 0.1789, 0.1937, 0.2034, and 0.2088 rad/m. The decimation filter was designed for a passband wavenumber range of 0.17–0.22 rad/m [ $\Delta r \leq 2\pi/(0.22 - 0.17) \sim 125.7$  m]. We set  $\Delta r$  to 125 m, resulting in an angular pole spread of  $125(0.2088 - 0.1789)$  rad =  $214^\circ$  around the unit circle.

Figure 3-17 compares four eigenvalue estimates using the peaks of an order-4 AR spectrogram, the roots of the order-4 AR coefficients estimated by competition between a single pair of Kalman identifiers, the roots estimated by competition of a pair of the VFF zero estimators, and the peaks of order-12 AR spectra obtained from the competition among four pairs of Kalman identifiers. The eigenvalues computed numerically from the actual TC3 environment properties are shown as dashed lines. The fifth mode in the

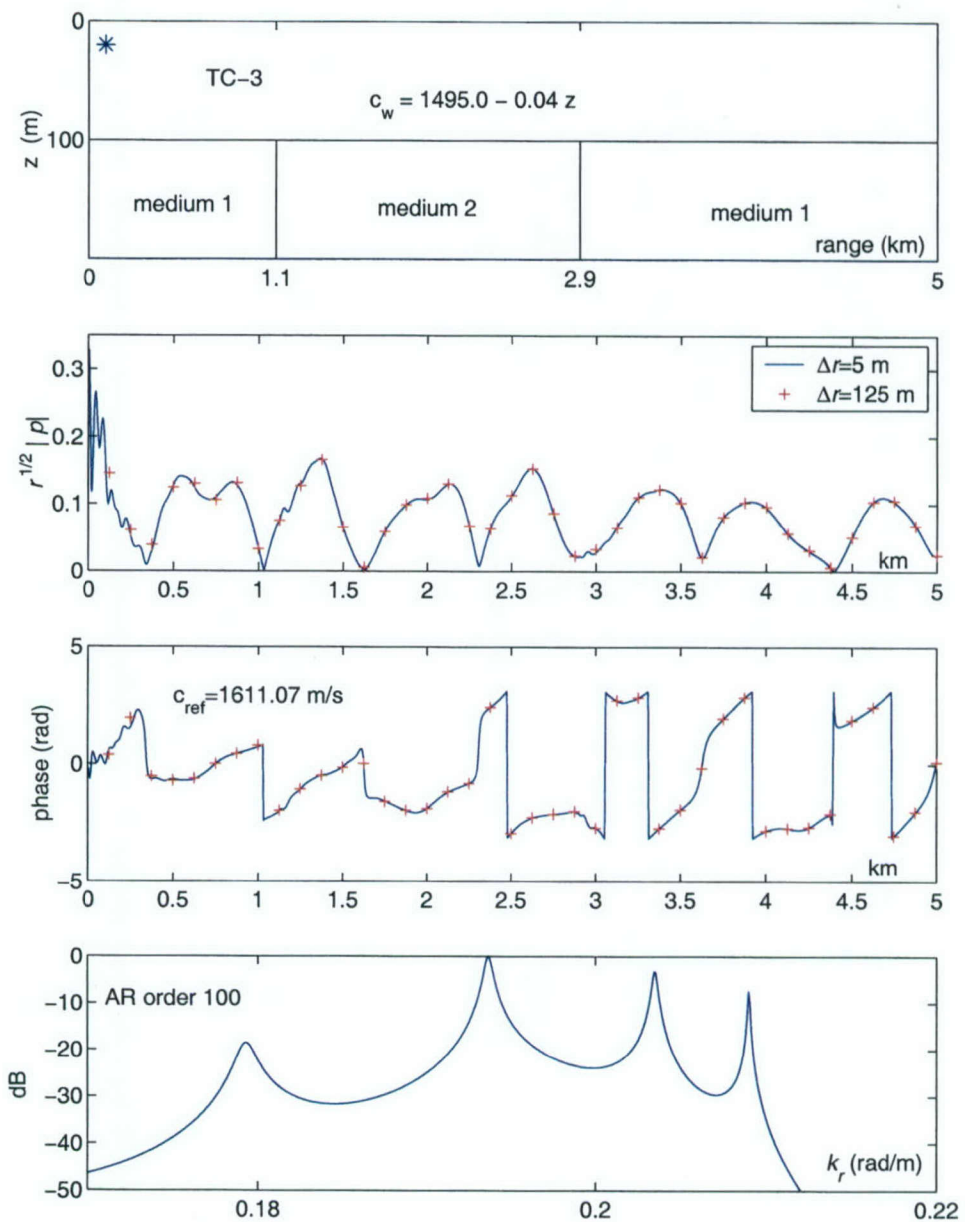


Figure 3-16: ITW TC-3 environment and 50 Hz signal and spectrum. Upper plot: the environment consists of an 100 m deep water layer overlaying two different subbottoms (media 1 and 2) with sharp transitions at  $r = 1.1$  km and 2.9 km. In the expression for sound velocity (m/s) in water,  $z$  is in meter. Two middle plots: magnitude and (residual) phase of the 50 Hz signal: original (solid lines) and decimated (crosses). Lower plot: order 100 AR wavenumber spectrum computed for the full 5 km aperture of the original signal. Four strong peaks, corresponding to propagating modes, are observed.

surrounding media was found numerically, but not observed in any of the estimates.

The abrupt change in the computed eigenvalues mark the transition between media. A fifth mode was computed for the surrounding medium, but was not observed in any estimate nor in the full aperture spectrum of Figure 3-16.

All estimators used the decimated signal ( $\Delta r = 125$  m). For the AR spectrogram, an order of four is equivalent to order 100 in the original signal ( $\Delta r = 5$  m) .

The improvement in spatial tracking of the order-4 AR competitive smoother over the AR spectrogram peaks is apparent in the highest mode (near 0.18 rad/m). The low order mode estimates degradation, compared to the AR peaks, is the result of the larger aperture (1500 m, corresponding to a number of samples three times the order for the AR spectrogram) associated with the lower variability of those modes.

The VFF zero estimator result is similar to the AR spectrogram peaks, suggesting comparable effective memory. The competition between a single pair of VFF estimators resulted in a marginal improvement in the spatial tracking.

The competition among five order 12 AR Kalman identifiers results in improved estimation variance without any degradation in the tracking characteristics. The parameter  $\xi$  was set at  $10^{-3}$  for the first filter and divided by four for the next one, in a sequence that translates into memory doubling. The change in eigenvalue can be now observed on the other modes. An AR spectrogram of order 12 would require at least 24 signal samples per window, corresponding to an aperture of 3000 m and a consequent degradation in the tracking characteristics.

### 3.4.3 Single-Mode Eigenvalue Estimation: Experimental Data

An acoustic signal from SWAT 2000/MOMAX III experiment 1 is shown in Figure 3-18. In experiment 1 a stationary source transmitted a 20 Hz tone in 75 m deep waters. The magnitude, phase, and a spectrum of a signal from one of the two drifting buoys are shown in Fig. 3-18. The spectrum was computed for the raw data, which includes strong, noise-like peaks. It shows a single mode, which is also indicated by the

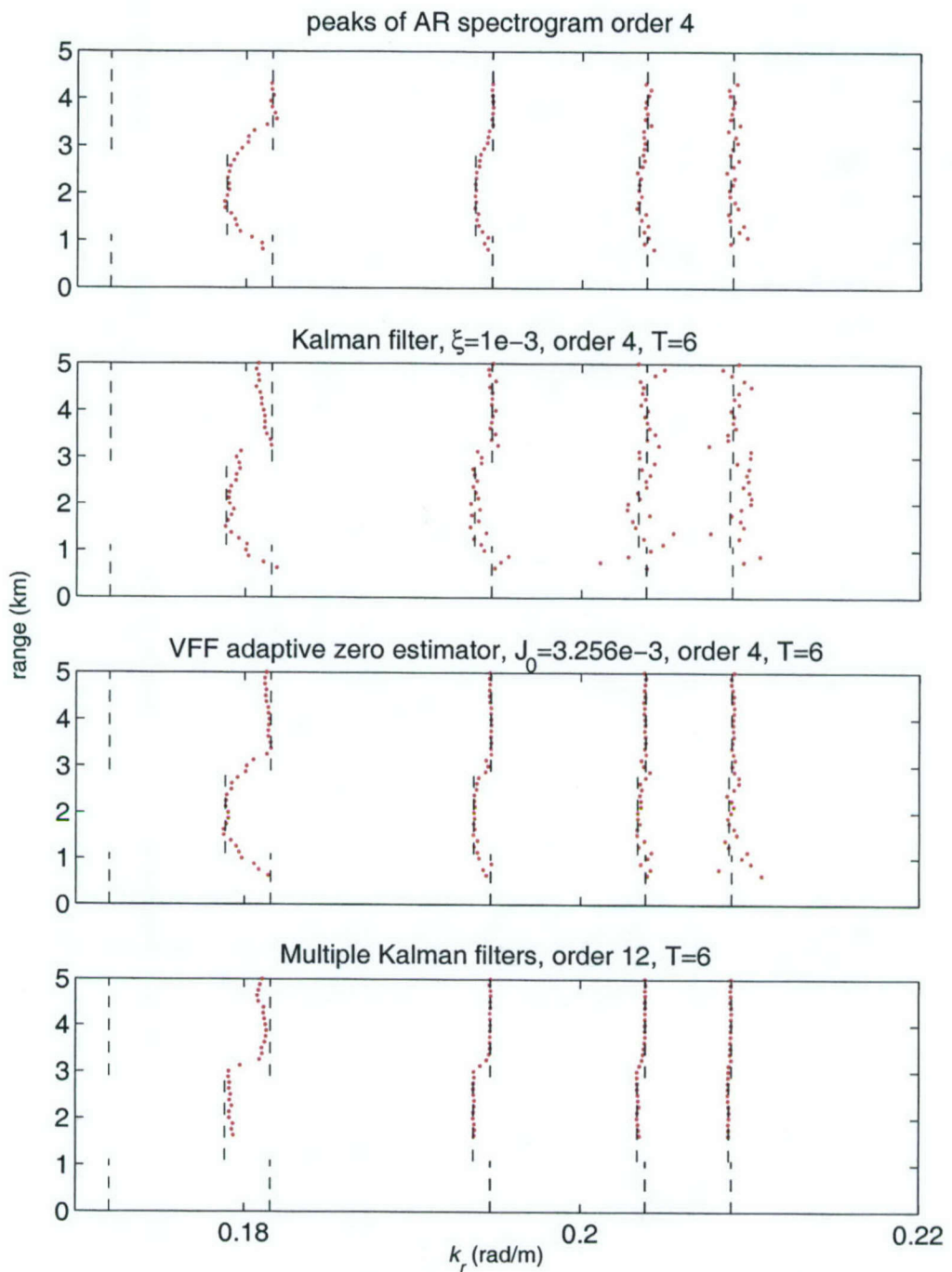


Figure 3-17: ITW TC-3 50 Hz eigenvalue estimation. The plots show wavenumber as a function of range, obtained by processing decimated signal ( $\Delta r = 125$  m) and four estimators. Dashed lines indicate the wavenumber computed from the “solution” given after the workshop. The dots represent wavenumber estimates.

absence of an interference pattern in the magnitude. The fact that the phase became nearly constant after removing a factor corresponding to a single eigenvalue at  $0.08 \text{ m}^{-1}$  strongly suggests, by itself, a single mode.

For a single mode,  $p\sqrt{r} \sim \exp\{i \int^r k_{r1}(r')dr'\}$ , and the local eigenvalue can be computed as the derivative of the pressure phase with respect to range, formally,

$$k_{r1}(r) = \frac{d}{dr} \Im \{ \ln(p\sqrt{r}) \},$$

where  $\Im\{\cdot\}$  denotes the imaginary part. The smoothness of the filtered phase in Figure 3-18 suggests that a reasonable numerical derivative can be computed. This is the reference eigenvalue used to compare other estimation results.

Figure 3-19 shows the results. The dashed line indicates the eigenvalue computed by numerical differentiation of the filtered pressure signal. The estimate indicated by the jagged, solid line is formed by the peaks of order 1 AR spectra (window aperture of 100 m, corresponding to  $100/\Delta r = 2$  points in range, the minimum possible window size for AR spectrum estimation) computed every 50 m. The estimate indicated by the triangular symbols was obtained by competition of three forward/backward Kalman identifiers (with  $\xi$  of 0.01, 0.001, and 0.0001) using a smoothing memory of  $T = 6$ .

Estimation of the varying single mode by the three methods gives essentially the same result. The numerical differentiation of the phase is equivalent to taking the phase of the ratio of adjacent samples. This ratio is the first-order pole  $c_1(n) = y(n)/y(n-1)$  that characterizes the single mode and whose phase, as discussed in connection with eq.(3.27), is approximately  $k_m(r)\Delta r$ .

For an order one AR model using two samples (window length = 2, overlap of 1 sample), the DE coefficient and the first-order pole are the same, and equal to the root of the characteristic equation,  $1 - c_1(n)s^{-1} = 0$ . Therefore, the order one TVAR method (using the root of the characteristic equation) estimates  $c_1(n)$ , and gives the same result as the differentiation of the phase. The three methods (differentiation, order one AR

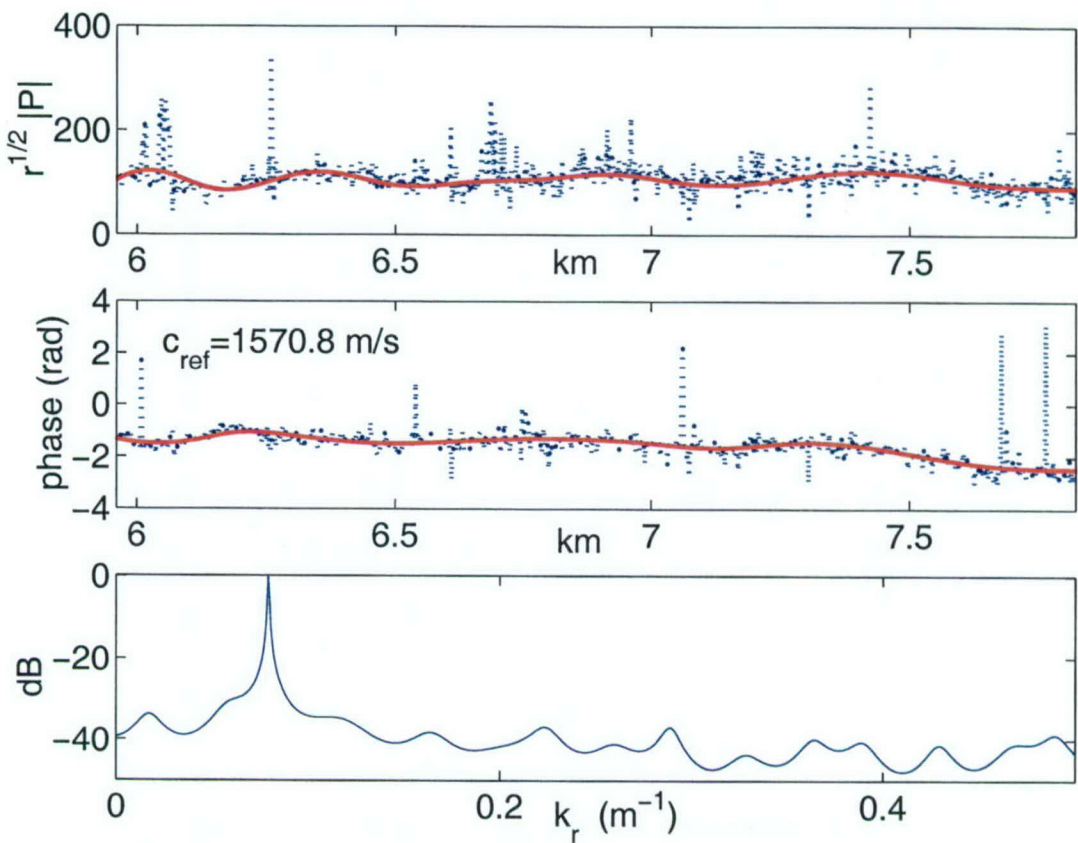


Figure 3-18: MOMAX 20 Hz signal and spectrum. Pressure magnitude multiplied by  $\sqrt{r}$  is shown in the upper plot as a function of range; the dotted line is raw data; the solid line represents filtered pressure preceding the decimation down-sampling stage. Residual phase (see Fig. 3-16) is shown in the middle. The lower plot shows the order 100 AR wavenumber spectrum using the full range aperture of the upper plots, and shows a single spectral line corresponding to a propagating mode at  $0.07905 \text{ m}^{-1}$ . The decimation filter was designed for an equivalent wavenumber range of  $0.06-0.1 \text{ m}^{-1}$  [ $\Delta r < 2\pi/(0.1 - 0.06) \sim 157 \text{ m}$ ;  $\Delta r = 50 \text{ m}$  was used].

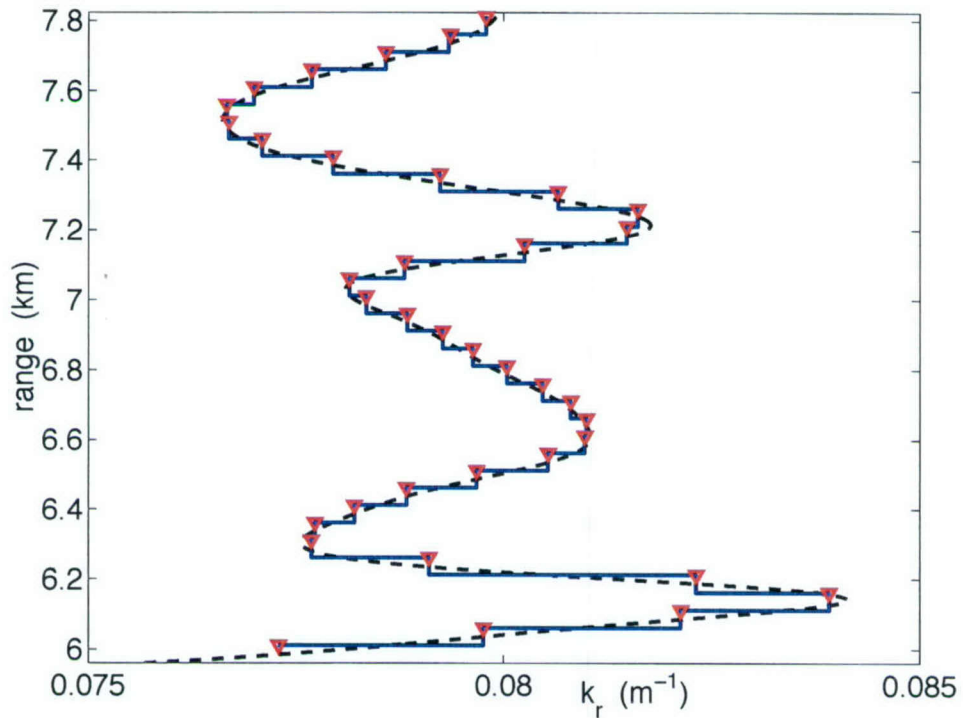


Figure 3-19: *MOMAX 20 Hz eigenvalue tracking*. The plot shows eigenvalue as a function of range, obtained by processing a decimated signal ( $\Delta r = 50$  m): (a) dashed line - differentiation of the signal phase; (b) solid line - peaks of an order 1 AR spectrogram; (c) triangle - 3 competing forward/backward Kalman filter pairs.

spectrogram using two samples with overlap of one sample between adjacent windows, and order one sequential TVAR estimator) are computing essentially the same quantity,  $c_1(n)$ , which explains the similar results.

### 3.4.4 Multiple Mode Estimation: Experimental Data - 50 Hz

The signal analyzed is from experiment 2 of MOMAX III and corresponds to the along-shelf portions of the tracks shown in Figure 3-6, where the local depth at the source was about 82 meters.

The signal is shown in Figure 3-20. Both original and filtered (preceding down-sampling) are shown, together with two spectra using the full available aperture (13 km). A Hann window periodogram and an AR spectrum of order of 200 are shown in the lower plot. Both spectra show two strong lines corresponding to propagating modes and some small peaks, barely noticeable in the scale shown. The original series from the processed MOMAX data has a non-uniform sampling space of 2.2 meters in average, and was interpolated to an uniform grid of 2.6 m spacing. The signal was decimated by  $D = 20$ , resulting in a final spacing of 52 m.

The AR spectrogram and the competitive smoother results are shown in Figure 3-21. The order 10 AR spectrogram uses a window of 1976 meters, with an overlap of 1768 m between adjacent window positions. The two strong spectral lines from figure 3-20 are clearly seen. In addition, the AR spectrogram shows a third mode that is detected at some ranges near  $k_r = 0.185$  rad/m, which suggests that the third mode was near the transition between propagating and evanescent. Weak transient spectral lines also appear near  $k_r = 0.215$  and  $0.23$  rad/m. These eigenvalues correspond to phase speeds,  $C_p = \omega/k_r$ , below the minimum sound speed in water (1494 m/s). These transient spectral lines have been observed in other experimental signals and are not consistent with a stationary, range-independent media model.

Thirteen forward/backward Kalman filters competed to obtain the results shown by dots. The underlying AR model is of order 12. After obtaining the AR filter coeffi-

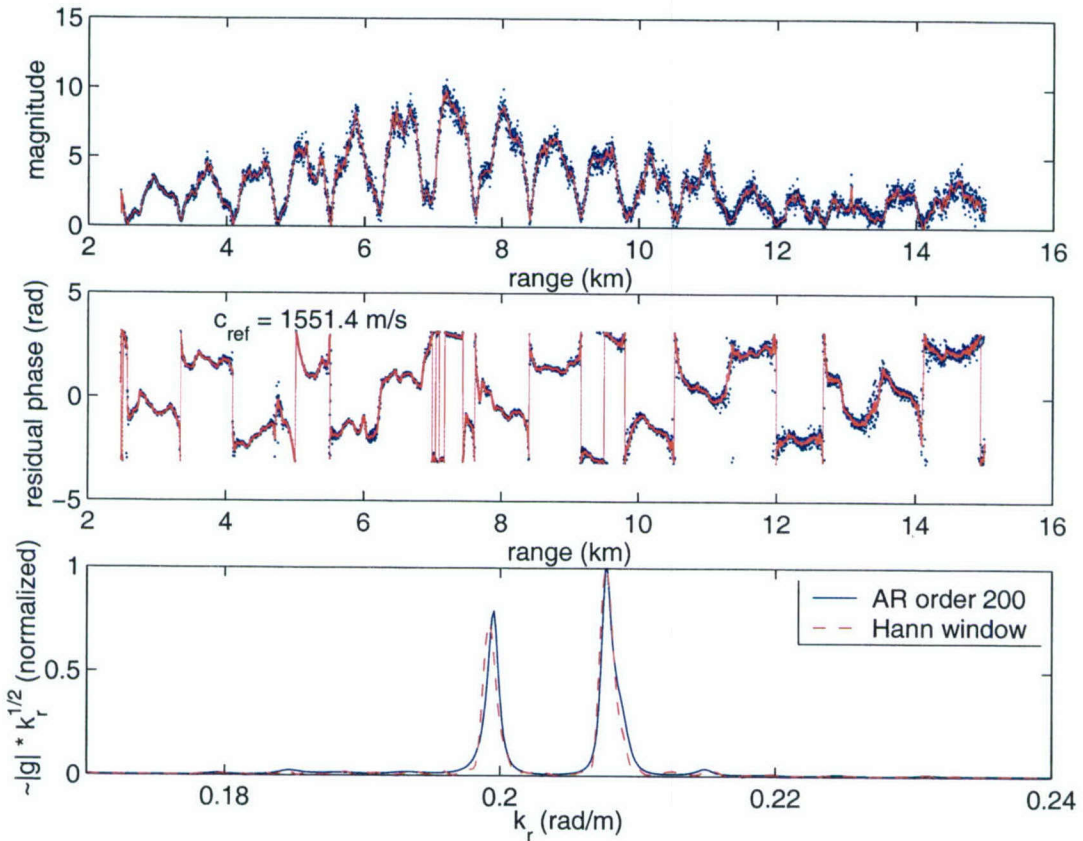


Figure 3-20: MOMAX 50 Hz signal and spectrum. Pressure magnitude multiplied by  $\sqrt{r}$  is shown in the upper plot as a function of range; raw data (dots) and filtered pressure (solid lines) are shown. The filtered pressure precedes the decimation down-sampling stage. Residual phase (see Fig. 3-16) is shown in the middle. The lower plot shows the order 200 AR wavenumber spectrum using the whole range aperture shown in the upper plots, and shows two strong spectral line corresponding to propagating modes near  $k_r = 0.2$  and  $0.21$  rad/m. The decimation filter was designed for an equivalent wavenumber range of  $0.17$ - $0.21$  rad/m [ $\Delta r < 2\pi/(0.21 - 0.17) \sim 157$  m;  $\Delta r = 52$  m was used].

ients, the eigenvalues at each range were inferred by locating the positions of the AR polynomial minima on the unit circle. The results in Figure 3-21 correspond to the 3 strongest spectral peaks at each range. The third mode is weakest of the three. The corresponding spectral line has the smallest and most variable magnitude of the three, again suggesting a barely excited or observed mode, as already suggested by the AR spectrogram.

### 3.4.5 Multiple Mode Estimation: Experimental Data - 125 Hz

The pressure signal analyzed in this subsection is from the same MOMAX III experiment 2 of the 50 Hz data, but acquired at a different time: the along-shelf portions of the tracks shown in Figure 3-6, where the local depth at the source was about 82 meters.

The analyzed signal  $(p(r)\sqrt{r})$  is shown in Figure 3-22, and corresponds to the along-shelf (NE) track of Figure 3-6. The original series from the processed MOMAX data has a non-uniform sampling space of 2.0 meters in average, and was interpolated to an uniform grid of 2.6 m spacing. The signal was then decimated by  $D = 16$  in two stages, resulting in a final spacing of 41.6 m, and a total wavenumber representation range of 0.1510 rad/m. Both original and filtered (preceding down-sampling) signals are shown, together with two spectra using the full available aperture (9.7 km).

The periodogram was computed using a Hann window. The AR spectrum is of order 1000, slightly below the 1/3 of number of data points (3746 points at  $\Delta r = 2.6$  m, rendering a Fourier resolution of  $6.45 \times 10^{-4}$  rad/m). For this large aperture, the periodogram and AR resolutions are similar, as observed in the plots. Both spectra show one strong spectral line corresponding to a propagating modes near  $k_r = 0.515$  rad/m. Other 10 to 11 peaks are visible, and some may correspond to modes.

As discussed above, one effect of decimation in the AR spectral analysis is the reduction in order requirement for the same resolution (which keeps the total range aperture the same. This effect can be observed in Figure 3-23. The order 1000 AR spectrum is the same of Figure 3-22, computed with a  $\Delta r$  of 2.6 m. After a decimation by 16,

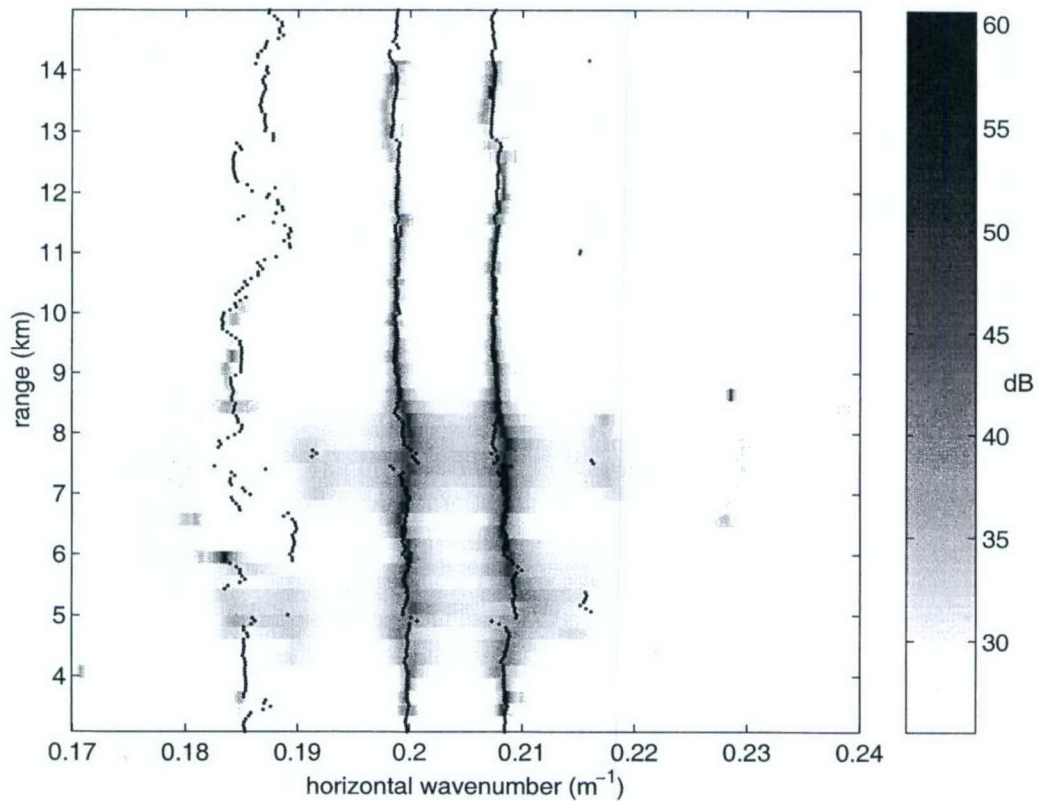


Figure 3-21: MOMAX 50 Hz wavenumber estimation. The plot shows wavenumber as a function of range, obtained by processing a decimated signal ( $\Delta r = 52$  m). The gray-scale (dB relative to an arbitrary reference) is shown in the left. The background plot is the order 10 AR spectrogram computed with a window aperture of 1976 m and 1768 m overlap between windows. The dots are eigenvalues from 13 competing forward/backward Kalman filter pairs, with  $\xi$  from  $1.5625 \times 10^{-5}$  to  $10^{-3}$  following a geometric progression with a ratio of  $\sqrt{2}$ . The AR model of the sequential estimator is of order 12.

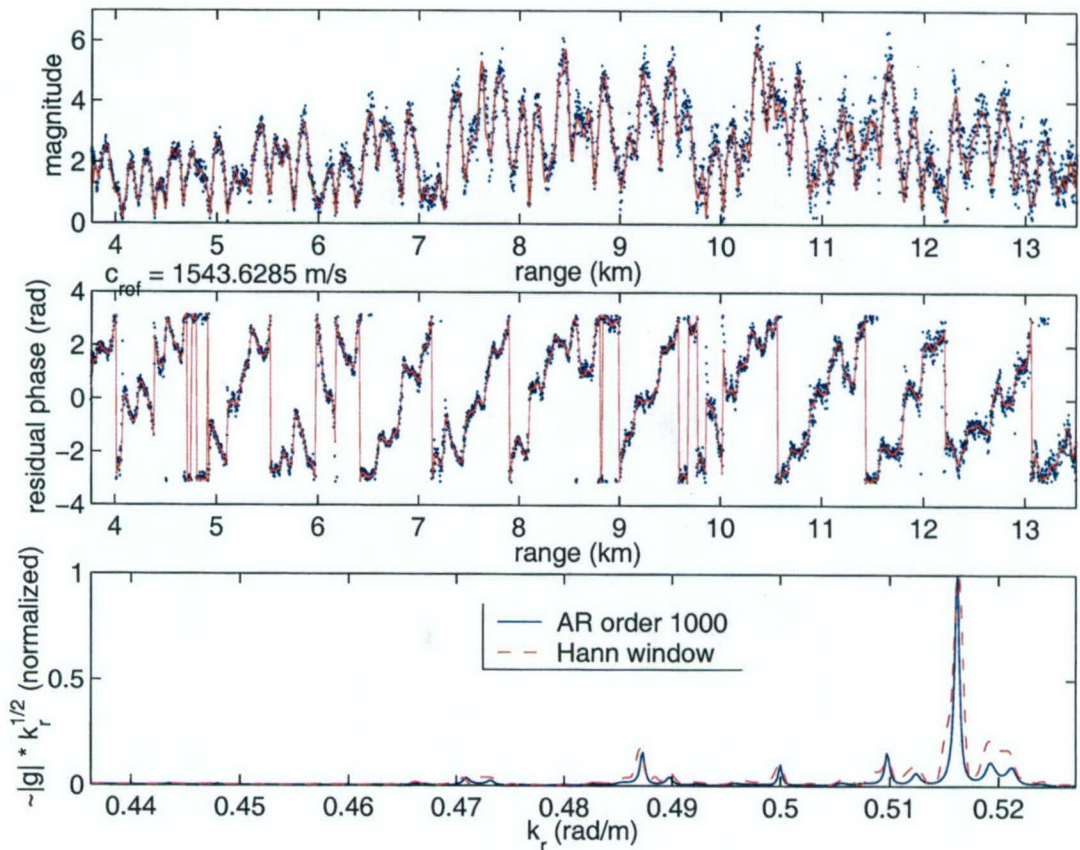


Figure 3-22: MOMAX 125 Hz signal and spectrum. Pressure magnitude multiplied by  $\sqrt{r}$  is shown in the upper plot as a function of range; raw data (dots) and filtered pressure (solid lines) are shown. The filtered pressure precedes the last decimation down-sampling stage. Residual phase (see Fig. 3-16) is shown in the middle. The lower plot shows the order 1000 AR wavenumber spectrum using the whole range aperture available, and the periodogram computed with a Hann window.

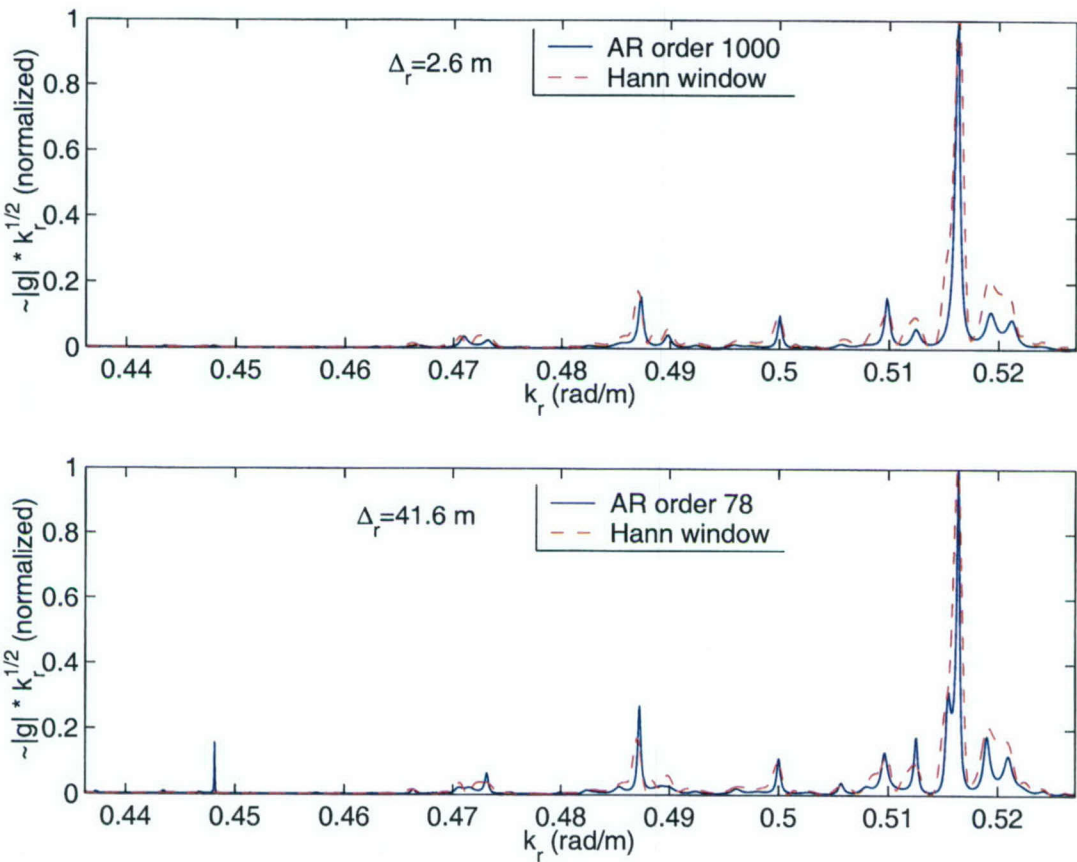


Figure 3-23: MOMAX 125 Hz spectrum estimation before and after decimation. This comparison is used to check the effect of decimation and to show that a significantly smaller order may lead to improved resolution after decimation. The decimation factor is  $D = 41.6/2.6 = 16$ .

a similar resolution is expected for an order  $1000/16 \sim 62$ . The lower plot shows an improved resolution using order 78. For example, the two peaks near  $k_r = 0.52$  rad/m are better resolved. A peak near  $k_r = 0.448$  is clearly detected. This peak is also present in the original spectrum, but its level is too low to be observed in the scale presented.

The AR spectrogram of the decimated signal is shown in Figure 3-24. The order 12 AR spectrogram uses a window of 2163.2 m, with an overlap of 1788.8 m between adjacent window positions. The dots mark the position of the six strongest peaks at each range cell. The strongest spectral line near  $k_r = 0.518$  rad/m is the same as

observed in Figure 3-22 and 3-23. The highest wavenumber spectral line ( $k_r = 0.534$  rad/m) corresponds to a phase-speed of  $2\pi f/k_r = 1470$  m/s, below the minimum sound speed in water of nearly 1490 m/s. As noted in the 50 Hz analysis, this spectral line is not consistent with a stationary environment. In addition to these lines, there are two weak ones around the strongest, and 3 stable lines in the range  $0.47 \leq k_r \leq 0.505$  rad/m. Other weaker lines are observed below that range. The six lines in the range  $0.47 \leq k_r \leq 0.525$  rad/m are possible stable modes. In order to reduce the interference of the other spectral components when estimating the AR coefficients, the signal was further decimated with  $D = 2$  and then filtered with a passband filter with cut-offs at 0.465 and 0.530 rad/m.

The AR spectrogram and the competitive smoother results for the new decimated signal ( $\Delta r = 83.2$  m) are shown in Figure 3-25. The order 10 AR spectrogram uses a window of 2163.2 m, with an overlap of 1747.2 m between adjacent window positions. The six spectral lines in the interval  $0.47 \leq k_r \leq 0.525$  rad/m from Figure 3-24 are clearly seen.

As in the 50 Hz analysis, 13 forward/backward Kalman filter pairs, with  $\xi$  from  $1.5625 \times 10^{-5}$  to  $10^{-3}$ , competed to obtain the results shown by the dots. The underlying AR model is of order 10. After obtaining the AR filter coefficients, the AR spectral peaks at each range were found by locating the positions the AR polynomial minima. The results in Figure 3-25 correspond to all spectral peaks at each range. This result suggests that at least six stable modes were propagating. Figure 3-24 suggests that higher order modes could also be present.

### 3.4.6 Sloping Bottom: Synthetic Data

In the cases analyzed so far, the acoustic field was measured or computed in regions of constant or nearly constant water depth. Changes in modal eigenvalues are caused mainly by changes in the geoacoustic properties of the environment, either in the seabed, or in the water column.

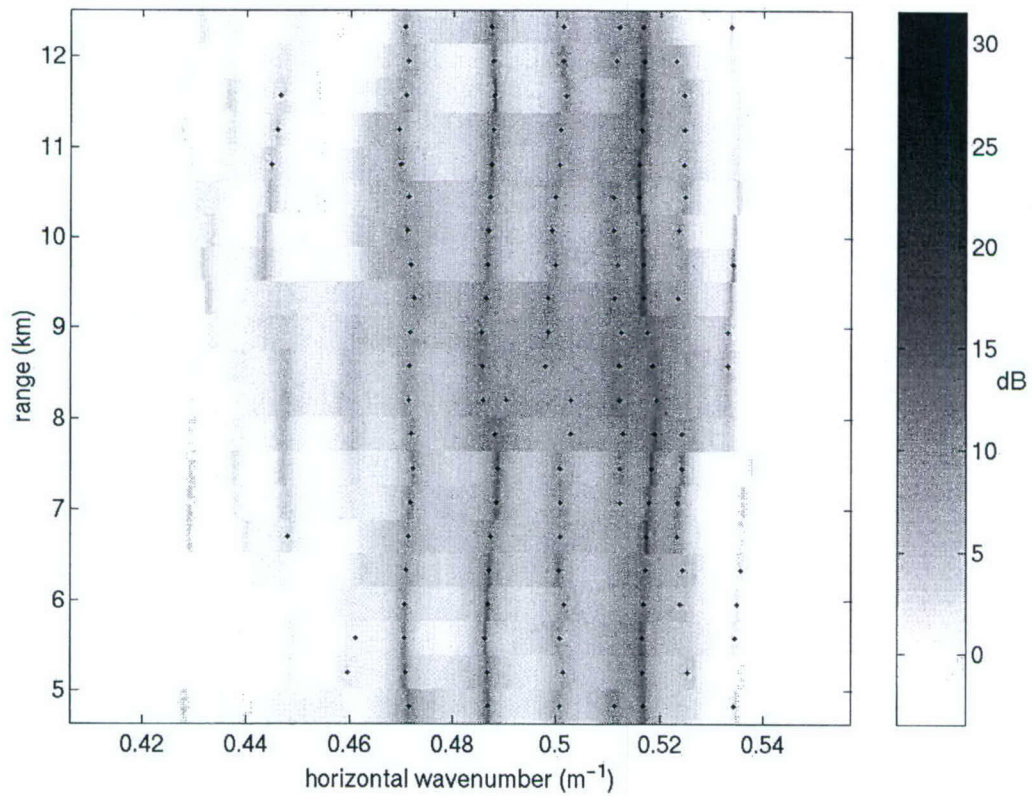


Figure 3-24: MOMAX 125 Hz AR spectrogram (range versus wavenumber) computed from the decimated signal ( $\Delta r = 41.6$  m). The shades of gray represent magnitude (dB relative to an arbitrary reference) corresponding to the scale on the right. The background plot is the order 12 AR spectrogram computed with a window aperture of 2163.2 m and 1788.8 m overlap between windows. The overlay dots are the six strongest peaks at each range cell. The full wavenumber scale allowed by the sampling space is shown ( $k_{max} - k_{min} = 2\pi/(D\Delta r) = 0.1510$  rad/m).

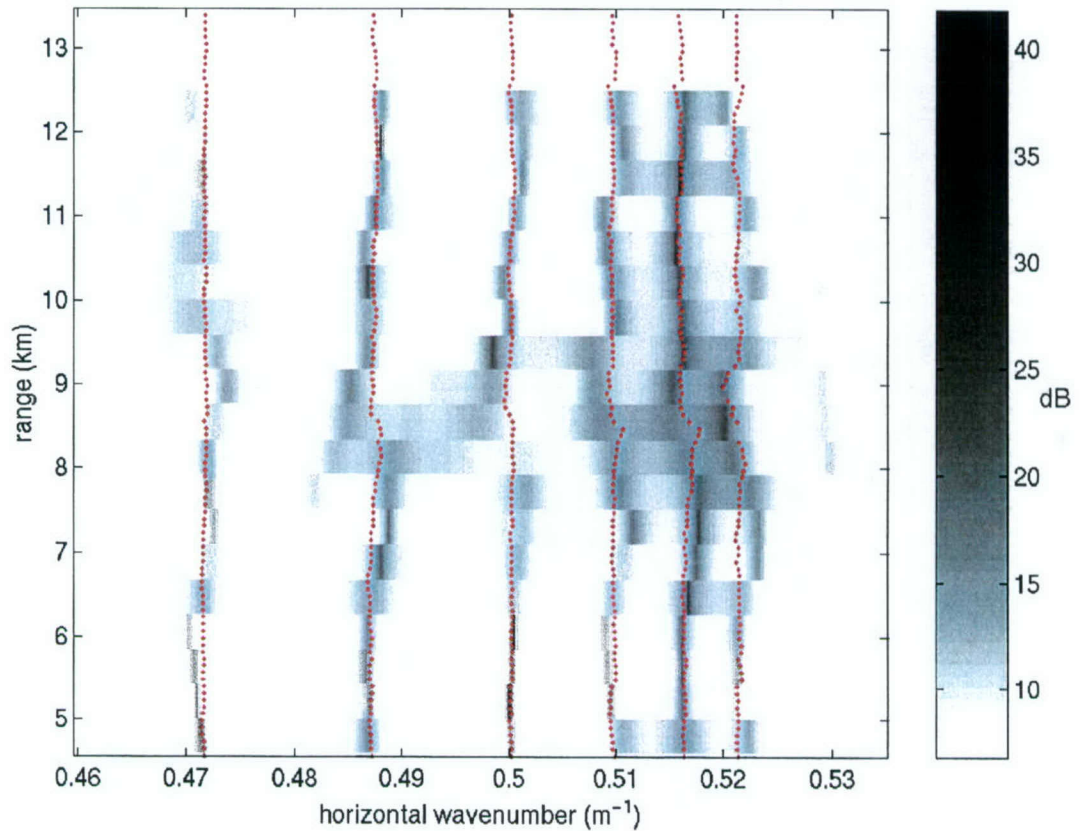


Figure 3-25: MOMAX 125 Hz wavenumber estimation. The plot shows wavenumber as a function of range, obtained by processing a decimated signal ( $\Delta r = 83.2$  m). The gray-scale (dB relative to an arbitrary reference) is shown on the right. The background plot is the order 10 AR spectrogram computed with a window aperture of 2163.2 m and 1747.2 m overlap between windows. The dots are eigenvalues from 13 competing forward/backward Kalman filter pairs. The AR order for the Kalman filters is also 10, and the dots are the only observed AR peaks at each range.

Although the sequential eigenvalue estimators have not been designed to deal with systematic changes in modes, such as those expected to occur over a sloping bottom, two simple tests have been conducted. They are based on the Inverse Techniques Workshop test case 2 discussed in Subsection 3.2.5 and shown in Figure 3-9.

As a first test, a signal was generated by summing the second and fourth mode components whose amplitudes and eigenvalues are shown in Figure 3-10. The exact DE coefficients for this two-component signal were computed for comparison with the estimated coefficients. The estimates shown in Figure 3-26 were obtained from a bank of second order Kalman identifiers (Appendix D) and an underlying AR model of order 2. The first forward/backward Kalman filter pair was initialized with an arbitrary set of AR coefficients. The second pair of filters (with a different parameter  $\xi$ ) was initialized with the coefficients estimated by the first backward filter, and so on. The set of parameters  $\xi$  was selected empirically for convergence.

In the range-independent region,  $r > 2.1$  km, the maximum relative error magnitude,  $|\hat{a}_j - a_j|/|a_j|$ , is less than 0.00035, except near  $r = 5$  km, where it reaches 0.004. In the range dependent region, the relative error magnitude never exceeds 0.04. The maximum error in eigenvalue (from the roots of the estimated characteristic equation) is  $2.4 \times 10^{-5}$  rad/m in the range-independent region, and  $3.3 \times 10^{-4}$  rad/m over the slope.

In simulations with three or more modes, the Kalman filters did not converge, precluding estimation of the exact DE coefficients of Section 3.2. The problem may be related to estimation of very low-noise (deterministic) range-varying (or time-varying) signals, which may not be considered “slowly changing” (as measured, for example, through the ratio of AR coefficient variances and measurement noise[52]), and, therefore, not amenable to estimation by adaptive systems. We have not pursued this issue. Nevertheless, as shown in the next example, eigenvalues may still be estimated for the TC-2 environment using sequential AR estimation of an order higher than the number of modes.

In the second test, the actual TC2 50 Hz signal provided for the workshop is analyzed.

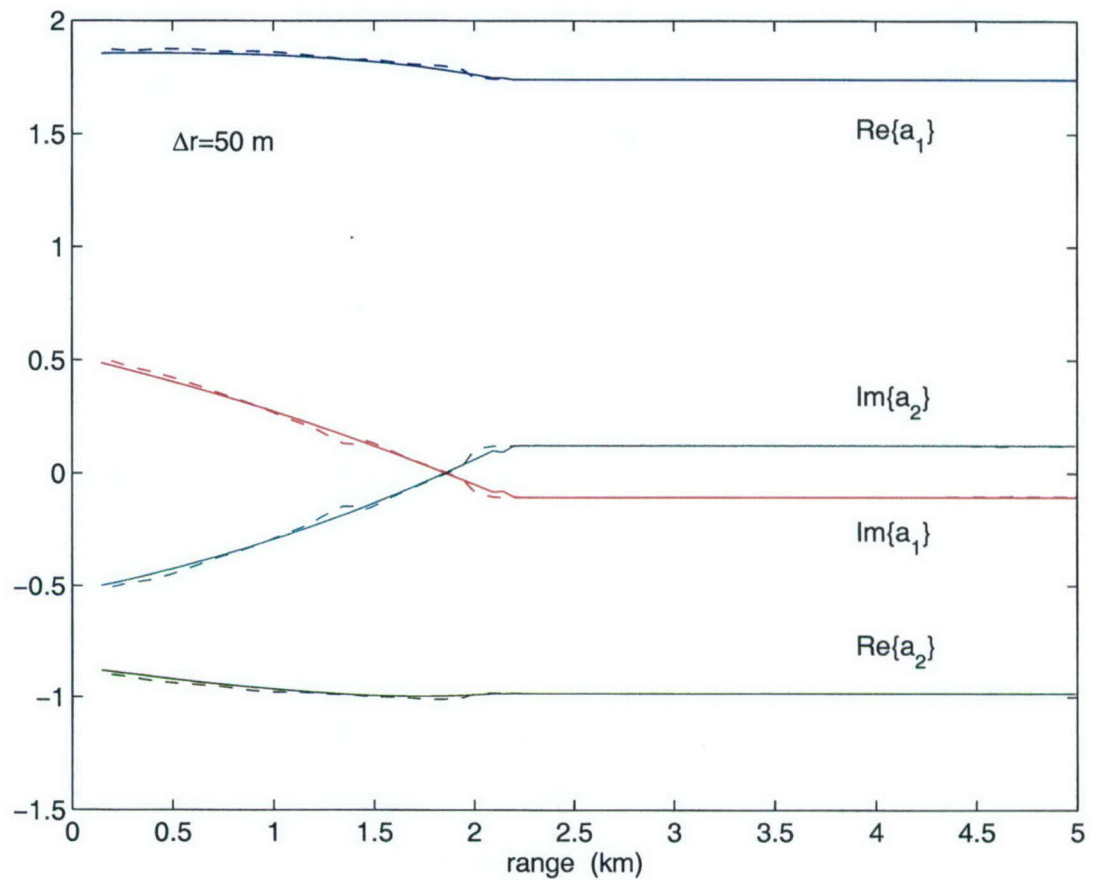


Figure 3-26: Estimation of DE coefficients. Solid lines are exact DE coefficients for a sum of two range-varying modes (modes 2 and 4 from Figure 3-10). Dashed lines are estimates from a competitive smoother formed by a bank of 2nd order Kalman Filters.

Figure 3-27 shows the magnitude and residual phase of the pressure data for a receiver depth of 25 m. Full aperture (5 km) spectrum estimations (AR and periodogram) are shown in the lower plot. The filtered signal preceding the last down-sample stage of decimation is also plotted. The only noticeable difference between the original and filtered signals is near  $r = 0$ , where the contribution from the low  $k_r$  continuous spectrum field was filtered out.

Figure 3-28 shows the order 10 AR spectrogram and the actual TC2 eigenvalues. The eigenvalues in the range-independent region are clearly detected. In the range-dependent region, the lower three modes are reasonably tracked, but the fourth and fifth eigenvalues, the ones with largest variations, although discernible, are poorly tracked. The present result is an improvement over a previous analysis using a model order 20 and a variable 20 to 66 order procedure, where only the first 4 modes were detected even in the range-independent region. The AR analysis of the decimated signal with an AR order of 10 should be comparable to an AR order 100 with the original signal.

Figure 3-29 shows the spectrogram of Figure 3-28 and the order 10 AR competitive smoother estimates. The trend of modes 3 to 5 can be observed, while the two lower order modes results are poorer than those of the AR spectrogram. The combined results of the spectrogram and the competitive smoother provide a clearer picture of the eigenvalue variations.

## 3.5 Summary and Conclusions

This chapter analyzed the exact representation of the modal sum by a difference equation (DE). This representation provides a justification for the use of time-varying AR (TVAR) models for the adiabatic modal sum. In AR analysis, the roots of the characteristic polynomial close to the unit circle at each sample (range) provide the estimates for eigenvalues, the frozen-time approach.

We derived expressions for the error in computing the first-order poles (the exact

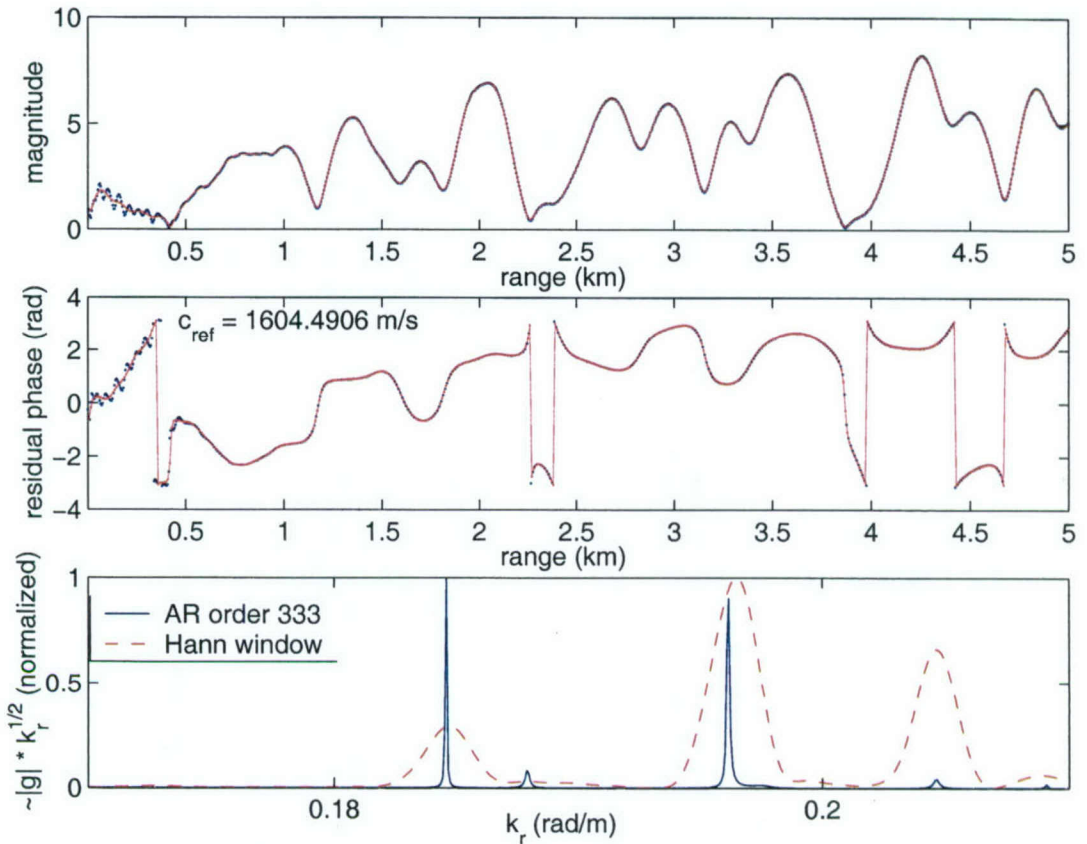


Figure 3-27: ITW TC2 50 Hz signal and spectrum. Pressure magnitude multiplied by  $\sqrt{r}$  is shown in the upper plot as a function of range; raw data (dots) and filtered pressure (solid lines) are shown. The filtered pressure precedes the last decimation down-sampling stage (original data at  $\Delta r = 5$  m was decimated to a  $D\Delta r = 50$  m). Residual phase (see Fig. 3-16) is shown in the middle. The lower plot shows the order 333 AR wavenumber spectrum using the whole range aperture available, and the periodogram computed with a Hann window.

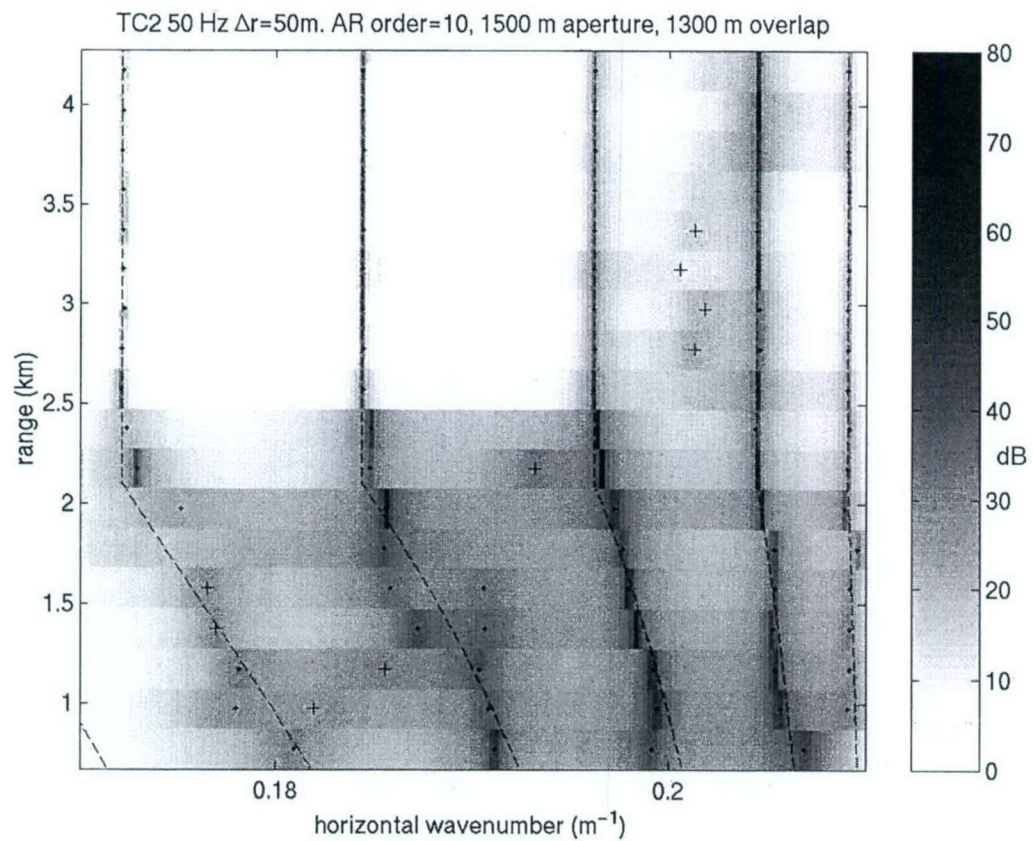


Figure 3-28: ITW TC2, 50 Hz AR spectrogram. The background (in shades of gray) is the order 10 AR spectrogram computed from the decimated signal with a window aperture of 1500 m and 1300 m overlap between windows. The dots mark the positions of the 5 strongest spectral peaks at each range. The crosses are the remaining detected peaks. The actual eigenvalues are shown as dashed lines.

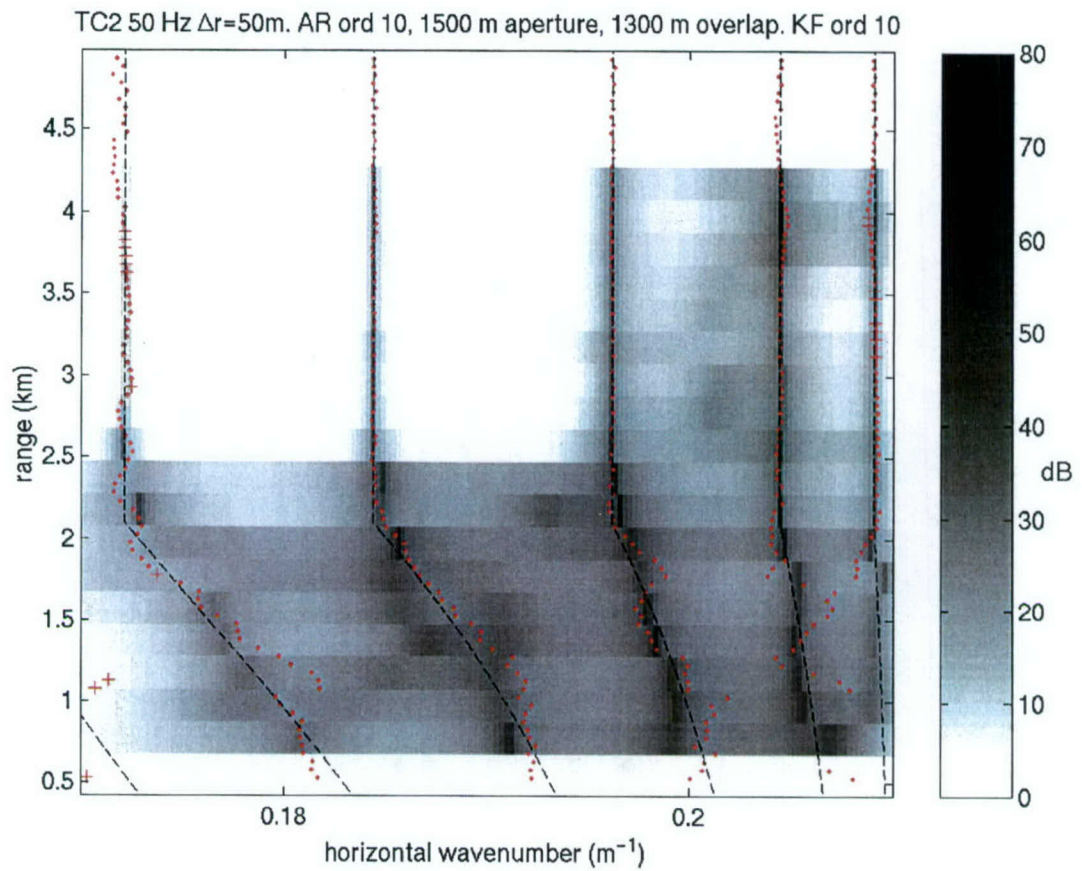


Figure 3-29: ITW TC2, 50 Hz AR spectrogram (from Figure 3-28) and competitive smoother results (dots for the 5 highest magnitude, crosses for the others). The Kalman filter underlying AR model is of order 10, the same used for the spectrogram.

representation of range-varying modes from which the eigenvalues should be estimated) as the roots of the characteristic equation. We showed that the error increases with the rate of variation of eigenvalues with range and with  $\Delta r$ , and decreases with separation between eigenvalues.

A simulation suggested, however, that an improvement in the numerical computation of polynomial roots with increasing  $\Delta r$  can compensate for the increased roots-first-order poles error.

Through the analysis of the asymptotic Cramer-Rao lower bound for closed spaced eigenvalues, we argued that, despite the prediction of reduced root-first-order pole error when  $\Delta r$  decreases, the net effect should be that of degradation of eigenvalue estimation, possibly due an increase in the error of DE coefficient estimation from an actual signal.

We proposed two sequential eigenvalue estimators, one for the estimation of AR coefficients, another for the estimation of polynomial roots directly. Competition among estimators was introduced in order to improve spatial tracking of eigenvalue changes. Decimation of the pressure field was introduced as a way to reduce the order of the AR models without reducing the actual range aperture. For the AR spectrogram, decimation results in significant reduction in computation cost and allows the use of larger effective orders (larger range apertures), contributing for improved eigenvalue resolution.

We showed that the Kalman filter effective memory length, which dictates range resolution, is a function of the wavenumber and decreases as the first-order poles approach the unit circle. Modes that decay faster with range are therefore associated with larger memory lengths. Ideally, however, memory length should be associated with the rate of change of eigenvalues: the faster they change, the smaller should be the effective memory length. The competition of filters with different  $\xi$ , which scale with the square of distance of the poles to the unit circle, can provide a compensation mechanism for this behavior. The VFF adaptive zero estimator, on the other hand, has effective memory independent of wavenumber, which allows the estimator to fit the variability of the signal without regard to specific mode behavior.

The 2001 Inverse Techniques Workshop test case 3, where eigenvalues change abruptly, was the initial motivation for this chapter. We showed that competition among sequential estimators resulted in a sharp definition of the abrupt eigenvalue change in this environment. For the single mode case, three different methods provide essentially the same estimate, an improvement over previous results. Eigenvalue estimates using the sequential estimators for two sets of experimental data show agreement with the AR spectrogram, if not improvement.

We showed that systematic eigenvalue change, as for a sloping bottom, degrades the performance of the AR estimator, a result previously observed [6]. In general, sequential estimators can identify [52] nonstationary parameters that drift slowly, or have infrequent abrupt changes, or a combination of these two behaviors. Most adaptive identification methods fail with fast varying parameters. Apparently, this is the case of TC2 with more than two modes. For two modes, we showed by simulation that competition among second order Kalman filters was able to track the DE coefficients. For more general cases, other methods, such as representation of variations by basis functions, may prove useful.

The MOMAX 20 Hz data analysis shows that eigenvalue estimation for a single complex exponential is a reasonably easy problem, provided the signal-to-noise ratio is high. Three apparently different methods give the same estimate. In such conditions, numerical differentiation from a densely sampled signal, a relatively simple algorithm, may provide a nearly continuous range-varying eigenvalue estimate.

The MOMAX 50 Hz analysis illustrates the importance of using the full aperture wavenumber spectrum, the spectrogram, and the AR sequential estimation in order to interpret the eigenvalue estimation results. They all reveal the presence of a third mode: weak in the full aperture analysis (Figure 3-20), with erratic range variations in the spectrogram and sequential (Figure 3-21) estimates. The estimation of the two first modes could still be improved by filtering out the “unstable” third mode, reducing the range of eigenvalues to be represented, and allowing for larger sampling distances.

The behavior of the third spectral line indicates that the mode is either near cutoff, or the source or the receiver were located near a null of that mode. In both cases, this was the highest observed mode and the associated phase speed ( $\omega/k_{r3} \sim 100\pi/0.185 = 1698$  m/s) is the closest to the 'basement' sound velocity.

The MOMAX 125 Hz analysis shows how decimation can contribute to improved eigenvalue resolution by effectively separating the first-order poles in the complex plane. The AR spectrogram of Figure 3-25 (spatial sampling of 83.2 m) has three strong lines corresponding to the first three modes, while in Figure 3-24 (spatial sampling 41.6 m) they are not well defined. The AR sequential estimation, when combined with the spectrogram, as in Figure 3-25, give a clearer picture of the modal structure and its variations with range.

As an aside, the 50 Hz and 125 Hz MOMAX data were acquired in the same region, at close tracks, although at slightly different times. As discussed above, the sound velocity of the 'basement' was estimated from the 50 Hz data as close to 1698 m/s. For this velocity, modes at 125 Hz should have eigenvalues above roughly  $k_r = 2\pi \times 125/1698 = 0.4625$  rad/m. The highest mode in Figure 3-25 is slightly above 0.47 rad/s, which is consistent with the 50 Hz analysis.

# Chapter 4

## Inversion for Subbottom Sound Velocity Profiles in the Shallow Ocean: Eigenvalue Inversion

### 4.1 Introduction

This chapter investigates the estimation of the seabed sound velocity profile in shallow water. The input is a series of eigenvalues measured as a function of range, as obtained with the techniques of Chapter 3. Section 4.1 provides the motivation for the eigenvalue inversion and gives an overview of the perturbative inverse technique of Rajan and co-workers [61]. The problem of inferring a sound speed profile from a finite set of eigenvalues is ill-posed, a characteristic of many inverse problems. Solving this problem requires some form of regularization. Section 4.1 gives an overview of regularization techniques, culminating with Franklin's stochastic inverse[17]. Finally, Section 4.1 summarizes the Backus-Gilbert (BG) resolution theory [4], which provides a physically meaningful measure of inversion quality for linear problems.

Section 4.2 investigates the inversion from sequences of modal eigenvalues. Building on Franklin's stochastic inversion, a state-space model of the problem is constructed,

leading to a regularized Kalman filter solution of the problem. The inverse eigenvalue problem is nonlinear. The linearization of the underlying mapping eigenvalue→sound-velocity-profile, required for the iterative solution using the Kalman filter, is investigated. Not surprisingly, linearization recovers the perturbative technique integral equation.

Section 4.3 analyzes the variance and resolution of the eigenvalue inverse. The Cramer-Rao lower bound (CRB) is compared with the predictions of the BG theory through an example of a shallow-water waveguide. We analyze the effects of frequency and number of modes on the inversion from the perspective of the BG theory, which provides a tool for acoustic experiment design.

Section 4.4 investigates the compensation of eigenvalues estimated from fields generated by moving sources. Source motion induces Doppler deviation that affect the modal eigenvalues and, ultimately, the inversion results. We perform a perturbative analysis of the modal ODE and propose a modification of the inversion technique to account for source motion.

Finally, Section 4.5 applies the techniques developed in Sections 4.3 and 4.4 to two environments, the shallow-water waveguide environment introduced in Section 4.3, and the test case 3 (TC3) of the Inverse Techniques Workshop described in Chapter 3.

#### 4.1.1 Eigenvalue Inverse Problem

According to Rundell [8], the modern starting point of the inverse eigenvalue theory was the proof that, if the eigenvalues of the Sturm–Liouville problem

$$Lu = -u'' + q(z)u = \lambda u, \quad u'(0) = u'(1) = 0 \quad (4.1)$$

are  $\lambda_n = n^2\pi^2$ , then the *potential*  $q(z)$  is identically zero. Since then, general conditions for the uniqueness of the solution of the inverse problem have been established. In a recent paper, for example, Athanassoulis and Papanicolaou [3] derived an inverse problem

related to a piecewise smooth *potential*  $q(z)$ , a case of interest in Ocean Acoustics. These theories can be regarded as exact in the sense that they describe the potential  $q(z)$  in terms of the problem eigenvalues. They are restricted to proper Sturm-Liouville problems, which have only a discrete spectrum and whose eigenfunctions  $u_m$  form a complete set.

These exact inverse theories can not be applied directly to the non-proper problems of Ocean Acoustics. The depth dependent equation can be written (using operator notation) as

$$Lu = - \left( \frac{u'}{\rho} \right)' + \frac{q(z)}{\rho} u = \frac{\lambda}{\rho} u, \quad u(0) = 0, \quad u(h) + Au'(h) = 0, \quad (4.2)$$

where  $q(z) = (\omega/c_{\min})^2 - k^2(z)$ ,  $\lambda = [\omega/c_{\min}]^2 - k_r^2$ ,  $A = i\xi/[\rho(h)\omega]$ ,  $c_{\min}$  is a reference sound velocity (chosen to make  $q(z)$  positive),  $k^2(z)$  is the depth-dependent wavenumber,  $k_r$  is the horizontal wavenumber and  $\xi$  is the normal boundary impedance. The coefficient  $A$  in the boundary condition at the lower interface is complex (when  $\xi$  has a nonzero real part) and depends on  $k_r$ . Alternatively, the lower boundary is taken at infinity ( $h \rightarrow \infty$ ), where the radiation condition applies. The boundary conditions allow for loss of energy through the lower interface and hence the problem is not proper, has a continuous spectrum and, in low frequency shallow-water acoustics, a typically small number of real eigenvalues<sup>1</sup>.

#### 4.1.2 The Inverse Perturbative Technique

Despite the presence of a continuous spectrum, normal modes are typically the most dominant feature in low-frequency, shallow water acoustic fields at long distances from the source. Rajan and co-workers [61] used modal eigenvalues in an inverse perturbative technique to infer the sound velocity profile in the seabed. Basically, they construct a

---

<sup>1</sup>Here, as is usual in Ocean Acoustics, the horizontal wavenumber  $k_{rm}$  associated to the eigenvalue  $\lambda_m = [\omega/c_{\min}]^2 - k_{rm}^2$  is referred to as “eigenvalue”.

background model of the seabed (the water column characteristics are assumed known), compute the corresponding eigenvalues and find the correction to the background sound velocity profile  $\Delta c(z)$  corresponding to the difference  $\Delta k_n$  between the measured and background eigenvalues. The method is based on the perturbation integral<sup>2,3</sup>

$$\begin{aligned}\Delta k_{rm} &= \frac{-1}{k_{rm}^{(0)}} \int_0^\infty \frac{1}{\rho} |u_m^{(0)}|^2 \left( \frac{\omega_m}{c^{(0)}} \right)^2 \frac{\Delta c}{c^{(0)}} dz, \quad m = 1 \dots, M, \\ &= \int_0^\infty g_m^{(0)}(z) \Delta c(z) dz\end{aligned}\quad (4.3)$$

where the (0) superscript refers to the background model: sound velocity profile  $c^{(0)}(z)$ , eigenvalue  $k_m^{(0)}$ , eigenfunction  $u_m^{(0)}(z)$ , and modal kernel  $g_m^{(0)}(z)$ . In the inverse perturbative technique, eq.4.3 is seen as an integral equation with unknown  $\Delta c(z)$ .

In general, the number  $M$  of measured eigenvalues is small and the characterization of the sound velocity profile requires a large number of points. The problem is under-determined and has an infinite number of least-squares (LS) solutions. A unique solution can yet be obtained, if some form of restriction is imposed. The minimum-norm solution or the solution that satisfies some optimality criterion are often used. The choice of solution may be somewhat arbitrary, not necessarily related to the physics of the problem.

The discretization of eq.(4.3) leads to the linear system

$$\mathbf{d} = G\Delta\mathbf{c} = G\mathbf{q}, \quad (4.4)$$

where  $\mathbf{d}$  is the  $M \times 1$  vector of eigenvalue differences,  $\Delta\mathbf{c} = \mathbf{q}$  is an  $N \times 1$  vector of sound velocity increments over some depth grid, and  $G$  is an  $M \times N$  matrix. As discussed above, in general  $M < N$  and  $G$  is of rank  $M$  (= number of measured eigenvalues). The

---

<sup>2</sup>Appendix F analyzes the effect of small sound velocity and frequency perturbations on the eigenvalues.

<sup>3</sup>Throughout this chapter, the frequency  $\omega$  is indexed by the mode number, as in  $\omega_m$  in eq.(4.3), so that each mode is associated with a frequency, and modes at different frequencies can be used in the same expression without the need to change notations.

corresponding least-squares problem is given by  $G^T \mathbf{d} = G^T G \mathbf{q}_{LS}$  and has, when the system is underdetermined, an infinite number of solutions (any solution added to a vector  $\mathbf{q}_h$  in the null space of  $G$  is still a solution). When the system is overdetermined ( $M > N$ ), the LS solution is  $\tilde{\mathbf{q}}_{LS} = (G^T G)^{-1} G^T \mathbf{d}$ . When the system is underdetermined ( $M < N$ ), the minimum-norm solution is  $\tilde{\mathbf{q}}_{LS} = G^T (G G^T)^{-1} \mathbf{d}$ . In both cases  $G$  must be full rank for the corresponding inverses to exist. When  $G$  is square and full rank, these solutions reduce to  $G^{-1} \mathbf{d}$ .

The LS solution (minimum-norm when underdetermined) can be represented using the singular value decomposition (svd) [1, 73, 32, 33],  $G = U_r \Lambda_r V_r^T$ , through the Moore-Penrose pseudo-inverse[32]  $\tilde{G}^\#$

$$\begin{aligned}\tilde{\mathbf{q}}_{LS} &= \tilde{G}^\# \mathbf{d} = V_r \Lambda_r^{-1} U_r^T \mathbf{d}, \\ &= \sum_{m=1}^r \lambda_m^{-1} (\mathbf{v}_m \mathbf{u}_m^T) \mathbf{d},\end{aligned}\tag{4.5}$$

which is valid irrespective of the rank  $r$  of  $G$ , and reduce to the above forms when  $G$  is full rank. In eq.(4.5),  $V_r$  is an  $N \times r$  matrix whose columns are right-singular vectors  $\mathbf{v}_m$  of  $G$ ,  $\Lambda_r$  is the  $r \times r$  diagonal matrix containing the singular values  $\lambda_m$  (assumed in decreasing order), and  $U_r$  is an  $M \times r$  matrix whose columns are left-singular vectors  $\mathbf{u}_m$  of  $G$ .

The sound velocity increment from eq.(4.5) is a combination of the right-singular vectors  $\mathbf{v}_m$  weighted by the inverse of the corresponding singular values. Solution (4.5) is minimum-norm because the right-singular vectors in  $V_r$  are orthogonal to the null space of the system matrix  $G$  (or  $G^T G$ ), i.e.,  $\tilde{\mathbf{q}}_{LS}$  does not include solutions of the homogeneous system  $G \mathbf{q}_h = 0$ .

This is a typical ill-posed problem characterized by singular values that decrease to zero, rendering the solution (involving  $\lambda_m^{-1} \rightarrow \infty$  unstable, sensitive to errors in  $\mathbf{d}$ ). <sup>4</sup>

---

<sup>4</sup>We have observed that in perturbative eigenvalue inversion, the smaller [ $m$  close to  $r$  in eq.(4.5)] singular values correspond to vectors  $\mathbf{v}_m$  with greater variability and contribute to oscillations in the solution (seen as a sequence, function of depth, the  $\mathbf{v}_m$  become more oscillatory as  $m$  increases).

In order to limit the variance of the solution, small singular values can be discarded altogether from the solution by truncating the sum in (4.5).

Alternatively, one can reduce the influence of small singular values by introducing some form of damping to each singular vector component of the solution, as is done in the Tikhonov's regularization method[27]. The regularization corresponds to choosing  $\mathbf{q}$  that minimizes the regularized LS cost function

$$J_{rLS} = (\mathbf{d} - G\mathbf{q})^T(\mathbf{d} - G\mathbf{q}) + \mu^2 \mathbf{q}^T H \mathbf{q}, \quad (4.6)$$

where  $H$  is a suitably chosen matrix and  $\mu^2$  is a positive scalar that controls the amount of damping. When  $\mu = 0$ , the problem becomes the standard least-squares (LS) problem whose minimum-norm solution is given by eq.(4.5).  $H$  is usually associated with some measure of the variations of the sound velocity increment, such as derivatives. In [61], for example,  $\mathbf{q}^T H \mathbf{q}$  corresponds to the discretization of the smoothness measure

$$\int_0^\infty \left[ \frac{d^2}{dz^2} \Delta c(z) \right]^2 dz. \quad (4.7)$$

The solution of the regularized problem that minimizes the cost function (4.6) is

$$\tilde{\mathbf{q}}_{rLS} = (G^T G + \mu^2 H)^{-1} G^T \mathbf{d}. \quad (4.8)$$

When  $G^T G$  is not full rank,  $H$  must be positive definite for the inverse in eq.(4.8) to exist. When  $H$  is the identity matrix (the standard form of the Tikhonov problem), the regularization consists of loading the diagonal of  $G^T G$  in eq.(4.8) with a small value  $\mu^2$ . The rank of the  $N \times N$  matrix  $G^T G$  in this application is usually equal to the number of modes  $M < N$ , and  $G^T G$  is not invertible. Diagonal loading increases the rank to  $N$  and reduces the spread of eigenvalues, which tends to stabilize the solution.

Equation (4.8) with  $H = I_N$  can be written in terms of the svd of  $G$  as[1]

$$\begin{aligned}
 \tilde{\mathbf{q}}_{LS} &= (G^T G + \mu^2 I_N)^{-1} G^T \mathbf{d}. \\
 &= V_r \Lambda_r (\Lambda_r^2 + \mu^2 I_r)^{-1} U_r^T \mathbf{d}, \\
 &= \sum_{m=1}^r [\lambda_m^{-1} / (1 + \mu^2 / \lambda_m^2)] (\mathbf{v}_m \mathbf{u}_m^T) \mathbf{d}.
 \end{aligned} \tag{4.9}$$

Comparing eqs.(4.5) and (4.9), the effect of  $\mu^2$  is to reduce the weight of singular values, the smaller the singular values, the larger the damping introduced. The net effect is the stabilization of the solution, which becomes smoother and less sensitive to data errors.

Another approach to solving the integral equation (4.3) is referred in [61] as the *spectral expansion method*, where  $\Delta c(z)$  is written as a linear combination of basis functions constructed from the modal kernels  $g_m(z)$  of eq.(4.3). This formulation also leads to a minimum norm solution similar to the pseudo-inverse solution described above.

This chapter explores the representation of  $\Delta c$  as a sum of basis functions. We show that the application of the simple trapezoidal rule to discretize the integral equation (4.3), or the spectral expansion method above correspond to basis functions representations leading to the linear system (4.4) with different matrices  $G$ .

It should be clear by now that regularization, in the form of truncation of small singular values, or the more sophisticated Tikhonov regularization, is critical to the solution of eq.(4.4). Next, we present an overview of the stochastic inverse, which leads to a generalization of the cost function (4.8), and is the basis for the sequential inversion technique introduced in Section 4.2.3.

#### 4.1.3 The Stochastic Inverse

In [17], Franklin proposed a regularization technique where  $\mathbf{q}$  is considered a zero-mean stochastic process with covariance  $R_q$ . Measurement errors are modeled by a zero-mean vector process  $\mathbf{e}$  independent of  $\mathbf{q}$ . The stochastic inverse  $\tilde{G}^S$  minimizes the mean square

error  $E [\varepsilon^T \varepsilon]$ , where  $\varepsilon = (\mathbf{q} - \tilde{G}^S \mathbf{d})$ .

The minimization of the mean square error can be alternatively described as the orthogonalization of the error  $\varepsilon$  with respect to the input data. This is the orthogonality principle or projection theorem[37, p. 386], according to which the inverse operator is the one that satisfies

$$\begin{aligned} 0 &= E [\varepsilon \mathbf{d}^T], \\ &= E [(\mathbf{q} - \tilde{G}^S \mathbf{d}) \mathbf{d}^T], \\ &= E [\mathbf{q} \mathbf{d}^T] - \tilde{G}^S [\mathbf{d} \mathbf{d}^T], \\ \Rightarrow \tilde{G}^S R_d &= R_{qd}, \end{aligned} \quad (4.10)$$

where  $R_d$  is the autocorrelation matrix of the data vector  $\mathbf{d}$ , and  $R_{qd}$  is the cross-correlation matrix between the true solution  $\mathbf{q}$  and the data vector  $\mathbf{d}$ . Using the linear measurement equation  $\mathbf{d} = G\mathbf{q} + \mathbf{e}$  [cf. eq.(4.4)], and taking into account the assumption  $E [\mathbf{q} \mathbf{e}^T] = 0$ , these two matrices can be computed in terms of the statistics of  $\mathbf{q}$  and  $\mathbf{e}$  as:

$$\begin{aligned} R_d &= E [\mathbf{d} \mathbf{d}^T], \\ &= E [(G\mathbf{q} + \mathbf{e})(G\mathbf{q} + \mathbf{e})^T] \\ &= E [G\mathbf{q}\mathbf{q}^T G^T + G\mathbf{q}\mathbf{e}^T + \mathbf{e}\mathbf{q}G^T + \mathbf{e}\mathbf{e}^T] \\ \Rightarrow R_d &= G R_q G^T + R_e, \end{aligned} \quad (4.11)$$

and

$$\begin{aligned} R_{qd} &= E [\mathbf{q} \mathbf{d}^T], \\ &= E [\mathbf{q} (G\mathbf{q} + \mathbf{e})^T], \\ &= E [\mathbf{q}\mathbf{q}^T G^T + \mathbf{q}\mathbf{e}^T], \\ \Rightarrow R_{qd} &= R_q G^T. \end{aligned} \quad (4.12)$$

Inserting eqs.(4.11) and (4.12) into eq.(4.10), we obtain the stochastic inverse<sup>5</sup>

$$\begin{aligned}\hat{\mathbf{q}}_S &= \tilde{G}^S \mathbf{d} = R_q G^T (G R_q G^T + R_e)^{-1} \mathbf{d}, \\ &= (G^T R_e^{-1} G + R_q^{-1})^{-1} G^T R_e^{-1} \mathbf{d}.\end{aligned}\quad (4.13)$$

The second form in eq.(4.13) is obtained from the first by applying the matrix inverse lemma[32]

$$(BCD + A)^{-1} = A^{-1} - A^{-1}B(DA^{-1}B + C^{-1})^{-1}DA^{-1}. \quad (4.14)$$

The stochastic inverse, eq. (4.13), is also the solution of the *regularized weighted deterministic least-square* problem that minimizes the cost function [cf. eq(4.6)]

$$J_{rwLS} = (\mathbf{d} - G\mathbf{q})^T R_e^{-1} (\mathbf{d} - G\mathbf{q}) + \mathbf{q}^T R_q^{-1} \mathbf{q}. \quad (4.15)$$

When the weight matrices  $R_e^{-1}$  and  $R_q^{-1}$  are diagonal, this cost function allows an easy interpretation of the effects of data and model variances on the result. The higher the variance of a component  $d_i$  of the data vector  $\mathbf{d}$ , the smaller is the contribution to the cost of the corresponding component of  $(\mathbf{d} - G\mathbf{q})$ . High variance data tend to have less effect on the (optimum) solution. The same rationale applies to how much  $\mathbf{q}$  may deviate from zero. The larger the variance of a component of the solution vector, the smaller its contribution to the cost and the lesser its effect on the minimization process. High variance solution components may deviate from zero without affecting significantly the cost.

Cost function (4.15) is a generalization of eq.(4.6) associated with the Tikhonov regularization (make  $R_e = \sigma_e^2 I_M$  and  $R_q^{-1} = \sigma_e^{-2} \mu^2 H$ ). Imposing a smoothness constraint through  $H$  is equivalent, in the stochastic sense, to choosing a suitable covariance matrix for  $\mathbf{q}$ . When  $R_e = \sigma_e^2 I_M$  (errors from different eigenvalues are uncorrelated and have

---

<sup>5</sup>Up to this point, we have used the tilde in vector  $\tilde{\mathbf{q}}$  to represent least-squares solutions of the linear system  $G\mathbf{q} = \mathbf{d}$ . From now on, the circumflex  $\hat{\mathbf{q}}$  designates estimates of the vector  $\mathbf{q}$  obtained from measurements contaminated by noise. The least-squares solutions we have discussed so far can be used as estimates. We will keep using  $\tilde{G}$  to represent any generalized inverse of a matrix  $G$ .

same variance) and  $R_q = \sigma_q^2 I_N$  (components of the solution have same variance and are uncorrelated), the stochastic solution reduces to eq.(4.9) with  $\mu^2 = \sigma_e^2/\sigma_q^2$ . The higher  $\mu^2$ , the larger the diagonal loading of matrices  $GG^T$  or  $G^T G$  in eq.(4.13), and the smoother the solution.

#### 4.1.4 The Backus-Gilbert (BG) Resolution Theory

This section reviews the Backus-Gilbert (BG) theory [4] related to the resolution and error variance of solutions to inverse problems described by the integral equation (4.3), which, when including the effects of measurement noise  $e_m$ , becomes

$$d_m = \int_a^b g_m(z) \Delta c(z) dz + e_m, \quad m = 1, \dots, M. \quad (4.16)$$

The integral is explicitly restricted to the interval  $[a, b]$  where the sound velocity is unknown.

Given a set of  $M$  measurements  $d_m$ , one seeks to estimate some property  $p(z_o)$  of the environmental quantity  $\Delta c(z)$  as a linear combination of the measurements:

$$\hat{p}(z_o) = \sum_{m=1}^M a_m(z_o) d_m = \int_a^b \left[ \sum_{m=1}^M a_m(z_o) g_m(z) \right] \Delta c(z) dz + \sum_{m=1}^M a_m(z_o) e_m, \quad (4.17)$$

or, in vector notation,

$$\hat{p}(z_o) = \mathbf{a}^T(z_o) \mathbf{d} = \int_a^b [\mathbf{a}^T(z_o) \mathbf{g}(z)] \Delta c(z) dz + \mathbf{a}^T(z_o) \mathbf{e}, \quad (4.18)$$

where  $\mathbf{a}(z_o) = [a_1(z_o), \dots, a_M(z_o)]^T$ ,  $\mathbf{d} = [d_1, \dots, d_M]^T$ ,  $\mathbf{g}(z) = [g_1(z), \dots, g_M(z)]^T$ , and  $\mathbf{e} = [e_1, \dots, e_M]^T$ . If  $\hat{p}(z_o)$  is an estimate of  $\Delta c(z_o)$ , eq.(4.18) shows that such estimate is a weighted averaged value over the interval  $(a, b)$ , with the weights given by the resolution kernel

$$A(z, z_o) = \mathbf{a}^T(z_o) \mathbf{g}(z) = \sum_{m=1}^M a_m(z_o) g_m(z). \quad (4.19)$$

In order to estimate  $\Delta c(z_0)$ , ideally we should have an impulsive kernel i.e.,  $A(z, z_0) = \delta(z - z_0)$ , corresponding to the best possible *resolution*. A measure of the actual kernel resolution is defined in [4] as the *spread of A from  $z_0$*

$$s_A(z_0) \equiv 12 \int_a^b (z - z_0)^2 A^2(z, z_0) dz, \quad (4.20)$$

where  $A$  is assumed of unit area. For an unit area rectangular pulse centered at  $z_0$ ,  $s_A(z_0)$  is the pulse width, which is an intuitive measure of the resolution power of  $A$ . Poor resolution occurs when  $A$  is nearly constant, in which case  $\hat{p}(z_o)$  is an estimate of a depth-averaged value of  $\Delta c$ .

The other measure of the quality of the estimate is the variance of  $\hat{p}(z_o)$ , given, from eq.(4.18), by

$$\sigma_{\hat{p}}^2(z_0) = \sum_{i=1}^M \sum_{j=1}^M a_i(z_0) a_j(z_0) (R_e)_{i,j} = \mathbf{a}^T(z_0) R_e \mathbf{a}(z_0), \quad (4.21)$$

where  $R_e = E[\mathbf{e}\mathbf{e}^T]$  is the covariance matrix of the measurement error vector  $\mathbf{e}$ , assumed zero mean. In [4], Backus and Gilbert solved the optimization problem of obtaining a unit area resolution kernel  $A(z, z_0)$  that minimizes the spread  $s_A(z_0)$  for a given variance level. This corresponds to the minimization of  $J_{BG} = \sigma_A(z_0) + \alpha \sigma_{\hat{p}}^2(z_0)$  constrained to  $\int_a^b A(z, z_0) dz = 1$ . In vector notation, find  $\mathbf{a}(z_0)$  that minimizes

$$J_{BG} = \mathbf{a}^T(z_0) S(z_0) \mathbf{a}(z_0) + \alpha \mathbf{a}^T(z_0) R_e \mathbf{a}(z_0) \quad (4.22)$$

under the constraint

$$\mathbf{a}^T(z_0) \mathbf{u} = 1, \quad (4.23)$$

where

$$s_A(z_0) = \mathbf{a}^T(z_0) S(z_0) \mathbf{a}(z_0), \quad (4.24)$$

$$(S(z_0))_{ij} = 12 \int_a^b (z - z_0)^2 g_i(z) g_j(z) dz, \quad (4.25)$$

$$(\mathbf{u})_i = \int_a^b g_i(z) dz, \quad (4.26)$$

and  $\alpha$  is a positive scalar chosen to set the variance level. The solution of this optimization problem is given by

$$\mathbf{a}(z_0) = \frac{W^{-1}\mathbf{u}}{\mathbf{u}^T W^{-1} \mathbf{u}}, \quad (4.27)$$

where

$$W = S(z_0) + \alpha R_e, \quad (4.28)$$

As  $\alpha$  in eq.(4.28) increases, the minimum estimate variance reduces monotonically with increasing spread. Figure 4-1 (dashed line) illustrates the variance-resolution trade-off curve<sup>6</sup>,  $\sigma_p^2(z_0)/\sigma_e^2$  versus spread  $s_A(z_0)$ , where the measurement error for the different eigenvalues are assumed to be independent and of same variance, i.e.,  $R_e = \sigma_e^2 I_M$ . The curve is obtained by varying  $\alpha$  in eq.(4.28) in the interval  $(0, \infty)$ .

One characteristic of the trade-off curve is the high variance associated with the best resolution. For the present example  $(\sigma_p^2)_{\max} \sim 10^{17} \sigma_e^2$  (for a spread of 6.4 m) at that point. If a sound velocity variance of 100 (m/s)<sup>2</sup> is required, the measurement error variance should be  $10^{-13}$  (rad/m)<sup>2</sup>, an unreasonably low value. Improvement in variance can only occur at expense of increased spread, but a large improvement from the worst case estimate variance is obtained with little resolution degradation (note the logarithmic vertical scale). Similarly, significant improvements from the worst case resolution are obtained at little cost to the variance.

Figure 4-1 also shows a plot of another measure of spread around the point  $z_0$  (solid

---

<sup>6</sup>The trade-off curves in Figure 4-1 were computed for the shallow-water waveguide discussed in Section 4.3.3 and shown in Figure 4-4. The inversion problem consists of estimating the sound velocity in the sediment region  $0 \leq z_o \leq 40$  m using 13 “measured” eigenvalues at 25, 50, 75, and 100 Hz. In Figure 4-1,  $z_0 = 8$  m, and the trade-off curves relate two measures of the quality (resolution and variance) of the inferred sound velocity increment at that depth.

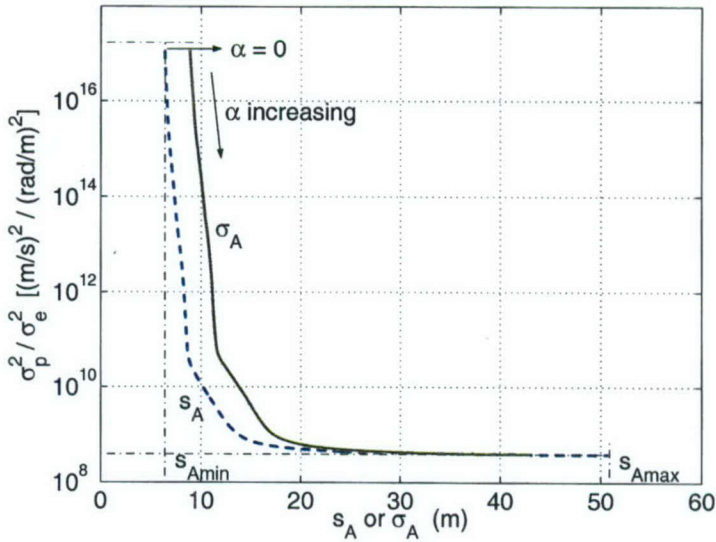


Figure 4-1: Backus-Gilbert spread-versus-variance trade-off curve for a fixed  $z_0$  and  $R_e = \sigma_e^2 I$ .

line), the *deviation*

$$\sigma_A(z_0) = \sqrt{12 \frac{\int_a^b (z - z_0)^2 A^2(z, z_0) dz}{\int_a^b A^2(z, z_0) dz}} = \sqrt{12 \frac{s_A(z_0)}{\mathbf{a}^T(z_0) S^{(0)} \mathbf{a}(z_0)}}, \quad (4.29)$$

where  $S^{(0)}$  is the scaled Gram matrix (matrix of inner products of  $g_i$ )

$$(S^{(0)})_{ij} = 12 \int_a^b g_i(z) g_j(z) dz. \quad (4.30)$$

Measures  $s_A$  and  $\sigma_A$  coincide for a unit area rectangular pulse centered at  $z_0$  and give comparable results for pulse-like functions  $A(z, z_0)$ . Contrary to the spread  $s_A$ , which is defined for an unit area kernel  $A(z, z_0)$ , the deviation  $\sigma_A$  does not rely on any particular property of the kernel. When  $z_0$  coincides with the mean of the distribution  $A^2(z, z_0) / \int_a^b A^2(z, z_0) dz$ , the deviation corresponds to  $\sqrt{12}$  times its standard deviation. As shown in Figure 4-1 the spread and the deviation trade-off curves have the same general behavior.

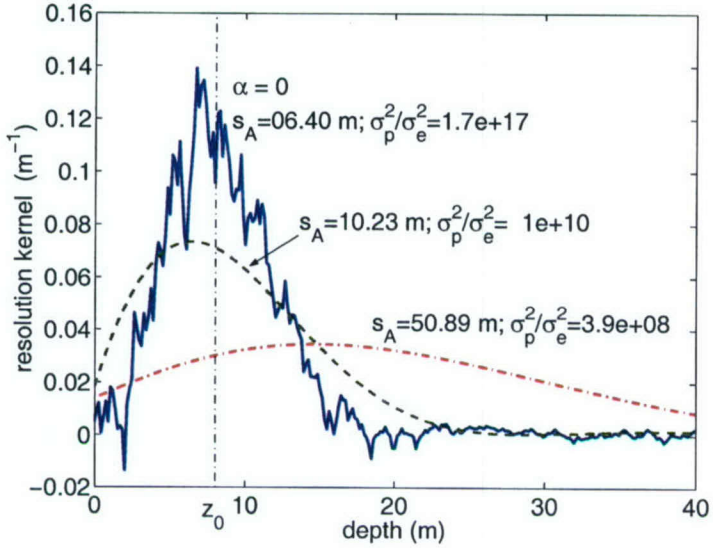


Figure 4-2: Resolution kernel  $A(z, z_0 = 8 \text{ m})$  corresponding to the two extremes and an intermediate point of the trade-off curve, Figure 4-1. The ratio of variances is shown in  $(\text{m/s})^2/(\text{rad/m})^2$ .

Figure 4-2 shows the resolution kernels  $A(z, z_0)$  corresponding to the two extremes and an intermediate point of the trade-off curve. Notice the variability of the kernel corresponding to the highest possible resolution, obtained by setting  $\alpha = 0$ . For the present example, where  $R_e = \sigma_e^2 I_M$ ,  $\alpha$  controls the amount of diagonal loading of the matrix  $S$  in eq.(4.27). For  $\alpha = 0$ , there is no diagonal loading, and the oscillations in the plot of Figure 4-2 are an indication of the ill-conditioning of  $S$ , which leads to the high variance  $\sigma_{\hat{p}}^2$  at the point of best resolution in Figure 4-1. As  $\alpha$  increases, the kernel becomes smoother (and  $\sigma_{\hat{p}}^2$  decreases), resulting in poorer resolution.

## 4.2 The Inverse Eigenvalue Problem

This section analyzes the inverse eigenvalue problem of inferring the sound velocity profile from measurements of series of normal mode eigenvalues, estimated as a function of source-receiver range. The eigenvalues may change with range, allowing for inversion in range-dependent environments.

### 4.2.1 The Measurement Equation

The eigenvalue measurement is described by

$$\mathbf{y}(r) = \mathbf{k}_r(c(z; r); r) + \mathbf{e}(r), \quad (4.31)$$

where  $\mathbf{k}_r$  is an  $M$ -dimensional real vector of distinct normal mode eigenvalues,  $c(z; r)$  is the local sound velocity profile to be estimated, and  $\mathbf{e}$  is the measurement error. The discrete variable  $r = 1, 2, \dots$  represents points over a uniform range grid.

For a slowly varying media, the sound velocity profile is related to the eigenvalue  $k_m$  of the  $m$ -th normal mode through the local (that is, for a fixed range) adiabatic eigenvalue ODE

$$\left( \frac{u'_m}{\rho} \right)' + \frac{\omega_m^2}{c^2} \frac{u_m}{\rho} = k_{rm}^2 \frac{u_m}{\rho}, \quad 0 < z < \infty, \quad (4.32)$$

where  $u_m$ ,  $\rho$ , and  $c$  are functions of the depth  $z$ ,  $u_m(0) = 0$ ,  $u_m(z)$  and  $u'_m(z)/\rho(z)$  satisfy continuity conditions at interfaces (where  $\rho$  may be discontinuous), and the eigenfunction  $u_m$  is normalized so that

$$\int_0^\infty \frac{u_m^2}{\rho} = 1. \quad (4.33)$$

The region  $z > h$  is an homogeneous medium (basement) with constant sound velocity  $c_\infty$  and density  $\rho_\infty$ .

The nonlinear measurement equation (4.31) is solved iteratively starting with profiles  $c_0(z; r)$  using a linearized measurement equation relating sound velocity increments to eigenvalue changes. In order to linearize the measurement equation (4.31), the issue of derivatives of eigenvalues with respect to sound velocity is discussed next.

## 4.2.2 The Derivative of the Modal Eigenvalues

### Layers of Constant Sound Velocity Variation

The eigenvalues are functionals of the sound velocity. The mapping  $c(z) \rightarrow k_{rm}$  is established through the boundary value problem of eq.(4.32). The derivatives of modal eigenvalues can be found by perturbing the eigenvalue equation (4.32) [see Appendix F]. A standard result relates a perturbation  $\Delta c(z)$  in the sound velocity profile to the resulting change in the characteristic wavenumber [cf. eqs.(4.3) and (4.16)]:

$$\Delta k_{rm} = -\frac{\omega_m^2}{k_{rm}} \int_a^b \frac{u_m^2}{\rho} \frac{\Delta c}{c^3} dz + O[(\Delta c)^2] = \int_a^b g_m(z) \Delta c dz + O[(\Delta c)^2]. \quad (4.34)$$

where

$$g_m(z) = -\frac{\omega_m^2}{k_m} \frac{u_m^2(z)}{\rho(z)} \frac{1}{c^3(z)}. \quad (4.35)$$

is the same defined in the integral equations (4.3) and (4.16).

In order to obtain an expression for the derivatives of the eigenvalues, divide the integration interval into segments  $\Delta_n = \{z | z_{n-1} \leq z < z_n \leq h\}$ ,  $n = 1, \dots, N$  and apply a perturbation  $\Delta c$  that is zero everywhere except in  $\Delta_n$ , where the sound velocity is incremented by a constant  $\delta c_n$ . The partial derivative is computed using (4.34) as

$$\partial_{c_n} k_{rm}(c) \equiv \lim_{\delta c_n \rightarrow 0} \frac{\delta k_{rm}}{\delta c_n} = \int_{\Delta_n} g_m(z) dz, \quad \delta c_j = 0, j \neq n. \quad (4.36)$$

If the basement  $z > h$  is perturbed as a whole, the above procedure gives, for the exponentially decreasing eigenfunction in the basement,

$$u_m(z) = u_m(h) \exp \{-\gamma_m(z-h)\},$$

$$\partial_{c_{N+1}} k_{rm}(c) = -\frac{\omega_m^2}{k_{rm}} \frac{u_m^2(h)}{2\gamma_m \rho_\infty c_\infty^3} = \frac{g_m(h^+)}{2\gamma_m}, \quad (4.37)$$

where  $\gamma_m = \sqrt{k_{rm}^2 - \omega_m^2/c_\infty^2}$ .

Define the  $N$ -dimensional vector  $\mathbf{q} = [\delta c_1, \dots, \delta c_N]^T$  as the perturbation of the sound velocity profile in the depth grid defined above. The derivative of the vector of measured eigenvalues is, from eq.(4.36), the  $M \times N$  matrix

$$(G)_{m,n} \equiv (\partial_c \mathbf{k}_r)_{m,n} = \partial_{c_n} k_{rm} = \int_{\Delta_n} g_m(z) dz. \quad (4.38)$$

Different discretization schemes lead to different expressions for the elements of matrix  $G$ .

### Arbitrary Discretization of the Sound Velocity Increment

The sound velocity variations can be represented by a combination of basis functions as

$$\Delta c(z) = \sum_{j=1}^N \delta c_j \phi_j(z) = \Phi^T(z) \mathbf{q}, \quad (4.39)$$

where  $\Phi(z) = [\phi_1(z), \dots, \phi_N(z)]^T$ . In eq. (4.38), for example,  $\phi_n$  is the unit rectangular pulse [1 for  $z_{n-1} \leq z < z_n$ , zero otherwise]. Inserting eq.(4.39) into (4.34), and setting, as before, all  $\delta c_j$  to zero except  $\delta c_n$ , we obtain a more general form of equation (4.38):

$$(G)_{m,n} = \int_a^b g_m(z) \phi_n(z) dz, \quad (4.40)$$

or, using vector notation,

$$G = \int_a^b \mathbf{g}(z) \Phi^T(z) dz. \quad (4.41)$$

If the sound velocity increment is approximated by a series of linear segments, the

basis functions are the unit triangular pulses

$$\phi_n(z) = \begin{cases} (z - z_{n-1}) / (z_n - z_{n-1}), & z_{n-1} < z \leq z_n, \\ & n = 2, \dots, N \\ (z_{n+1} - z) / (z_{n+1} - z_n), & z_n < z \leq z_{n+1}, \\ & n = 1, \dots, N-1, \\ 0, & \text{otherwise.} \end{cases} \quad (4.42)$$

The resulting  $M \times N$  matrix is given by

$$(G)_{m,j} = \int_{z_{j-1}}^{z_j} g_m(z) \frac{1}{c^3} \frac{z - z_{j-1}}{z_j - z_{j-1}} dz + \int_{z_j}^{z_{j+1}} g_m(z) \frac{z_{j+1} - z}{z_{j+1} - z_j} dz. \quad (4.43)$$

A set of basis functions can be defined in terms of the integrand modal kernel  $g_m$ , eq. (4.35), using the Gram matrix  $S^{(0)}$  of eq. (4.30)<sup>7</sup>.  $S^{(0)}$  is symmetric, positive semidefinite<sup>8</sup>, and can be decomposed as  $S^{(0)} = 12\Gamma\Gamma^T = 12Q\Lambda Q^T$ , where  $\Gamma = Q\Lambda^{1/2}$ ,  $\Lambda = \text{diag}(\lambda_1, \dots, \lambda_M)$  is the matrix of the eigenvalues of  $S^{(0)}/12$ , and  $Q$  is the orthogonal matrix whose columns are the eigenvectors. The basis function is given by

$$\phi_j(z) = \lambda_j^{-1/2} \sum_{m=1}^M Q_{jm} g_m(z), \quad (4.44)$$

or, in vector notation,

$$\Phi(z) = \Lambda^{-1/2} Q^T \mathbf{g}(z). \quad (4.45)$$

Note that these basis functions are not localized in depth, i.e., the components of vector  $\mathbf{q}$ ,  $\delta c_n$  of eq.(4.39), do not represent a localized sound velocity change, as in the case of rectangular and triangular pulse bases.

With this set of basis functions, the  $M \times M$  derivative matrix  $G$  becomes, from eqs.

---

<sup>7</sup>This is the spectral expansion method mentioned in Section 4.1.2 [61].

<sup>8</sup>For any  $M \times 1$  vector  $\mathbf{x}$ ,  $\mathbf{x}^T S^{(0)} \mathbf{x} = \int_a^b \mathbf{x}^T \mathbf{g} \mathbf{g}^T \mathbf{x} dz = \int_a^b (\mathbf{x}^T \mathbf{g})^2 dz \geq 0$ .

(4.41) and (4.45),

$$G = \int_a^b \mathbf{g}(z) \Phi^T(z) dz = \int_a^b \mathbf{g}(z) \mathbf{g}^T(z) Q \Lambda^{-1/2} dz = \frac{1}{12} S^{(0)} Q \Lambda^{-1/2} = \Gamma. \quad (4.46)$$

The trapezoidal rule is an easily implemented, common way to discretize eq.(4.34), particularly when it is seen as the integral equation of the inverse perturbative technique. We show that this discretization can also be represented through a basis function.

One approximation consistent with the trapezoidal rule is that  $\Delta c(z)$  changes linearly between depth grid points. Therefore, the triangular pulse representation of eq.(4.42) over the dense grid required by the trapezoidal rule would be valid. Another possible assumption is that the product  $g_m(z)\Delta c(z)$  of the integrand is linear between depth grid points. Appendix E shows that this assumption leads to [cf. eq.(4.39)]

$$\phi_n(z) = \frac{\sum_{m=1}^M g_m(z_n)}{\sum_{m=1}^M g_m(z)} \begin{cases} (z - z_{n-1}) / (z_n - z_{n-1}), & z_{n-1} < z \leq z_n, \\ & n = 2, \dots, N, \\ (z_{n+1} - z) / (z_{n+1} - z_n), & z_n < z \leq z_{n+1}, \\ & n = 1, \dots, N-1, \\ 0, & \text{otherwise.} \end{cases} \quad (4.47)$$

for  $\sum_{m=1}^M g_m(z) \neq 0$ , a slight modified triangular basis.

## A Formal Functional Differentiation

The above *ad hoc* approach to the derivative of modal eigenvalues with respect to the sound velocity profile is consistent with the more rigorous definition of *functional differentiation*.

Seen as a functional of the sound velocity, the eigenvalue  $k_m(c(z))$  is defined for sound velocity profiles from some domain  $X$  in a Hilbert space  $\mathbb{H}$ , formally,  $k_m : X \subseteq \mathbb{H} \rightarrow \mathbb{R}$ . In this context, the concept of derivative is generalized to functional differentiation. For

example,  $k_m$  is said to be Fréchet-differentiable<sup>9</sup> if one can find  $D_{k_m} \in \mathbb{H}$  such that

$$k_m(c + \Delta c) = k_m(c) + \langle D_{k_m}, \Delta c \rangle + R_m(\Delta c), \quad (4.48)$$

for some  $\|\Delta c\| < \epsilon$  and with  $R_m(\Delta c)/\|\Delta c\| \rightarrow 0$ .  $\langle u, v \rangle$  indicates the inner product defined in  $\mathbb{H}$ .

The perturbative integral (4.34) is in the form described in (4.48), from which the Fréchet derivative  $D_{k_m}$  of  $k_m$  is given by  $D_{k_m} = g_m(z)$ . The underlying (real) Hilbert space is  $L_2(a, b)$  with inner product  $\langle u, v \rangle = \int_a^b u v dz$ . For the vector of eigenvalues  $\mathbf{k}_r$ , the derivative is constructed as the vector formed by the derivative of each eigenvalue,  $\mathbf{D} = [D_{k_1}, \dots, D_{k_M}]^T$ .

Using the basis function representation of  $\Delta c$ , eq.(4.39), the vector version of (4.48) is

$$\mathbf{k}_r(c + \Delta c) = \mathbf{k}_r(c) + G\mathbf{q} + O[(\Delta c)^2], \quad (4.49)$$

which shows that the use of matrix  $G$  as a representation of the derivative of eigenvalues is consistent with the more rigorous notion of functional differentiation, and leads to a convenient representation of the mapping  $\mathbf{k}_r$  in the neighborhood of a “point” [of the space  $L_2(a, b)$ ]  $c(z)$ .

### Linearizing the Measurement Equation

Let the sound velocity profile be given by  $c(z; r) = c_0(z; r) + \Delta c(z; r) = c_0(z; r) + \Phi^T(z)\mathbf{q}(r)$ , where  $c_0(z; r)$  and  $\Phi^T(z)$  are known. Neglecting the high order terms in  $\Delta c$ , the measurement equation (4.31) becomes, after substituting eq.(4.49),

$$\mathbf{d}_0(r) \equiv \mathbf{y}(r) - \mathbf{k}_r(c_0(z; r)) = G_0(r)\mathbf{q}(r) + \mathbf{e}(r), \quad (4.50)$$

where the subscript '0' indicates quantities related to the profile  $c_0(z; r)$ .

---

<sup>9</sup>Rajan [60] showed that  $k_m$  is Fréchet-differentiable with respect to the sound velocity in fluids.

At this point, one should suspect that the linearized equation (4.50) is equivalent to the discretization of the integral equation (4.16) [or (4.3)] of the inverse perturbative technique. In fact, if the basis function representation of  $\Delta c(z)$  is exact, the two are one and the same. From eqs. (4.16), (4.39), and (4.40),

$$\begin{aligned} d_m &= \int_a^b g_m(z) \Delta c(z) dz + e_m \\ &= \sum_{t=1}^N \delta c_t \int_{\Delta_i} g_m(z) \phi_t(z) dz + e_m = \sum_{t=1}^N (G)_{mt} \delta c_t + e_m, \end{aligned} \quad (4.51)$$

which is the scalar version of the linearized measurement equation (4.50). The integral equation of the perturbative inverse technique (4.3) is the linearized eigenvalue equation.

### 4.2.3 The Range-Varying Eigenvalue Inverse

Nonlinear estimation is an iterative process. The measurement equation is linearized around a profile  $c_{i-1}(z)$ , and the equation

$$\mathbf{d}_{i-1}(r) \equiv \mathbf{y}(r) - \mathbf{k}_r(c_{i-1}(z; r); r) = G_{i-1}(r) \mathbf{q}_i(r) + \mathbf{e}, \quad i = 1, 2, \dots, \quad (4.52)$$

is solved for  $\mathbf{q}_i$ . The sound velocity profile is updated,  $c_i(z) = c_{i-1}(z) + \Phi^T \mathbf{q}_i$ , and the process is iterated with the new sound velocity profile. This iterative process is the approach of the perturbative inverse technique [61] described in Section 4.1.2. In principle, this process should be repeated at each range step.

The goal of the iteration process in nonlinear problems<sup>10</sup> is to minimize a cost function related to the actual error  $[\mathbf{y} - \mathbf{k}_r(c_i(z))]$ , the new eigenvalue difference  $\mathbf{d}_i$ . At each iteration, solving eq.(4.52) involves minimizing a cost function associated with  $(\mathbf{d}_{i-1} - G_{i-1} \mathbf{q}_i)$ , which, as discussed in Sections 4.1.2 and 4.1.3, requires some form of regularization.

---

<sup>10</sup>A survey of algorithms can be found in[58].

Extrapolating Franklin's stochastic inverse technique, assume that  $\mathbf{q}_i(r)$  is described as a Gaussian-Markov process evolving in range according to

$$\mathbf{q}_i(r+1) = \mathbf{q}_i(r) + \mathbf{w}_i(r), \quad r = 1, \dots, N_r \quad (4.53)$$

where  $\mathbf{w}_i(r)$  is a white process (in  $r$ ) with covariance  $R_{w,i}(r)$ .

Equations (4.52) and (4.53) are a state-space description of the inverse problem. Under additional assumptions of independence between the processes  $\mathbf{w}_i$  and  $\mathbf{e}$ , that both are zero-mean Gaussian, and the initial value  $\mathbf{q}_i(0)$  is also Gaussian, the solution to this linear problem is the Kalman filter described in Algorithm 3. The forward/backward notation of Chapter 3 is used here.

The above approach of iteration and range evolution corresponds to a nonlinear Kalman filter that solves the actual measurement equation (4.31) in a preset "range trajectory"  $c_{i-1}(z; r)$ [33]. The trajectory is updated at each iteration using the Kalman filter solution to the linearized equation,  $\hat{\mathbf{q}}_i(r|r)$ .

The connection with Franklin's method is that eq.(4.53) defines a (now range-varying) covariance for the "process"  $\mathbf{q}_i(r)$ . Assuming that the initial value  $\mathbf{q}_i(0)$  has covariance  $R_{q0,i}$ , the covariance of  $\mathbf{q}_i(r)$  is given by[2]

$$R_{q,i}(r) = R_{q0,i} + \sum_{n=0}^{r-1} R_{w,i}(n). \quad (4.54)$$

Equation (4.54) may be seen as a statement of the uncertainty of the knowledge of the sound velocity profile, which increases with range. This would be the case, for example, when inverting a series of modal eigenvalues measured in the neighborhood of a point where the sound velocity profile is reasonably well known (as quantified by  $R_{q0,i}$ ). One would expect that, in a range-dependent environment, the uncertainty regarding the profile increases with the distance from the position where the profile is known.

---

**Algorithm 3** *Kalman filter solution to the range-dependent stochastic perturbative inverse.* Initial values of the solution  $\mathbf{q}$  and associated covariance  $R_q$  must be provided. Forward filter: initialize with values  $\hat{\mathbf{q}}^-(1|0) = \mathbf{q}_0$  and  $P^-(0|0) = R_{q0}$ , and estimate the  $\mathbf{q}$  for  $r = 1, \dots, N_r$ . Backward filter: initialize with  $\hat{\mathbf{q}}^+(N_r + 1|N_r + 1) = \mathbf{q}_{N_r+1}$  and  $P^+(L_r|L_r + 1) = R_{qN_r}$ , and estimate the  $\mathbf{q}$  for  $r = N_r, N_r - 1, \dots, 1$ .

---

1. Prediction: given the background profile and measured eigenvalues at  $r$ , compute  $G(r)$ ,  $\mathbf{d}(r)$ , and

$$\begin{aligned}\hat{\mathbf{q}}^\oplus(r|r \oplus 1) &= \hat{\mathbf{q}}^\oplus(r \oplus 1|r \oplus 1), \\ \epsilon^\oplus(r) &= \mathbf{d}(r) - G(r)\hat{\mathbf{q}}^\oplus(r|r \oplus 1).\end{aligned}\tag{4.55}$$

2. Update

$$\begin{aligned}P^\oplus(r|r \oplus 1) &= P^\oplus(r \oplus 1|r \oplus 1) + R_w, \\ P^\oplus(r|r) &= P^\oplus(r|r \oplus 1) \times \\ \{I_N - G^T(r) [R_e + G(r)P^\oplus(r|r \oplus 1)G^T(r)]^{-1} G(r)P^\oplus(r|r \oplus 1)\}, \\ \hat{\mathbf{q}}^\oplus(r|r) &= \hat{\mathbf{q}}^\oplus(r|r \oplus 1) + P^\oplus(r|r)G^T(r)R_e^{-1}\epsilon^\oplus(r).\end{aligned}\tag{4.56}$$


---

## 4.3 Variance and Resolution of the Inverse Eigenvalue Problem

### 4.3.1 Cramer-Rao Bound for the Eigenvalue Inversion

Intuitively, one can expect that a smaller measurement noise level (variance), results in a better estimate. Assuming a zero mean measurement noise, the probability density function of the measurement  $\mathbf{y}$  in eq. (4.31) will be that of the noise  $\mathbf{e}$ , but with mean  $\mathbf{k}_r(c(z))$ —the density of  $\mathbf{y}$  is a function of the unknown profile. Figure 4-3 shows hypothetical distributions for a scalar measurement  $y$ . The more *peaked* the density (smaller variance) the more the measurement is sensitive to the sound velocity i.e., small variations in the mean  $k_m(c(z))$  are more easily detected. Therefore, the second derivative of the distribution function (w.r.t. the profile) near the mean can be used as

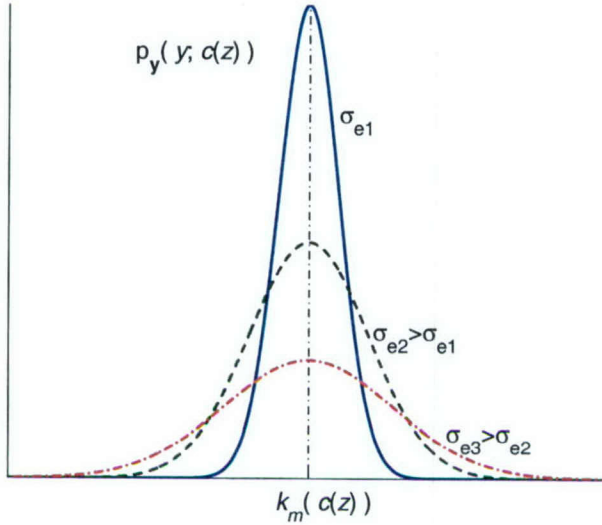


Figure 4-3: An illustration of the distribution density function of the measurement for 3 values of noise variance.

a measure of how sensitive the measurement is to the sound velocity.

In order to reduce the problem to a finite dimension  $N$ , assume that the sound velocity profile is exactly given, for a known set of functions  $\{\phi_n(z)\}$  and a known profile  $c_0(z)$ , by the basis function representation of Section 4.2.2, i.e.,

$$c(z) = c_0(z) + \Phi^T(z)\mathbf{q}. \quad (4.57)$$

The eigenvalue vector is a function of the  $N \times 1$  vector  $\mathbf{q}$  and, allowing for a slight abuse of notation, write  $\mathbf{k}_r(c(z)) \equiv \mathbf{k}_r(\mathbf{q})$ . The derivative  $\partial_q \mathbf{k}_r$  is given by eq.(4.41).

The Fisher information matrix  $I_y(\mathbf{q})$  is defined as the expected value of the second derivative of the logarithm of the density of  $\mathbf{y}$ ,  $p_y(\mathbf{y}, \mathbf{q})$ , seen as a function the parameter  $\mathbf{q}$  to be estimated:

$$I_y(\mathbf{q}) = -E \{ [\partial_q^2 \ln p_y(\mathbf{y}, \mathbf{q})] \}. \quad (4.58)$$

$I_y(\mathbf{q})$  is a measure of how much information the measurement  $\mathbf{y}$  has of that parameter  $\mathbf{q}$ . An equivalent expression involving only first derivatives is given by [56]

$$I_y(\mathbf{q}) = E \left\{ [\partial_{\mathbf{q}} \ln p_y(\mathbf{y}, \mathbf{q})]^T [\partial_{\mathbf{q}} \ln p_y(\mathbf{y}, \mathbf{q})] \right\}. \quad (4.59)$$

Assuming a zero mean Gaussian measurement noise  $\mathbf{e}$  with covariance  $R_e$ ,  $p_y(\mathbf{y}, \mathbf{q})$  is obtained from the measurement equation (4.31) as

$$p_y(\mathbf{y}, \mathbf{q}) = \frac{1}{(2\pi)^{M/2} |R_e|^{1/2}} \exp \left\{ -\frac{1}{2} [\mathbf{y} - \mathbf{k}_r(\mathbf{q})]^T R_e^{-1} [\mathbf{y} - \mathbf{k}_r(\mathbf{q})] \right\}, \quad (4.60)$$

where  $M$  is the number of modes, the dimension of  $\mathbf{k}_r$ . The derivative of the logarithm of the density function in (4.59) is, therefore,

$$\begin{aligned} \partial_{\mathbf{q}} \ln p_y(\mathbf{y}, \mathbf{q}) &= [\mathbf{y} - \mathbf{k}_r(\mathbf{q})]^T R_e^{-1} \partial_{\mathbf{q}} \mathbf{k}_r(\mathbf{q}). \\ &= [\mathbf{y} - \mathbf{k}_r(\mathbf{q})]^T R_e^{-1} G_c, \end{aligned} \quad (4.61)$$

and the  $N \times N$  Fisher information matrix becomes, from (4.59),

$$I_y(\mathbf{q}) = G_c^T R_e^{-1} G_c. \quad (4.62)$$

The subscript  $c$  in  $G_c$  indicates that the derivatives are computed at the actual sound velocity profile.

Any estimator  $\hat{\mathbf{q}}(\mathbf{y})$  of  $\mathbf{q}$  based on  $\mathbf{y}$  has a covariance bounded by [56]

$$\Sigma_{\hat{\mathbf{q}}} \geq \mathcal{M} I_y^{-1}(\mathbf{q}) \mathcal{M}^T, \quad (4.63)$$

where  $\mathcal{M} = I_N + \partial_{\mathbf{q}} \mathbf{b}$ , and  $\mathbf{b}(\mathbf{q}) = E[\hat{\mathbf{q}}] - \mathbf{q}$  is the estimator bias. When the estimator is *unbiased*,  $\mathbf{b} = 0$ ,  $\mathcal{M} = I_M$  and eq.(4.63) reduces to the Cramer-Rao inequality

$$\Sigma_{\hat{\mathbf{q}}} \geq I_y^{-1}(\mathbf{q}) = (G_c^T R_e^{-1} G_c)^{-1}. \quad (4.64)$$

This matrix inequality is interpreted in terms of quadratic forms, i.e., for any  $N \times 1$

vector  $\mathbf{x}$ ,  $\mathbf{x}^T \Sigma_{\hat{\mathbf{q}}} \mathbf{x} \geq \mathbf{x}^T I_{\mathbf{y}}^{-1}(\mathbf{q}) \mathbf{x}$ . In particular, the diagonal elements of  $I_{\mathbf{y}}^{-1}(\mathbf{q})$  are the Cramer-Rao lower bounds (CRB) on the variance of each element of the estimated vector  $\hat{\mathbf{q}}$ . An efficient estimator, one whose variance is given by the CRB, does not exist due to the nonlinearity of the relation  $\mathbf{k}_r(\mathbf{q})$ .

If  $N_R$  independent measurements of the eigenvalue vector are available, and if the measurement noise covariance is the same for all measurements, then the CRB is reduced by a factor  $N_R$ .

### 4.3.2 Sound Velocity Variance and Resolution

The CRB is a bound on the covariance of the estimated vector  $\hat{\mathbf{q}}$ . At an arbitrary depth  $z_0$ , the sound velocity increment estimate is obtained from eq.(4.39) as

$$\Delta \hat{c}(z_0) = \Phi^T(z_0) \hat{\mathbf{q}}, \quad (4.65)$$

with mean  $E[\Delta \hat{c}(z_0)] = \Phi^T(z_0) E[\hat{\mathbf{q}}]$  and variance

$$\begin{aligned} \sigma_{\hat{c}}^2(z_0) &= E[(\Delta \hat{c}(z_0) - E[\Delta \hat{c}(z_0)])^2] \\ &= \Phi^T(z_0) \Sigma_{\hat{\mathbf{q}}} \Phi(z_0) \geq \Phi^T(z_0) (G_c^T R_e^{-1} G_c)^{-1} \Phi(z_0), \end{aligned} \quad (4.66)$$

where the inequality follows from eq.(4.64). Equation (4.66) defines a bound, derived from the CRB, on the variance of the sound velocity increment estimate at  $z_0$  and, from eq.(4.57), on the sound velocity estimate itself.

When the components of  $\mathbf{q}$  represent actual sound velocity increment at points  $z_j$  on a depth grid (rectangular, triangular, or trapezoidal rule bases), then  $\Delta c(z_j) = (\mathbf{q})_j = \delta c_j$ ,  $\Phi(z_j)$  is a unit vector and eq. (4.66) reduces to

$$\sigma_{\hat{c}}^2(z_j) = (\Sigma_{\hat{\mathbf{q}}})_{jj} \geq \left[ (G^T R_e^{-1} G)^{-1} \right]_{jj}. \quad (4.67)$$

Therefore, for these localized basis functions, the sound velocity variance bound at the depth grid points is given by the CRB.

The resolution associated with  $\Delta\hat{c}(z_0)$  is measured by the deviation defined in eq.(4.29). The Backus-Gilbert theory assumes a linear relation between the eigenvalue differences and the sound velocity increment. Assuming the estimated sound velocity profile is close to the actual one and the linear approximation is valid, the depth resolution can be obtained using the estimated profile. The best BG resolution computed from the estimated profile can be considered as an estimate of the actual resolution.

Alternatively, the resolution can be estimated directly from the inverse operator. If the last iteration inverse is  $\tilde{G}$ , then  $\Delta\hat{c}(z_0) = \Phi^T(z_0)\hat{\mathbf{q}} = \Phi^T(z_0)\tilde{G}\mathbf{d}$ , which, by comparison with eq.(4.18), leads to

$$\mathbf{a}(z_0) = \tilde{G}^T\Phi(z_0) \quad (4.68)$$

as the analogous of the BG inverse. The resolution kernel from eq.(4.19) becomes  $A(z, z_0) = \Phi^T(z_0)\tilde{G}\mathbf{g}(z)$  (not necessarily of unit area), and the deviation, from eq.(4.29), becomes

$$\hat{\sigma}_A(z_0) = \sqrt{12 \frac{\int_a^b (z - z_0)^2 A^2(z, z_0) dz}{\int_a^b A^2(z, z_0) dz}} = \sqrt{12 \frac{\Phi^T(z_0)\tilde{G} S(z_0)\tilde{G}^T\Phi(z_0)}{\Phi^T(z_0)\tilde{G} S^{(0)}\tilde{G}^T\Phi(z_0)}}, \quad (4.69)$$

where matrices  $S(z_0)$  and  $S^{(0)}$  are given, respectively, by eqs.(4.25) and (4.30). For a localized basis function (rectangular and triangular pulses, or trapezoidal rule),  $\Phi(z_j)$  is the unit vector  $\phi_n(z_j) = \delta_{n,j}$ , then  $\mathbf{a}(z_j) = (\tilde{G})_{\text{column } j}$  and  $A(z, z_j) = (\tilde{G}^T)_{\text{row } j}\mathbf{g}(z)$ .

### 4.3.3 Analysis of a Prototype Problem

This section analyzes the typical shallow-water waveguide of Figure 4-4. We show that the CRB is high, leading to the requirement of unreasonably low eigenvalue measurement variance in order to achieve small sound velocity variance. This is consistent with the BG trade-off curve of Figure 4-1, where the best resolution (analogous to the unbiased

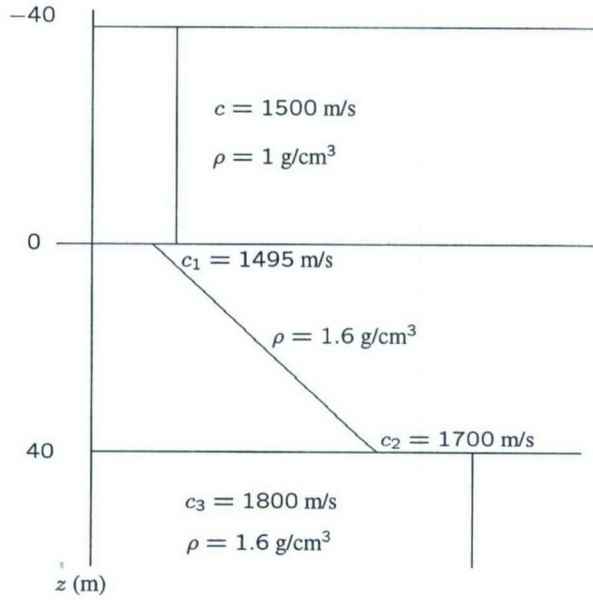


Figure 4-4: Shallow-water environment for the inverse problem analysis example.

estimate) is attained at a cost of high variance. As in the BG analysis, one should expect to reduce the variance by decreasing the resolution, i.e., by introducing bias in the estimator. This is illustrated in Section 4.3.3 through the stochastic inverse.

Another objective of the present section is to show how the BG analysis can be used in the design of experiments for eigenvalue inversion. It is shown that, as the number of modes increases, the best resolution and minimum BG variance improve. The analysis is a tool for the choice of frequencies and to establish goals for the eigenvalue measurement error and expected sound velocity variance and resolution.

The shallow-water waveguide of Figure 4-4 consists of an isovelocity water layer overlaying a sediment layer of increasing sound velocity and a homogeneous basement. The “data” are the 13 modal eigenvalues at 25, 50, 75, and 100 Hz, which should be inverted for the sound velocity in the sediment,  $0 \leq z \leq 40$  m. The measurement error is assumed to be uncorrelated and equally distributed, i.e.,  $R_e = \sigma_e^2 I$ , as in Section 4.1.4, Figures 4-1 and 4-2.

Figure 4-5 shows the normalized modal functions at the frequencies of interest. The

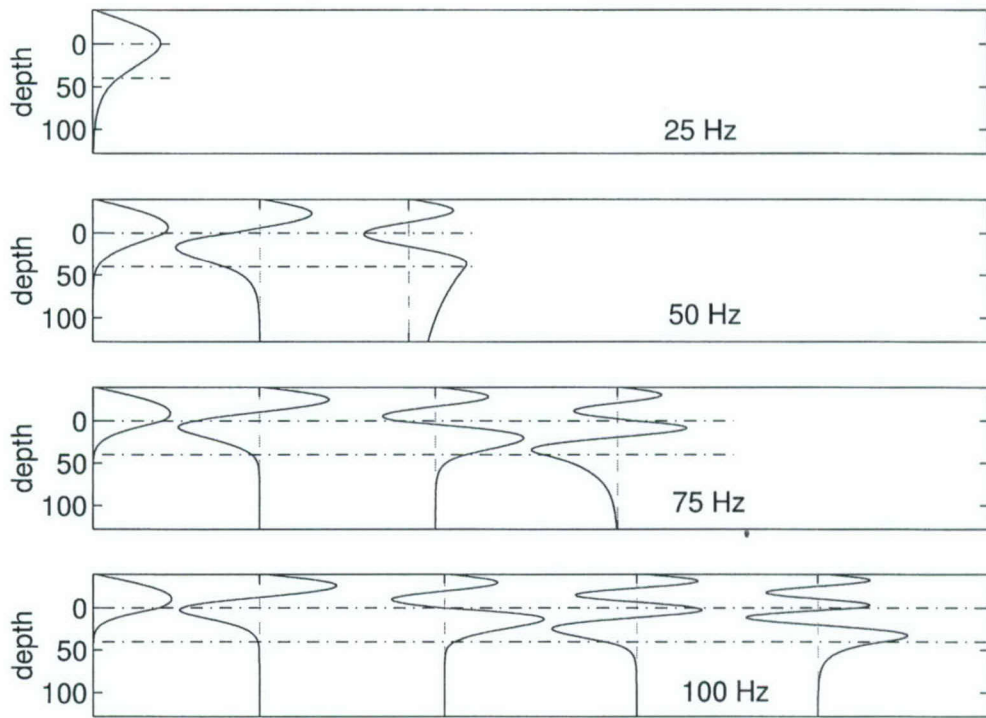


Figure 4-5: Mode functions for the prototype environment.

vertical, dashed lines represent the zero axis for each mode. The horizontal, dash-dot lines indicate the interfaces at 0 and 40 m depth. The mode magnitude scale is the same on all plots.

### Cramer-Rao Lower Bound

Assuming the sediment layer thickness of Figure 4-4 is known, the sound velocity profile is characterized by only two parameters, the velocities at zero and 40 m, for example. The inversion involves the estimation of these two parameters. In order to allow for a more general example, assume that the sediment profile is represented by the sound velocity at 11 depths. The region  $0 \leq z_0 \leq 40$  m is divided into 10 segments where the sound velocity is assumed to change linearly, the triangular pulse basis function representation of eq. (4.43). For this basis function, the CRB for the sound velocities

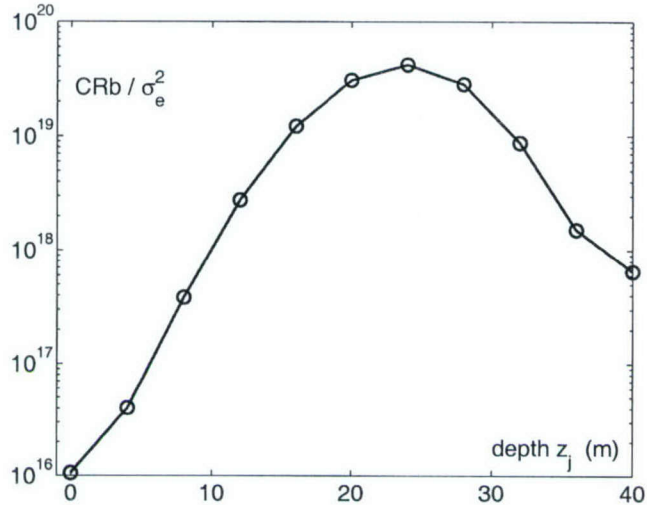


Figure 4-6: The Cramer-Rao bound for the variances of the sound velocity estimate in the sediment layer shown in Figure 4-4 [CRB in  $(\text{m/s})^2$ ,  $\sigma_e^2$  in  $(\text{rad/m})^2$ ].

at the grid points is given by eq.(4.67).

The CRB (relative to  $\sigma_e^2$ ) is shown in Figure 4-6. It was computed using the exact sound velocity profile and all 13 eigenvalues. The CRB at  $z = 8\text{m}$  is  $3.8 \times 10^{17} \sigma_e^2$   $(\text{m/s})^2$ , comparable to the  $1.7 \times 10^{17} \sigma_e^2$   $(\text{m/s})^2$  obtained by the Backus-Gilbert analysis at the best resolution [cf. Figure 4-2]. The error variance bound varies with depth between  $10^{16}$  and  $3 \times 10^{19}$  times the measurement variance. If the required estimate error is to be below 5% (approximately 80 m/s) in the first three sub-layers, the required eigenvalue measurement standard deviation should be  $\sigma_e = 80/\sqrt{3 \times 10^{17}} \sim 1.5 \times 10^{-7}$  rad/m. In order to reach a more reasonable figure of  $\sigma_e = 10^{-4}$  m $^{-1}$ , nearly 700 independent measurements of the 13 eigenvalues would be required. In typical experiments, just a single measurement is available at a given range.

Large variances are typical of the eigenvalue inverse problem, unless some form of regularization is imposed, as discussed in Sections 4.1.2 and 4.1.3. In the linear case, large oscillations in the solution are related to the large spread of the singular values of the matrix  $G$ . In the present example, the derivative of eigenvalues, matrix  $G_c$ , is

full rank, but only the first six singular values are “reasonably large”, above 1% of the largest one. As discussed below, reducing the effect of low singular values has the effect of reducing the variance bound (that is, regularizing the problem) at the cost of introducing bias.

In order to obtain estimate variances smaller than the (unbiased) CRB, bias has to be accepted. This is suggested by eq.(4.63): a “reduction” in  $\mathcal{M}I_y^{-1}(\mathbf{q})\mathcal{M}^T$  from the case  $\mathcal{M} = I_N$  (the CRB), can only be achieved by some non identity  $\mathcal{M}$ , i.e., by introducing bias. This is achieved when the problem is regularized.

### Regularized Inverse

In order to illustrate the effect of bias on variance, the standard form of the Tikhonov regularization<sup>11</sup>, eq.(4.9), is used with  $G_c$ , the actual eigenvalue derivative, to obtain the inverse operator  $\tilde{G}_c$ ,

$$\hat{\mathbf{q}} = \tilde{G}_c \mathbf{d} = (G_c^T G_c + \mu^2 I_N)^{-1} G_c^T \mathbf{d}. \quad (4.70)$$

As in Section 4.3.3, the sediment layer of the environment of Figure 4-4 is divided in 10 intervals and the sound velocity profile described by the triangular pulse basis. The rank of  $13 \times 11$  matrix  $G_c$  is 11.

The expected value for the linear estimator (4.70) is given, from the linear measurement equation (4.50), by  $E[\hat{\mathbf{q}}] = \tilde{G}_c E[\mathbf{d}] = \tilde{G}_c G_c \mathbf{q}$ , the bias by  $\mathbf{b} = (\tilde{G}_c G_c - I_N) \mathbf{q}$  and the covariance by

$$\Sigma_{\tilde{q}} = \tilde{G}_c R_e \tilde{G}_c^T = \sigma_e^2 \tilde{G}_c \tilde{G}_c^T. \quad (4.71)$$

When  $\mu = 0$ ,  $\tilde{G}_c = (G_c^T G_c)^{-1} G_c^T$ ,  $E[\hat{\mathbf{q}}] = \mathbf{q}$ ,  $\mathbf{b} = 0$ , and  $\Sigma_{\tilde{q}} = \sigma_e^2 (G_c^T G_c)^{-1}$ , which is the CRB, eq.(4.64). The parameter  $\mu$  scales with the singular values of  $G_c$ , as suggested by the svd representation in eq.(4.9). As discussed in Section 4.1.2, there is a significant damping of the singular values smaller than  $\mu$ .

We compare changes in variance with the BG resolution, which has a more direct

---

<sup>11</sup>or, equivalently, the stochastic inverse of eq.(4.13) with  $R_e = \sigma_e^2 I_M$  and  $R_q = \sigma_e^2 \mu^{-2} I_N$ .

physical interpretation than estimator bias. For the present example,  $\hat{\mathbf{q}}$  represents sound speed increment at the grid points  $z_j$ . From eq.(4.68),  $\mathbf{a}(z_j) = (\tilde{G}_c)_{\text{column } j}$ . Once  $\tilde{G}_c$  is computed, the resolution kernel is obtained from eq.(4.19),  $A(z, z_j) = \mathbf{a}^T(z_j)\mathbf{g}(z)$  and the deviation  $\sigma_A(z_j)$  from eq.(4.69).

The variances, resolution kernels and associated deviations are shown in Figure 4-7 [cf. Figure 4-2] for  $\mu$  set to zero (CRB) and the 3rd, 5th and 7th largest singular values. For reference, the maximum singular value of the matrix  $G$  is  $1.12 \times 10^{-4}$  (using the triangular pulse basis). As  $\mu$  increases, variance decreases, deviation increases, and resolution, the ability to resolve details of the sound velocity profile, decreases. For  $\mu = 3.5 \times 10^{-7}$ , the seventh largest singular value, the estimate variance is considerable smaller than the Cramer-Rao bound and the degradation in resolution from the optimum predicted in the trade-off curve of Figure 4-1 is comparatively small.

Notice that the resolution kernel corresponding to the CRB differ significantly from the optimum BG kernel in Figure 4-2. In fact, either as described by the deviation, or by examining the plot of the kernel directly, the unbiased estimator has a poor resolution performance. In this sense, deviation is more meaningful than bias to describe estimate quality.

## BG Resolution and Variance

Figure 4-8 shows the BG resolution as a function of depth for different combinations of eigenvalues. Plots on the right show the minimum possible deviation  $\sigma_A$  (m) for different combinations of “measured” eigenvalues. The minimum deviation is obtained from eq.(4.24) when  $\alpha$  in eq.(4.28) is set to zero (no contribution from the error covariance  $R_e$  to the inversion). The corresponding plots on the right are for the resolution kernel at  $z_0 = 8$  m corresponding to the minimum deviation.

The values of relative estimate variance ( $\sigma_e^2/\sigma_e^2$  in  $(\text{m/s})^2/(\text{rad/m})^2$  indicated in the plots correspond to the minimum possible variance (worst resolution) for a unit area resolution kernel. Minimum variance is obtained from eq.(4.21) when  $\alpha$  in eq.(4.28) is

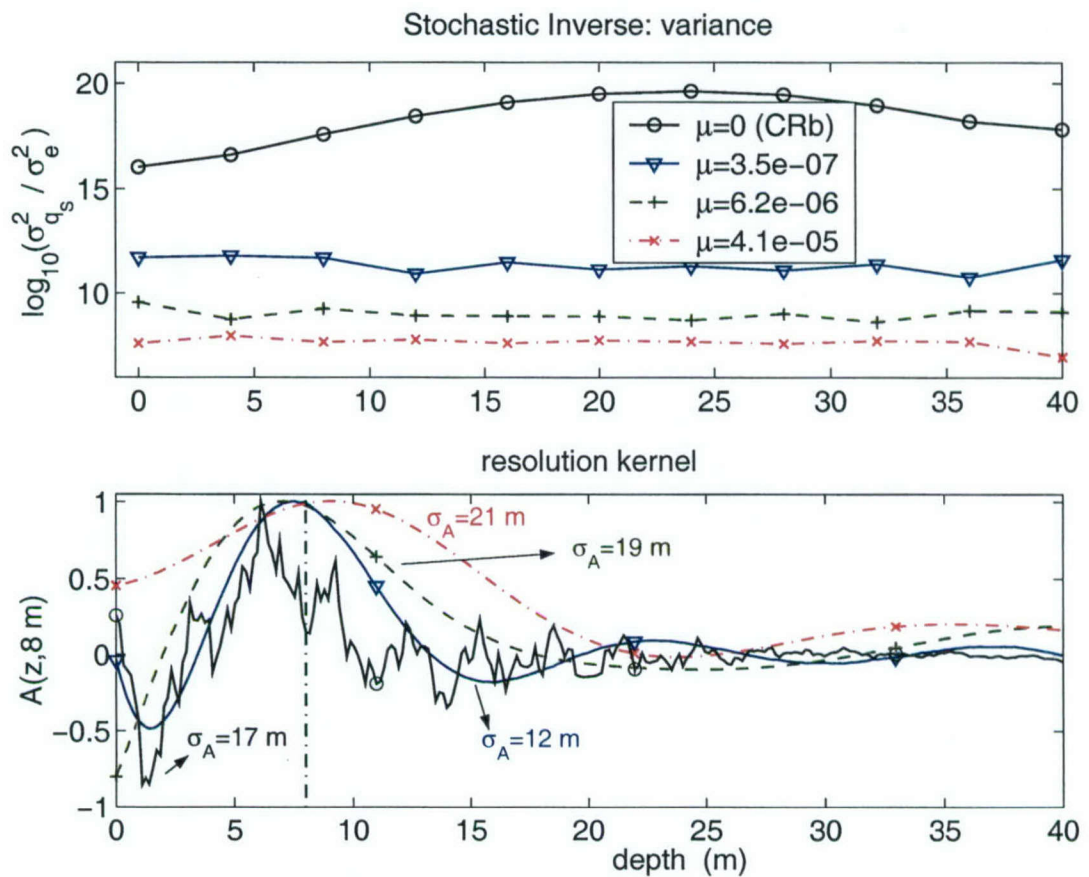


Figure 4-7: Simplified stochastic inverse for the example from Figures 4-4 and 4-6. (a) estimate variances  $\sigma_q^2(z_j)/\sigma_e^2$  and (b) resolution kernel  $A(z, z_0)$  for  $z_0 = 8$  m (indicated by the vertical line), normalized for a maximum value of unit for plotting.

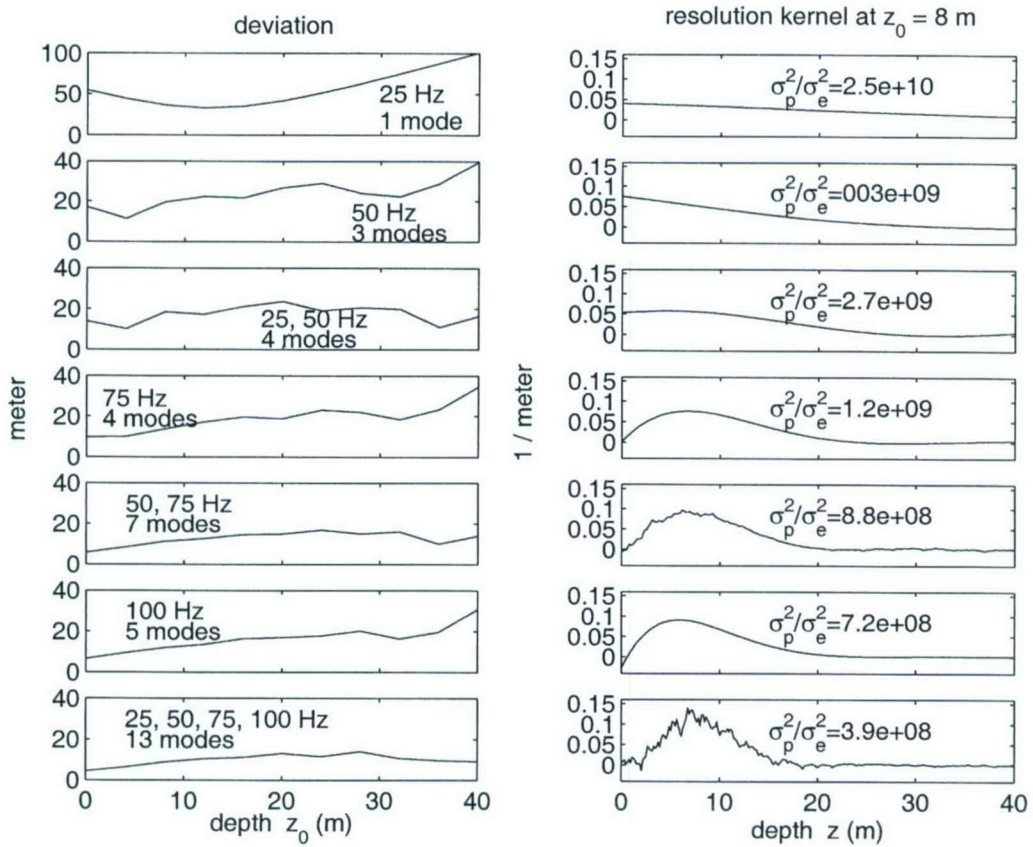


Figure 4-8: Minimum deviation  $\sigma_A(z_0)$  and corresponding resolution kernel  $A(z, z_0)$ ,  $z_0 = 8$  m, for the eigenvalue inversion of the environment of Figure 4-4. The relative error variance, shown in  $(\text{m/s})^2/(\text{rad/m})^2$ , corresponds to the minimum attainable BG variance (extreme right of the trade-off curve, Figure 4-1).

set to infinity, leading to  $\sigma_{\hat{p}}(z_0) = (\mathbf{u}^T R_e^{-1} \mathbf{u})^{-1}$ , independent of  $z_0$ . The last two plots at the bottom of Figure 4-8 correspond to the ones shown in Figures 4-1 and 4-2, where all 13 eigenvalues are used in the inversion.

The upper plots of Figure 4-8 show the poor resolution and high estimate variances that can be expected when using a single mode (note the different scale on the plot for the single, 25 Hz mode inversion case). The resolution is nearly equal to the whole depth interval, indicating that the inversion will result in an average sound velocity increment. This is better illustrated by the plot of the resolution kernel  $A(z, z_0 = 8 \text{ m})$  on the right.

In general, as the frequency and the number of modes increase, the resolution and the minimum variance decrease. There are two cases with 4 modes, one involving two frequencies (25 and 50 Hz) and the other a single frequency (75 Hz). The resolution near the lower interface,  $z_0 = 40 \text{ m}$ , improves remarkably when using two frequencies. The mode plots in Figure 4-5 indicate that the 25/50 Hz combination has 3 modes with significant magnitude at that depth, while, at 75 Hz, only 2 modes are significantly different from zero. On the other hand, an examination of the resolution kernels suggests improved performance of the 75 Hz data over the 25/50 Hz combination.

The influence of the contribution of the number of modes to resolution is also illustrated by comparing the 75 Hz and 100 Hz single frequency cases. At the 40 m interface, both give roughly the same resolution, despite the larger number of 100 Hz modes. The mode amplitude plot reveals that, in fact, both frequencies have two modes with significant magnitude at that depth.

This suggests that the number of modes with significant magnitude at a certain depth is an indicator of improved resolution at that depth, albeit not the only one. The apparently monotonic decrease of deviation with increasing number of modes at the upper interface suggests other factors are at play, possibly, the degree of independence between the different modal kernels  $g_m(z)$  near  $z = 0 \text{ m}$ .

## 4.4 Source Speed Compensation

### 4.4.1 Eigenvalue Bias due to Doppler Deviation

Effects of source motion in the modal representation is discussed by Hawker [31], and Schmidt and Kuperman [63]. Source motion introduces, due to the Doppler effect, a deviation in the eigenvalue:

$$k_{rm}^d = k_{rm}(\omega + \omega_D) = k_{rm}(\omega) + \omega_D \left. \frac{dk_{rm}}{d\omega} \right|_{\omega} + O(\omega_D^2), \quad (4.72)$$

where  $k_{rm}^d$  is the measured eigenvalue for mode  $m$ ,  $\omega$  is the source frequency,  $\omega_D = k_{rm}^d v_s$  is the Doppler deviation, and  $v_s$  is the component of the sound velocity in the direction of the receiver. The derivative is the inverse of the modal group speed  $V_m(\omega)$  and, to the first order in  $\omega_D$ , this expression reduces to

$$k_{rm}^d = k_{rm}(\omega) + k_{rm}^d v_s V_m^{-1}(\omega). \quad (4.73)$$

In experiments where the range aperture is obtained by towing the source, eigenvalues are shifted and should be compensated for source motion when inverting for sound velocity. The actual group speeds depend on the unknown profile and the eigenvalues can not be correctly compensated.

One possible compensation scheme is to invert for a sound velocity profile using the measured eigenvalues, then compute the group speeds, and iterate the inversion with compensated eigenvalues. Depending on the method of inversion and the amount of deviation, some inversion algorithms may fail to converge.<sup>12</sup> Another simple pre-

---

<sup>12</sup>Kazuhiko Otha, private communication regarding the use of a genetic algorithm.

compensation is to use some velocity  $c_o$  instead of the group speed, resulting in<sup>13</sup>

$$\begin{aligned} k_{rm}^d &\sim k_{rm}(\omega) + k_{rm}^d v_s / c_o, \\ \Rightarrow k_{rm}(\omega) &\sim k_{rm}^d (1 - v_s / c_o). \end{aligned} \quad (4.74)$$

Here, we propose to include the correction in the inverse formulation itself.

#### 4.4.2 Perturbative Formulation

The eigenvalue equation is given in eq.(4.32), repeated here for convenience:

$$\begin{aligned} \left( \frac{u'_m(z)}{\rho} \right)' + \frac{k^2(z) - k_{rm}^2}{\rho} u_m(z) &= 0, \\ 0 \leq z < \infty, u_m(0) = 0, \int_0^\infty \frac{u_m^2}{\rho} dz &= 1. \end{aligned} \quad (4.75)$$

Interfaces are introduced at density discontinuities where the boundary conditions of continuity of  $u_m$  and  $u'_m/\rho$  are imposed. The medium wavenumber is perturbed by small variations in the sound velocity profile and frequency,

$$\begin{aligned} k^2(\omega + \Delta\omega, c + \Delta c) &= \frac{(\omega + \Delta\omega)^2}{(c + \Delta c)^2}, \\ &= \frac{\omega^2 + 2\omega\Delta\omega + (\Delta\omega)^2}{c^2} \left[ 1 - 2\frac{\Delta c}{c} + 3\left(\frac{\Delta c}{c}\right)^2 + \dots \right], \\ &= \frac{\omega^2}{c^2} \left( 1 - 2\frac{\Delta c}{c} + 2\frac{\Delta\omega}{\omega} - 4\frac{\Delta c}{c} \frac{\Delta\omega}{\omega} + \dots \right), \\ &= k_o^2 + \epsilon k_{1c}^2 + \eta k_{1\omega}^2 + \epsilon \eta k_{2\omega c}^2 + O[(\Delta c/c)^2], \end{aligned} \quad (4.76)$$

where  $k_0 \equiv k(\omega, c)$ , and the dummy variables  $\epsilon$  and  $\eta$  (which assume value 0, when  $\Delta c = 0$  or  $\Delta\omega = 0$ , respectively, and 1 otherwise) were introduced for bookkeeping. The

---

<sup>13</sup>Otha proposes a single correction using the phase speed evaluated at the source frequency,  $C_m = \omega/k_{rm}(\omega)$ , resulting in  $k_{rm}(\omega) = k_{rm}^d / (1 + k_{rm}^d v_s / \omega)$ .

subscripts in  $k^2$  indicate the order of the corresponding perturbation and which quantity is being incremented. For example,  $k_{2wc}^2$  designates a second order perturbation: first order in both frequency and sound speed. As usual, *small* means  $\Delta c/c, \Delta\omega/\omega \ll 1$ .

The details of the perturbative analysis are given in Appendix F. The final result is that the perturbative integral becomes [cf. eq.(4.34)]

$$\Delta k_{rm} = k_{rm}^d - k_{rm} (1 - v_s k_{rm} V_m^{-1}) \simeq \frac{-\omega_m^2}{k_{rm}} \left( 1 + 2 \frac{v_s k_{rm}}{\omega_m} \right) \int_0^\infty \frac{u_m^2}{\rho} \frac{\Delta c}{c^3} dz, \quad (4.77)$$

where  $k_{rm}, u_m, V_m$  are, respectively, the unperturbed eigenvalue, eigenfunction, and group speed at frequency  $\omega_m$ . This approximation is valid for very low Mach numbers  $v_s V_m^{-1}$ . The subscript  $m$  is added to the frequency to allow for eigenvalues measured at different frequencies.

The meaning of the terms involving group speeds in eq.(4.77), as compared to eq.(4.34) becomes clear when one recognizes the approximations, valid for small Mach numbers,  $k_{rm}(k_{rm}^d - k_{rm}) \simeq 0.5[(k_{rm}^d)^2 - k_{rm}^2]$ ,  $1 + 2v_s k_{rm}/\omega_m \simeq (1 + v_s k_{rm}/\omega_m)^2$ , and  $1 + 2v_s V_m^{-1} \simeq (1 + v_s V_m^{-1})^2$ , under which eq.(4.77) can be rewritten as

$$(k_{rm}^d)^2 - k_{rm}^2 (1 + v_s V_m^{-1})^2 \simeq -2\omega_m^2 \left( 1 + \frac{v_s k_{rm}}{\omega_m} \right)^2 \int_0^\infty \frac{u_m^2}{\rho} \frac{\Delta c}{c^3} dz. \quad (4.78)$$

Doppler deviation is introduced in the unperturbed eigenvalue (using group speed) and frequency (using phase speed).

Using eq.(4.77), the modal kernel  $g_m(z)$  used to compute the eigenvalue derivative matrix  $G$  becomes [cf. eq.(4.35)]

$$g_m(z) = \frac{-\omega_m^2}{k_{rm}} \left( 1 + 2 \frac{v_s k_{rm}}{\omega_m} \right) \frac{u_m^2(z)}{\rho(z)} \frac{1}{c^3(z)}. \quad (4.79)$$

The difference in eigenvalues in the linear measurement equations (4.50) and (4.52) becomes  $d_m = y_m - k_{rm} (1 + v_s V_m^{-1})$ .

## 4.5 Data Analysis

### 4.5.1 Prototype Problem with Source Speed Compensation

As the first example, we invert the eigenvalues of the prototype, shallow-water environment of Figure 4-4 for the sound velocity profile in the intermediate sediment layer. First, a single realization of a zero-mean uncorrelated Gaussian noise vector is added to the 13 eigenvalues at 25, 50, 75, and 100 Hz. In the second inversion, we use only the eigenvalues at 50 and 75 Hz, and compare the results with the richer data set. A third example, where we invert eigenvalues with and without the source speed compensation of Section 4.4, illustrates the effect of the source speed. We show that the result with source speed zero is recovered when speed compensation is applied. Finally, we simulate a series of measurements by adding 20 realizations of a white Gaussian noise vector to the computed eigenvalues at 50 and 75 Hz.

For the initial background, the sediment sound velocity is constant, 1600 m/s. Table 4.1 shows the eigenvalues and group speeds (in increasing mode order) of the prototype environment and the initial background.

#### Single Stochastic Inversion - 13 Eigenvalues

For this example, we added a single realization of a zero-mean, uncorrelated Gaussian noise vector of variance  $\sigma_e^2 = 10^{-10}$  (rad/m)<sup>2</sup> to the  $M = 13$  eigenvalues at frequencies 25, 50, 75, and 100 Hz. The sediment layer is divided into five intervals where  $\Delta c(z)$  is assumed to change linearly with depth [triangular pulse basis of eq.(4.42)], for a total of  $N = 6$  depth points (one each at the water and basement interfaces, and four intermediate, uniformly spaced depths). We used the stochastic inverse, eq.(4.13), with  $R_e = \sigma_e^2 I_M$   $R_q = \sigma_q^2 I_N$ , and  $\sigma_q^2 = 100$  (m/s)<sup>2</sup>, which reduces the inverse to eq.(4.9), with  $\mu^2 = \sigma_e^2 / \sigma_q^2$ .

In order to control convergence, we varied  $\mu^2$  logarithmically from  $10^{-8.4875}$  to  $10^{-12}$ , starting at the square of the 4th singular value of the first (initial background) system

Table 4.1: Prototype and background environment eigenvalues and group speeds

Hz	eigenvalues (rad/m)		group speeds (m/s)	
	actual	background	actual	background
25	9.6888703e-02	9.6092233e-02	1.4496980e+03	1.4682446e+03
50	2.0407988e-01	2.0267080e-01	1.4771008e+03	1.4789501e+03
	1.8810603e-01	1.8815864e-01	1.4736053e+03	1.5267036e+03
	1.7495476e-01	1.7515289e-01	1.5474714e+03	1.4744818e+03
75	3.1000870e-01	3.0862886e-01	1.4871434e+03	1.4855094e+03
	2.9555055e-01	2.9188322e-01	1.4560558e+03	1.4825096e+03
	2.8277135e-01	2.8466005e-01	1.4700669e+03	1.4920331e+03
	2.6610607e-01	2.6715294e-01	1.4866457e+03	1.4772420e+03
100	4.1545598e-01	4.1421381e-01	1.4916451e+03	1.4896005e+03
	4.0324674e-01	3.9933974e-01	1.4626610e+03	1.4565425e+03
	3.8898459e-01	3.8678277e-01	1.4813835e+03	1.5626671e+03
	3.7397136e-01	3.7444496e-01	1.4436658e+03	1.4517155e+03
	3.6057555e-01	3.6306981e-01	1.4490004e+03	1.4210734e+03

matrix  $G$  and ending at  $\sigma_e^2/\sigma_q^2$ . In addition, we updated the sound velocity profile, at each iteration, using only half of the computed increment  $\Delta c(z)$ . Large  $\mu^2$  and reduced  $\Delta c$  help convergence by reducing large sound velocity corrections in the first iterations, when the background may be far from the final solution.

Figure 4-9 shows the inversion result after 10 iterations. The dashed, thin line is the constant sound velocity initial background. Two intermediate iterations are shown by dash-dot lines. The actual sound velocity profile (thick dashed line) and the final result (solid line) are almost indistinguishable.

The convergence of the inversion is shown in Figure 4-10. Iteration zero refers to the initial background. The upper plot is the standard deviation of the sound velocity error at the six depths (inverted - actual). The error decreases monotonically with the iterations. The middle plot illustrates convergence in terms of the magnitude of components of the eigenvalue difference vector  $\mathbf{d}_i = \mathbf{k}_r(c(z)) - \mathbf{k}_r(c_i(z))$ . As the solution converges, these components decrease. In the presence of measurement noise (also plotted for reference),  $\mathbf{d}$  can not reduce to zero.

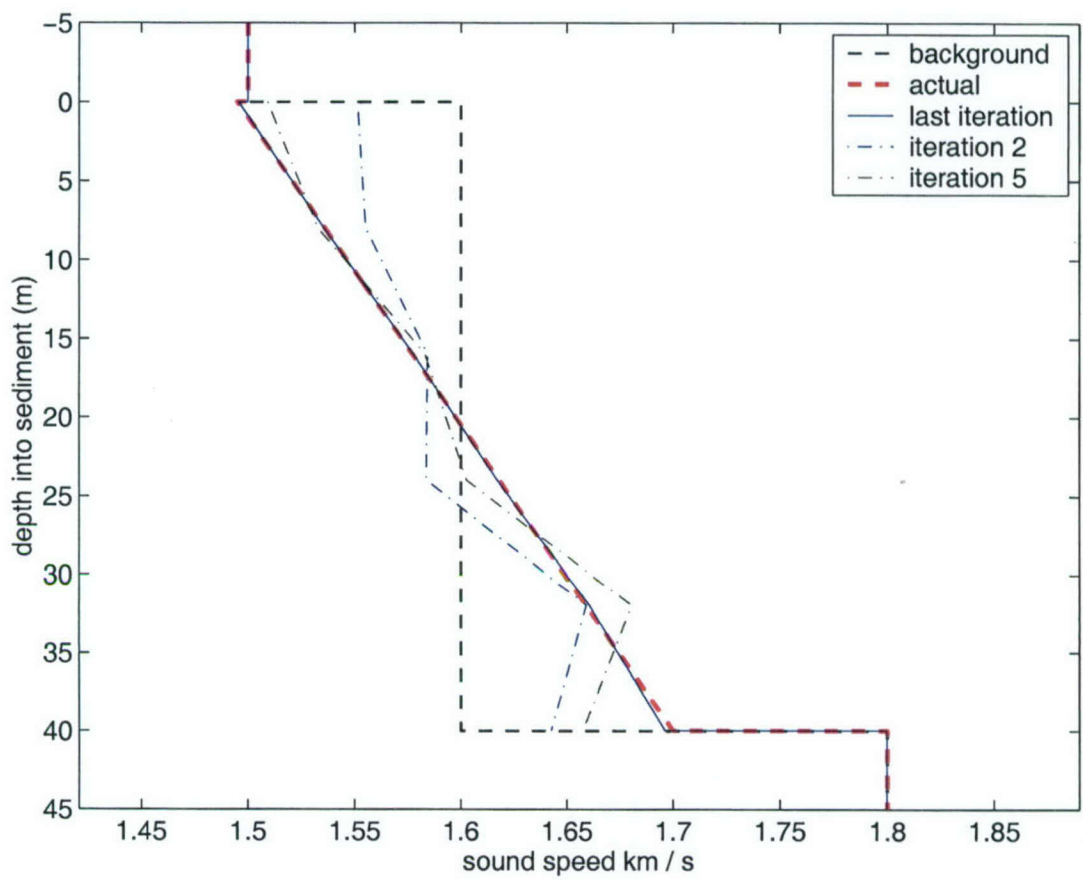


Figure 4-9: Prototype problem inversion.

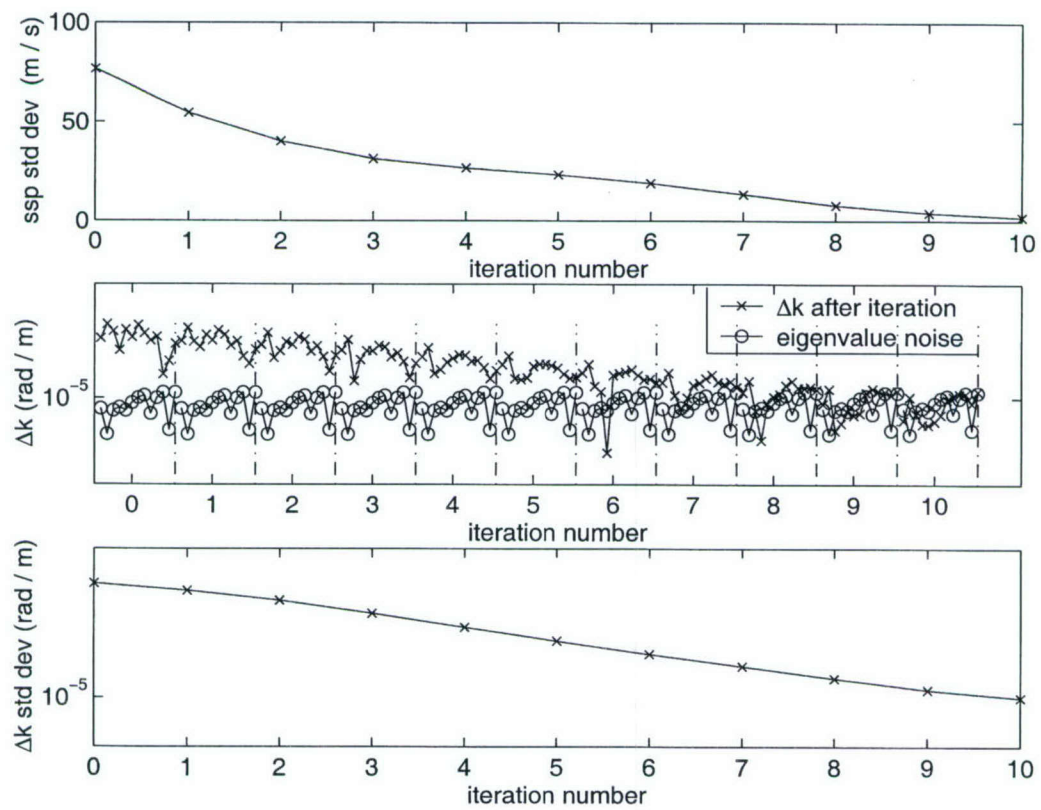


Figure 4-10: Prototype inversion: convergence.

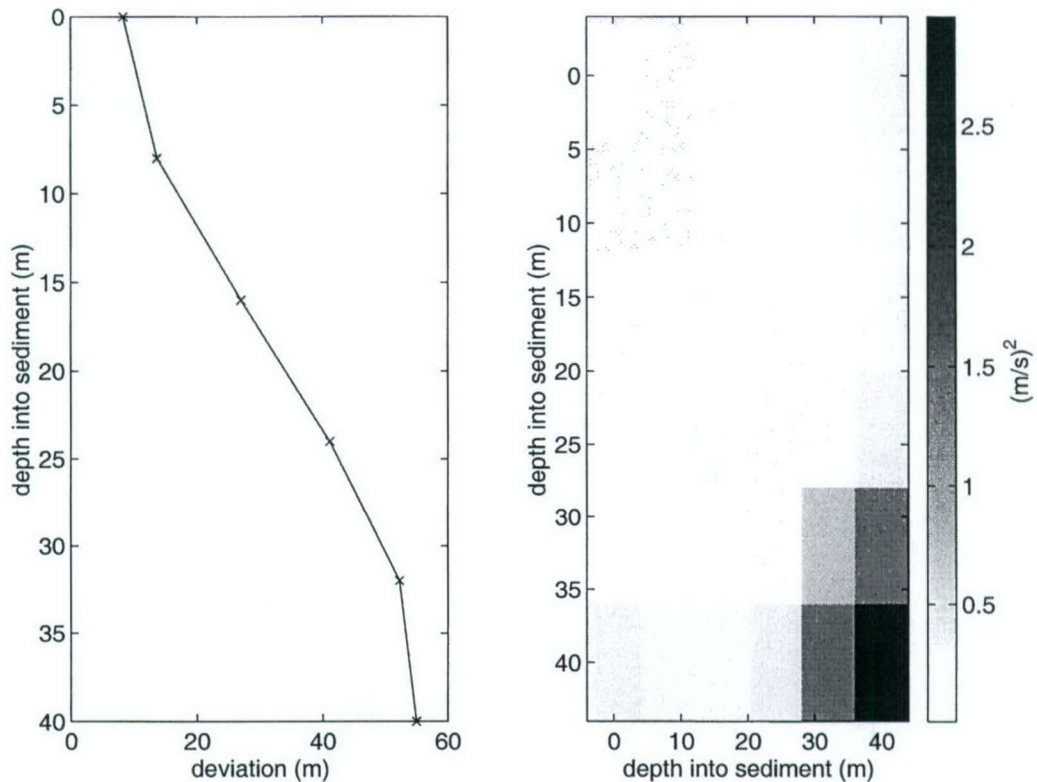


Figure 4-11: Prototype inversion: resolution and covariance.

A criterion for convergence is to allow the eigenvalue differences to reach the level of the measurement noise, which is the case of the 10th iteration. The lower plot illustrates the convergence through the standard deviation of the components of  $\mathbf{d}_i$  (viewed as a set of numbers that approach zero). At iteration 10, it reaches  $10^{-5}$  rad/m, the standard deviation of the added noise. All three plots indicate that the solution converges at iteration 10, but only the third can be used in practice, when the actual profile and measurement noise realization are unknown.

Figure 4-11 shows the resolution (plot at left) and error covariance matrix of the solution at the six depths of the inversion grid. The deviation  $\sigma_A$  (m) was computed through eq.(4.69), using the last iteration inverse. The covariance matrix was computed using eq.(4.71).

As expected, the deviation is larger than the minimum value predicted by the Backus-Gilbert theory, shown in Figure 4-8, which, as predicted in the theory, is the price to be paid for lower error variance. For the profile of the prototype problem, without any small (depth) scale variations, the high values of deviation are not an indication of poor performance. In addition, it should be taken into account that the definition of deviation in eq.(4.29) is  $\sqrt{12}$  larger than the standard deviation (for a distribution centered at the reference depth  $z_0$ ). The low values of the covariance matrix are, for this example, a better indicator of the quality of the result.

### Single Stochastic Inversion - Seven Eigenvalues

In actual experiments, a small number of frequencies and eigenvalues are available. In MOMAX, for example, one or two frequencies are transmitted at a time. As a second example, we inverted only the 7 eigenvalues at 50 and 75 Hz. The inversion parameters are the same as before, except the number of iterations, 12, and  $\mu^2$ , which was varied from  $10^{-8.7993}$  to  $10^{-12}$ . Figure 4-12 shows the inversion result. Despite the smaller number of eigenvalues, the inferred profile is a reasonable approximation to the actual profile.

Figure 4-13 shows that convergence is attained at the 12th iteration. A comparison with Figure 4-10 reveals that, for this environment and set of inversion parameters, the convergence characteristics, in terms of final eigenvalue differences, are unaffected by the smaller number of eigenvalues.

The resolution and covariance of the estimate are shown in Figure 4-14. The higher deviation near the basement interface at 40 m is consistent with the poorer result in Figure 4-12 at those depths, as compared with the 13 eigenvalue inversion.

### Source Speed Compensation

The effect of source speed on the inversion is illustrated by adding a Doppler deviation to the "measured" eigenvalues of the previous example, using eq.(4.73) with  $v_S = -3\text{m/s}$

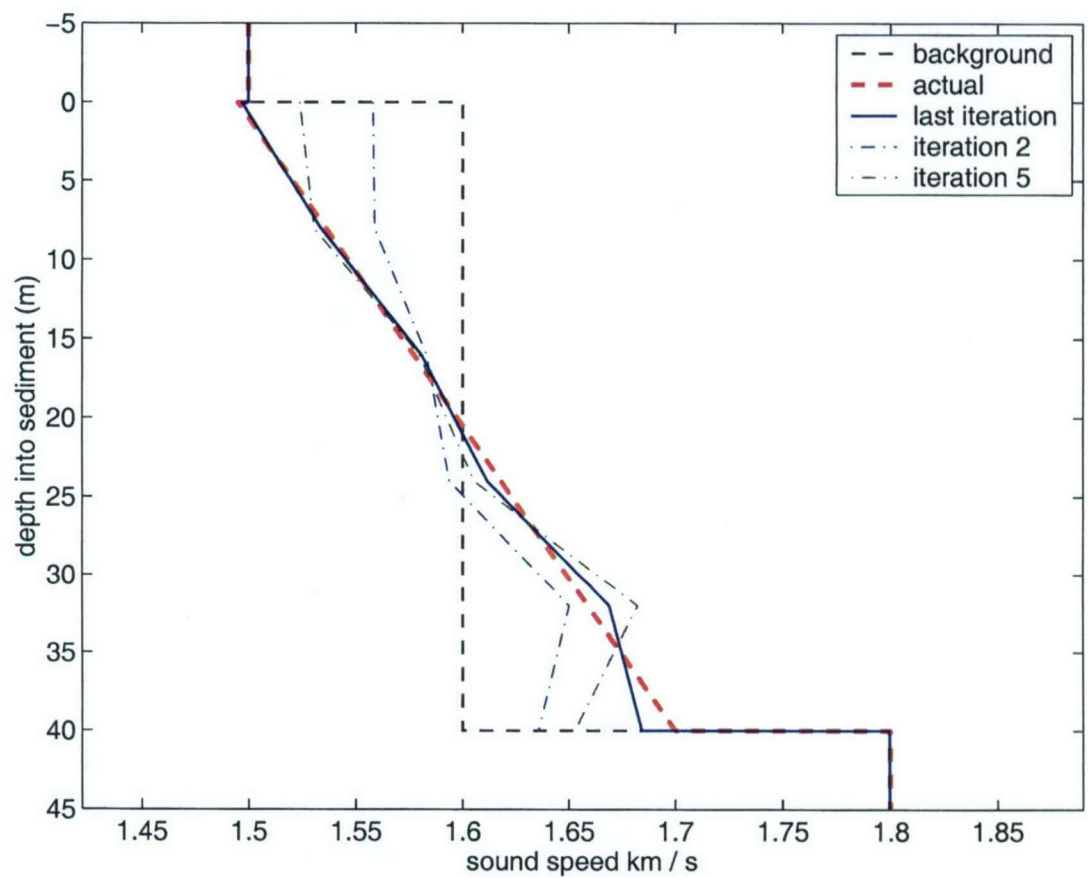


Figure 4-12: Prototype inversion using modes at 50 and 75 Hz.

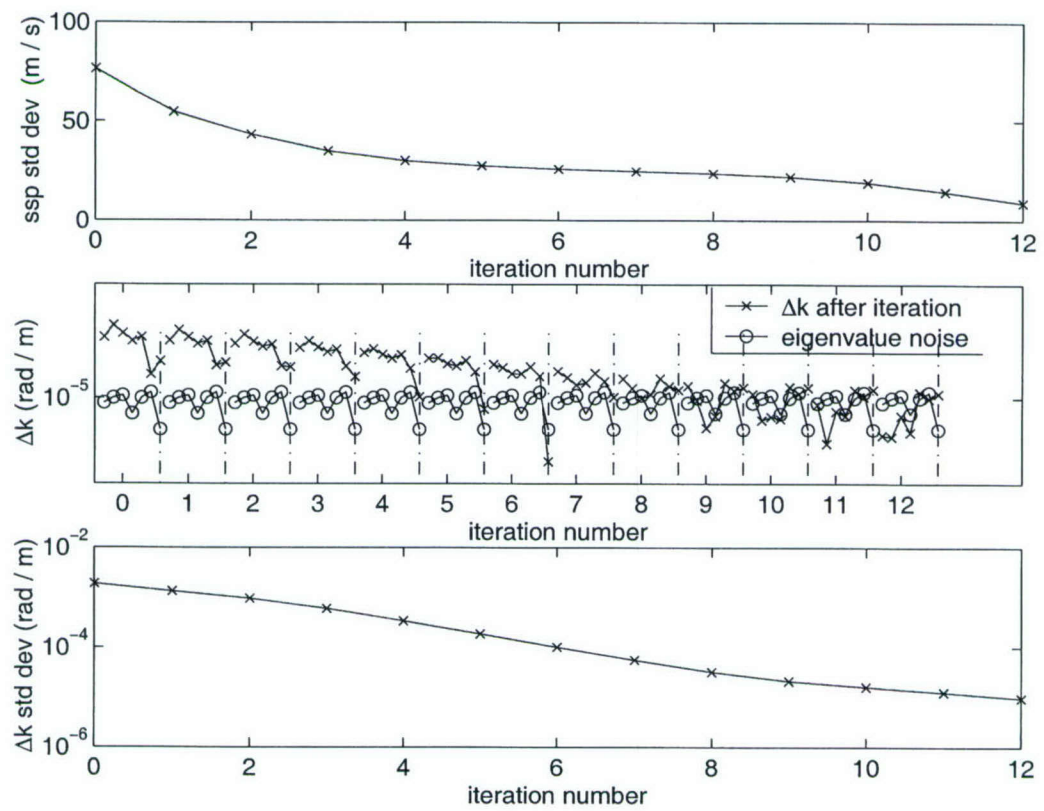


Figure 4-13: Prototype 50/75 Hz inversion: convergence.

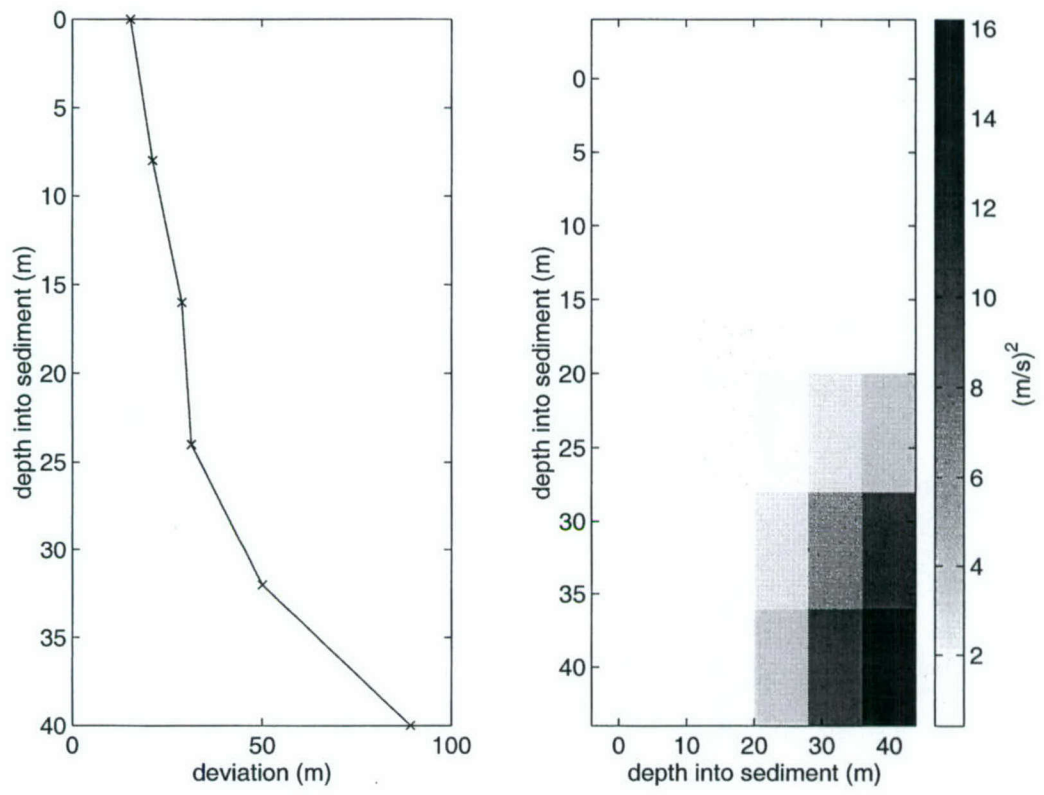


Figure 4-14: Prototype 50/75 Hz inversion: resolution and covariance.

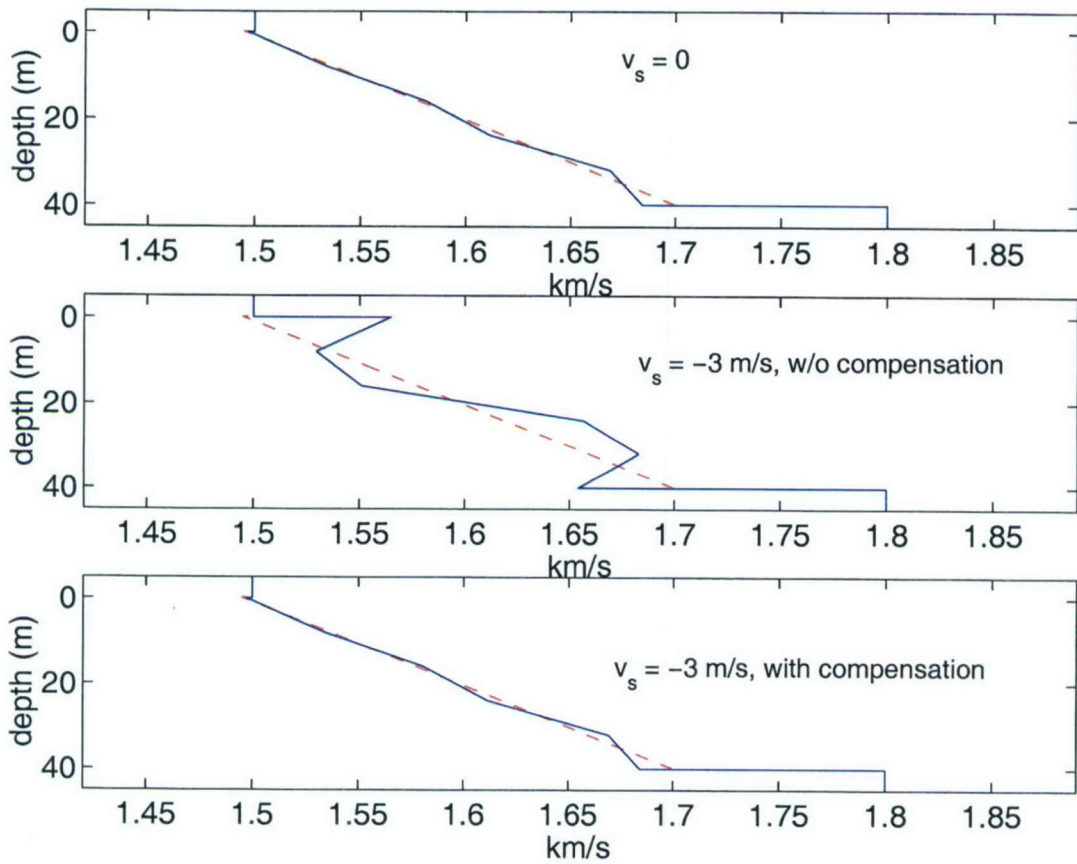


Figure 4-15: Prototype 50/75 Hz inversion: - source speed effects.

(source speed of 3 m/s moving away from the receiver). Figure 4-15 shows the results. The upper plot is the inversion from the previous example ( $v_s = 0$ ), using the 7 eigenvalues at 50 and 75 Hz, repeated from Figure 4-12.

The middle plot shows the degradation in the inversion when the Doppler deviation is not compensated for in the inversion algorithm, i.e., when eq.(4.35) is used to compute the eigenvalue derivative at each iteration. As shown in the lower plot, when the Doppler compensated background is used [eq.(4.79)], the results is indistinguishable from the  $v_s = 0$  case.

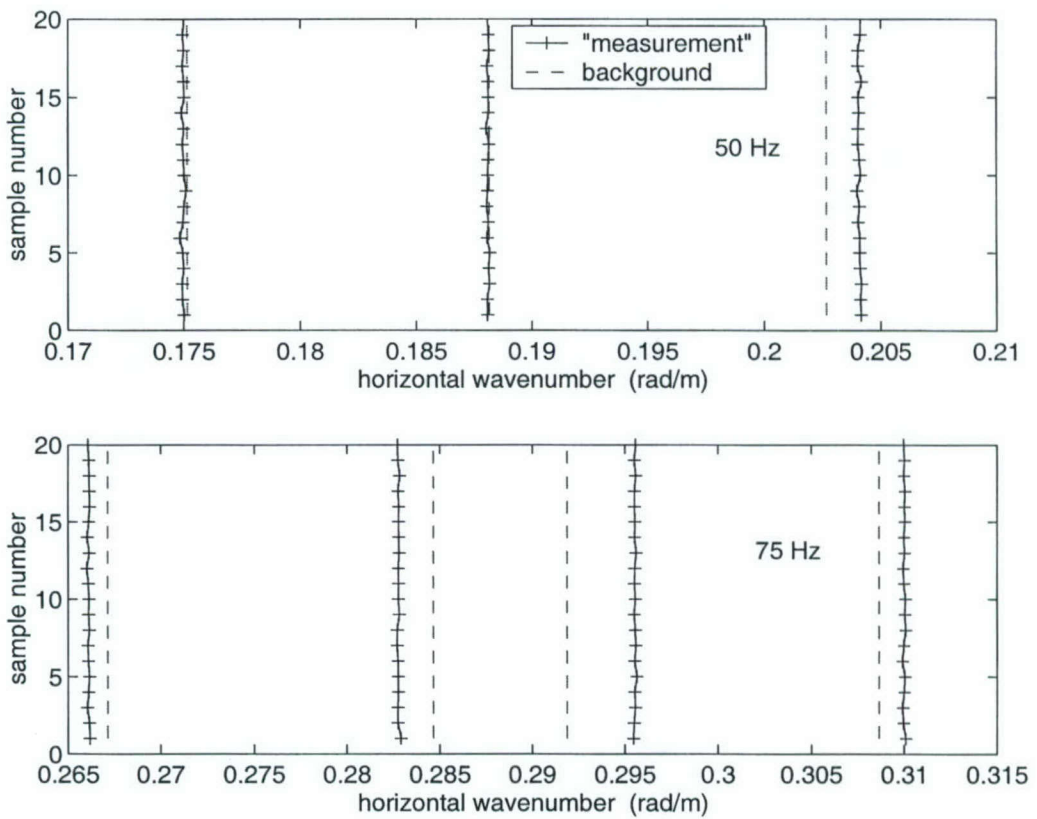


Figure 4-16: Prototype environment, “measured” eigenvalues at 50 and 75 Hz as a function of sample number (crosses). The dashed lines are the initial background eigenvalues.

### Sequential (in Range) Inversion

We added 20 realizations of an uncorrelated noise vector to the prototype environment eigenvalues at 50 and 75 Hz. The noise variance is 20 times larger than in the example above,  $\sigma_e^2 = 20 \times 10^{-10} \text{ (rad/m)}^2$ . These “measured” eigenvalues simulate estimates as a function of range for an horizontal aperture generated by a drifting receiver, or a time series of estimated eigenvalues at a fixed horizontal array, for example. The background is the same as before, with sound velocity 1600 m/s in the sediment. Figure 4-16 shows the set of measurements and the corresponding initial background eigenvalues.

As in the single stochastic inversion, the sediment layer is divided into five segments

where the sound velocity difference is assumed to change linearly with depth [triangular pulse basis, eq.(4.42)]. The measurement noise covariance matrix is  $R_e = \sigma_e^2 I_M$  and the state noise covariance is  $R_w = \sigma_w^2 I_N$ , with  $\sigma_w^2 = 1 \text{ (m/s)}^2$ . The initial solution is assumed to be  $\mathbf{q}_0 = 0$  with covariance  $P_0 = \sigma_{q0}^2 I_N$ , and  $\sigma_{q0}^2 = 100 \text{ (m/s)}^2$ .

First, we inverted one set of 7 noisy eigenvalues using the stochastic inverse, as described in Section 4.5.1. The final result was then used as the initial background for the remaining inversions, using the Kalman filter. Figure 4-17 shows the inversion result, and, for comparison, the inversion at each range step using the stochastic inverse. The dashed, thin line is the initial background, the actual sound velocity profile is the thick dashed line. Twenty final profiles (one for each “range” step) are shown by thin solid lines.

The sequential inversion result is comparable to that of inverting each eigenvalue set, albeit with smaller variance. The individual inversions took 12 iterations each ( $1 + 20 \times 11 = 221$  eigenvalue computations). The sequential inversion needed 12 iterations of a single profile plus 3 iterations of the Kalman Filter (53 eigenvalue computations: 12 for the stochastic inverse plus  $1 + 2 * 20 = 41$  for the 3 Kalman filter iterations).

In order to control convergence, we updated the sound velocity at the end of each iteration using 1/3 of the computed increment. This is simpler than the adjustment of covariance matrices described in Sections 4.5.1 and 4.5.1 and, for the present example, has similar results. In addition, the Kalman filter was run three times in cascade at each iteration, twice forward and once backward, with the last solution  $\mathbf{q}$  at each run used to initialize the next filter. This allows the filter to converge to a solution (at all range steps) at each iteration and offsets the small number of available range samples. Most of the inversion computational cost is due to the evaluation of background eigenvalues (20 backgrounds, once per iteration). Running the Kalman filter multiple times contributes little to the overall cost.

Figure 4-18 illustrates the inversion convergence. The upper plot is the standard deviation of each component of the forward ( $\epsilon^-$ ) and backward ( $\epsilon^+$ ) prediction errors

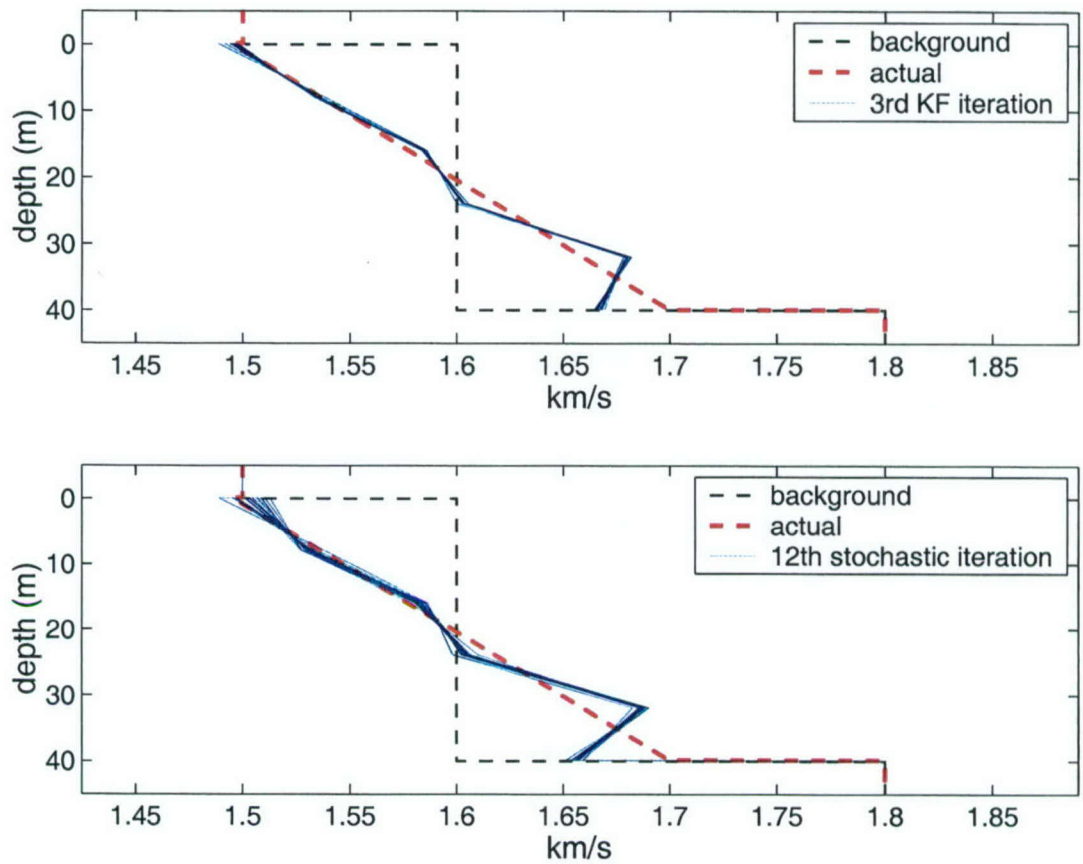


Figure 4-17: Prototype 50/75 Hz inversion: results from the “range-dependent” eigenvalue data of Figure 4-16 [cf. Figure 4-12]. Upper plot: sequential inversion; lower plot: individual stochastic inversions.

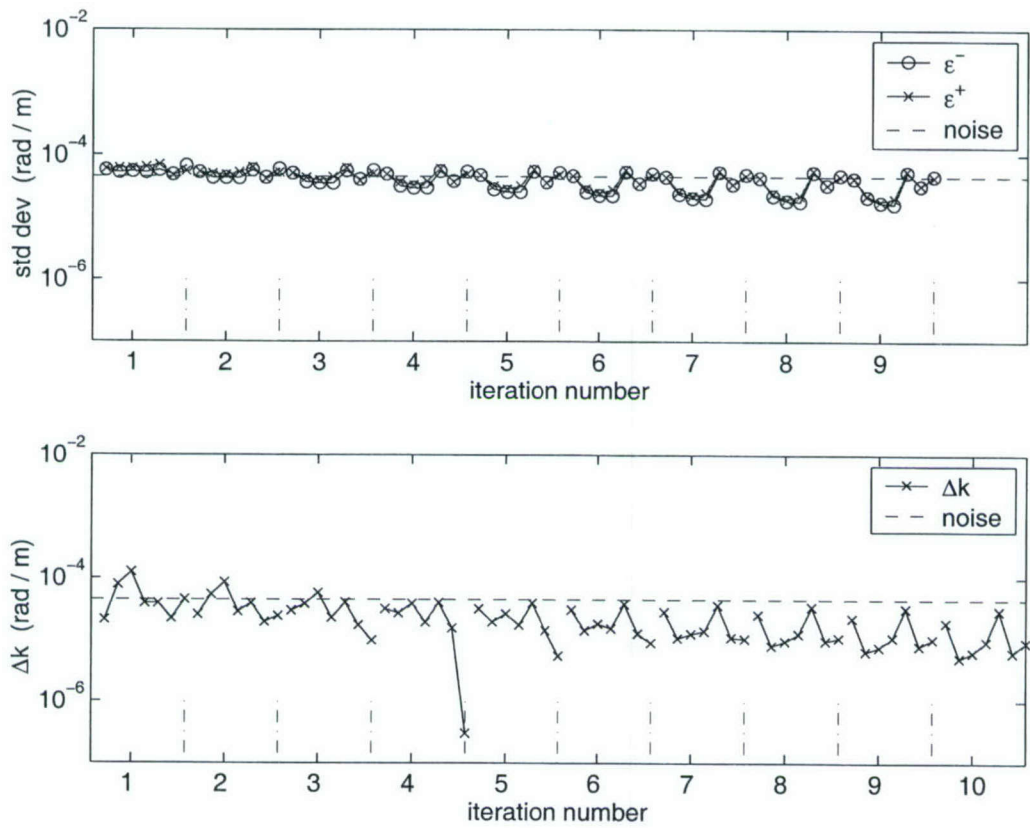


Figure 4-18: Prototype 50/75 Hz sequential inversion: convergence.

(not including the first Kalman filter processing at each iteration). The dashed line is the standard deviation of the measurement noise ( $4.5 \times 10^{-5}$  rad/m), for reference. At each iteration, the prediction errors have nearly equal standard deviation, an indication that convergence was attained. As the number of iterations increases, the forward and backward standard deviations decrease until they are at, or slightly below the noise standard deviation of  $4.4721\text{e-}05$  rad/m.

The lower plot shows the magnitude of the components of one of the eigenvalue differences at each iteration [cf. Figure 4-13]. Convergence is indicated by the reduction of the eigenvalue differences to a level comparable to that of the noise standard deviation. The Kalman filter was run for nine iterations, but convergence (in the sense that the

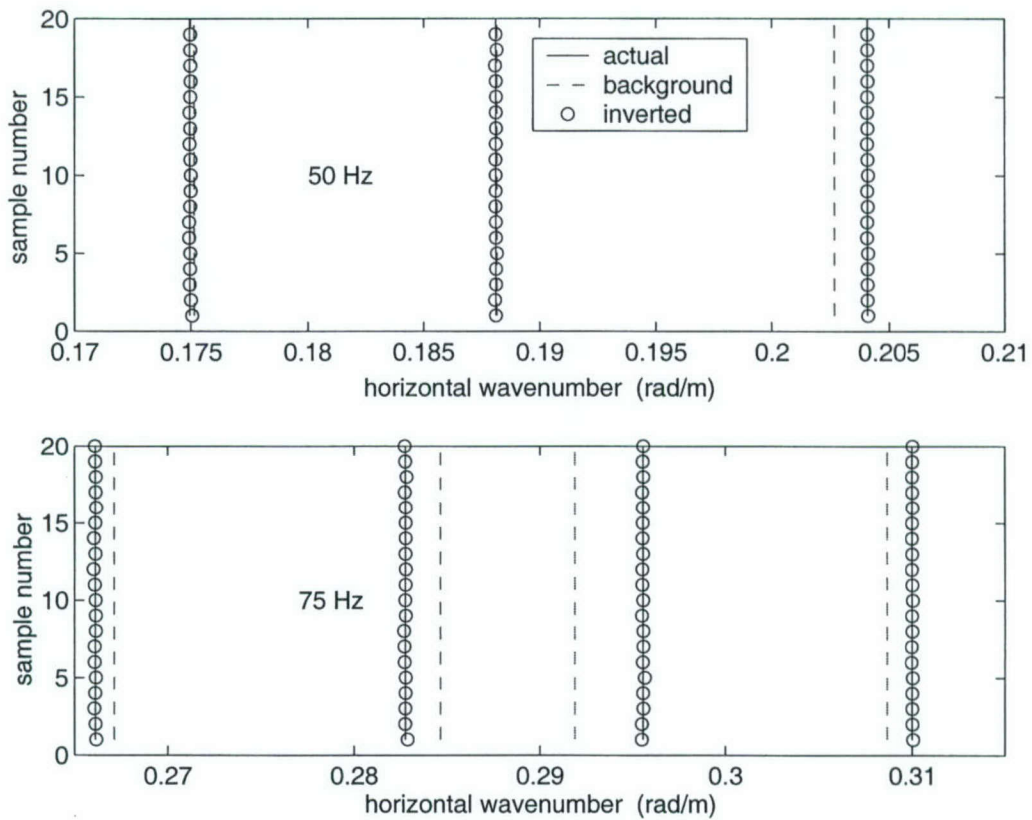


Figure 4-19: Prototype 50/75 Hz inversion: eigenvalues of sequentially inverted profiles

standard deviation of the prediction error covariance or eigenvalue difference reached the noise standard deviation) was attained at the third iteration, whose results are shown in Figure 4-17. Figure 4-19 shows the eigenvalues for the actual, background, and inverted profiles [cf. the “measured” eigenvalues of Figure 4-16].

The resolution and covariance of the estimate are shown in Figure 4-20. The higher deviation near the basement interface at 40 m is consistent with the poorer result in Figure 4-17 at those depths.

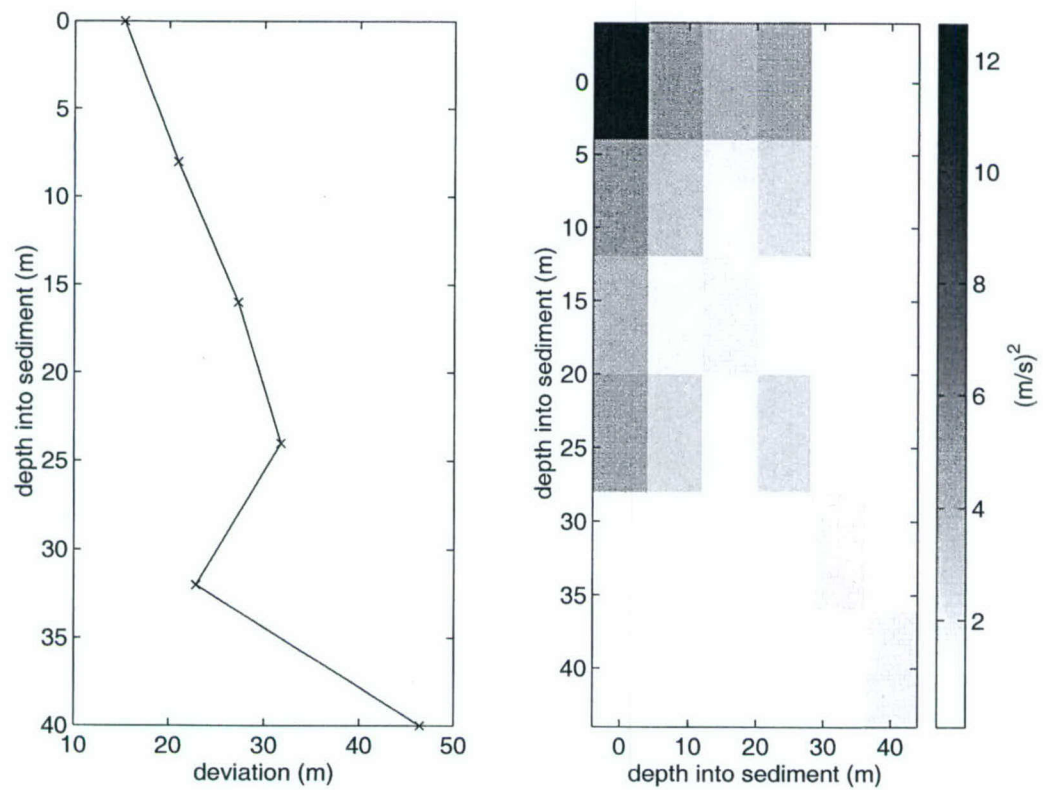


Figure 4-20: Prototype 50/75 Hz inversion: sequential inversion resolution and covariance.

Table 4.2: TC3 Eigenvalue sample variances

mode nr.	variance (rad/m) <sup>2</sup>	
	region 1	region 2
1	$3.0 \times 10^{-10}$	$4.6 \times 10^{-10}$
2	$4.16 \times 10^{-9}$	$4.56 \times 10^{-9}$
3	$1.25 \times 10^{-9}$	$6.4 \times 10^{-10}$
4	$2.24 \times 10^{-8}$	$1.18 \times 10^{-8}$

#### 4.5.2 Synthetic Data: Abrupt Modal Change

The Inverse Techniques Workshop test case 3 (TC3) is discussed in Chapter 3, Figure 3-16. The eigenvalues measured at 50 Hz are shown in Figure 4-21. A sequence of 28 eigenvalue vectors were estimated from a signal sampled at 125 meters, using an AR model of order 12. The abrupt transition between two different media, as described in Chapter 3, is readily identified. Only the second transition is shown. The first one occurs at 1.1 km, inside the region where the pressure data was used to initialize the AR algorithm. The region below 1.1 km and above 3 km (called here 'region 1') have same properties. Region 2, between 1.1 and 3 km, is called the "intrusion" in the description of this test case. The eigenvalue variances are given in Table 4.2. The covariance was computed as the sample covariance in each region where the estimated eigenvalues are nearly constant.

##### Blind Inversion

The inversion based solely on the measured eigenvalues is *blind*, in the sense that no geoacoustic information about the seabed was available. The next example shows an application where prior sound velocity profiles and some geoacoustic information is available, and the eigenvalue measurements are used to update the estimate.

The 28 inverted profiles are shown in Figure 4-22, obtained after 9 iterations of the Kalman Filter. On the left, a single initial background, shown as a dashed line, is used

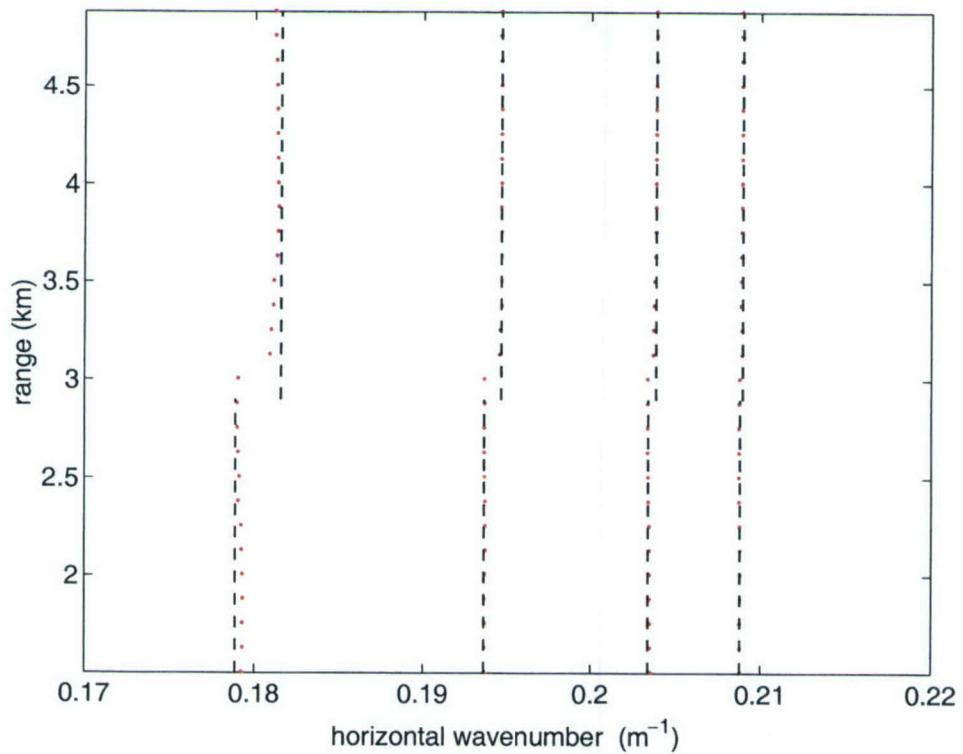


Figure 4-21: TC3 estimated eigenvalues (dots) and computed (dashed lines) from the actual environment description.

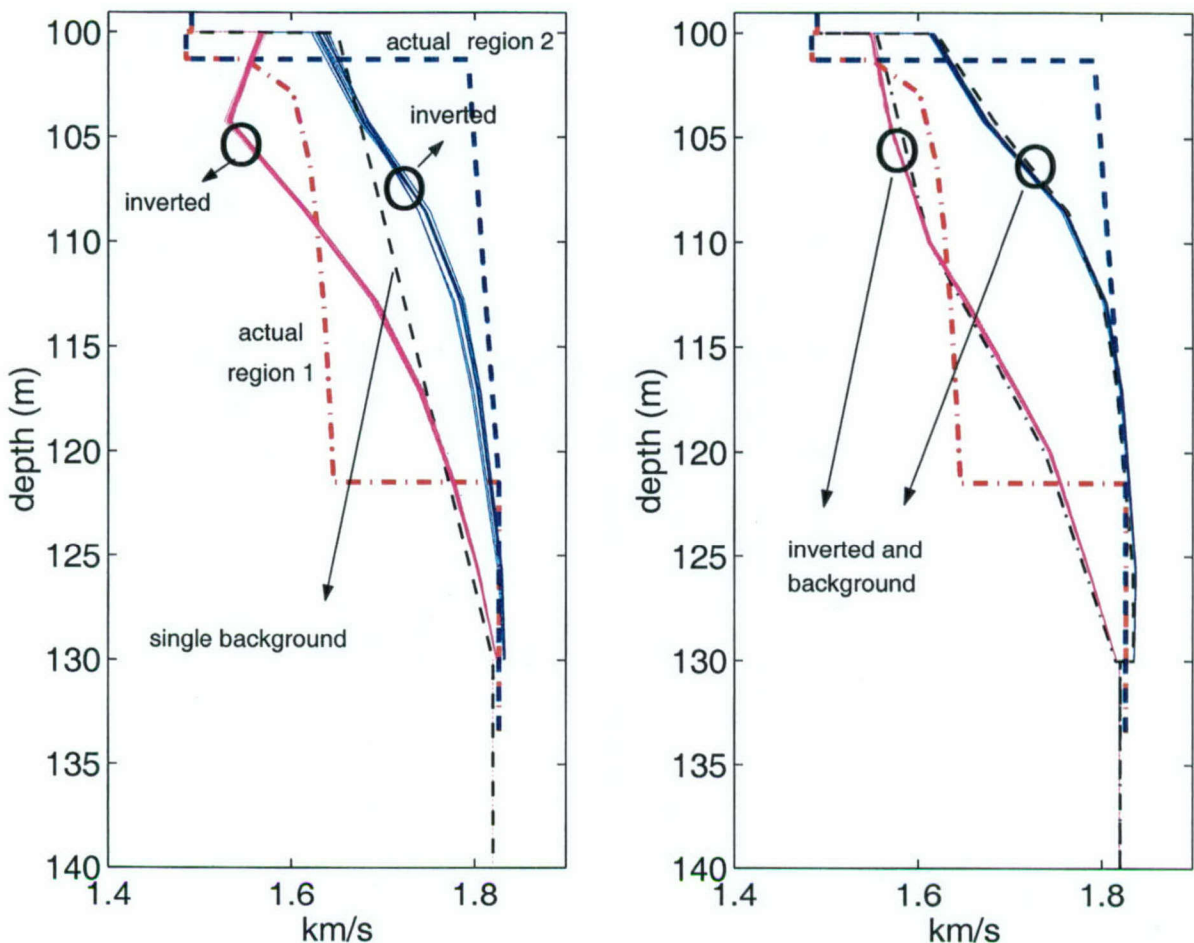


Figure 4-22: TC3 inverted profiles. From a single background (upper plot) and from one background for each region.

for all ranges. The background density and absorption coefficient are at  $1.8 \text{ g/cm}^3$  and  $0.2 \text{ dB}/\lambda$ , independent of depth. The basement sound speed of  $1.82 \text{ km/s}$  was selected, based on the wavenumber spectra at different frequencies, as slightly above the maximum observed modal phase speed  $k_{rm}/\omega_m$ .

We set the initial covariance  $R_{q0} = 100I_N$  (m/s) $^2$ , and the state noise variance,  $R_w = I_N$  (m/s) $^2$ . The velocity increments are approximated by 8 triangular basis functions equally distributed between 100 and 130 m. At each iteration, we divided the computed velocity increments by three. The average of the forward and backward

Kalman filters were used.

We obtained improved estimates, shown on the right panel of Figure 4-22, when the initial background was first inverted using a nonlinear estimator whose input data were the eigenvalues sample means on each region. The two resulting profiles were used as background for the inversion in range. The final profiles are comparable with the previous single background result, but provide a better approximation to the actual environments. The improved result suggests this to be a better approach when regions of nearly constant eigenvalues are identified.

Both approaches indicate the presence of two regions of different sound velocities, as suggested by the eigenvalue variations with range. The thin low velocity layer (1.3 m thickness) was not identified, which is to be expected at this frequency, and is consistent with the estimated resolution, shown in Figure 4-23. The sharp change in sound velocity at the basement interface (near  $z = 122$  m) was not identified, which is also consistent with the resolution at that depth, where the deviation is larger than 70 m.

The estimate covariance, given by the Kalman filter last iteration, is shown on the right panel of Figure 4-23. The standard deviation of the estimated sound velocity is  $\sqrt{55} = 7.4$  m, which is much smaller than the difference in estimated velocities at the two regions. The separation of the inverted profiles in two regions is, therefore, statistically significant.

As shown in Figure 4-24, the eigenvalues for the inverted profiles match closely the actual values. The fifth eigenvalue computed for the actual environment in region 1 was not detected in the pressure field, and hence not included in the inversion.

### Updating an Available Environment Model

One possible application of the inversion technique is to update a previously estimated velocity profile using a new set of measurements. In order to test this application, the TC3 data were inverted using initial backgrounds closer to the two actual environments, as shown in Figure 4-25. The thin ( $100 \leq z \leq 101.3$  m) low velocity (1485 m/s) layer of

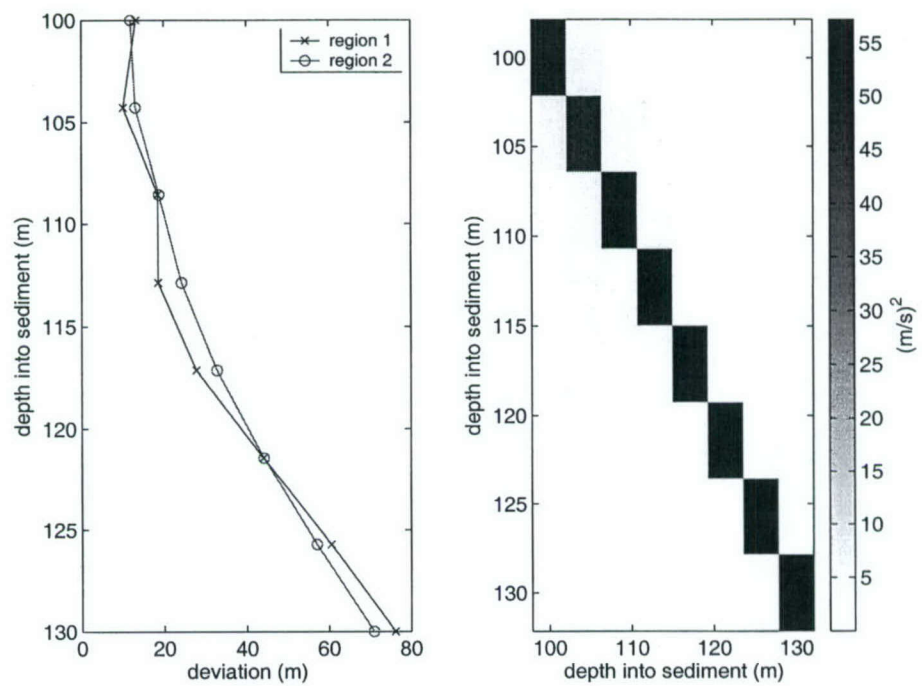


Figure 4-23: TC3 resolution and covariance of inverted profiles.

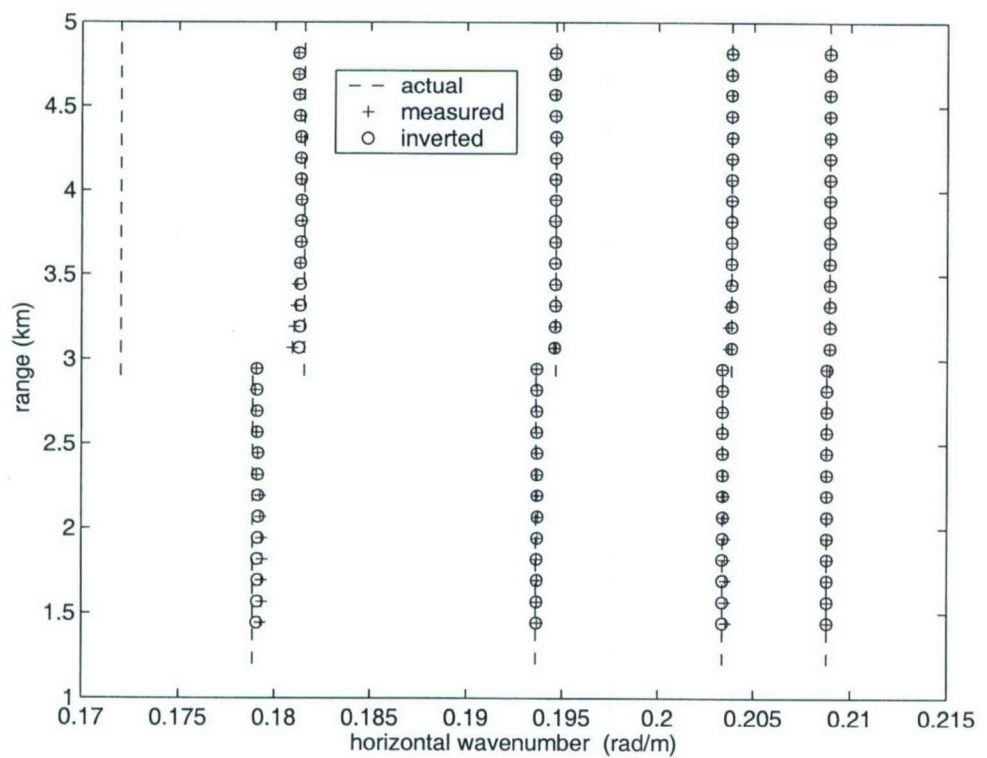


Figure 4-24: TC3 50 Hz eigenvalues: computed from the actual environment, measured, and from inverted profiles.

the actual environments was incorporated into the backgrounds.

Both regions are modeled, below the initial low velocity layer, by an isovelocity layer down to 125 m, overlaying an 1.82 km/s basement. In region 1 this intermediate layer has a velocity of 1.60 km/s, and region 2, 1.80 km/s. These are values that correspond roughly to the velocities of the actual environments near the surface, as could have been measured, for example, by sampling the materials near the water interface.

As in the case of the blind inversion, the basement sound velocity was estimated from the analysis of phase speeds associated with the wavenumber spectra at different frequencies. The density was set to 2.0 g/cm<sup>2</sup>, and the absorption coefficient, 0.2 dB/λ.

This example also illustrates the use of a smoothing constraint in the sequential inversion. As mentioned in Section 4.1.2 and suggested by comparing the cost functions in eqs.(4.6) and (4.15), we set the inverse of the covariance of  $\mathbf{q}$  to the sum of the inverse covariance of the background  $\sigma_{q0}^{-2} I_N$ , and a matrix  $H$  that models the smoothing constraint. Here, as the sediment layers are believed to be isovelocity or nearly so, the constraint imposed is related to the first derivative of  $\Delta c(z) = \Phi^T(z)\mathbf{q}$  measured by

$$\int_a^b \left( \frac{d}{dz} \Delta c \right)^2 dz = \mathbf{q}^T \int_a^b \frac{d\Phi}{dz} \frac{d\Phi^T}{dz} dz \mathbf{q} = \mathbf{q}^T H \mathbf{q}.$$

For the triangular pulse basis function of eq.(4.42), the  $N \times N$  matrix  $H$  is given by

$$H = \begin{bmatrix} 1 & -1 & 0 & 0 & \dots & 0 \\ -1 & 2 & -1 & 0 & & 0 \\ 0 & -1 & 2 & -1 & & 0 \\ & & & \ddots & & \\ 0 & & & -1 & 2 & -1 \\ 0 & \dots & & 0 & -1 & 1 \end{bmatrix}.$$

A constraint based on  $H$  penalizes deviations of  $\Delta c$  from a constant. Finally, the initial

covariance matrix is set to

$$R_{q0} = (\sigma_{q0}^{-2} I_N + \lambda H)^{-1}.$$

For this example,  $\sigma_{q0}^2 = 20$  (m/s)<sup>2</sup> and  $\lambda = 0.5$ . The state covariance noise  $R_w$  is set to zero.

The results in Figure 4-25 were obtained after 40 iterations of the Kalman filter, although no change was observed after the 30th iteration. The sound speed increments were the average of the forward and backward filter outputs. The profile in region 2 was correctly adjusted. In region 1, the sound velocity for most of the depths was also correctly adjusted, but not the reduction in sound velocity at the top of the layer. The agreement or disagreement of the resulting profiles in both regions are consistent with the constraint imposed of low  $|d\Delta c(z)/dz|$ .

## 4.6 Summary and Conclusions

This chapter investigated the estimation of subbottom sound velocity profiles in the shallow ocean. We proposed a sequential estimator, whose input data are modal eigenvalues measured as a function of range. This nonlinear problem is solved iteratively by first linearizing the measurement equation at a given initial background velocity profile.

The linearization of the eigenvalue measurement equation lead to the perturbative technique integral equation. We formulated the linearization by first representing the profile as a sum of basis functions, a process akin to the finite element method. Previously proposed perturbative integral solvers, including the spectral expansion method and the discretization of the integral equation using the trapezoidal rule, are shown to be particular cases of the basis function representation. We showed that the derivative of eigenvalues with respect to sound velocity variations, obtained from the perturbative integral using the basis function representation, is consistent with the formal Fréchet differentiation.

We proposed a description of the sound velocity increment  $\mathbf{q}$  as a Gaussian Markov

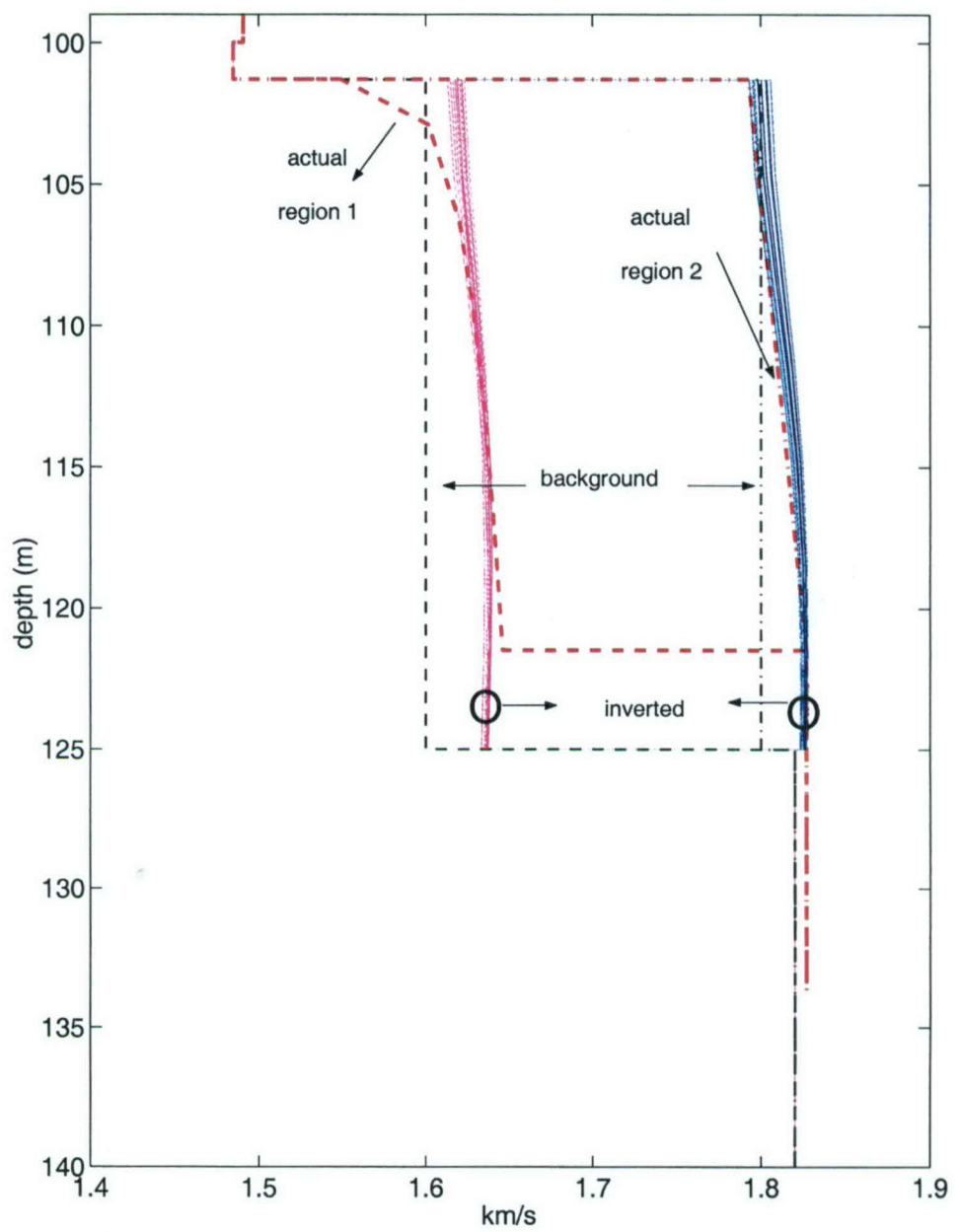


Figure 4-25: TC3 inversion from close profiles.

process, which corresponds to attributing a covariance to the sound velocity increments, as in Franklin's stochastic inverse, that regularizes this ill-posed problem. The covariance of the sound velocity increment is defined by the initial and state-noise covariance matrices. Smoothing constraints can be imposed through modification of these matrices. The state-space description of the inverse problem lead to a Kalman filter implementation. The solution to the nonlinear inverse problem consists of solving the problem in range for a given set of background profiles  $c_i(z; r)$  though the Kalman filter, updating the profiles to the new set  $c_{i+1}(z; r)$  and iterating until the solution converges.

We analyzed the characteristics of the eigenvalue inverse problem from the perspective of estimation theory and the Backus-Gilbert (BG) resolution theory. The results from both perspectives are consistent. The lower bound on the unbiased estimator variance, the Cramer-Rao bound, CRB, and the BG estimate variance for the best possible resolution are both very high. Bias or reduction in resolution have to be introduced in order to reduce the estimate variance to acceptable levels. This is accomplished through regularization, as exemplified by the stochastic inverse of a prototype shallow-water waveguide problem.

We illustrated the use of the BG theory for the design of experiments. We showed that resolution and variance improve, in general, with frequency and number of modes, and by combining eigenvalues from different frequencies.

We developed a method to compensate for eigenvalue Doppler deviation introduced by source motion. It consists of a modification of the linear perturbative integral and the eigenvalue derivatives. We show the effectiveness of this formulation through an example.

The proposed sequential technique is for inversion of sound velocity profiles, and assumes that the seabed density structure is known. We show that blind inversion, where no geoacoustic information is available, may, nevertheless, provide trends in the velocity profile, in particular with range, that are compatible with the BG resolution. The technique is most useful for updating previous estimates when a reasonable description is

given, particularly including details of the profile that can not be resolved by the technique but affect the results. We also showed the application of a smoothing constraint by a modification of the assumed initial covariance matrix.

# Chapter 5

## Summary

### 5.1 Contributions

#### 5.1.1 Chapter 2

Chapter 2 investigated the application of Merab's exact inverse theory to infer the sound velocity profile from complex, plane-wave reflection coefficients estimated from monochromatic experimental data. We investigated the application of the technique developed by Frisk and co-workers [22, 46] for the measurement of the reflection coefficient. A sound velocity profile was inferred from the Icelandic Basin experiment data.

In Chapter 2 we extended Merab's method to deal with a density discontinuity at the water-seabed interface, an important extension for ocean environments. The criterion for seabed trapped mode cutoff was corrected for the case of reflection at the water interface, and a method for checking for velocity minima after the inversion was tested.

We inverted for the sound velocity profile in the seabed using a reflection coefficient inferred from experimental data, a result not previously available. The recovered sound velocity profile has characteristics similar to the synthetic case, suggesting similar error mechanisms, in addition to the possible density variations in the experiment site.

Merab's method reveals some of the advantages and restrictions of methods based

in exact theories. The requirements for uniqueness are well established, and the effects of not fulfilling the requirements can be easily understood. In the present application, the lack of information about the residue of the reflection coefficient poles in the lower  $k_z$  complex plane leads to absence of sound velocity minima in the inferred profile. In practical applications, information about poles are not required if the source frequency is below the expected mode cutoff.

### 5.1.2 Chapter 3

In Chapter 3 we demonstrated the applicability of AR models with varying coefficients (the time-varying AR model–TVAR) to represent adiabatic modal sums. We derived expressions for the error between the AR characteristic equation roots and the actual first-order poles that represent range-varying modal sums. In AR analysis, the roots of the characteristic polynomial close to the unit circle at each sample (range) provide the estimates for eigenvalues. We analyzed the influence of spatial sampling, eigenvalue spread, and eigenvalue rate of variation on the error between roots and first-order poles.

Chapter 3 proposes two sequential eigenvalue estimators, a Kalman filter for the estimation of AR coefficients, and an adaptive filter for the estimation of polynomial roots. Competition among estimators was introduced in order to improve spatial tracking of eigenvalue changes. We examined the relation between the Kalman identifier and modal parameters that affect the effective memory length and dictates range resolution. The adaptive filter effective memory length is not dependent on the specific modal structure.

Decimation of the pressure field was introduced as a way to reduce the order of the AR models without reducing the actual range aperture. For the AR spectrogram, we show that decimation results in significant reduction in computation cost and allows the use of relatively larger orders, contributing for improved eigenvalue resolution. We established a criterion for maximum sampling distance  $\Delta r$  that imposes a limit on the amount of decimation. In all AR spectrograms showed in the data analysis section of Chapter 3, we obtained improved results using orders equal or slightly above the number

of eigenvalues.

The 2001 NRL Inverse Techniques Workshop (ITW) test case 3 was the initial motivation for Chapter 3. We showed that competition among sequential estimators resulted in a sharp definition of the abrupt eigenvalue change in this environment. Previously, the eigenvalue jump was detected through a degradation in the estimated AR spectrogram.

For the single mode case, three different methods provide essentially the same estimate, an improvement over previous results. Eigenvalue estimates using the sequential estimators for two sets of experimental data show agreement with the AR spectrogram, if not improvement.

We showed through simulation that systematic eigenvalue change, as in sloping bottom environments, degrades the performance of the AR estimator, confirming a previously observed result [6].

Appendix A analyzes the MOMAX raw acoustic data processing, and establishes conditions to minimize distortions of the modal content of the fields in terms of spatial sampling and selection of spectral analysis windows. We show that, under these conditions, the processed MOMAX data, such as the ones used in the data analysis section of Chapter 3, actually represent modal sums.

### 5.1.3 Chapter 4

Chapter 4 investigated the estimation of sound velocity profiles in the shallow ocean. We proposed a sequential estimator whose input data are modal eigenvalues measured as a function of range. This nonlinear problem is solved iteratively by first linearizing the measurement equation at a given initial background velocity profile.

The linearization of the eigenvalue measurement equation led to the perturbative technique integral equation. We formulated the linearization by first representing the profile as a sum of basis functions, a process akin to the finite element method. Previously proposed perturbative integral solvers, including the spectral expansion method and the discretization of the integral equation using the trapezoidal rule, are shown to

be particular cases of the basis function representation. We showed that the derivative of eigenvalues with respect to sound velocity variations, obtained from the perturbative integral using the basis function representation, is consistent with the formal Fréchet differentiation.

We proposed a description of the sound velocity increment  $\mathbf{q}$  as a Gaussian Markov process, which corresponds to attributing a covariance to the sound velocity increments, as in the stochastic inverse. The covariance of the sound velocity increment is defined by the initial and state-noise covariance matrices. Smoothing constraints can be imposed through modification of these matrices. The (state) equation for  $\mathbf{q}$  and the eigenvalue measurement equation form a state-space description of the inverse problem that lead to a Kalman filter implementation. The solution to the nonlinear inverse problem we implemented solves the problem in range for a given set of background profiles  $c_i(z; r)$  though the Kalman filter, updates the profiles to the new set  $c_{i+1}(z; r)$  and iterates until the solution converges. Other implementations, such as the Schmidt extended Kalman filter (EKF)[33], where the background profile is updated at each range step using the previous range result, may be possible.

We analyzed the relation between spatial resolution, variance, and bias of the eigenvalue inverse problem. With the Backus–Gilbert resolution theory as a background, we analyzed the influence of frequency and number of modes on the best possible resolution for a given environment, and showed, by example, how to apply this analysis to the design of experiments. We showed that resolution and variance improve, in general, by increasing frequency and number of modes, and by combining eigenvalues from different frequencies.

We developed a method to compensate for eigenvalue Doppler deviation introduced by source motion. It consists of a modification of the linear perturbative integral and the eigenvalue derivatives. We show the effectiveness of this formulation through an example.

We proposed a technique for sound velocity inversion. The seabed density structure

is, in principle, assumed known. Nevertheless, using the ITW test case 3 mentioned above, we show that blind inversion, where no geoacoustic information is available, may provide trends in the velocity profile, in particular with range, that are compatible with the expected depth resolution.

The influence of the water column variability is critical when analyzing experimental data acquired in coastal waters. In [6], for example, simulations suggested that the net effect of internal waves is to excite, through weak mode coupling, modes that would not be otherwise observed, without affecting the eigenvalues. In the presence of strong fluctuations, such as those caused by tides or tide induced solitary waves, on the other hand, the eigenvalues can fluctuate, as suggested by Field and co-workers [15].

The technique proposed in Chapter 4 assumes the sound velocity profile in water to be known. In shallow-water experiments, it is not possible to have an accurate picture of the time and spatial variations of the sound velocity profile in water, which compounds the problem of fluctuating environments.

One way to circumvent this problem is to include the water column in the inversion. When the background profile is closer to the actual solution in some depths (as is to be expected in the water, compared to the seabed), smaller corrections can be imposed through the solution covariance matrix. Lower sound velocity increment variances should be imposed at those depths.

## 5.2 Suggestions for Future Work

Merab's method is based on the time-independent Schrödinger wave equation, equivalent to the depth-dependent acoustic wave equation when density is constant or varies smoothly with depth. As pointed out in [45], the effect of smooth density variations on the velocity profile can be compensated for by measuring the reflection coefficient at two frequencies, an extension of the input data requirement of the original Gelfand-Levitan theory. Density discontinuities have to be taken into account for applications.

In Chapter 2, we proposed a simple compensation technique for the water-seabed discontinuity and showed that it worked in simulations. On the actual data, however, we did not observe any significant effect, suggesting that other density discontinuities may be present.

The method has to be extended in order to deal with density discontinuities that may be present at various depths. This extension may require the reformulation of the original theory using the acoustic wave equation. Another possibility is to investigate the Riccati equation for the evolution of the reflection coefficient with depth [75], whose boundary condition led to the compensation technique proposed in Chapter 2.

The techniques of Chapter 3 have to be extended to deal with systematic modal changes typical of coastal waters near the continental slope. In general, as stated in [52], adaptive estimators can identify nonstationary parameters that drift slowly, or have infrequent abrupt changes, or a combination of these two behaviors. Most adaptive identification methods fail with fast varying parameters. Apparently, this is the case of the ITW test case 2 analysis of Chapter 3 with more than two modes. For two modes, we showed by simulation that competition among second order Kalman filters was able to track the DE coefficients<sup>1</sup>. For more general cases, other methods, such as the expansion of eigenvalue and modal amplitude, or AR coefficient variations by basis functions, may be useful. The “fast” variations are modeled by the bases, and the problem is reduced to the estimation of constant, or nearly constant expansion coefficients.

As mentioned in Chapter 4, exact (in fact, asymptotic) inverse eigenvalue theories have been developed for the proper (self-adjoint) Sturm-Liouville problem. One possibility for applying such results to shallow-water inverse problems is to define a totally reflecting interface deep enough not to interfere with actual propagating modes in the water and upper sediment layers. Another possibility is to define a Hilbert space, through the definition of a suitable inner product, that renders the shallow-water problem self-adjoint. Such an approach has been investigated for laser cavities[41, 42]. Application

---

<sup>1</sup>In [38] only results for parameter estimation for sums of two chirp signals are presented.

of exact methods when a small number of eigenvalues are available can also be found in the literature[53].

Exact methods in shallow-water can also be based on measurements of the continuous spectrum of the field, as in Merab's method. They may be feasible if, first, no modes are excited (requiring a sufficiently low frequency in typical coastal environments), and second, the data can be acquired in small range apertures in order to be considered representative of *local* properties. In fact, by requiring that no mode be excited, the field may fall-off fast enough with range to be considered representative of the local environment. Stickler[70], for example, has proposed a method for shallow-water whose requirement is that no mode be excited.

# Appendix A

## MOMAX Raw Data Signal Processing

### A.1 Introduction

This appendix analyzes the *modal mapping experiment* (MOMAX) acoustic signal processing algorithm and establishes conditions under which the processed signal represents a sum of normal modes. The main results are eq.(A.25), which describes the operations required to extract monofrequency signals from the raw data  $p(t, \mathbf{r}; \mathbf{r}_s)$ , and Figure A-2.

The MOMAX raw acoustic data consist of acoustic pressure time series. Sources aboard a ship (either moored or moving) emit continuous tones of known frequencies. The receivers (hydrophones) are mounted on drifting buoys.

The position of the source and buoys is measured using *global positioning system* (GPS) receivers. Time series of either latitude and longitude, or E-N distances referred to the source are also available. From the acoustic and GPS time series, monofrequency data is generated in the form of pressure versus range or pressure versus 2-D position, suitable for spatial processing.

As implemented, the raw signal processing algorithm generates, for each frequency and for each acoustic receiver, time series of complex (quadrature demodulated) acoustic

signals at lower sampling rates than the raw data. For a source emitting  $F$  tones  $(\Omega_1, \dots, \Omega_F)$ , the raw data can be modeled, in terms of complex envelope, as

$$p(t_k, \mathbf{r}; \mathbf{r}_s) = \sum_{n=1}^F \Re \left\{ \tilde{f}_n(t_k, \mathbf{r}; \mathbf{r}_s) e^{-i\Omega_n t_k} \right\} + v(t_k), \quad (\text{A.1})$$

where  $t_k$  is the time instant corresponding to the  $k$ -th raw data sample,  $\mathbf{r}$  is the receiver position,  $\mathbf{r}_s$  is the source position,  $\Re\{g\}$  is the real part of  $g$ ,  $\tilde{f}_n$  is the complex envelope of the received signal corresponding to the transmitted frequency  $\Omega_n$ , and  $v(t_k)$  is the noise, assumed uncorrelated to the signal. The goal of the MOMAX raw data signal processing is to obtain the complex time series  $\tilde{f}_n$ ,  $n = 1 \dots F$ .

The processing algorithm consists of computing the discrete Fourier transform (DFT) of windowed segments of the data; selecting DFT frequencies (bins) close to the transmitted frequencies, generating new, decimated time series; and demodulating the new time series (multiplication by a complex exponential). For each transmitted frequency  $\Omega_l$ , the algorithm generates a time series

$$\begin{aligned} P_{\Omega_l}(mT, \mathbf{r}; \mathbf{r}_s) &= \frac{2}{N_{DFT}} e^{+i\Omega_l mT} \sum_{k=0}^{N_{DFT}-1} a_k p(t_k, \mathbf{r}; \mathbf{r}_s) e^{i\frac{2\pi}{N_{DFT}} qk}, \\ &= \frac{2}{N_{DFT}} e^{+i\Omega_l mT} \left( DFT \{a_k p(t_k, \mathbf{r}; \mathbf{r}_s)\}_{\omega_q} \right)^*, \end{aligned} \quad (\text{A.2})$$

$$t_k = mT + kT_s, \quad k = 0 \dots N_{DFT} - 1,$$

where  $T$  is the sampling interval of the new time series;  $N_{DFT}$  is the number of samples in each segment of raw data;  $T_s$  is the raw data sampling period (in MOMAX I to III,  $T_s = 10^{-7} \times 6 \times 512$  seconds = 307.2 microseconds, corresponding to a sampling frequency of 3255.2 Hz);  $a_k$  is the window;  $q < N_{DFT}/2$ , is the selected DFT frequency bin corresponding to  $\omega_q = 2\pi q/(N_{DFT}T_s)$  (close to the source frequency  $\Omega_l$ ); and '\*' indicates complex conjugate. Usually,  $T$  is taken as  $N_{DFT}T_s/2$ , corresponding to an overlap of half data segment, and an effective decimation factor (raw-to-processed) of

$N_{DFT}/2$ . In the present analysis, no overlap is considered and, therefore,  $T = N_{DFT}T_s$ . The effect of overlapping data segments is just to interpolate the processed time series.

As an example of complex envelope, consider the case of a range-independent, shallow-water environment. During the time interval  $N_{DFT}T_s$  corresponding to an analysis window, the source is assumed to move at a constant depth  $z_s$  with a constant speed  $v_s$  *toward* a receiver that moves at a constant speed  $v_R$  *away* from the source, at a constant depth  $z$ . The source-receiver range is  $r(t) = r_0 - (v_s - v_R)(t - t_0)$ . The complex envelope of the received signal at the source frequency  $\Omega_n$  has a normal mode representation (for large  $K_m^{(d)}r$ )

$$\begin{aligned} \tilde{f}_n(t_k, r(t_k), z; z_s) = S_{\Omega_n} \sum_m e^{-iK_{nm}^{(d)}(v_s - v_R)(t_k - t_0)} \times \\ u_{nm}^{(d)}(z) u_{nm}^{(d)}(z_s) \sqrt{\frac{2}{\pi K_m^{(d)}r}} e^{i(K_m^{(d)}r_0 - \pi/4)} \end{aligned} \quad (\text{A.3})$$

where  $S_{\Omega_n}$  is a function of the source strength and phase, and receiver response; and  $K_{nm}^{(d)}$  and  $u_{nm}^{(d)}(z)$  are, respectively, the eigenvalues and eigenfunctions evaluated at the Doppler-shifted frequencies  $\Omega_n + K_{nm}^{(d)}v_s$  [63]. The complex envelope  $\tilde{f}_n$  consists of a set of tones, one for each propagating mode, located at the frequencies  $K_{nm}^{(d)}(v_s - v_R)$ . Its bandwidth depends on the source and receiver speeds.

For a waveguide with a basement half-space of sound speed  $c_b$  and wavenumber  $k_b = \Omega_n/c_b$ , and a water column of sound speed  $c_0 < c_b$  and wavenumber  $k_0 = \Omega_n/c_0 > k_b$ , the eigenvalues corresponding to the propagating modes are in the range  $k_b < K_{nm}^{(d)} < k_0$  and, therefore, the complex envelope will contain tones in the region  $k_b |v_s - v_R| < |\omega| < k_0 |v_s - v_R|$ , at any given instant. The *momentary bandwidth* (rad/s) can be roughly defined as

$$B_{mom} = |v_s - v_R| (k_0 - k_b) = \frac{\Omega_n}{c_0} |v_s - v_R| \left( 1 - \frac{c_0}{c_b} \right). \quad (\text{A.4})$$

During an experiment, however, the source can be towed toward to or away from the receiver, which can also be drifting toward to or away from the source. The *total*

*bandwidth* that the complex envelope can occupy during an experiment is, therefore, not larger than

$$B \sim 2k_0 |v_S - v_R|_{\max} = 2\Omega_n \frac{|v_S - v_R|_{\max}}{c_0} = 4\pi \frac{|v_S - v_R|_{\max}}{\lambda_0}, \quad (\text{A.5})$$

where  $|v_S - v_R|_{\max}$  is the maximum possible magnitude of the range rate, and  $\lambda_0 = 2\pi/k_0$  is the wavelength in water.  $B$  is also the Nyquist rate for the complex envelope, from which the required sampling interval  $T$  [same as time aperture of raw data segments,  $N_{DFT}T_s$  in eq.(A.2), when no overlap is used], can be estimated:

$$T = N_{DFT}T_s < \frac{2\pi}{B} \sim \frac{2\pi c_0}{2\Omega_n |v_S - v_R|_{\max}} = \frac{\lambda_0}{2 |v_S - v_R|_{\max}}. \quad (\text{A.6})$$

Note that eq.(A.6) predicts that a processed signal sample is needed every

$$N_{DFT}T_s \times |v_S - v_R|_{\max} < \lambda_0/2 \quad (\text{A.7})$$

meters, i.e., more than 2 samples per wavelength must be measured, which can be interpreted as a spatial Nyquist rate.

For a typical towed source experiment,  $|v_S| = 1.5$  m/s,  $|v_R| = 0.25$  m/s,  $c_0 = 1500$  m/s, and the total bandwidth of the complex envelope at  $\Omega_n$  is, from eq.(A.5),  $B = 2.333 \times 10^{-3}\Omega_n$ . MOMAX experiments typically use frequencies between 20 Hz and 500 Hz, resulting, for the above towed source experiment, a total bandwidth between 0.04667 Hz ( $20 \pm 0.0233$  Hz) and 1.167 Hz ( $500 \pm 0.583$  Hz), for the different source frequencies. For suitable spatial sampling at 20 Hz, the processed sampling period (raw segment size to be processed) is, from eq.(A.6),  $N_{DFT}T_s < 21.43$  seconds ( $\sim 1$  point of processed data for every 69,750 points or less of raw data,  $N_{DFT} < 69,750$ ). At 500 Hz,  $N_{DFT}T_s < 0.8571$  seconds ( $\sim 1$  point of processed data for every 2,790 points or less of raw data,  $N_{DFT} < 2,790$ ). For a moored source experiment ( $v_S = 0$ ), the bandwidths would be seven times smaller, and the required maximum sampling periods

of the processed data, seven times larger.

After the time series of eq.(A.2) is obtained, and before further processing, additional filtering may be used to increase the signal-to-noise ratio. The subsequent analysis of the processed signal is usually restricted to regions where the range-rate and the Doppler deviation are nearly constant. In these regions, the effective signal bandwidth is close to the momentary bandwidth  $B_{mom}$ . The bandwidth  $B$ , as computed in eq.(A.5), is much larger than the momentary bandwidth. From eqs.(A.4) and (A.5),

$$\frac{B}{B_{mom}} = \frac{2k_0 |v_S - v_R|_{max}}{|v_S - v_R| (k_0 - k_b)} = 2 \frac{|v_S - v_R|_{max}}{|v_S - v_R|} \frac{1}{1 - c_0/c_b} > 2$$

(typically,  $B/B_{mom} \gg 1$ ).

After  $N_{DFT}$  is chosen, the frequency domain representation of the signal is limited to a range of frequencies  $2\pi/(N_{DFT}T_s) > B$  [from inequality (A.6)]. Therefore, the ratio  $D_{max}$  of processed signal bandwidth to signal momentary bandwidth, follows the inequality

$$\begin{aligned} D_{max} &= \frac{2\pi/(N_{DFT}T_s)}{B_{mom}} \\ &= \frac{2\pi/(N_{DFT}T_s)}{|v_S - v_R| (k_0 - k_b)} \\ &> \frac{B}{B_{mom}} > 2 \frac{|v_S - v_R|_{max}}{|v_S - v_R|} \frac{1}{1 - c_0/c_b} > 2. \end{aligned} \tag{A.8}$$

If decimation in time is applied, the decimation factor should be smaller than  $D_{max}$ .

$D_{max}$  is also the maximum decimation factor for the processed signal seen as a function of range (assuming  $v_S - v_R$  is constant over the whole analysis aperture) [cf. Section 3.3.5]. For a given  $N_{DFT}$ , the spatial sampling space is  $\Delta r = N_{DFT}T_s|v_S - v_R| = \lambda_0/n_\lambda$ ,  $n_\lambda > 2$ . In order to represent the range of eigenvalues  $k_b < k_{rm} < k_0$  in the wavenumber domain, the spatial sampling can not be larger than  $D\Delta r = 2\pi/(k_0 - k_b)$ , leading to a (maximum) decimation rate of  $D\Delta r/\Delta r = [2\pi/(k_0 - k_b)]/[N_{DFT}T_s|v_S - v_R|]$ , which is eq.(A.8).

## A.2 The Short-Term Fourier Transform of the Raw Data

The operation indicated in eq.(A.2) can be interpreted in terms of the short-term Fourier transform

$$P_{STFT}(\omega_q; t) = \int_t^{t+\Delta T} a(t' - t - \Delta T/2) p(t', \mathbf{r}; \mathbf{r}_s) e^{i\omega_q t'} dt', \quad (\text{A.9})$$

where  $a(t)$  is a window, a slowly-varying, real-valued, even function of  $t$  with support on  $|t| \leq \Delta T/2$ ; and  $\Delta T = N_{DFT} T_s$ . Substituting eq.(A.1) into eq.(A.9), neglecting the noise component for simplification, and using  $\Re\{z\} = (z + z^*)/2$ , one obtains

$$\begin{aligned} P_{STFT}(\omega_q; t) = & \sum_{n=1}^F \frac{1}{2} \int_t^{t+\Delta T} a(t' - t - \Delta T/2) \tilde{f}_n(t', \mathbf{r}; \mathbf{r}_s) e^{i(\omega_q - \Omega_n)t'} dt' + \\ & \frac{1}{2} \int_t^{t+\Delta T} a(t' - t - \Delta T/2) \tilde{f}_n^*(t', \mathbf{r}; \mathbf{r}_s) e^{i(\omega_q + \Omega_n)t'} dt'. \end{aligned} \quad (\text{A.10})$$

The complex envelope is, by hypothesis, a slowly-varying function of time. Assume, for simplification, that it is constant along the interval of integration (this approximation is discussed below). The above expression then simplifies to

$$\begin{aligned} P_{STFT}(\omega_q; t) = & \sum_{n=1}^F e^{i(\omega_q - \Omega_n)t} \frac{\tilde{f}_n(t + \Delta T/2, \mathbf{r}; \mathbf{r}_s)}{2} \int_0^{\Delta T} a(\eta - \Delta T/2) e^{i(\omega_q - \Omega_n)\eta} d\eta + \\ & e^{i(\omega_q + \Omega_n)t} \frac{\tilde{f}_n^*(t + \Delta T/2, \mathbf{r}; \mathbf{r}_s)}{2} \int_0^{\Delta T} a(\eta - \Delta T/2) e^{i(\omega_q + \Omega_n)\eta} d\eta. \end{aligned} \quad (\text{A.11})$$

The above integrals are the Fourier transform of the shifted window function evaluated at the frequencies  $(\omega_q \pm \Omega_n)$ . For example, the rectangular window

$$a_{rect}(t) = \begin{cases} 1, & |t| \leq \Delta T/2 \\ 0, & \text{otherwise} \end{cases} \quad (\text{A.12})$$

has transform

$$A_{rect}(\omega) = \mathcal{F}\{a_{rect}\} = \int_{-\Delta T/2}^{\Delta T/2} e^{i\omega\eta} d\eta = \Delta T \text{Sa} \left[ \frac{\Delta T}{2} \omega \right], \quad (\text{A.13})$$

where  $\text{Sa}[x] = \sin x / x$  is the sampling function. For the rectangular window, eq.(A.11) becomes

$$\begin{aligned} P_{STFTrect}(\omega_q; t) = \sum_{n=1}^F e^{i(\omega_q - \Omega_n)(t + \Delta T/2)} \frac{\Delta T \tilde{f}_n(t + \Delta T/2, \mathbf{r}; \mathbf{r}_s)}{2} \text{Sa} \left[ \frac{\Delta T}{2} (\omega_q - \Omega_n) \right] + \\ e^{i(\omega_q + \Omega_n)(t - \Delta T/2)} \frac{\Delta T \tilde{f}_n^*(t + \Delta T/2, \mathbf{r}; \mathbf{r}_s)}{2} \text{Sa} \left[ \frac{\Delta T}{2} (\omega_q + \Omega_n) \right]. \end{aligned} \quad (\text{A.14})$$

One additional assumption is that the source frequencies  $\Omega_n, n = 1, \dots, F$  are sufficiently far apart that we can consider the individual sampling functions  $\text{Sa} \left[ \frac{\Delta T}{2} (\omega_q \mp \Omega_n) \right]$  to be zero, except the one corresponding to a source frequency  $\Omega_l$  close to the analysis frequency  $\omega_q$  (that is, for  $\omega_q - \Omega_l \sim 0$ ). Therefore, the operation of selecting a DFT bin ( $\omega_q$ ) close to the source frequency ( $+\Omega_l$ ) corresponds to obtaining a time-series

$$\begin{aligned} p_{STFTrect}(t; \Omega_l) = & \tilde{f}_l(t + \Delta T/2, \mathbf{r}; \mathbf{r}_s)/2 \times \quad [\text{envelope}/2] \\ & \Delta T \text{Sa} \left[ \frac{\Delta T}{2} (\omega_q - \Omega_l) \right] \times \quad [\text{'filter gain'}] \\ & e^{i(\omega_q - \Omega_l)(t + \Delta T/2)} \quad [\text{oscillations}]. \end{aligned} \quad (\text{A.15})$$

The first term in eq.(A.15) is the desired (scaled) complex envelope. The second term, filter complex gain [=  $A_{rect}(\omega_q - \Omega_l)$ ], is the Fourier transform of the rectangular window. Its magnitude decreases as the chosen frequency  $\omega_q$  moves away from the source frequency  $\Omega_l$ . Noise, not included in the analysis, will impose a cost in terms of reduced signal-to-noise ratio as this filter gain magnitude decreases. The analysis frequency  $\omega_q$  must be chosen as close as possible to the source frequency  $\Omega_l$ . The third factor is an

oscillatory term that can be easily compensated for because its frequency is known.

The complex envelope can be recovered from eq.(A.15) as  $[2p_{STFT}(t, \Omega_l) \div 'filter gain' \times \exp\{-i(\omega_q - \Omega_l)(t + \Delta T/2)\}]$ . We substitute a generic filter gain  $A(\omega)$  for the rectangular window filter gain factor in eq.(A.15) to obtain

$$\tilde{f}_l(t + \Delta T/2, \mathbf{r}; \mathbf{r}_s) = e^{-i(\omega_q - \Omega_l)(t + \Delta T/2)} \frac{2}{A(\omega_q - \Omega_l)} p_{STFT}(t; \Omega_l). \quad (\text{A.16})$$

As an example of another filter gain factor, consider the Hamming window

$$a_{Hamm}(t) = \begin{cases} 0.54 + 0.46 \cos\left(\frac{2\pi t}{\Delta T}\right), & |t| \leq \Delta T/2 \\ 0, & otherwise \end{cases} \quad (\text{A.17})$$

whose transform is

$$A_{Hamm}(\omega) = 0.08\Delta T \frac{27\pi^2 - \Delta T^2\omega^2}{4\pi^2 - \Delta T^2\omega^2} \text{Sa}\left[\frac{\Delta T}{2}\omega\right]. \quad (\text{A.18})$$

Equation (A.18) with  $\omega = \omega_q - \Omega_l$  is the filter gain factor in eqs.(A.15) and (A.16) when a Hamming window is used. Figure A-1 on the next page compares the spectrum of the rectangular and Hamming windows. As mentioned above in relation to eq.(A.14), the contribution of the individual sampling functions is considered negligible for source frequencies far from the analysis frequencies. This is better approximated by the Hamming window due to its lower *sidelobes* (local magnitude maxima away from  $\omega = 0$ ). The broader *main lobe* of the Hamming window helps reduce the distortion of the complex envelope in the processed signal, as discussed below. In general, the lower the side lobes, the broader the main lobe, resulting in better measurements of the complex envelope,

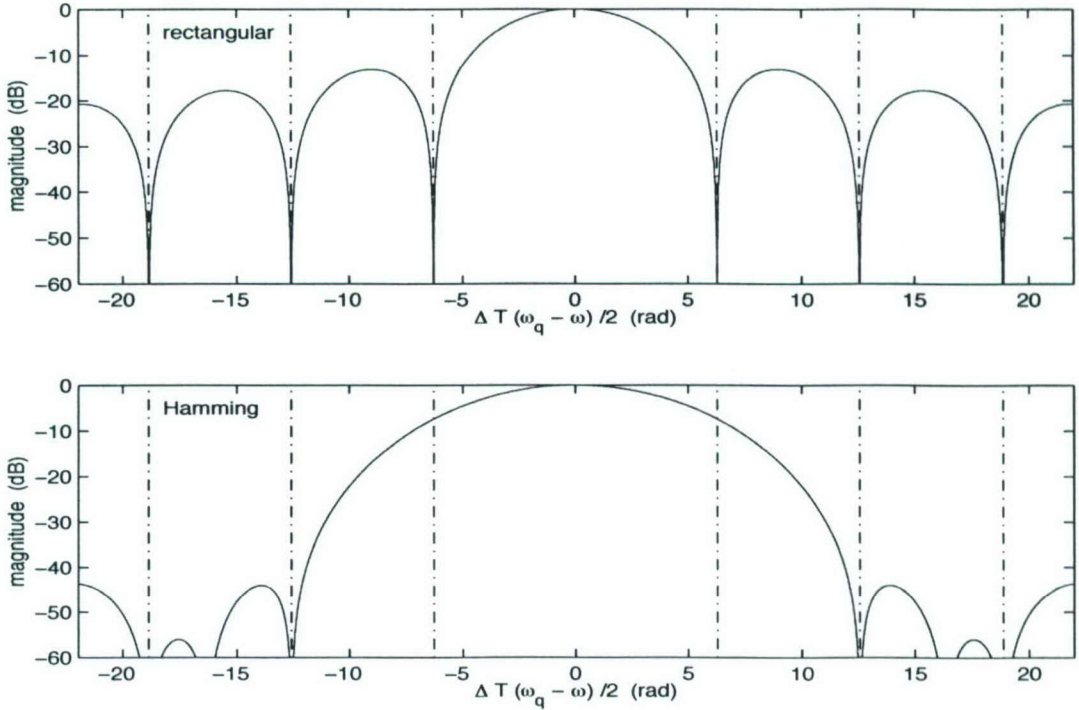


Figure A-1: The Fourier transform of the rectangular and Hamming windows (normalized magnitude). The vertical dot-dash lines indicate the position of the neighbor DFT frequency bins

as long as the signal-to-noise is high (see, for example, [30] for a detailed discussion of windows used in spectral analysis). In order to verify the validity of the assumption of constant  $\tilde{f}$  in eq.(A.15), we use the normal mode representation of eq.(A.3). For notational simplicity, rewrite eq.(A.3) as

$$\tilde{f}_n(t', \mathbf{r}; \mathbf{r}_s) \equiv \sum_m e^{-iK_{nm}^{(d)}(v_s - v_R)t'} h_{nm}(r, z, z_s). \quad (\text{A.19})$$

Substituting eq.(A.19) into (A.10) and neglecting the contribution of the sampling functions corresponding to analysis frequencies  $\omega_q$  far from the selected source frequency  $\Omega_l$ ,

one obtains the output time series [cf. eqs.(A.10) and (A.15)]:

$$\begin{aligned}
p_{STFT}(t; \Omega_l) &= \frac{1}{2} \sum_m h_{lm}(r, z, z_s) \int_t^{t+\Delta T} a(t' - t - \Delta T/2) e^{-iK_{lm}^{(d)}(v_S - v_R)t'} e^{i(\omega_q - \Omega_l)t'} dt' \\
&= \frac{1}{2} e^{i(\omega_q - \Omega_l)t} \sum_m e^{-iK_{lm}^{(d)}(v_S - v_R)t} h_{lm}(r, z, z_s) \times \\
&\quad \int_0^{\Delta T} a(\eta - \Delta T/2) e^{i(\omega_q - \Omega_l - K_{lm}^{(d)}(v_S - v_R))\eta} d\eta. \quad (\text{A.20})
\end{aligned}$$

The integral in the above expression is the Fourier transform of the window function evaluated at  $\omega = \omega_q - \Omega_l - K_{lm}^{(d)}(v_S - v_R)$ . The processed time series is, therefore, given by [cf. eq. (A.15)]

$$\begin{aligned}
p_{STFT}(t; \Omega_l) &= e^{i(\omega_q - \Omega_l)(t + \Delta T/2)} && [\text{oscillations}] \\
&\times \sum_m \left[ e_m^{-iK_{lm}^{(d)}(v_S - v_R)(t + \Delta T/2)} h_{lm}(r, z, z_s) \right] && [\text{envelope}] \quad (\text{A.21}) \\
&\quad \text{and} \\
&\times A(\omega_q - \Omega_l - (v_S - v_R)K_{lm}^{(d)})/2 && [\text{'filter gain'}]
\end{aligned}$$

It is not possible to isolate the effect of the window (filter gain), from the complex envelope itself, as in eq.(A.15). Instead, a distorted version of the complex envelope is obtained, as seen by comparing eqs.(A.19) and (A.21).

As discussed in Section A.1 regarding shallow water waveguides, the complex envelope frequencies  $(v_S - v_R)K_{lm}^{(d)}$  are spread, at any given instant, in the bandwidth  $B_{mom}$  given by eq.(A.4). The main lobe width of the rectangular window spectrum [see Figure A-1 and eq.(A.13)] is  $4\pi/\Delta T = 4\pi/(N_{DFT}T_s)$ . As shown in eq.(A.8),  $B_{mom}$  is smaller than the width of the main lobe by, at least, a factor of 4. In fact, it is usually much smaller. For example, using  $c_0 = 1490$  m/s,  $c_b = 1800$  m/s, the momentary bandwidth is about 24 times smaller than the main lobe width. For the broader Hamming window, the ratio is twice that value and the momentary bandwidth is at most 2% of the main

lobe width. If the complex envelope spectrum is not near the main lobe null, the term  $A$  inside the summation in eq.(A.21) can be considered constant (independent of the mode number  $m$ ), and the approximation of eq.(A.16) is valid. A better approximation takes into account the Doppler of the source frequency, leading to

$$\tilde{f}_l(t + \Delta T/2, \mathbf{r}; \mathbf{r}_s) \simeq \frac{2e^{-i(\omega_q - \Omega_l)(t + \Delta T/2)}}{A(\omega_q - \Omega_l - (v_s - v_R)k_0)} p_{STFT}(t; \Omega_l), \quad (\text{A.22})$$

where  $k_0$  is some significant wavenumber. The broader the main lobe, the better the approximation.

### A.3 DFT Implementation of the Short-Term Fourier Transform

The short-term Fourier transform of the raw data is given by eq.(A.9), repeated here for convenience:

$$P_{STFT}(\omega_q; t) = \int_t^{t + \Delta T} a(t' - t - \Delta T/2) p(t', \mathbf{r}; \mathbf{r}_s) e^{i\omega_q t'} dt'. \quad (\text{A.23})$$

In order to obtain the discrete version of this expression, let  $t = m\Delta T$ ,  $m = 0, 1, \dots$  (assuming no overlap between adjacent segments),  $t' = t_k = t + kT_s$ ,  $\Delta T = N_{DFT}T_s$ ,  $dt' = T_s$ ,  $\omega_q = q\delta_\omega$ ,  $T_s\delta_\omega = 2\pi/N_{DFT}$ , with  $k, q = 0, \dots, N_{DFT} - 1$ . The result is

$$P_{STFT}(\omega_q; t) \simeq P_{DFT}(\omega_q; t) = T_s e^{i\omega_q t} \sum_{k=0}^{N_{DFT}-1} a_k p(t_k, \mathbf{r}; \mathbf{r}_s) e^{i\frac{2\pi}{N_{DFT}} q k}, \quad (\text{A.24})$$

where  $a_k \equiv a(kT_s - \Delta T/2)$  is the discrete version of the window function.

From the analysis of the previous section, the desired complex envelope is obtained by selecting the frequency bin  $q$  closest to the chosen source frequency, i.e.,  $\omega_q \simeq \Omega_l$ , multiplying the resulting time series by  $\exp\{-i(\omega_q - \Omega_l)(t + \Delta T/2)\}$ , and compensating

for the “filter gain.” Equation (A.22), when using the DFT, eq.(A.24), becomes

$$\tilde{f}_l(t + \Delta T/2, \mathbf{r}; \mathbf{r}_s) = \frac{2e^{-i(\omega_q - \Omega_l)(t + \Delta T/2)}}{A(\omega_q - \Omega_l - (v_s - v_R)k_0)} \times \\ T_s e^{i\omega_q t} \sum_{k=0}^{N_{DFT}-1} a_k p(t_k, \mathbf{r}; \mathbf{r}_s) e^{i\frac{2\pi}{N_{DFT}} q k}.$$

In the main lobe, the transform of the window can be written as  $A(\omega) = b(\omega)N_{DFT}T_s$ , where  $|b|$  is maximum at  $\omega = 0$  [see Table A.1, column *max 'filter gain'*, for  $|b(0)|$ ]. Therefore,

$$\tilde{f}_l(t + \Delta T/2, \mathbf{r}; \mathbf{r}_s) = \frac{e^{-i\omega_q \Delta T/2}}{b(\omega_q - \Omega_l - (v_s - v_R)k_0)} \frac{2}{N_{DFT}} \times \\ e^{i\Omega_l(t + \Delta T/2)} \sum_{k=0}^{N_{DFT}-1} a_k p(t_k, \mathbf{r}; \mathbf{r}_s) e^{i\frac{2\pi}{N_{DFT}} q k}, \quad (\text{A.25})$$

which, except for a multiplicative complex constant, is the operation described in eq.(A.2). The additional phase  $\Omega_l \Delta T/2$  can be discarded by associating the result of each DFT to the instant  $t + \Delta T/2 = t + N_{DFT}T_s/2$ , the center of the window, instead of its beginning [that is, substitute  $t'' = m\Delta T + \Delta T/2$  for  $t + \Delta T/2$  in eq.(A.25)]. The term  $b$  depends on the Doppler deviation, which changes during an experiment. As a first approximation,  $b$  can be set at its value at the bin center  $\omega = 0$  (given in Table A.1 for 4 windows, together with the worst-case magnitude error in dB). Another level of approximation is to compute  $b$  at  $\omega = \omega_q - \Omega_l$ . Further accuracy can be achieved by computing  $b$  as a function of time for a given experiment and window, and using it as a variable correction factor for the different portions of the data.

### A.3.1 Selection of the Transform Size and Window Function

The transform size is constrained by the required spatial Nyquist rate, as expressed in eq.(A.7). For a spatial sampling  $\Delta r \leq \lambda_0/n_\lambda$  (that is,  $n_\lambda$  range points per wavelength),

the criterion for the selection of transform size becomes, after substituting  $\lambda_0/n_\lambda$  for  $\lambda_0/2$  in eq.(A.7),

$$N_{DFT} \leq \frac{c_0}{n_\lambda f_l T_s |v_S - v_R|_{\max}}, \quad (\text{A.26})$$

where  $f_l = \Omega_l/2\pi$  is the source frequency in Hz. Figure A-2 shows plots of the relation in eq.(A.26), for the values of raw sample period  $T_s$  used in MOMAX I to III.

The choice of window function affects the distortion of the complex envelope and the signal-to-noise ratio of the processed signal. In order to reduce changes in the magnitude response of the analysis system, the frequency response should be flat for received frequencies in the band  $\Omega_l \pm B_l/2$ , where  $B_l$  is the maximum bandwidth excursion of the complex envelope at frequency  $\Omega_l$  during an experiment, as given by eq.(A.5). The DFT bin separation  $\delta_\omega$  is given by  $\delta_\omega = 2\pi/(N_{DFT}T_s)$ , as discussed above [see discussion preceding eq.(A.24)]. In terms of bin separation, the criterion of eq.(A.26) becomes, using eq.(A.5),

$$\delta_\omega = \frac{2\pi}{N_{DFT}T_s} \geq \frac{n_\lambda \Omega_l |v_S - v_R|_{\max}}{c_0} = \frac{n_\lambda}{2} B_l. \quad (\text{A.27})$$

The worst-case scenario in terms of signal attenuation occurs when the source frequency falls exactly midway between two bins,  $\Omega_l = \omega_q + \delta_\omega/2$ , there is an up-Doppler of  $B_l/2$ , and the minimum bin separation is used [equality in eq.(A.27)]. The signal frequency would be close to  $\omega_q + \delta_\omega/2 + \delta_\omega/n_\lambda$ . Using, for example  $n_\lambda = 4$  samples per wavelength the signal would be  $3\delta_\omega/4$  away from the bin center, closer, in fact, to the next bin. From Figure A-1, the attenuation due to the window would be about 10 dB below the maximum response for the rectangular, and 4 dB for the Hamming window.

Once the transform size is selected according to the above criterion, the processed value [eq.(A.25)] at the bin closest to the source frequency represents the desired complex envelope at a suitable sampling rate. In this sense, overlapping data for the Fourier transform only adds to computation cost. If closer samples are required, one should select a smaller  $N_{DFT}$ , with the advantage of broader  $\delta_\omega$ , a smaller worst-case loss, and a smaller complex envelope distortion, as discussed in connection to eq.(A.21).

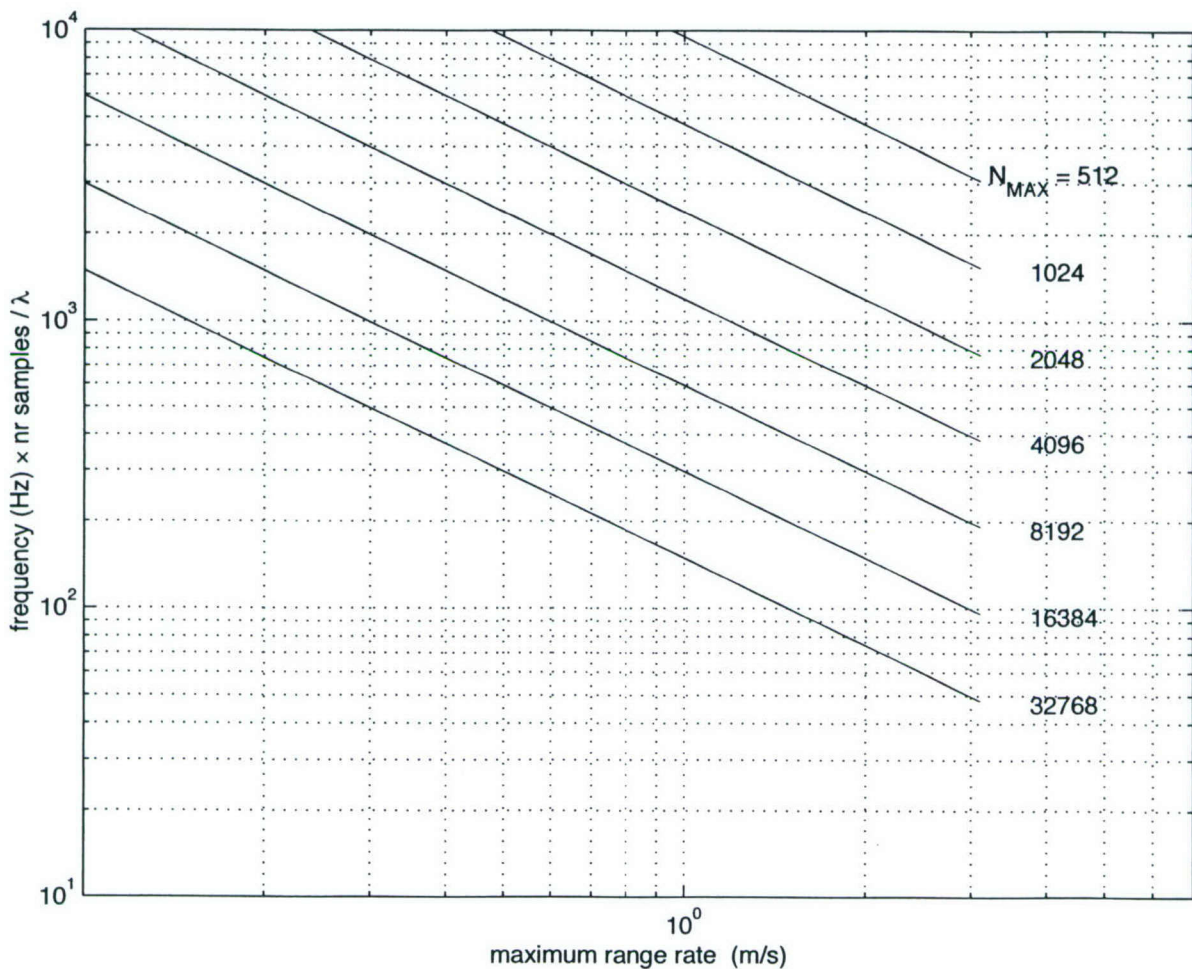


Figure A-2: This plot reflects the criterion of eq.(A.26), for the particular values  $T_s = 307.2 \mu s$  and  $c_0 = 1500 \text{ m/s}$ . The x-axis is the maximum source-receiver range rate during an experiment; the y-axis is the source frequency to be analyzed times the desired number of samples per wavelength. The line just above a point (range rate, frequency  $\times$  nr. samples  $/ \lambda$ ) gives the maximum size of the raw data DFT. For example, at 1 m/s, source frequency 100 Hz, and 4-points-per-wavelength spatial sampling ( $f \times$  nr. samples  $/ \lambda = 400$ ): the point (1, 400) falls below the  $N_{MAX} = 8192$  line, which is the maximum size of DFT that should be used. If different frequencies are processed simultaneously, the smallest  $N_{DFT}$  should be used.

### A.3.2 Four Discrete Windows

The discrete version and the characteristics of 4 windows are presented here. In addition to the two windows already discussed, rectangular and Hamming, the Hann and the 4-term Blackman-Harris windows are presented. The Hann window has been used in the MOMAX raw data processing. The Blackman-Harris window, with its broad main lobe ( $4 \delta_\omega$ ) and extremely low side-lobe levels (-92 dB), is well suited for the present application. A detailed analysis of these and many other windows is presented in [30].

The windows are defined for  $n = 0, \dots, N_{DFT} - 1$ . The ones presented here are called “DFT-even” or simply “DFT” in [30]. Some of them are defined as “periodic” in Matlab®. Their expressions are

- Rectangular:

$$a_n = 1; \quad (\text{A.28})$$

- Hamming window:

$$a_n = 0.54 - 0.46 \cos \left( \frac{2\pi}{N_{DFT}} n \right); \quad (\text{A.29})$$

- Hann window:

$$a_n = 0.5 - 0.5 \cos \frac{2\pi n}{N_{DFT}}; \quad (\text{A.30})$$

- minimum 4-term Blackman-Harris:

$$a_n = 0.35875 - 0.48829 \cos \left( \frac{2\pi}{N_{DFT}} n \right) + 0.14128 \cos \left( \frac{4\pi}{N_{DFT}} n \right) - 0.01168 \cos \left( \frac{6\pi}{N_{DFT}} n \right). \quad (\text{A.31})$$

Figures A-3 and A-4 show the Fourier transform of these windows. Table A.1 shows some of the windows characteristics. Twenty bins are represented in Figure A-3 in order to show the sidelobes (except for the 4-term Blackman-Harris, whose -92 dB sidelobe level is off-scale). In Figure A-4 only one bin is shown. The vertical line at (bin number –

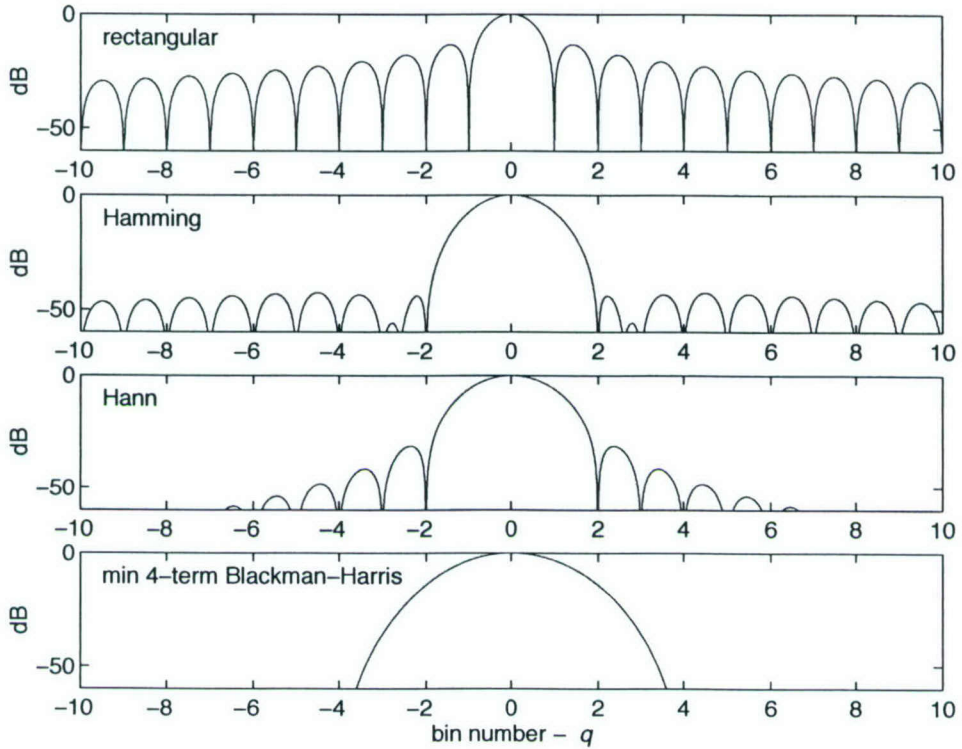


Figure A-3: Normalized Fourier transform magnitude (in dB) of four windows. The horizontal axis scale is normalized (bin numbers): zero corresponds to  $\omega_q$ , 1 corresponds to  $\omega_{q+1}$  (the total horizontal axis range corresponds to 20 bins—a bandwidth of  $20\delta_\omega$ ).

$q) = 0.75$  corresponds to the worst-case signal attenuation discussed above (with  $n_\lambda = 4$  samples per wavelength). When the source and receiver pass through the point of closest approach, the signal frequency changes the most and, in the worst-case scenario, it changes from the 0.75 to the 0.25 line, causing a sudden variation of the processed signal magnitude.

In Table A.1 the worst-case additional attenuation is indicated in the last column. The column *maximum 'filter gain'* corresponds to the signal gain at the bin center (that is, when the signal and bin frequency coincide). Notice that the maximum gain is a fraction of the number of DFT points [this fraction is the maximum value of  $b$  in eq.(A.25)]. The *equivalent noise bandwidth* (ENBW) is a measure of how much noise is reflected in the bin output. For example, a value of 2 indicates that if white noise of

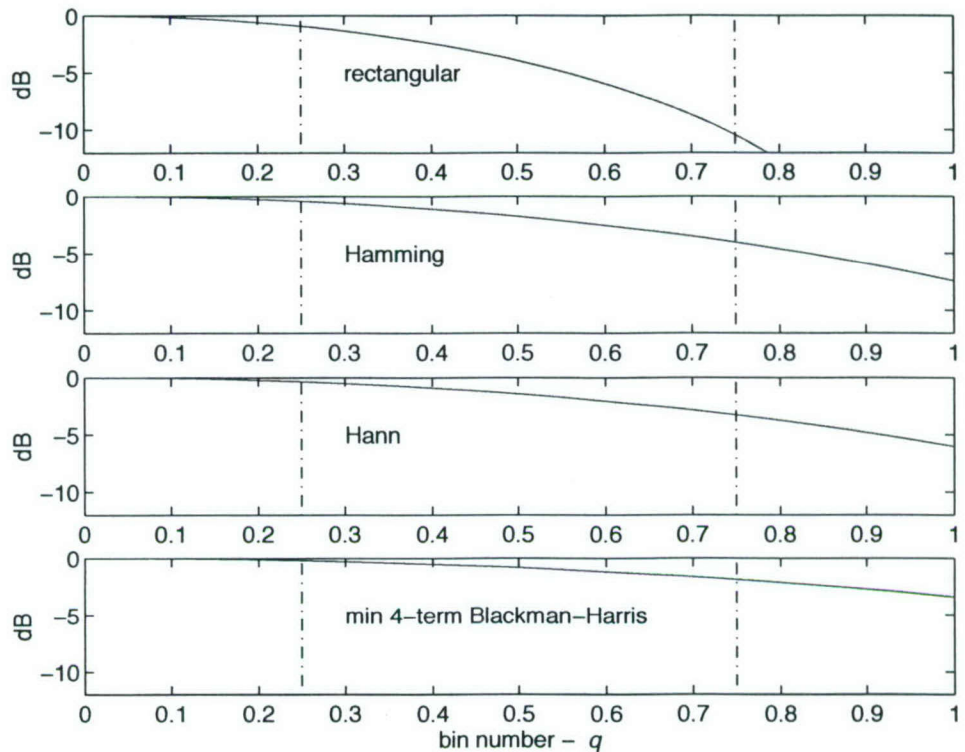


Figure A-4: Normalized Fourier transform magnitude of four windows (zoom). The vertical lines represent a variation of  $\pm\delta_\omega/4$  around the middle point between bins, corresponding to the (worst case) total frequency variation during an experiment (assuming the criterion  $N_{DFT}T_s \leq \lambda_0/4$  is obeyed).

Table A.1: Characteristics of four analysis windows. The *max filter gain* is the value of the window transform magnitude at the center frequency; the equivalent noise bandwidth (*ENBW*, in number of bins) is a measure of the bandwidth of the window that indicates how large the response to noise is (it is roughly the 3 dB bandwidth, but include effects of the whole Fourier transform); the *sidelobe* column indicates the maximum sidelobe level; the *max attenuation* is the worst-case scenario of extra attenuation due to Doppler deviation (when  $n_\lambda = 4$  samples per wavelength).

window	max 'filter gain'	ENBW	sidelobe	max attenuation
rectangular	$N_{DFT}$	1.00	-13	9.95
Hamming	$0.54N_{DFT}$	1.36	-43	4.03
Hann	$0.50N_{DFT}$	1.50	-32	3.21
min 4-term BH	$0.35875N_{DFT}$	2.00 bins	-92 dB	1.80 dB

noise level  $N_0$  “power units” per unit bandwidth is present in the signal, the bin output noise power is  $2\delta_\omega N_0$ .

The rectangular window has a large maximum attenuation and high sidelobe level, and should not be normally used. The bin closest to the source frequency must be selected in order to reduce distortions and magnitude variations due to changing range rates, and to improve the signal-to-noise ratio. The 4-term Blackman-Harris window is well suited for the MOMAX raw data processing. It has an extremely low sidelobe level and nearly constant magnitude over one bin. The increased noise power due to its broad main lobe (larger ENBW in Table A.1) can be compensated for by filtering the processed signal in regions where the Doppler is constant, before additional analysis. The Hann window also offers a reasonable compromise. Considering that MOMAX source frequencies are typically far apart, the Hann window larger sidelobe level (which decays fast away from the bin center) should not be an issue.

If signal-to-noise ratio becomes an issue, a window with smaller ENBW (and, consequently, smaller main lobe width and larger maximum attenuation) could be selected. In this case, the worst-case scenario can be avoided and the distortion caused by the sharper main lobe variation minimized by reducing  $N_{DFT}$  (increasing  $n_\lambda$ ). Post-processing filtering can be used later to compensate for the larger resulting analysis bandwidth.

## Appendix B

# Difference Equation (DE) for a Sum of Varying Complex Exponentials

This appendix develops the expression for the coefficients of the DE that represents the sum of an arbitrary number of time-varying complex exponentials, and for the initial value problem of computing the first-order poles given the series of DE coefficients. We follow the procedure in [38]. We also analyze the errors between the roots of the DE characteristic equation and the actual first-order poles, an issue important in understanding the errors in time-varying autoregressive analysis of these signals.

## B.1 DE for a Sum of $M$ Complex Exponentials[35]

The signal to be represented is a sum of complex exponentials  $y_m(n)$  whose phase rates and magnitudes are varying. The signal and the corresponding DE are given by

$$\begin{aligned}
 y(n) &= \sum_{m=1}^M y_m(n) = \sum_{m=1}^M c_m(n)y_m(n-1), \\
 &= \sum_{j=1}^M a_j(n)y(n-j), \\
 &= \sum_{j=1}^M a_j(n) \sum_{m=1}^M y_m(n-j),
 \end{aligned} \tag{B.1}$$

where the individual complex exponentials are given by

$$y_m(n) = U_m(n) \exp \{-A_m(n) + iK_m(n)\}, \quad m = 1, \dots, M.$$

The first-order DE,  $M = 1$ , is given by:

$$y_m(n) = c_m(n)y_m(n-1), \tag{B.2}$$

where

$$\begin{aligned}
 c_m(n) &= |c_m(n)| \exp \{i\delta K_m(n)\} \\
 &= \frac{U_m(n)}{U_m(n-1)} \exp \{-\delta A_m(n)\} \exp \{i\delta K_m(n)\},
 \end{aligned} \tag{B.3}$$

$$\delta K_m(n) = K_m(n) - K_m(n-1) = \int_{r_{n-1}}^{r_n} k_m(r') dr', \tag{B.4}$$

$$\delta A_m(n) = A_m(n) - A_m(n-1) = \int_{r_{n-1}}^{r_n} \alpha_m(r') dr', \tag{B.5}$$

$k_m(r)$  is the range-varying eigenvalue associated with mode  $m$ , and  $\alpha_m(r)$  is the corre-

sponding absorption coefficient. For the present application, typically  $k_m \gg \alpha_m$ . In the above expressions, the index  $n$  refers to points along a uniform range grid  $r_n = r_0 + n\Delta r$ , corresponding to the discretization of a continuous range signal, i.e.,  $y(n) \equiv y(r)|_{r=r_n}$ .

From the first-order DE, one obtains

$$\begin{aligned}
 y_m(n-j) &= c_m^{-1}(n-j+1)y_m(n-j+1) \\
 &\vdots \\
 &= c_m^{-1}(n-j+1)c_m^{-1}(n-j+2) \cdots c_m^{-1}(n-1)y_m(n-1) \\
 &= d_{m,j}(n)y_m(n-1),
 \end{aligned} \tag{B.6}$$

where

$$d_{m,j}(n) = \begin{cases} 1, & j = 1, \\ c_m^{-1}(n-j+1)d_{m,j-1}, & 2 \leq j \leq M. \end{cases} \tag{B.7}$$

Substituting eq.(B.6) into eq.(B.1), one obtains

$$y(n) = \sum_{m=1}^M y_m(n-1) \sum_{j=1}^M d_{m,j} a_j(n),$$

which. Comparing the first line of eq.(B.1) with the above expression, one obtains the system

$$\sum_{j=1}^M d_{m,j} a_j(n) = c_m(n),$$

that relates first-order poles and DE coefficients. In matrix form,

$$D(n)\mathbf{a}(n) = \mathbf{c}(n), \tag{B.8}$$

where  $(D)_{i,j} = d_{i,j}$ ,  $\mathbf{a}(n) = [a_1(n), \dots, a_M(n)]^T$ , and  $\mathbf{c}(n) = [c_1(n), \dots, c_M(n)]^T$ .

Note that each of the rows in the system (B.8) can be written, after multiplying by

the corresponding  $d_{m,M}^{-1} = \prod_{j=1}^{M-1} c_m(n-j)$ , as a recursion in the first-order poles:

$$\begin{aligned} & \prod_{j=1}^{M-1} c_m(n-j) a_1(n) + \prod_{j=2}^{M-1} c_m(n-j) a_2(n) + \cdots \\ & + c_m(n-M+1) a_{M-1}(n) + a_M(n) = c_m(n) \prod_{j=1}^{M-1} c_m(n-j). \quad (\text{B.9}) \end{aligned}$$

## B.2 From DE Coefficients to First-Order Poles

In order to find a recursion for the right-pole analogous to eq.(3.36), [35] used a procedure similar to the one followed in Section 3.2 for the sum of 2 signals. Using the  $z$  operator defined in eq.(3.32),  $[a(n)z^{-j}]f(n) = a(n)f(n-j)$ , and the product  $[a(n)z^{-j}] \circ f(n) = a(n)f(n-j)z^{-j}$ , the DE (B.1) can be written as

$$[1 - a_1(n)z^{-1} - \cdots - a_M(n)z^{-M}]y(n) = \left[ 1 - \sum_{j=1}^M a_j(n)z^{-j} \right] y(n) = 0.$$

The polynomial in  $z$  can be decomposed as

$$\left[ 1 - \sum_{j=1}^M a_j(n)z^{-j} \right] y(n) = \left[ 1 - \sum_{j=1}^{M-1} e_j(n)z^{-j} \right] \circ [1 - p_M(n)z^{-1}] y(n)$$

which is used to obtain a recursive system involving the  $a_j$ 's,  $e_j$ 's, and the right poles  $p_M$ , and, finally, a recursion for the right pole, analogous to eqs.(3.35) and (3.36).

The resulting right-pole iteration is, not surprisingly, the same shown for the first-order poles in eq.(B.9), i.e.,

$$\begin{aligned} p_M(n) \prod_{j=1}^{M-1} p_M(n-j) &= a_M(n) + p_M(n-M+1)a_{M-1}(n) \\ &+ \sum_{j=1}^{M-2} a_j(n) \prod_{k=j}^{M-1} p_M(n-k). \quad (\text{B.10}) \end{aligned}$$

When initialized with  $p_M(n_0 - 1) = c_m(n_0 - 1)$  to  $p_M(n_0 - M + 1) = c_m(n_0 - M + 1)$ , eq.(B.10) recovers the series  $c_m(n)$  for  $n \geq n_0$ . A backward recursion can be similarly implemented.

### B.3 Error Between DE Characteristic Polynomial Roots and First-Order Poles

When a first-order pole  $c_m(n)$  is constant over an interval  $n_0 - M + 1 \leq n \leq n_0$ , say  $c_m(n) = c_{mO}$ , eq.(B.9) becomes

$$c_{mO}^M - a_1(n_0)c_{mO}^{M-1} - \cdots - a_M(n_0) = 0, \quad (\text{B.11})$$

and  $c_m(n_0) = c_{mO}$  coincide with one of the roots of the  $M$ -th degree characteristic equation

$$s^M - a_1(n_0)s^{M-1} - \cdots - a_M(n_0) = - \sum_{t=0}^M a_t(n_0)s^{M-t} = 0, \quad (\text{B.12})$$

where  $a_0(n_0) \equiv -1$ . A varying first-order pole  $c_m(n)$  will differ from the characteristic polynomial roots. In order to compute the poles, one should use the recursion (B.10).

Nevertheless, the roots of the characteristic equation play an important role in frequency estimation. For example, initial values could be estimated in a region where the polynomial coefficients are nearly constant. In such region, one would expect that the characteristic equation roots are a reasonable approximation to all first-order poles. In fact, in the frozen-time analysis approach, the roots are taken as the first-order poles, even when the coefficients are not constant.

We analyze the error between the polynomial roots and the first-order poles by first expanding the roots of the characteristic equation in a Taylor series. first-order poles of the form given by eqs.(B.3) through (B.5) are used, as an example, with range variations

given locally (that is,  $r_{n_0-M+1} \leq r \leq r_{n_0}$ ) by

$$k_m(r) = k_{mO} + \beta_m(r - r_{n_0-M+1}) \quad (\text{B.13})$$

and  $\alpha_m = \alpha_{mO}$ .

The region  $r_{n_0-M+1} \leq r \leq r_{n_0}$  corresponds to the sequence  $c_m(n)$  of first-order poles involved when iterating for  $c_m(n_0)$  according to eqs.(B.9) or (B.10). If these poles are the same ( $\beta_m = 0$ ), they coincide with one root of the characteristic polynomial. If there is a small relative change among them, then  $c_m(n_0)$  will differ from that root. Only relative variations in that set will influence the error between  $c_m(n_0)$  and the corresponding root. We expand the roots of the characteristic polynomial in a Taylor series essentially in the neighborhood of  $\beta_m = 0$ .

For simplicity, it is assumed that the modal magnitudes are locally constant, resulting in first-order poles of the form [after integrating eq.(B.13), see eq.(B.3)]

$$c_m(n) = e^{-\alpha_{mO}\Delta r} e^{i[k_{mO}\Delta r + \beta_m(n-n_0+M-3/2)(\Delta r)^2]}. \quad (\text{B.14})$$

An analysis for the two simplest cases,  $M = 2$  and  $M = 3$ , leads to reasonably simple expressions that reveal the issues in approximating the first-order coefficients by the roots of characteristic equation. Higher  $M$  can be dealt with using the same procedure, but the algebraic manipulations and final expression become quickly cumbersome and unrevealing.

### B.3.1 Error for Sums of Two Complex Exponentials

Let  $M = 2$ . Without loss of generality, let us analyze the characteristic polynomial zero corresponding to the first mode,  $m = 1$ . Start with

$$c_{1O} \equiv c_1^{(0)}(n_0) = c_1(n_0 - 1) = e^{-\alpha_{1O}\Delta r} e^{iK_{1O}\Delta r}, \quad (\text{B.15})$$

$$c_{2O} \equiv c_2^{(0)}(n_0) = c_2(n_0 - 1) = e^{-\alpha_{2O}\Delta r} e^{iK_{2O}\Delta r}, \quad (\text{B.16})$$

where, from eq.(B.14),  $K_{mO} = k_{mO} - \beta_m \Delta r/2$ , which is the eigenvalue  $k_m(r_{n_0-3/2})$  at the intermediate point  $(n_0 - 3/2)$ . These initial poles are the roots of the second degree unperturbed equation [cf. eq.(B.12)]

$$s^2 - a_1^{(O)}(n_0)s - a_2^{(O)}(n_0) = 0,$$

where  $a_1^{(O)}(n_0) = c_{1O} + c_{2O}$  and  $a_2^{(O)}(n_0) = -c_{1O}c_{2O}$ . Keep the initial coefficients fixed at  $c_m(n_0 - 1) = c_{mO}$  and let the coefficients  $c_m(n_0)$  change from their unperturbed values according to<sup>1</sup>

$$c_1(n_0) = c_{1O} + \epsilon_{10}, \quad (\text{B.17})$$

$$c_2(n_0) = c_{2O} + \epsilon_{20}, \quad (\text{B.18})$$

From eq.(B.14) with  $n = n_o, M = 2$ , one obtains

$$c_m(n_0) = \exp\{-\alpha_{mO}\Delta r\} \exp\{i(k_{mO}\Delta r + \beta_m(\Delta r)^2/2\}$$

---

<sup>1</sup>In the following development the double subscript notation in the change  $\epsilon_{mj}$  identifies the mode and how far back the affected sample is from  $n_0$ , the most recent in a series. For example,  $\epsilon_{20}$  refers to a perturbation of the first-order pole  $c_2(n_0)$ . The second subscript is irrelevant for  $M = 2$ , [only '0' is used because  $c_m(n_0 - 1)$  is fixed] but is kept for consistence with the general case.

which, when compared to eqs.(B.15) and (B.16), gives the perturbations

$$\epsilon_{m0} = c_{mO} \left( e^{i\beta_m(\Delta r)^2} - 1 \right). \quad (\text{B.19})$$

Assume the new root  $s(c_1(n_0), c_2(n_0))$  can be represented by the Taylor expansion

$$\begin{aligned} s = c_{1O} + (\partial_{10}s)_O \epsilon_{10} + (\partial_{20}s)_O \epsilon_{20} \\ + \frac{1}{2} (\partial_{10}^2 s)_O \epsilon_{10}^2 + \frac{1}{2} (\partial_{20}^2 s)_O \epsilon_{20}^2 + (\partial_{20}\partial_{10}s)_O \epsilon_{10}\epsilon_{20} + \text{H.O.T.}, \end{aligned} \quad (\text{B.20})$$

where  $\partial_{m0} \equiv d/dc_m(n_0)$ , the subscript  $O$  in  $()_O$  indicates derivatives computed at the unperturbed condition, and *H.O.T.* stands for higher order terms.

For the present case  $M = 2$ , the roots have a closed form [omitting the argument  $(n_0)$  for simplicity],

$$s = \frac{a_1 + \sqrt{a_1^2 + 4a_2}}{2}.$$

The actual, perturbed coefficients  $a_1(n)$  and  $a_2(n)$  can be computed exactly from eq.(B.8). The derivatives in the Taylor series could be computed from the above formula for the roots.

A more general approach, one that does not rely on a closed formula for the roots, is to take the derivatives of the characteristic equation (B.12) (which has to be satisfied as the first-order poles change), leading, for  $k, m = 1, 2$ , to

$$\partial_{m0}s = \frac{s\partial_{m0}a_1 + \partial_{m0}a_2}{2s - a_1}, \quad (\text{B.21})$$

$$\partial_{k0}\partial_{m0}s = \frac{(-2\partial_{k0}s + \partial_{k0}a_1)\partial_{m0}s + (\partial_{k0}s)\partial_{m0}a_1 + s\partial_{k0}\partial_{m0}a_1 + \partial_{k0}\partial_{m0}a_2}{2s - a_1}. \quad (\text{B.22})$$

The derivatives of the coefficients  $a_j$  can be obtained directly from eq.(B.8), which,

using eq.(B.9), can be written as

$$\begin{bmatrix} c_1(n_0 - 1) & 1 \\ c_2(n_0 - 1) & 1 \end{bmatrix} \begin{bmatrix} a_1(n_0) \\ a_2(n_0) \end{bmatrix} = \begin{bmatrix} c_1(n_0)c_1(n_0 - 1) \\ c_2(n_0)c_2(n_0 - 1) \end{bmatrix} \quad (\text{B.23})$$

or

$$D_\pi \mathbf{a} = \mathbf{c}_\pi. \quad (\text{B.24})$$

Taking the derivatives of eq.(B.24), considering that  $D_\pi$  is independent of  $c_m(n_0)$ , and assuming  $D_\pi$  to be full rank, one obtains [recall  $\partial_{m0} \equiv d/dc_m(n_0)$ ]

$$\begin{aligned} D_\pi \partial_{m0} \mathbf{a} &= c_m(n_0 - 1) \mathbf{e}_m \\ \Rightarrow \partial_{m0} \mathbf{a} &= \frac{(-1)^m}{c_1(n_0 - 1) - c_2(n_0 - 1)} \begin{bmatrix} -1 \\ c_m(n_0 - 1) \end{bmatrix}, \end{aligned} \quad (\text{B.25})$$

where  $\mathbf{e}_m$  is the unit vector with one at position  $m$ :  $\mathbf{e}_1 = [1, 0]^T$ ,  $\mathbf{e}_2 = [0, 1]^T$ . Finally, the derivative  $\partial_{m0} \mathbf{a}$  is independent of all  $c_j(n_0)$ , leading, for all  $k$  and  $m$ , to

$$D_\pi \partial_{k0} \partial_{m0} \mathbf{a} = 0 \Rightarrow \partial_{k0} \partial_{m0} \mathbf{a} = 0. \quad (\text{B.26})$$

At the initial point  $O \equiv (c_{1O}, c_{2O})$ ,  $s = c_{1O}$  and eqs.(B.21), (B.22), (B.25), and (B.26) give the only non-zero derivatives (up to second order) as

$$\begin{aligned} (\partial_{10} s)_O &= \frac{c_{1O}}{c_{1O} - c_{2O}}, \\ (\partial_{10} \partial_{20} s)_O &= \frac{-c_{1O} c_{2O}}{(c_{1O} - c_{2O})^3}. \end{aligned}$$

Substituting these expressions into the Taylor series, eq.(B.20), and using  $c_1(n_0) = c_{1O} + \epsilon_{10}$ , the error in estimating the first-order pole  $c_1(n_0)$  as the root of the characteristic

equation is given by

$$\Delta c_1 = s - c_1(n_0) = \frac{c_{2O}}{c_{1O} - c_{2O}} \epsilon_{10} - \frac{c_{1O}c_{2O}}{(c_{1O} - c_{2O})^3} \epsilon_{10}\epsilon_{20} + H.O.T. \quad (B.27)$$

This equation indicates that the ratios  $\epsilon/\Delta c$  between the change in the first-order poles and the initial pole distance are significant parameters in the root-pole approximation, an intuitive result.

When both changes  $\epsilon_{10}$  and  $\epsilon_{20}$  are small, the error magnitude is obtained by substituting the expressions for the poles  $c_{mO}$  and perturbations  $\epsilon$ , eqs.(B.15), (B.16), and (B.19), into eq.(B.27), and retaining only the first term<sup>2</sup>:

$$\begin{aligned} |\Delta c_1| &\sim \frac{|\epsilon_{10}|}{|c_{1O}/c_{2O} - 1|} \\ &\sim \frac{e^{-\alpha_{1O}\Delta r} \sqrt{2 - 2 \cos [\beta_1 (\Delta r)^2]}}{\sqrt{1 - 2e^{-(\alpha_{1O} - \alpha_{2O})\Delta r} \cos [(K_{1O} - K_{2O}) \Delta r] + e^{-2(\alpha_{1O} - \alpha_{2O})\Delta r}}}. \end{aligned} \quad (B.28)$$

This expression clearly indicates that, if  $\Delta r$  and the remaining parameters are fixed, the error is minimized when  $(K_{1O} - K_{2O}) \Delta r = \pi$ , in which case the denominator reduces to  $1 + e^{-(\alpha_{1O} - \alpha_{2O})\Delta r} \sim 1$ , and  $\Delta c_1 \sim |\epsilon_{10}|$ . This is the farthest the initial poles can be when close to the unit circle (or restricted to any finite region of the complex plane, for that matter) and leads to the smallest error magnitude, which is that of the perturbation itself.

As the sampling distance  $\Delta r$  decreases, the initial poles become closer, which would tend to increase the error, but the perturbations  $\epsilon$  themselves decrease. To the first-order in  $\Delta r$ , the magnitude of the error, now including both the  $\epsilon_{10}$  and  $\epsilon_{10}\epsilon_{20}$  terms, is given, after expanding eq.(B.27) and using eqs. (B.15) , (B.16), and (B.19), by

$$|\Delta c_1| \sim \sqrt{\frac{\beta_2^2}{(K_{1O} - K_{2O})^4} + 4 \frac{\beta_2}{(K_{1O} - K_{2O})^2} \frac{\alpha_{1O} - \alpha_{2O}}{K_{1O} - K_{2O}} + 1} \frac{|\beta_1| \Delta r}{|K_{1O} - K_{2O}|}, \quad (B.29)$$

---

<sup>2</sup>At this approximation level,  $K_{mO} = k_{mO}$ , the eigenvalue at  $r_{n_0-1}$ .

where the absorption coefficients  $\alpha$ 's are neglected compared to the corresponding  $K$ 's. It becomes apparent that the significant parameter is the ratio between the change in eigenvalue  $|\beta_1|(\Delta r)^2$  (a measure of  $\epsilon_{10}$ ) and the poles initial angular "distance",  $|K_{1O} - K_{2O}| \Delta r$ . The influence of the "other" eigenvalue rate of change amounts to a typically small correction factor to  $\Delta c_1$ .

### B.3.2 Taylor Expansion of the Roots - General Case

Before proceeding with the  $M = 3$  case, let us generalize the expressions for the derivatives of roots and polynomial coefficients with respect to the first-order poles. As before, the first poles  $c_m(n_0 - M + 1)$  are kept constant at  $c_{mO}$  and the remaining poles  $\{c_m(n_0 - M + 2), \dots, c_m(n_0)\}$  [for a total of  $M(M - 1)$  variables] are allowed to change from the initial value  $c_{mO}$  to  $c_m(n_0 - k) = c_{mO} + \epsilon_{mk}$ .

The general form of the Taylor expansion of the root [again, expanding the root corresponding to  $c_{1O}$  without loss of generality] is given by

$$s = c_{1O} + [(\epsilon_{1,M-2}\partial_{1,M-2} + \dots + \epsilon_{M0}\partial_{M0})s]_O + \frac{1}{2!} [(\epsilon_{1,M-2}\partial_{1,M-2} + \dots + \epsilon_{M0}\partial_{M0})^2 s]_O + H.O.T. \quad (B.30)$$

From the assumed locally linear eigenvalue variation in eq.(B.14), the perturbation of the first-order poles are given, for  $k = 0, \dots, M - 2$ , by

$$\begin{aligned} \epsilon_{mk} &= c_m(n_0 - k) - c_{mO} \\ &= c_m(n_0 - k) - c_m(n_0 - M + 1) = c_{mO} \left( e^{i\beta_m(M-k-1)(\Delta r)^2} - 1 \right) \end{aligned} \quad (B.31)$$

As in the  $M = 2$  case, the derivatives are obtained directly from the characteristic

equation (B.12), for  $k, m = 1, \dots, M$  and  $j, l = 0, \dots, M-2$ , as

$$\partial_{ml}s = \frac{\sum_{t=1}^M s^{M-t} \partial_{ml}a_t}{-\sum_{t=0}^{M-1} (M-t)s^{M-t-1}a_t}, \quad (\text{B.32})$$

$$\begin{aligned} \partial_{kj}\partial_{ml}s = & \left\{ (\partial_{ml}s) \left[ (\partial_{kj}s) \sum_{t=0}^{M-2} (M-t)(M-t-1)s^{M-t-2}a_t + \right. \right. \\ & \left. \sum_{t=1}^{M-1} (M-t)s^{M-t-1}\partial_{kj}a_t \right] + (\partial_{kj}s) \sum_{t=1}^{M-1} (M-t)s^{M-t-1}\partial_{ml}a_t + \\ & \left. \left. \sum_{t=1}^M s^{M-t}\partial_{kj}\partial_{ml}a_t \right] \right\} \frac{1}{-\sum_{t=0}^{M-1} (M-t)s^{M-t-1}a_t}, \quad (\text{B.33}) \end{aligned}$$

which reduces, for  $M = 2$ , to eqs.(B.21) and (B.22).

The generalization of the eq.(B.23) for the vector of coefficients  $\mathbf{a}$  is, again from eq.(B.9) [cf. eq.(B.8)],

$$D_\pi \mathbf{a} = \mathbf{c}_\pi, \quad (\text{B.34})$$

with

$$(D_\pi)_{m,j} = \begin{cases} \prod_{t=j}^{M-1} c_m(n-t), & j = 1, \dots, M-1, \\ 1, & j = M, \end{cases} \quad (\text{B.35})$$

and

$$(\mathbf{c}_\pi)_m = \prod_{t=0}^{M-1} c_m(n-j). \quad (\text{B.36})$$

Taking the derivatives of eq.(B.34) one obtains

$$\begin{aligned} D_\pi \partial_{ml} \mathbf{a} &= -(\partial_{ml} D_\pi) \mathbf{a} + \partial_{ml} \mathbf{c}_\pi, \\ &= \left[ -(1 - \delta_{l,0}) \sum_{t=1}^l a_t \prod_{i=t, i \neq l}^{M-1} c_m(n-i) + \prod_{i=0, i \neq l}^{M-1} c_m(n-i) \right] \mathbf{e}_m, \quad (\text{B.37}) \end{aligned}$$

$$\begin{aligned}
D_\pi \partial_{kj} \partial_{ml} \mathbf{a} &= -(\partial_{kj} \partial_{ml} D_\pi) \mathbf{a} - (\partial_{kj} D_\pi) \partial_{ml} \mathbf{a} - (\partial_{ml} D_\pi) \partial_{kj} \mathbf{a} + \partial_{kj} \partial_{ml} \mathbf{c}_\pi, \\
&= - \left[ \delta_{k,m} (1 - \delta_{l,j}) (1 - \delta_{j,0}) (1 - \delta_{l,0}) \sum_{t=1}^{\min(j,l)} a_t \prod_{i=t, i \neq j, l}^{M-1} c_m(n-i) \right] \mathbf{e}_m \\
&\quad - \left[ (1 - \delta_{j,0}) \sum_{t=1}^j (\partial_{ml} a_t) \prod_{i=t, i \neq j}^{M-1} c_k(n-i) \right] \mathbf{e}_k \\
&\quad + \left[ -(1 - \delta_{l,0}) \sum_{t=1}^l (\partial_{kj} a_t) \prod_{i=t, i \neq l}^{M-1} c_m(n-i) + \delta_{k,m} (1 - \delta_{j,l}) \prod_{i=0, i \neq j, l}^{M-1} c_m(n-i) \right] \mathbf{e}_m, \quad (\text{B.38})
\end{aligned}$$

where  $\delta_{n,m}$  is the Kronecker delta,

$$\delta_{n,m} = \begin{cases} 1, & n = m, \\ 0, & n \neq m, \end{cases}$$

and  $\mathbf{e}_m$  is the unit vector with one at position  $m$ :  $\mathbf{e}_m = [\delta_{m,1}, \dots, \delta_{m,M}]^T$ . The computation of the derivatives involve the solution of the linear systems in eqs.(B.37) and (B.38), which is simplified by noting that  $D_\pi^{-1} \mathbf{e}_j = (D_\pi^{-1})_{\text{column } j}$ .

At the initial point  $O \equiv (c_{1O}, \dots, c_{MO})$ ,  $s = c_{1O}$ , eqs.(B.32) and (B.33) reduce to<sup>3</sup>

$$(\partial_{ml} s)_O = \delta_{1,m} \frac{\sum_{t=l+1}^M a_t^{(O)} c_{mO}^{M-t-1}}{\prod_{t=2}^M (c_{1O} - c_{tO})}, \quad (\text{B.39})$$

$$\begin{aligned}
(\partial_{kj} \partial_{ml} s)_O &= \left\{ \delta_{1,m} (\partial_{ml} s)_O \left[ \delta_{1,k} (\partial_{kj} s)_O \sum_{t=0}^{M-2} (M-t)(M-t-1) c_{1O}^{M-t-2} a_t^{(O)} + \right. \right. \\
&\quad \left. \sum_{t=1}^{M-1} (M-t) c_{1O}^{M-t-1} (\partial_{kj} a_t)_O \right] + \delta_{1,k} (\partial_{kj} s)_O \sum_{t=1}^{M-1} (M-t) c_{1O}^{M-t-1} (\partial_{ml} a_t)_O + \\
&\quad \left. \left. \sum_{t=1}^M c_{1O}^{M-t} (\partial_{kj} \partial_{ml} a_t)_O \right\} \frac{1}{\prod_{t=2}^M (c_{1O} - c_{tO})} \right\}, \quad (\text{B.40})
\end{aligned}$$

---

<sup>3</sup>Notice that the influence of the difference (distance) between  $c_{1O}$  and the others poles in the initial configuration, as observed in the  $M = 2$  case, is also manifested explicitly in the computation of the derivatives in the general case.

and eqs.(B.37) and (B.38) reduce to

$$\begin{aligned} D_\pi^{(O)} (\partial_{ml} \mathbf{a})_O &= \left[ -(1 - \delta_{l,0}) \sum_{t=1}^l a_t^{(O)} c_{mO}^{M-t-1} + c_{mO}^{M-1} \right] \mathbf{e}_m \\ &= \mathbf{e}_m \frac{1}{c_{mO}} \sum_{t=l+1}^M a_t^{(O)} c_{mO}^{M-t}, \end{aligned} \quad (\text{B.41})$$

$$\begin{aligned} D_\pi^{(O)} (\partial_{kj} \partial_{ml} \mathbf{a})_O &= - \left[ \delta_{k,m} (1 - \delta_{l,j}) (1 - \delta_{j,0}) (1 - \delta_{l,0}) \sum_{t=1}^{\min(j,l)} a_t^{(O)} c_{mO}^{M-t-2} \right] \mathbf{e}_m \\ &\quad - \left[ (1 - \delta_{j,0}) \sum_{t=1}^j (\partial_{ml} a_t)_O c_{kO}^{M-t-1} \right] \mathbf{e}_k \\ &\quad - \left[ (1 - \delta_{l,0}) \sum_{t=1}^l (\partial_{kj} a_t)_O c_{mO}^{M-t-1} \right] \mathbf{e}_m + \mathbf{e}_m \delta_{k,m} (1 - \delta_{j,l}) c_{mO}^{M-2}. \end{aligned} \quad (\text{B.42})$$

### B.3.3 Error for Sums of Three Complex Exponentials

For  $M = 3$ , substituting  $c_1(n_0) = c_{1O} + \epsilon_{10}$  and the derivatives given in eqs.(B.39) to (B.42) into the Taylor expansion (B.30), one obtains [cf. eq.(B.27)]

$$\begin{aligned} \Delta c_1 = s - c_1(n_0) &= \frac{1}{(c_{1O} - c_{2O})(c_{1O} - c_{3O})} \left\{ -(c_{2O} + c_{3O})c_{1O}\epsilon_{11} \right. \\ &\quad + [(c_{2O} + c_{3O})c_{1O} - c_{2O}c_{3O}] \epsilon_{10} + \frac{(c_{2O} + c_{3O})c_{1O}^2\epsilon_{11}^2 - [(c_{2O} + c_{3O})c_{1O} - c_{2O}c_{3O}] c_{1O}\epsilon_{11}\epsilon_{10}}{(c_{1O} - c_{2O})(c_{1O} - c_{3O})} \\ &\quad + \frac{c_{1O}\epsilon_{11}}{(c_{2O} - c_{3O})} \left[ \frac{(c_{1O} + c_{3O})c_{2O}}{(c_{1O} - c_{2O})^2} [-(c_{1O} + c_{3O})\epsilon_{21} + c_{2O}\epsilon_{20}] \right. \\ &\quad \left. + \frac{(c_{1O} + c_{2O})c_{3O}}{(c_{1O} - c_{3O})^2} [(c_{1O} + c_{2O})\epsilon_{31} - c_{3O}\epsilon_{30}] \right] \\ &\quad + \frac{c_{1O}^2\epsilon_{10}}{(c_{2O} - c_{3O})} \left[ \frac{c_{2O}}{(c_{1O} - c_{2O})^2} [(c_{1O} + c_{3O})\epsilon_{21} - c_{2O}\epsilon_{20}] \right. \\ &\quad \left. \left. + \frac{c_{3O}}{(c_{1O} - c_{3O})^2} [-(c_{1O} + c_{2O})\epsilon_{31} + c_{3O}\epsilon_{30}] \right] + H.O.T. \right\}. \end{aligned} \quad (\text{B.43})$$

Substituting the expressions for the perturbations  $\epsilon_{mk}$ , eq.(B.31) with  $M = 3$ , in

the above expression, and expanding  $|\Delta c_1|$  in terms of  $\Delta r$  (including the first-order terms  $\epsilon_{10}$  and  $\epsilon_{11}$ ), one obtains [neglecting the absorption coefficients  $\alpha$ 's relative to the eigenvalues  $K$ 's], for small  $\Delta r$ ,

$$|\Delta c_1| \sim \frac{|(K_{2O} - K_{1O}) + (K_{3O} - K_{1O})||\beta_1|\Delta r}{|K_{1O} - K_{2O}||K_{1O} - K_{3O}|}. \quad (\text{B.44})$$

Compared to eq.(B.29), the relevant parameter is also the ratio between the change of the eigenvalue and the pole angular distances. Here the relative position of the poles also play a role [through the term  $(K_{2O} - K_{1O}) + (K_{3O} - K_{1O})$  in the numerator]. The correction factor due to the rate of change of the other poles [such as  $\beta_2$  in eq.(B.29)] is not included in eq.(B.44) because only the first-order terms (in  $\epsilon_{10}$  and  $\epsilon_{11}$ ) of  $\Delta c_1$  were included in the expansion in  $\Delta r$ .

## Appendix C

# The VFF Adaptive Zero Estimator Design

### C.1 Basic Design

The design of the adaptive filter follows the design of a general class of algorithms proposed by Ljung[44]. In the present application, the parameter to be estimated is the vector formed by the magnitude and phase of the zeros of the characteristic polynomial,  $\theta = [\rho_1, \dots, \rho_p, \Omega_1, \dots, \Omega_p]^T$ , where the zeros are given by  $s_j = \rho_j \exp i\Omega_j$ ,  $j = 1, \dots, p$ . For a given  $\theta(n-1)$ , the polynomial coefficients  $\mathbf{a}(\theta(n-1))$  are computed. The estimation error is given by

$$\epsilon(n, \theta) = y(n) - \hat{y}(n, \theta) = y(n) - \varphi^T(n) \mathbf{a}(\theta). \quad (\text{C.1})$$

The estimator must minimize the mean square prediction error  $\bar{V}(n, \theta) = E \{|\epsilon(n, \theta)|^2\}$ . Instead of minimizing directly this measure, solve  $\partial \bar{V}(\theta) / \partial \theta = 0$ . Using eq.(C.1), the equation to solve is  $E \{ \Re [-\psi^T(n, \theta) \epsilon^*(n, \theta)] \} = 0$ , where  $\psi^T = \partial \hat{y} / \partial \theta = -\partial \epsilon / \partial \theta$  ( $\psi$  is

a  $2p \times 1$  vector). The recursive solution of this equation is given by [44, p. 93]:

$$\widehat{\theta}(n) = \widehat{\theta}(n-1) + \gamma(n) \Re \left[ \psi \left( n, \widehat{\theta}(n-1) \right) \epsilon^* \left( n, \widehat{\theta}(n-1) \right) \right],$$

where, for a constant parameter vector  $\theta$ ,  $\gamma(n)$  is a sequence of positive scalars tending to zero. [44] proposes to use the Newton direction, for which the gradient is multiplied by an estimate of the inverse of the second derivative of  $\bar{V}(\theta)$ , whose approximation

$$R(n) = \sum_{k=1}^n \beta(n, k) \Re \left[ \psi \left( k, \widehat{\theta}(k-1) \right) \psi^H \left( k, \widehat{\theta}(k-1) \right) \right], \quad (\text{C.2})$$

is valid for slowly varying  $\widehat{\theta}(n)$ . This matrix and, more important, its inverse can be computed recursively for the particular choice of weighting coefficients

$$\beta(n, k) = \begin{cases} \gamma(k) \prod_{j=k+1}^n [1 - \gamma(j)], & k < n, \\ \gamma(n), & k = n, \end{cases} \quad (\text{C.3})$$

with  $\gamma(1) = 1$ . The resulting expressions are

$$R(n) = [1 - \gamma(n)] R(n-1) + \gamma(n) \Re \left[ \psi \left( n, \widehat{\theta}(n-1) \right) \psi^H \left( n, \widehat{\theta}(n-1) \right) \right] \quad (\text{C.4})$$

and, after applying the matrix inverse lemma[32] twice,

$$R^{-1}(n) = A^{-1} - \frac{\gamma(n)}{2} \frac{A^{-1} \psi^* \left( n, \widehat{\theta}(n-1) \right) \psi^T \left( n, \widehat{\theta}(n-1) \right) A^{-1}}{1 + \frac{\gamma(n)}{2} \psi^T \left( n, \widehat{\theta}(n-1) \right) A^{-1} \psi^* \left( n, \widehat{\theta}(n-1) \right)}, \quad (\text{C.5})$$

where

$$A^{-1} = \left[ R^{-1}(n-1) - \frac{1}{2} \frac{R^{-1}(n-1)\psi(n, \hat{\theta}(n-1))\psi^H(n, \hat{\theta}(n-1))R^{-1}(n-1)}{\frac{1-\gamma(n)}{\gamma(n)} + \frac{1}{2}\psi^H(n, \hat{\theta}(n-1))R^{-1}(n-1)\psi(n, \hat{\theta}(n-1))} \right] / [1 - \gamma(n)]. \quad (\text{C.6})$$

The final recursive solution is, therefore,

$$\hat{\theta}(n) = \hat{\theta}(n-1) + \gamma(n)R^{-1}(n)\Re\left[\psi(n, \hat{\theta}(n-1))\epsilon^*(n)\right], \quad (\text{C.7})$$

where the prediction error is given by

$$\epsilon(n) = y(n) - \mathbf{a}^T(\hat{\theta}(n-1))\varphi(n). \quad (\text{C.8})$$

Equations (C.5), (C.6), (C.7), and (C.8) form the adaptive zero estimator. These equations correspond to the algorithm described in Table I of [48] using  $P(n) = \gamma(n)R^{-1}(n)$ ,  $L = \gamma(n)A^{-1}(n)$ , and  $w(n) = 1 - \gamma(n)$ . The algorithm proposed in [48] uses an exact expression for the derivative  $\psi$ , which is derived below. The forgetting factor  $w(n)$  used in the present estimator is data adaptive, as proposed in [16].

## C.2 Error Gradient

The expressions for the error gradient vector are obtained following the procedure in [48]. From eq.(C.1),

$$-\psi(n, \theta) = \left[ \frac{\partial \epsilon(n, \theta)}{\partial \theta} \right]^T = -\frac{\partial \mathbf{a}^T(n, \theta)}{\partial \theta} \varphi(n) = -\begin{bmatrix} \frac{\partial \mathbf{a}^T}{\partial \rho_1} \\ \vdots \\ \frac{\partial \mathbf{a}^T}{\partial \rho_p} \\ \frac{\partial \mathbf{a}^T}{\partial \Omega_1} \\ \vdots \\ \frac{\partial \mathbf{a}^T}{\partial \Omega_p} \end{bmatrix} \varphi(n), \quad (\text{C.9})$$

where, for convenience, the arguments of  $\mathbf{a}$  were dropped in the last term. The derivatives of the coefficient vector can be obtained by using the two representations of the characteristic polynomial:

$$A(s^{-1}) = - \sum_{j=0}^p a_j s^{-j} = \prod_{j=1}^p (1 - s^{-1} \rho_j \exp\{i\Omega_j\}), \quad (\text{C.10})$$

where  $a_0 = -1$ , and it is assumed that the roots are distinct and do not form conjugate pairs. The derivatives w.r.t. the root magnitudes are given by

$$\frac{\partial A}{\partial \rho_k} = - \sum_{j=0}^p \frac{\partial a_j}{\partial \rho_k} s^{-j} = -s^{-1} \exp\{i\Omega_k\} \prod_{j=1, j \neq k}^p (1 - s^{-1} \rho_j \exp\{i\Omega_j\}).$$

Multiply the above expression by the missing factor  $(1 - s^{-1} \rho_k \exp\{i\Omega_k\})$  and substitute eq.(C.10) to obtain

$$-(1 - s^{-1} \rho_k \exp\{i\Omega_k\}) \sum_{j=0}^p \frac{\partial a_j}{\partial \rho_k} s^{-j} = s^{-1} \exp\{i\Omega_k\} \sum_{j=0}^p a_j s^{-j},$$

from which, after some trivial algebraic manipulation, follows the recursion

$$\sum_{j=0}^p \frac{\partial a_j}{\partial \rho_k} s^{-j} = -\exp\{i\omega_k\} \sum_{j=0}^p a_j s^{-j-1} + \rho_k \exp\{i\omega_k\} \sum_{j=0}^p \frac{\partial a_j}{\partial \rho_k} s^{-j-1}, \quad (\text{C.11})$$

or, explicitly,

$$\begin{cases} a_0 = -1, & \partial a_0 / \partial \rho_k = 0, \\ \partial a_j / \partial \rho_k = \exp\{i\Omega_k\} (-a_{j-1} + \rho_k \partial a_{j-1} / \partial \rho_k), & j = 1, \dots, p. \end{cases} \quad (\text{C.12})$$

The same procedure leads to the recursion for the derivatives w.r.t. the root phases,

$\Omega_k$ :

$$\begin{aligned}
\frac{\partial A}{\partial \Omega_k} &= - \sum_{j=0}^p \frac{\partial a_j}{\partial \Omega_k} s^{-j} = -i\rho_k \exp\{i\Omega_k\} s^{-1} \prod_{j=1, j \neq k}^p (1 - s^{-1} \rho_j \exp\{i\Omega_j\}), \\
& - (1 - s^{-1} \rho_k \exp\{i\Omega_k\}) \sum_{j=0}^p \frac{\partial a_j}{\partial \Omega_k} s^{-j} = i\rho_k \exp\{i\Omega_k\} s^{-1} \sum_{j=0}^p a_j s^{-j}, \\
\sum_{j=0}^p \frac{\partial a_j}{\partial \Omega_k} s^{-j} &= -i\rho_k \exp\{i\Omega_k\} \sum_{j=0}^p a_j s^{-j-1} + \rho_k \exp\{i\Omega_k\} \sum_{j=0}^p \frac{\partial a_j}{\partial \Omega_k} s^{-j-1}, \quad (C.13)
\end{aligned}$$

$$\begin{cases} a_0 = -1, & \partial a_0 / \partial \Omega_k = 0, \\ \partial a_j / \partial \Omega_k = \rho_k \exp\{i\Omega_k\} (-ia_{j-1} + \partial a_{j-1} / \partial \rho_k), & j = 1, \dots, p. \end{cases} \quad (C.14)$$

Equations (C.9), (C.12), and (C.14) are the analytical expressions to be used in the adaptive algorithm, eqs.(C.5) to (C.8), to evaluate the error gradient at range step  $n$  with  $\theta = \widehat{\theta}(n-1)$ .

### C.3 The Variable Forgetting Factor (VFF)

The forgetting factor  $w(n) = 1 - \gamma(n)$  [ $0 < w(n) \leq 1$ ] in eqs.(C.5) and (C.6), controls the speed of convergence of the adaptive estimator. As shown eq.(C.4), it controls the weight of past data on the update of the matrix  $R$ , and, through eq.(C.7), the influence of past data on the parameter update. In the original adaptive zero estimator[48], the forgetting factor  $w(n)$  is variable, computed through a fixed rule, function of two parameters,  $[w_0, w_\infty]$ , and an initial value  $w(1)$ , as  $w(n) = w_\infty - [w_\infty - w(n-1)] w_0$ . These forgetting factor parameters must be chosen to match the expected evolution of the parameter to be estimated,  $\theta(n)$ .

Fortescue and co-workers[16] introduced a self-tuning estimator, where the forgetting factor is updated at each step as a function of the square prediction error, becoming data-adaptive. For high signal-to-noise ratio signals, the strategy is to have a forgetting factor

close to one (use most past information) when the signal statistics, as indicated by a low prediction error, is stationary, improving the estimator variance. When the prediction error increases due to changes in signal parameters, the forgetting factor should decrease (use mostly new information), allowing the estimator to adapt quickly to the changing statistics. The algorithm assumes that the measurement noise statistics do not change.

The measure of information content in [16] is the weighted sum of squares of the *a posteriori* errors

$$\tilde{\epsilon}(n) = y(n) - \mathbf{a}^T(\widehat{\theta}(n)) \varphi(n) \quad (\text{C.15})$$

[compare with the prediction error, eq.(C.8)], given by

$$\begin{aligned} J(n) &= \sum_{k=1}^n \tilde{\beta}(n, k) |\tilde{\epsilon}(k)|^2, \\ &= \sum_{k=1}^n \tilde{\beta}(n, k) \left| y(k) - \mathbf{a}^T(\widehat{\theta}(k)) \varphi(k) \right|^2, \\ &= \sum_{k=1}^n \tilde{\beta}(n, k) \left| y(k) - \left[ \mathbf{a}^T(\widehat{\theta}(k-1)) + \Delta \mathbf{a}^T(k) \right] \varphi(k) \right|^2, \\ &= \sum_{k=1}^n \tilde{\beta}(n, k) |\epsilon(k) - \Delta \mathbf{a}^T(k) \varphi(k)|^2, \end{aligned} \quad (\text{C.16})$$

where, in the last step, eq.(C.8) was used,

$$\tilde{\beta}(n, k) = \begin{cases} \prod_{j=k+1}^n w(j), & k < n, \\ 1, & k = n, \end{cases} \quad (\text{C.17})$$

and  $\Delta \mathbf{a}^T(k) = \mathbf{a}^T(k) - \mathbf{a}^T(k-1)$ . Substitute eq.(C.17) into (C.16) to obtain the recursion relation

$$J(n) = w(n) J(n-1) + |\epsilon(n) - \Delta \mathbf{a}^T(n) \varphi(n)|^2.$$

At step  $n$ , when the forgetting factor  $w(n)$  is needed, the new coefficient vector  $\mathbf{a}^T(n)$  is

not known. Use, instead, the *a posteriori* error from the previous step,

$$J(n) \simeq w(n)J(n-1) + |\epsilon(n-1) - \Delta \mathbf{a}^T(n-1)\varphi(n-1)|^2. \quad (\text{C.18})$$

In order to maintain a constant *amount of information* at each step, require that  $J(n) = J(n-1) = \dots = J_0$ , resulting, from eq.(C.18), in the VFF

$$w(n) = 1 - |\epsilon(n-1) - \Delta \mathbf{a}^T(n-1)\varphi(n-1)|^2 / J_0. \quad (\text{C.19})$$

For a constant forgetting factor  $w$ , the effective number of past samples used by the estimator is  $N_{eff} = 1/(1-w)$ . In the case of the VFF,

$$N_{eff}(n) = 1/[1-w(n)] = J_0 / |\epsilon(n-1) - \Delta \mathbf{a}^T(n-1)\varphi(n-1)|^2 \quad (\text{C.20})$$

can be interpreted as an asymptotic memory length if  $w = w(n)$  were used during the operation of the estimator[16]. If the process were stationary, then  $\Delta \mathbf{a} \rightarrow 0$ ,  $E\{|\epsilon|^2\} \rightarrow \sigma_v^2$  as  $n \rightarrow \infty$ , where  $\sigma_v^2$  is the measurement noise variance, and eq.(C.20) indicates that a choice for the effective memory length would be  $N_0 = J_0/\sigma_v^2$ . This is the rule used in [16] for choosing the parameter  $J_0$ , using an estimated measurement noise variance and an initial  $N_0$  based on a desired speed of adaptation:

$$J_0 = \sigma_v^2 N_0. \quad (\text{C.21})$$

## Appendix D

### The Second Order Kalman Filter

When the AR coefficients tend to change continuously with range, the competition between the first-order Kalman filter described in Algorithm 1 tends to have large variance. For example, if a coefficient is increasing linearly with range, the forward filter tends to lag the actual value variations, while the backward filter tends to lead them, as shown in Fig. D-1. The error of the two estimators is comparable and the competition result tends to switch between the two, resulting in a large estimate variance.

To counter this effect, [51] suggests introducing a higher order Kalman filter in the competition, which tends to win when the coefficients are changing continuously. The estimate from a forward second order Kalman filter is also shown in Fig. D-1, for comparison. The filter order is given by the state equation. The first-order state equation, eq.(3.51), is equivalent to  $\Delta \mathbf{a}(n) = \mathbf{a}(n) - \mathbf{a}(n - 1) = \mathbf{w}(n)$ . The generalization for a  $k$ -th order filter is

$$\Delta^k \mathbf{a}(n) = \mathbf{w}^{(k)}(n), \quad (\text{D.1})$$

where  $\mathbf{w}^{(k)}$  is a  $p \times 1$  white Gaussian noise vector, as before. A first-order equation describes a system whose parameters are locally constant (difference between adjacent steps state is a zero mean white noise). A second order describes a system whose parameter variation is locally linear (with respect to the step number). Expanding the

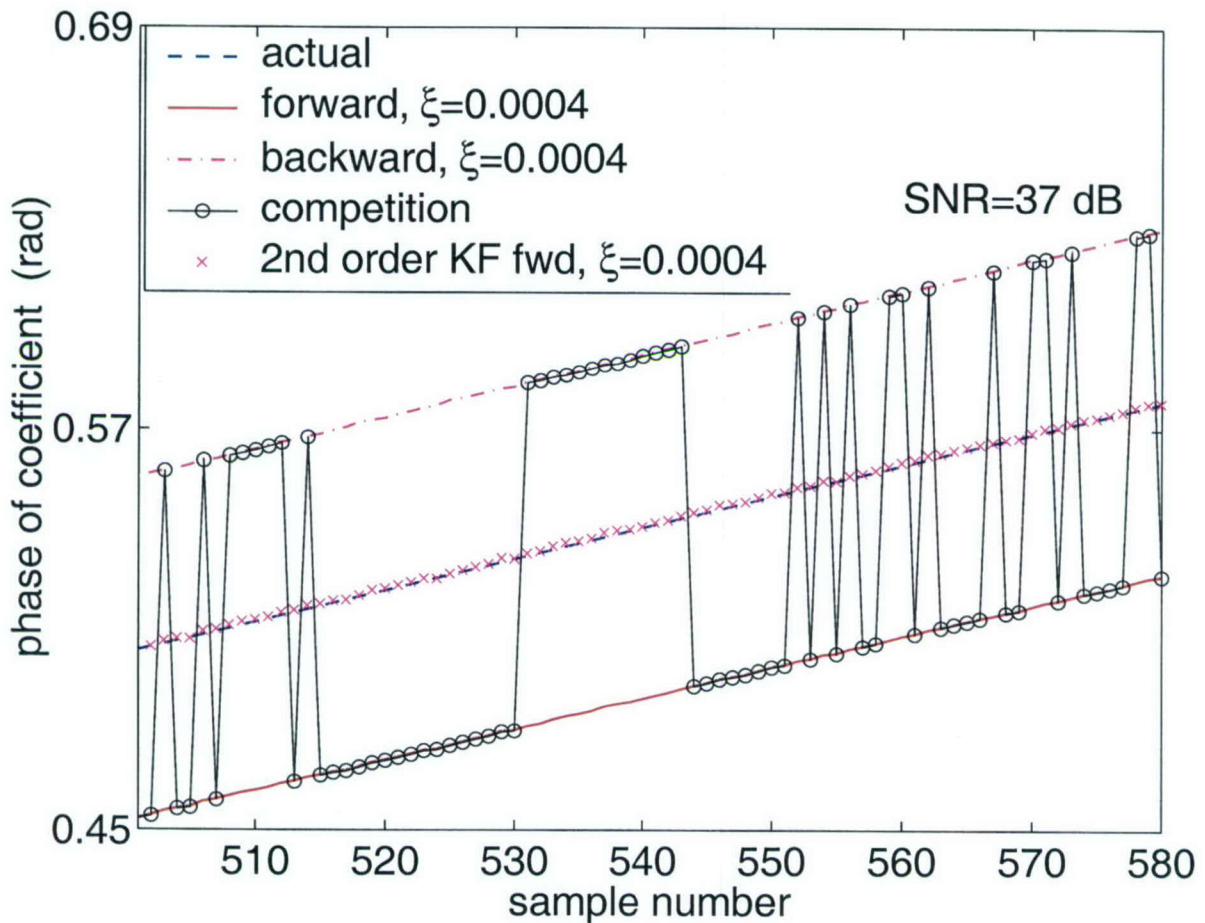


Figure D-1: *Switching noise caused by a continuously varying parameter.* The competition between forward and backward Kalman identifiers tends to introduce jitter in the estimate. In this example, a linear frequency modulated signal (LFM chirp) is modeled as a order one AR process. The plots show estimates of the AR coefficient phase, from which the instantaneous frequency is computed. The forward Kalman estimate (lower, solid line) tends to lag the actual AR coefficient by nearly the same amount as the backward (upper, dash-dot line) tends to lead it. The competition is 'won' alternatively by each estimate, resulting in the jagged line shown (solid line with circles). For comparison, the figure shows the estimate by a single forward, second-order Kalman identifier (symbol 'x' close to the actual value, the center dashed line) which, if included in the competition, would have won.

state equation (D.1), one obtains[51]

$$\underbrace{\begin{bmatrix} \mathbf{a}(n) \\ \vdots \\ \mathbf{a}(n-(k-1)) \end{bmatrix}}_{A^{(k)}(n)} = \underbrace{\begin{bmatrix} -f_1 I_p & -f_2 I_p & \cdots & -f_k I_p \\ I_p & 0 & & 0 \\ 0 & I_p & & 0 \\ \vdots & & & \\ 0 & 0 & & 0 \end{bmatrix}}_F \underbrace{\begin{bmatrix} \mathbf{a}(n-1) \\ \vdots \\ \mathbf{a}(n-k) \end{bmatrix}}_{A^{(k)}(n-1)} + \underbrace{\begin{bmatrix} I_p \\ 0 \\ \vdots \\ 0 \end{bmatrix}}_G \mathbf{w}^{(k)}(n), \quad (\text{D.2})$$

where

$$f_m = (-1)^m \begin{pmatrix} k \\ m \end{pmatrix} = (-1)^k f_{k-m}, \quad (\text{D.3})$$

and the zeros are matrices of appropriate size. The  $k$ -th order Kalman filter can be implemented, therefore, by using the augmented vector  $A^{(k)}$  as the quantity to be estimated, where the state equation is given by eq.(D.2), the measurement equation is given by

$$y(n) = A^{(k)T}(n) \Phi(n) + v(n),$$

and  $\Phi(n) = [y(n-1), \dots, y(n-p), 0, \dots, 0]^T$ . The desired estimate  $\hat{\mathbf{a}}(n)$  can be recovered by the simple operation  $\hat{\mathbf{a}}(n) = [I_p \ 0 \ \cdots \ 0]^T \hat{A}^{(k)}(n) = G^T \hat{A}^{(k)}(n)$ . The second-order Kalman identifier is described in Algorithm 4. The matrices  $V^\oplus(n/n \oplus 1)$  and  $V^\oplus(n/n)$  have definitions analogous to eqs.(3.55) and (3.56), and

$$A^\oplus(n) = \begin{bmatrix} \mathbf{a}^\oplus(n) \\ \mathbf{a}^\oplus(n \oplus 1) \end{bmatrix}.$$

---

**Algorithm 4** *Forward and Backward second-order Kalman AR identifier.* Initialize the forward filter with values  $A^-(p/p)$  and  $V^-(p/p)$ , and estimate the coefficients for  $n = p + 1, \dots, N$ . Initialize the backward filter with values  $\hat{A}^+(N + 1/N + 1)$  and  $V^-(N + 1/N + 1)$ , and estimate the coefficients for  $n = N, N - 1, \dots, p + 1$ . The only parameter in this implementation is  $\xi$ , which controls the speed of convergence, as in the first-order identifier.

---

1. Prediction

$$\begin{aligned}\Phi(n) &= [ y(n-1), \dots, y(n-p), 0, \dots, 0 ], \\ \hat{A}^\oplus(n/n \oplus 1) &= F \hat{A}^\oplus(n \oplus 1/n \oplus 1), \\ \epsilon^\oplus(n) &= y(n) - \Phi^T(n) \hat{A}^\oplus(n/n \oplus 1),\end{aligned}\tag{D.4}$$

2. Update

$$\begin{aligned}V^\oplus(n/n \oplus 1) &= F V^\oplus(n \oplus 1/n \oplus 1) F^T + \xi \begin{bmatrix} I_p & 0 \\ 0 & 0 \end{bmatrix}, \\ V^\oplus(n/n) &= V^\oplus(n/n \oplus 1) \times [I_p - \Phi^*(n) \Phi^T(n) V^\oplus(n/n \oplus 1)], \\ &/ [1 + \Phi^T(n) V^\oplus(n/n \oplus 1) \Phi^*(n)], \\ \hat{A}^\oplus(n/n) &= \hat{A}^\oplus(n/n \oplus 1) + V^\oplus(n/n) \Phi^*(n) \epsilon^\oplus(n).\end{aligned}\tag{D.5}$$


---

## Appendix E

# Trapezoidal Rule and the Basis Function Representation

This appendix shows that the basis function representation of sound velocity variations in eqs. (4.39) and (4.40) is valid when the integral in eq.(4.34) is computed through the trapezoidal rule. The case where the sound velocity increment  $\Delta c(z)$  can be represented by a set of first degree polynomials was treated in Section 4.2.2 as the triangular pulse basis functions.

In the present discussion, the integrand  $g_m(z)\Delta c(z)$  itself [ $g_m$  is defined in eq.(4.35)] is approximated by a first degree polynomial in each depth grid interval. The trapezoidal rule is implemented as:

$$\begin{aligned}\Delta k_m &= \int_a^b g_m(z)\Delta c(z)dz \\ &= \sum_{n=1}^N w_n g_m(z_n) \Delta c(z_n) = [w_1 g_m(z_1), \dots, w_N g_m(z_N)] \mathbf{q},\end{aligned}\quad (\text{E.1})$$

where  $w_1 = 0.5h_1$ ,  $w_N = 0.5h_{N-1}$ ,  $w_n = 0.5(h_{n-1}+h_n)$ ,  $n = 2, \dots, N-1$ ,  $h_n = z_{n+1} - z_n$ ,  $\mathbf{q} = [\delta c_1, \dots, \delta c_N]$ , and  $\delta c_n = \Delta c(z_n)$ . The equality sign in eq.(E.1) indicates the assumption that the integrand can be described by a linear-by-parts function, which

usually requires a relatively dense sampling grid.

The assumption, therefore is that, in each interval  $z_j \leq z \leq z_{j+1}$ ,  $j = 1, \dots, N - 1$ ,

$$g_m(z)\Delta c(z) = \alpha_{1j}^{(m)}(z - z_j) + \alpha_{2j}^{(m)}. \quad (\text{E.2})$$

The coefficients the linear representation,  $\alpha_{ij}^{(m)}$ , are obtained by setting  $z = z_j$  and  $z = z_{j+1}$  in eq.(E.2), resulting in

$$g_m(z)\Delta c(z) = \left[ \frac{z_{j+1} - z}{h_j} g_m(z_j), \frac{z - z_j}{h_j} g_m(z_{j+1}) \right] \begin{bmatrix} \delta c_j \\ \delta c_{j+1} \end{bmatrix}. \quad (\text{E.3})$$

This result can be seen as a representation for  $\Delta c(z)$  in terms of sums of basis functions, but depends only on one function in the set  $\{g_m\}$ . Adding (E.3) over all modal kernels  $g_m$  one obtains, for  $\sum_{m=1}^M g_m(z) \neq 0$ ,

$$\Delta c(z) = \left[ \frac{z_{j+1} - z}{h_j} \frac{\sum_{m=1}^M g_m(z_j)}{\sum_{m=1}^M g_m(z)}, \frac{z - z_j}{h_j} \frac{\sum_{m=1}^M g_m(z_{j+1})}{\sum_{m=1}^M g_m(z)} \right] \begin{bmatrix} \delta c_j \\ \delta c_{j+1} \end{bmatrix}. \quad (\text{E.4})$$

This expression can be written, in terms of basis functions as

$$\Delta c(z) = [\phi_j(z), \phi_{j+1}(z)] \begin{bmatrix} \delta c_j \\ \delta c_{j+1} \end{bmatrix}, \quad z_j \leq z \leq z_{j+1},$$

which must be represented as  $\Delta c(z) = \sum_{n=1}^N \phi_n(z)\delta c_n$ . Therefore,

$$\phi_n(z) = \frac{\sum_{m=1}^M g_m(z_n)}{\sum_{m=1}^M g_m(z)} \begin{cases} (z - z_{n-1}) / (z_n - z_{n-1}), & z_{n-1} < z \leq z_n, \\ & n = 2, \dots, N, \\ (z_{n+1} - z) / (z_{n+1} - z_n), & z_n < z \leq z_{n+1}, \\ & n = 1, \dots, N - 1, \\ 0, & \text{otherwise.} \end{cases} \quad (\text{E.5})$$

In order to verify that this basis function results in the trapezoidal rule given in eq.(E.1), compute

$$\Delta \mathbf{k}_r = \int_a^b \mathbf{g}(z) \Delta c(z) dz = \left[ \int_a^b \mathbf{g}(z) \Phi^T(z) dz \right] \mathbf{q} = \left[ \sum_{j=1}^N w_j \mathbf{g}(z_j) \Phi^T(z_j) \right] \mathbf{q},$$

where  $\{w_j\}$  are the trapezoidal weights defined in eq.(E.1). At the grid points  $z = z_j$ , eq.(E.5) gives  $\phi_j(z_j) = 1$ , and  $\phi_j(z_n) = 0$ ,  $n \neq j$ . The vector  $\Phi(z_j)$  is, therefore, the unit vector  $[\delta_{1,j}, \dots, \delta_{N,j}]^T$ , where  $\delta_{m,n}$  is the Kronecker delta. Therefore,

$$\mathbf{g}(z_j) \Phi^T(z_j) = \begin{bmatrix} 0 & \cdots & \mathbf{g}(z_j) & \cdots & 0 \end{bmatrix},$$

a matrix of zeros, except for the  $j$ -th column. The above integral then becomes

$$\begin{aligned} \int_a^b \mathbf{g}(z) \Delta c(z) dz &= \left[ \int_a^b \mathbf{g}(z) \Phi^T(z) dz \right] \mathbf{q} \\ &= \left[ w_1 \mathbf{g}(z_1), \dots, w_N \mathbf{g}(z_N) \right] \mathbf{q}, \end{aligned} \quad (\text{E.6})$$

which is the matrix version of the original expression, eq.(E.1). In conclusion, eq.(E.5) describes a set of basis function representation of the sound velocity variation  $\Delta c$  corresponding to the application of trapezoidal rule when computing  $\Delta \mathbf{k}_r$ .

## Appendix F

# Analysis of Sound Velocity and Frequency Perturbations

The eigenvalue equation is

$$\left( \frac{u'_m(z)}{\rho} \right)' + \frac{k^2(z) - k_m^2}{\rho} u_m(z) = 0, \\ 0 \leq z < \infty, u_m(0) = 0, \int_0^\infty \frac{u_m^2}{\rho} dz = 1. \quad (\text{F.1})$$

Interfaces are introduced at density discontinuities where the boundary conditions of continuity of  $u_m$  and  $u'_m/\rho$  are imposed. The medium wavenumber is perturbed by small variations in the sound velocity profile and frequency,

$$\begin{aligned} k^2(\omega + \Delta\omega, c + \Delta c) &= \frac{(\omega + \Delta\omega)^2}{(c + \Delta c)^2}, \\ &= \frac{\omega^2 + 2\omega\Delta\omega + (\Delta\omega)^2}{c^2} \left[ 1 - 2\frac{\Delta c}{c} + 3\left(\frac{\Delta c}{c}\right)^2 + \dots \right], \\ &= \frac{\omega^2}{c^2} \left( 1 - 2\frac{\Delta c}{c} + 2\frac{\Delta\omega}{\omega} - 4\frac{\Delta c}{c}\frac{\Delta\omega}{\omega} + \dots \right), \\ &= k_o^2 + \epsilon k_{1c}^2 + \eta k_{1\omega}^2 + \epsilon\eta k_{2\omega c}^2 + O[(\Delta c/c)^2], \end{aligned} \quad (\text{F.2})$$

where the dummy variables  $\epsilon$  and  $\eta$  (which assume value 0, when  $\Delta c = 0$  or  $\Delta\omega = 0$ , respectively, and 1 otherwise) were introduced for bookkeeping. The subscripts in  $k^2$  indicate the order of the corresponding perturbation and which quantity is being incremented. For example,  $k_{2\omega c}$  designates a second order perturbation: first order in both frequency and sound speed. As usual, *small* means  $\Delta c/c, \Delta\omega/\omega \ll 1$ . In the perturbative inverse technique, the zero-th order quantities correspond to the background environment.

## F.1 Eigenvalues

The eigenvalues<sup>1</sup>  $k_m^2$  and eigenfunctions  $u_m$  in eq.(F.1) are expanded as [cf. eq.(F.2)]

$$k_m^2(\omega + \Delta\omega, c + \Delta c) = k_{mo}^2 + \epsilon k_{m1c}^2 + \eta k_{m1\omega}^2 + \epsilon\eta k_{m2\omega c}^2 + \dots, \quad (\text{F.3})$$

and

$$u_m(\omega + \Delta\omega, c + \Delta c) = u_{mo} + \epsilon u_{m1c} + \eta u_{m1\omega} + \epsilon\eta u_{m2\omega c} + \dots, \quad (\text{F.4})$$

where all terms in the eigenfunction expansion satisfy the same boundary conditions as  $u_n(z)$  and the radiation condition at infinity. The normalization is imposed to the zero-th order eigenfunction as defined in eq.(F.1).

Substitute the above expansions into eq.(F.1) and collect similar terms up to order 1 in the dummy variables [i.e, up to  $O((\Delta c/c)(\Delta\omega/\omega))$ ] to obtain

$$\epsilon^0, \eta^0 : (u'_{mo}/\rho)' + (k_o^2 - k_{mo}^2) u_{mo}/\rho = 0, \quad (\text{F.5})$$

$$\epsilon^1, \eta^0 : (u'_{m1c}/\rho)' + (k_o^2 - k_{mo}^2) u_{m1c}/\rho = - (k_{1c}^2 - k_{m1c}^2) u_{mo}/\rho, \quad (\text{F.6})$$

$$\epsilon^0, \eta^1 : (u'_{m1\omega}/\rho)' + (k_o^2 - k_{mo}^2) u_{m1\omega}/\rho = - (k_{1\omega}^2 - k_{m1\omega}^2) u_{mo}/\rho, \quad (\text{F.7})$$

---

<sup>1</sup>The subscript  $r$  of the eigenvalues  $k_{rm}$  is dropped here for simplicity.

and

$$\begin{aligned} \epsilon^1, \eta^1 : \quad & (u'_{m2\omega c}/\rho)' + (k_o^2 - k_{mo}^2) u_{m2\omega c}/\rho = \\ & = - (k_{2\omega c}^2 - k_{m2\omega c}^2) u_{mo}/\rho - (k_{1c}^2 - k_{m1c}^2) u_{m1\omega}/\rho - (k_{1\omega}^2 - k_{m1\omega}^2) u_{m1c}/\rho. \end{aligned} \quad (\text{F.8})$$

The perturbative equation for  $k_{1c}^2$  is obtained by multiplying eq.(F.5) by  $u_{m1c}$  and eq.(F.6) by  $u_{mo}$ , subtracting the result and integrating over the whole domain. The left-hand side becomes, after integrating by parts twice,

$$\int_0^\infty [(u'_{mo}/\rho)' u_{m1c} - (u'_{m1c}/\rho)' u_{mo}] dz = \frac{u'_{mo} u_{m1c} - u_{mo} u'_{m1c}}{\rho} \Big|_0^\infty = 0,$$

as a consequence of the boundary conditions imposed to the solutions. Therefore,

$$0 = \int_0^\infty (k_{1c}^2 - k_{m1c}^2) \frac{u_{mo}^2}{\rho} dz,$$

and, due to the normalization imposed to  $u_{mo}$ ,

$$k_{m1c}^2 = \int_0^\infty k_{1c}^2 \frac{u_{mo}^2}{\rho} dz = -2 \int_0^\infty \frac{\omega^2}{c^2} \frac{\Delta c}{c} \frac{u_{mo}^2}{\rho} dz. \quad (\text{F.9})$$

Note that, from eq.(F.3),

$$k_{m1c}^2 = k_m^2(\omega, c + \Delta c) - k_{mo}^2 + O[(\Delta c/c)^2]. \quad (\text{F.10})$$

Equations for  $k_{m1\omega}^2$  and  $k_{m2\omega c}^2$  are similarly obtained:

$$k_{m1\omega}^2 = k_m^2(\omega + \Delta\omega, c) - k_{mo}^2 + O[(\Delta\omega/\omega)^2] = 2 \int_0^\infty \frac{\omega^2}{c^2} \frac{\Delta\omega}{\omega} \frac{u_{mo}^2}{\rho} dz, \quad (\text{F.11})$$

and

$$k_{m2\omega c}^2 = \int_0^\infty \frac{1}{\rho} \left[ k_{2\omega c}^2 u_{mo}^2 + (k_{1c}^2 - k_{m1c}^2) u_{mo} u_{m1\omega} + (k_{1\omega}^2 - k_{m1\omega}^2) u_{mo} u_{m1c} \right] dz \quad (\text{F.12})$$

This last expression can be simplified. Multiply eq.(F.6) by  $u_{m1\omega}$  and eq.(F.7) by  $u_{m1c}$ , again subtract and integrate to obtain

$$0 = \int_0^\infty \left[ - (k_{1c}^2 - k_{m1c}^2) \frac{u_{mo} u_{m1\omega}}{\rho} + (k_{1\omega}^2 - k_{m1\omega}^2) \frac{u_{mo} u_{m1c}}{\rho} \right] dz,$$

and, upon substitution into eq.(F.12), one obtains

$$\begin{aligned} k_{m2\omega c}^2 &= \int_0^\infty \frac{1}{\rho} \left[ k_{2\omega c}^2 u_{mo}^2 + 2 (k_{1\omega}^2 - k_{m1\omega}^2) u_{mo} u_{m1c} \right] dz, \\ &= \int_0^\infty \frac{1}{\rho} \left[ -4 \frac{\omega^2}{c^2} \frac{\Delta c}{c} \frac{\Delta \omega}{\omega} u_{mo}^2 + 2 \left( 2 \frac{\omega^2}{c^2} \frac{\Delta \omega}{\omega} - k_{m1\omega}^2 \right) u_{mo} u_{m1c} \right] dz. \end{aligned} \quad (\text{F.13})$$

## F.2 Group Speeds

The group speed for the unperturbed (background) problem is given by

$$V_{mo}^{-1} = V_m^{-1}(\omega, c) = \frac{\partial k_m(\omega, c)}{\partial \omega} = \frac{1}{2k_m(\omega, c)} \frac{\partial k_m^2(\omega, c)}{\partial \omega}.$$

The derivative of the square eigenvalue is given by

$$\frac{\partial k_m^2(\omega, c)}{\partial \omega} = \lim_{\Delta \omega \rightarrow 0} \frac{k_m^2(\omega + \Delta \omega, c) - k_m^2(\omega, c)}{\Delta \omega},$$

where  $k_m^2(\omega + \Delta \omega, c)$  is obtained from eq.(F.3) setting  $\epsilon = 0$  and  $\eta = 1$ :  $k_m^2(\omega + \Delta \omega, c) = k_{mo}^2 + k_{m1\omega}^2 + O[(\Delta \omega / \omega)^2]$ , and  $k_m^2(\omega, c) = k_{mo}^2$  is the unperturbed eigenvalue ( $\epsilon = \eta = 0$ )

[see eq.(4.76)]. As a result,

$$\frac{1}{2} \lim_{\Delta\omega \rightarrow 0} \frac{k_{m1\omega}^2}{\Delta\omega} = k_{mo} V_{mo}^{-1} = \frac{1}{\omega} \int_0^\infty \frac{\omega^2}{c^2} \frac{u_{mo}^2}{\rho} dz, \quad (\text{F.14})$$

where eq.(F.11) was used.

For the perturbed sound velocity profile, the group speed is given by

$$V_m^{-1}(\omega, c + \Delta c) k_m(\omega, c + \Delta c) = \frac{1}{2} \frac{\partial k_m^2(\omega, c + \Delta c)}{\partial \omega},$$

where

$$\frac{\partial k_m^2(\omega, c + \Delta c)}{\partial \omega} = \lim_{\Delta\omega \rightarrow 0} \frac{k_m^2(\omega + \Delta\omega, c + \Delta c) - k_m^2(\omega, c + \Delta c)}{\Delta\omega},$$

and  $k_m^2(\omega, c + \Delta c)$  is obtained by setting  $\epsilon = 1$  and  $\eta = 0$  in eq.(F.3). The subtraction in the above expression will leave the terms with an  $\eta$  multiplier [i.e., terms in  $\Delta\omega$  and  $(\Delta\omega)^2$ ]. Keeping the terms up to order 1 in  $\Delta\omega$  (the ones in order 2 will be set to zero when  $\Delta\omega \rightarrow 0$ ) and order 1 in  $\Delta c$ , the group speed  $V_{m1}$  is obtained as

$$V_{m1}^{-1} k_m(\omega, c + \Delta c) \simeq \frac{1}{2} \lim_{\Delta\omega \rightarrow 0} \frac{k_{m1\omega}^2 + k_{m2\omega c}^2}{\Delta\omega}.$$

Using eqs.(F.11), (F.13), and (F.14) one then obtains

$$\begin{aligned} V_{m1}^{-1} k_m(\omega, c + \Delta c) \simeq k_{mo} V_{mo}^{-1} + \frac{-2}{\omega} \int_0^\infty & \left[ \frac{\omega^2}{c^2} \frac{\Delta c}{c} \frac{u_{mo}^2}{\rho} \right. \\ & \left. - \left( \frac{\omega^2}{c^2} - \omega k_{mo} V_{mo}^{-1} \right) \frac{u_{mo} u_{m1c}}{\rho} \right] dz. \quad (\text{F.15}) \end{aligned}$$

### F.3 Perturbative Integral with Source Speed Compensation

Equation (4.73) suggests that the measured, Doppler shifted wavenumbers be corrected using

$$k_m^d = k_m(\omega + \Delta\omega, c + \Delta c) = k_m(\omega, c + \Delta c) + k_m^d v_s V_{m1}^{-1},$$

which, to the first order in  $v_s V_{m1}^{-1}$ , results in

$$k_m^d = k_m(\omega, c + \Delta c) (1 - v_s V_{m1}^{-1})^{-1} \simeq k_m(\omega, c + \Delta c) (1 + v_s V_{m1}^{-1}). \quad (\text{F.16})$$

To the first order in  $\Delta c$ , the correction in the eigenvalue due to a change in sound velocity alone is  $k_{m1c}^2$ , as given by eq.(F.3):

$$\begin{aligned} k_m^2(\omega, c + \Delta c) - k_{mo}^2 &\simeq 2 [k_m(\omega, c + \Delta c) - k_{mo}] k_{mo} \simeq -2 \int_0^\infty \frac{\omega^2}{c^2} \frac{\Delta c}{c} \frac{u_{mo}^2}{\rho} dz, \\ \Rightarrow k_m(\omega, c + \Delta c) - k_{mo} &\simeq \frac{-1}{k_{mo}} \int_0^\infty \frac{\omega^2}{c^2} \frac{\Delta c}{c} \frac{u_{mo}^2}{\rho} dz. \end{aligned} \quad (\text{F.17})$$

This is the usual perturbative integral [cf. eq.(4.3)]. What is needed for source motion compensation is the difference between the background and measured eigenvalue,  $k_m^d - k_{mo}$ . Using eqs.(F.16) and (F.17), one obtains

$$\begin{aligned} k_m^d - k_{mo} &= k_m(\omega, c + \Delta c) - k_{mo} + k_m(\omega, c + \Delta c) v_s V_{m1}^{-1} \\ &\simeq \frac{-1}{k_{mo}} \int_0^\infty \frac{\omega^2}{c^2} \frac{\Delta c}{c} \frac{u_{mo}^2}{\rho} dz + k_m(\omega, c + \Delta c) v_s V_{m1}^{-1}. \end{aligned}$$

Neglecting the contribution from  $u_{m1c}$  in eq.(F.15), the above expression becomes, after a few manipulations,

$$k_m^d - k_{mo} \simeq \frac{-1}{k_{mo}} \left( 1 + 2 \frac{v_s k_{mo}}{\omega} \right) \int_0^\infty \frac{\omega^2}{c^2} \frac{\Delta c}{c} \frac{u_{mo}^2}{\rho} dz + v_s k_{mo} V_{mo}^{-1}, \quad (F.18)$$

which is the desired result.

# Bibliography

- [1] K. Aki and P. G. Richards. *Quantitative Seismology: theory and methods*. W. H. Freeman, San Francisco, CA, 1980.
- [2] Brian D. O. Anderson and John B. Moore. *Optimal Filtering*. Prentice-Hall, Englewood Cliffs, NJ, 1979.
- [3] G. Athanassoulis and V. Papanicolaou. Eigenvalue asymptotics of layered media and their application to the inverse problems. *SIAM J. Appl. Math.*, 57:453–471, 1997.
- [4] G. Backus and F. Gilbert. Uniqueness in the inversion of inaccurate gross earth data. *Phil. Trans. Royal Soc. A*, 266(1173):187–269, March 1970.
- [5] K. M. Becker, S. D. Rajan, and G. V. Frisk. Results from the geoacoustic inversion techniques workshop using modal inverse methods. *IEEE Journal of Oceanic Engineering*, 28(3):331–341, July 2003. Special issue on geoacoustic inversion in range-dependent shallow-water environments.
- [6] Kyle M. Becker. *Geoacoustic inversion in laterally varying shallow-water environment using high-resolution wavenumber estimation*. PhD thesis, MIT and WHOI, Cambridge and Woods Hole, MA, 2001.
- [7] Kyle M. Becker and George V. Frisk. High resolution modal mapping in a complex shallow-water environment. *Journal of the Acoustical Society of America*, 105(2):1310, 1999.

[8] Khosrow Chadan, David Colton, Lassi P  iv  rinta, and William Rundell. *An Introduction to Inverse Scattering and Inverse Spectral Problems*. SIAM, Philadelphia, PA, 1997.

[9] N. Ross Chapman, Stanley Chin-Bing, David King, and Richard B. Evans. Benchmarking geoacoustic inversion methods for range-dependent waveguides. *IEEE Journal of Oceanic Engineering*, 28(3):320–330, July 2003. Special issue on geoacoustic inversion in range-dependent shallow-water environments.

[10] Clarence S. Clay and Herman Medwin. *Acoustical Oceanography: Principles and Applications*. John Wiley, New York, NY, 1977.

[11] L. Cohen. *Time-frequency analysis*. Prentice-Hall, Englewood Cliffs, NJ, 1995.

[12] C. de Boor. *Spline Toolbox User's Guide version 3*. The MathWorks, Inc., Natick, MA, 2000.

[13] Christian de Moustier and Luiz L. Souza, Chairs. Acoustical surveys of ocean bottom geology I and II. *Journal of the Acoustical Society of America*, 107(5 Pt. 2), May 2000. Special Sessions of the 139th Meeting of the Acoustical Society of America, Atlanta, GA, 30 May–3 June.

[14] Robert Field, George Frisk, Patrick Gallacher, Zachariah Hallock, Hisayuki Kanda, John Kemp, Sayuri Matsumoto, Shinya Matsumoto, Peter Mignerey, Itaru Morishita, Joal Newcomb, Kazuhiko Ohta, Keiichi Ohkawa, Masamichi Oikawa, Kouki Okabe, Marshall Orr, William Sawyer, James Showalter, , Luiz Souza, Gaku Takei, Altan Turgut, Chad Vaughan, Don Walter, Tokuo Yamamoto, and Haruhiko Yamada. An overview of the 2000 SWAT experiments. *IEEE Journal of Oceanic Engineering*, 2004. submitted.

[15] Robert Field, Joal Newcomb, James Showalter, and Jacob George. Horizontal wavenumbers from a fluctuating waveguide. *Journal of the Acoustical Society of America*, 2004. submitted.

ciety of America, 112(5):2310, November 2002. Presented at the First Pan-American/Iberian Meeting on Acoustics, Cancun, Mexico, 2–6 December.

- [16] T. R. Fortescue, L. S. Kershenbaum, and B. E. Ydstie. Implementation of self-tuning regulators with variable forgetting factors. *Automatica*, 17(6):831–835, 1981.
- [17] Joel N. Franklin. Well-posed stochastic extensions of ill-posed linear problems. *Journal of Mathematical Analysis and Applications*, 31:682–716, 1970.
- [18] G. V. Frisk, K. M. Becker, and J. A. Doutt. Modal mapping in shallow water using synthetic aperture horizontal arrays. In *OCEANS 2000 MTS/IEEE Conference and Exhibition, 11–14 Sep. 2000, Providence, RI*, volume 1, pages 185–188, September 2000.
- [19] George V. Frisk. *Ocean and Seabed Acoustics: a theory of wave propagation*. Prentice-Hall, Englewood Cliffs, NJ, 1994.
- [20] George V. Frisk. LWAD 99-1 modal mapping experiment II (MOMAX II). Technical report, Woods Hole Oceanographic Institution, January 3 2000.
- [21] George V. Frisk, James A. Doutt, and Earl E. Hays. Geoacoustic models for the Icelandic Basin. *Journal of the Acoustical Society of America*, 80(2):591–600, August 1986.
- [22] George V. Frisk, Alan V. Oppenheim, and D. R. Martinez. A technique for measuring the plane-wave reflection coefficient of the ocean bottom. *Journal of the Acoustical Society of America*, 68(2):602–612, August 1980.
- [23] George V. Frisk, Luiz Souza, Douglas R. Mook, James A. Doutt, Earl E. Hays, Michael S. Wengrovitz, and Alan V. Oppenheim. The application to experimental data of a technique for measuring the plane-wave reflection coefficient of the ocean bottom. Woods Hole Oceanographic Institution, to be submitted, 2004.

[24] George V. Frisk, Luiz L. Souza, and Kyle M. Becker. Application of the Gelfand-Levitan method to inversion of the sound velocity profile in the seabed: Theory and experiment. *IPMS 2002 The First International Conference "Inverse Problems: Modeling and Simulation", Fethiye, Turkey, July 14–21, 2002*.

[25] I. M. Gelfand and B. M. Levitan. On the determination of a differential equation from its spectral function. *American Mathematical Society Transactions, Series 2*, 1955.

[26] Peter Gerstoft and N. Ross Chapman, Chairs. Geoacoustic inversion I and II. *Journal of the Acoustical Society of America*, 113(4 Pt. 2), April 2003. Special Sessions of the 145th Meeting of the Acoustical Society of America, Nashville, TN, 28 April–2 May.

[27] Gene H. Golub, Per Christian Hansen, and Dianne P. O'Deary. Tikhonov regularization and total least squares. *SIAM Journal of Matrix Analysis and Applications*, 21(1):185–194, 1999.

[28] F. Gustafsson, S. Gunnarsson, and L. Ljung. Shaping frequency-dependent time resolution when estimating spectral properties with parametric methods. *IEEE Transactions on Signal Processing*, 45(4):1025–1035, 1997.

[29] W. Hackbusch. *Integral equations : Theory and Numerical Treatment*. Birkhauser Verlag, Boston, MA, 1995.

[30] Fredric J. Harris. On the use of windows for harmonic analysis with the discrete fourier transform. *Proceedings of the IEEE*, 66(1):51–83, January 1978.

[31] K. E. Hawker. A normal mode theory of acoustic doppler effects in the oceanic waveguide. *Journal of the Acoustical Society of America*, 65(unknown):675–681, unknown 1979.

- [32] Stanley Lawrence Marple Jr. *Digital Spectral Analysis with Applications*. Prentice-Hall, Englewood Cliffs, NJ, 1987.
- [33] Thomas Kailath, Ali H. Sayed, and Babak Hassibi. *Linear Estimation*. Prentice-Hall, Upper Saddle River, NJ, 2000.
- [34] Edward W. Kamen. On the inner and outer poles and zeros of a linear time-varying system. In *Proceedings of the 27th IEEE Conference on Decision and Control, 7–9 Dec, Austin, TX*, volume 2, pages 910–914. IEEE, 1988.
- [35] Edward W. Kamen. The poles and zeros of a linear time-varying system. *Linear Algebra and Its Applications*, 98:263–289, 1988.
- [36] Edward W. Kamen, P. P. Khargonekar, and K. R. Poola. A transfer-function approach to linear time-varying discrete-time systems. *SIAM Journal Control and Optimization*, 23(4):550–565, July 1985.
- [37] Steven M. Kay. *Fundamentals of Statistical Signal Processing: estimation theory*. Prentice-Hall, Upper Saddle River, NJ, 1993.
- [38] A. Salim Kayhan. Difference equation representation of chirp signals and instantaneous frequency/amplitude estimation. *IEEE Transactions on Signal Processing*, 44(12):2948–2958, December 1996.
- [39] Bui Doan Khanh. A numerical resolution of the Gelfand- Levitan equation. *J. Comput. Appl. Math.*, 72:235–244, 1996.
- [40] Harry B. Lee. The Cramér-Rao bound on frequency estimates of signals closely spaced in frequency. *IEEE Transactions on Signal Processing*, 40(6):1508–1517, June 1992.
- [41] P. T. Leung, S. Y. Liu, and K. Young. Completeness and time-independent perturbation of the quasinormal modes of an absorptive and leaky cavity. *Physical Review A*, 49(5):3982–3989, May 1994.

[42] P. T. Leung, S. S. Tong, and K. Young. Two-component eigenfunction expansion for open systems described by the wave equation I: completeness of expansion. *Journal of Physics A: Mathematical and General*, 30(6):2139–2151, March 1997. Quasinormal modes (QNM) are defined as the set of eigenfunctions of open systems, like laser optical cavities, where energy leaks to the outside and the eigenfunctions are not normal. Under certain conditions, the QNM form a complete set in a finite interval.

[43] Ying-Tsong Lin, Chi-Fang Chen, and James F. Lynch. An equivalent transform method for evaluating the effect of water column mismatch on geoacoustic inversion. *Journal of the Acoustical Society of America*, 115(5, Pt. 2):2409, 2004. Presented at the 147th Meeting of the Acoustical Society of America, 24–28 May, New York, NY.

[44] L. Ljung. Analysis of a general recursive prediction error identification algorithm. *Automatica*, 17(1):89–99, 1981.

[45] Andre Merab. *Exact reconstruction of ocean bottom velocity profiles from monochromatic scattering data*. PhD thesis, MIT/WHOI Joint Program, Cambridge and Woods Hole, MA, 1987.

[46] Douglas R. Mook. *The Numerical Synthesis and Inversion of Acoustic Fields using the Hankel Transform with Application to the Estimation of the Plane-Wave Reflection Coefficient of the Ocean Bottom*. PhD thesis, MIT/WHOI Joint Program, Cambridge and Woods Hole, MA, 1983.

[47] Douglas R. Mook, George V. Frisk, and Alan V. Oppenheim. A hybrid numerical/analytic technique for the computation of wave fields in stratified media based on the Hankel transform. *Journal of the Acoustical Society of America*, 76(1):222–243, July 1984.

[48] A. Nehorai and D. Starer. Adaptive pole estimation. *IEEE Transactions on Acoustics, Speech, and Signal Processing*, ASSP-38(5):825–838, 1990.

[49] Maciej Niedźwiecki. Identification of nonstationary stochastic systems using parallel estimation schemes. *IEEE Transactions on Automatic Control*, 35(3):329–334, 1990.

[50] Maciej Niedźwiecki. Multiple-model approach to finite memory adaptive filtering. Presented at the 11th World Congress of the International Federation of Automatic Control (IFAC), Tallinn, Estonia, 13-17 August, 1990.

[51] Maciej Niedźwiecki. Identification of time-varying systems with abrupt parameter changes. *Automatica*, 30(3):447–459, 1994.

[52] Maciej Niedźwiecki. *Identification of Time-varying Processes*. Wiley, Chichester, England, 2000.

[53] N. N. Novikova. An application of the Padé approximation to the inverse problem of monochromatic vibrosounding. *Inverse Problems*, 11(1):217–229, February 1995.

[54] K. Ohta and George V. Frisk. Modal evolution and inversion for seabed properties in weakly range-dependent shallow-water waveguides. *IEEE Journal of Oceanic Engineering*, 22(3):501–521, July 1997. abstract in folder.

[55] Alan V. Oppenheim and Alan S. Willsky. *Signals & Systems*. Prentice Hall, Upper Saddle River, NJ, 2 edition, 1997. With S. Hamid Nawab.

[56] Sophocles J. Orfanidis. *Optimum Signal Processing: an introduction*. McGraw-Hill, New York, NY, 2 edition, 1988.

[57] Michael B. Porter. The KRAKEN normal mode program. Technical report, SACLANT Undersea Research Center, La Spezia, Italy, 1991.

[58] William H. Press, Saul A. Teukolsky, William T. Vetterling, and Brian P. Flannery. *Numerical Recipes in C: The Art of Scientific Computing*. Cambridge University, New York, NY, 2, reprint edition, 1996.

[59] M. P. Quirk. Improving resolution for autoregressive spectral estimation by decimation. *IEEE Transactions on Acoustics, Speech, and Signal Processing*, ASSP-31(3):630–637, 1983.

[60] Subramaniam D. Rajan. Determination of geoacoustic parameters of the ocean bottom–data requirements. *Journal of the Acoustical Society of America*, 92(4):2126–2140, October 1990.

[61] Subramaniam D. Rajan, James F. Lynch, and George V. Frisk. Perturbative inversion methods for obtaining bottom geoacoustic parameters in shallow water. *Journal of the Acoustical Society of America*, 82(3):998–1017, September 1987.

[62] D. C. Rife and R. R. Boorstyn. Multiple tone parameter estimation from discrete-time observations. *Bell System Technical Journal*, 55(9):1389–1410, November 1976.

[63] Henrik Schmidt and W. A. Kuperman. Spectral and modal representations of the Doppler-shifted field in ocean waveguides. *Journal of the Acoustical Society of America*, 96(1):386–395, July 1994.

[64] P. Shan and A. A. Beex. High-resolution instantaneous frequency estimation based on time-varying ar modeling. In *Proceedings of the IEEE-SP International Symposium on Time-frequency and Time-Scale Analysis, 6-9 October, Pittsburgh, PA*, pages 109–112, 1998.

[65] James G. Simmonds and James E. Mann Jr. *A First Look at Perturbation Theory*. Dover, Mineola, NY, 2 edition, 1998.

[66] Luiz L. Souza, Kyle M. Becker, and George V. Frisk. Practical approaches for utilizing the plane-wave reflection coefficient as input data for inferring geoacoustic

properties of the seabed. *Journal of the Acoustical Society of America*, 107(5, Pt. 2):2775, 2000. Presented at the 139th Meeting of the Acoustical Society of America, 30 May–3 June, Atlanta, GA.

[67] Luiz L. Souza and George V. Frisk. Perturbative inversion method for range-varying seabed sound speed profile estimation. *Journal of the Acoustical Society of America*, 115(5, Pt. 2):2407, 2004. Presented at the 147th Meeting of the Acoustical Society of America, 24–28 May, New York, NY.

[68] Luiz L. Souza, George V. Frisk, and Kyle M. Becker. Application of the Gelfand-Levitin method to inverse problems in seabed acoustics. In *2001 SIAM annual Meeting July 9-13, 2001, San Diego, CA: final program and abstracts*, 2001.

[69] William M. Steedly and Randolph L. Moses. The the Cramér-Rao bound for pole and amplitude coefficient estimates of damped exponential signals in noise. *IEEE Transactions on Signal Processing*, 41(3):1305–1318, March 1993.

[70] David Stickler. A shallow water ocean acoustic inverse problem. *Journal of the Acoustical Society of America*, 115(5, Pt. 2):2407, 2004. Presented at the 147th Meeting of the Acoustical Society of America, 24–28 May, New York, NY.

[71] R. D. Stoll, G. M. Bryan, R. Flood, D. Chayes, and P. Manley. Shallow seismic experiments using shear waves. *Journal of the Acoustical Society of America*, 83(1):93–102, January 1988.

[72] Robert D. Stoll. *Sediment Acoustics*. Springer-Verlag, Berlin, 1989.

[73] Gilbert Strang. *Linear Algebra and Its Applications*. Harcourt Brace, Orlando, FL, 3 edition, 1986.

[74] Michael I. Taroudakis and George Makrakis, editors. *Inverse Problems in Underwater Acoustics*. Springer, New York, NY, 2001.

- [75] Ivan Tolstoy and C. S. Clay. *Ocean Acoustics: Theory and Experiment in Underwater Sound*. American Intitute of Physics, New York, NY, 1987.
- [76] G. N. Watson. *Theory of Bessel Functions*. Cambridge Un. Press, New York, NY, 2 edition, 1966.

<b>REPORT DOCUMENTATION PAGE</b>		<b>1. REPORT NO.</b> <b>MIT/WHOI 2005-03</b>	<b>2.</b>	<b>3. Recipient's Accession No.</b>
<b>4. Title and Subtitle</b>  Inversion for Subbottom Sound Velocity Profiles in the Deep and Shallow Ocean		<b>5. Report Date</b> February 2005		
		<b>6.</b>		
<b>7. Author(s)</b> Luiz L. Souza		<b>8. Performing Organization Rept. No.</b>		
<b>9. Performing Organization Name and Address</b>  MIT/WHOI Joint Program in Oceanography/Applied Ocean Science & Engineering		<b>10. Project/Task/Work Unit No.</b> MIT/WHOI 2005-03		
		<b>11. Contract(C) or Grant(G) No.</b> N00014-03-1-0397 (C) (G)		
<b>12. Sponsoring Organization Name and Address</b>  Office of Naval Research WHOI Academic Programs Office		<b>13. Type of Report &amp; Period Covered</b> Ph.D. Thesis		
		<b>14.</b>		
<b>15. Supplementary Notes</b> This thesis should be cited as: Luiz L. Souza, 2004. Inversion for Subbottom Sound Velocity Profiles in the Deep and Shallow Ocean. Ph.D. Thesis. MIT/WHOI, 2005-03.				
<b>16. Abstract (Limit: 200 words)</b> We investigate the application of acoustic measurements in the ocean to measure the sound velocity profile (svp) in the subbottom. For the deep water ocean, an exact method based on the Gelfand-Levitant integral equation is evaluated. The input data is the complex plane-wave reflection coefficient. We apply the method to experimental acoustic data and estimate the reflection coefficient and the svp in the seabed.  For the shallow ocean, an inverse eigenvalue technique is developed. The input data are range-varying eigenvalues associated with propagating modes. We investigate the estimation of eigenvalues from fields measured in laterally varying shallow environments, in particular the errors associated with autoregressive (AR) methods. We propose and analyze two sequential estimators, one for AR coefficients, another for the zeros of the AR characteristic polynomial. The decimation of pressure fields is analyzed as a tool to improve eigenvalue estimation.  The solution to the inverse eigenvalue problem is proposed in the form of a Kalman filter. The resolution and variance of the inferred svp are analyzed in terms of the Cramer--Rao lower bound and the Backus--Gilbert (BG) resolution theory. A method is developed to compensate for the Doppler deviation observed in experiments with moving sources.				
<b>17. Document Analysis</b> <b>a. Descriptors</b> Geoacoustic inversion Normal modes Gelfand-Levitant method				
<b>b. Identifiers/Open-Ended Terms</b>				
<b>c. COSATI Field/Group</b>				
<b>18. Availability Statement</b>  Approved for publication; distribution unlimited.		<b>19. Security Class (This Report)</b> <b>UNCLASSIFIED</b>	<b>21. No. of Pages</b> 301	
		<b>20. Security Class (This Page)</b>	<b>22. Price</b>	